

**INTERACTION BETWEEN WEAR AND ROLLING
CONTACT FATIGUE IN PEARLITIC RAIL STEELS**

Thesis submitted for the degree of
Doctor of Philosophy
at the University of Leicester

by
Wa'il Radwan Ali Tyfour

Supervisor: Dr. John H. Beynon
Co-supervisor: Dr. Ajay Kapoor

Department of Engineering
University of Leicester

April 1995

UMI Number: U068868

All rights reserved

INFORMATION TO ALL USERS

The quality of this reproduction is dependent upon the quality of the copy submitted.

In the unlikely event that the author did not send a complete manuscript and there are missing pages, these will be noted. Also, if material had to be removed, a note will indicate the deletion.



UMI U068868

Published by ProQuest LLC 2015. Copyright in the Dissertation held by the Author.
Microform Edition © ProQuest LLC.

All rights reserved. This work is protected against
unauthorized copying under Title 17, United States Code.



ProQuest LLC
789 East Eisenhower Parkway
P.O. Box 1346
Ann Arbor, MI 48106-1346



INTERACTION BETWEEN WEAR AND ROLLING CONTACT FATIGUE IN PEARLITIC RAIL STEELS

Wa'il Radwan Ali Tyfour

ABSTRACT

The work presented in this thesis is aimed at investigating the interaction between wear and rolling contact fatigue, which are two of the most serious forms of deterioration caused by the wheel on rail contact stresses. Wheel-rail contact conditions were simulated by a two disc contact using the LEROS (LEicester university ROLLing-Sliding wear testing machine). Investigation of the wear behaviour of BS11 pearlitic rail steel showed that steady state wear behaviour is established after a certain number of rolling-sliding cycles. Contact surface failure by ratchetting (accumulation of unidirectional plastic strain) was found to be the dominant failure mechanism during the period leading to the steady state. This mechanism was confirmed by the drop in the wear rates when the direction of rolling-sliding; *i.e.* strain in the surface layer, was reversed at predetermined numbers of cycles. The effect of repeated rolling direction reversals on crack morphology, propagation and rolling contact fatigue (RCF) life of BS11 rail steel was also investigated. It was established that rolling direction reversal has a beneficial effect on RCF life. A new mechanism, the "variable crack face friction mechanism", was proposed to explain this effect.

Interaction between wear and RCF fatigue was investigated through rolling-sliding experiments where specimens were run dry for certain number of cycles, to induce different levels of wear damage, before the fatigue performance was investigated. It was shown that initial dry cycles above a critical number causes sudden and significant deterioration in RCF life. This deterioration has been explained in terms of the role of the accumulation unidirectional plastic strain (ratchetting) in initiating and propagating the early cracks during the dry phase. A strong correlation was found between the total ratchetting strain induced during the dry phase and the deterioration in RCF life. An empirical relationship to estimate this deterioration was concluded.

PREFACE

It has been a privilege for the author to be a member of the Mechanical Materials Research Group of the Department of Engineering at Leicester University. It was a great pleasure to work with a group of such a wide spectrum of academic backgrounds. The work presented in this thesis could not have been possible without the continuous help and support of the staff and colleagues in the Department. In this regard, the author wishes to thank the Head of Department Professor N. B. Jones for the excellent availability of the research facilities.

The author is grateful to his supervisor Dr. John H. Beynon for his patience, encouragement, guidance and helpful comments and suggestions. Dr Beynon is thanked for all the time and resources he devoted for the project. When the author's co-supervisor Dr Ajay Kapoor joined the department, in January 1994, his suggestions, encouragement and experience added another momentum to the project. The author wishes to thank him for his support and help.

The opportunity given to the author to discuss parts of his work with some of the very distinguished scientists in the field of the research topic is highly appreciated. The invaluable comments of Professor K. L. Johnson, Professor A. R. S. Ponter and Professor P. B. Oxley, Dr. David Kelly and many of those who showed interest in the results, is acknowledged. The helpful comments of Dr. Kevin Sawley and Dr. W. Manners, who was the author's co-supervisor during the first two years of the project, are also acknowledged. John E. Garnham is thanked for making his collection of references accessible.

The experimental phase of the project could not have been accomplished without the collaboration of experimental officer Colin Morrison and all the technical staff in the laboratories and workshops, particularly Peter Barwell, Alan Wale, Tony Forryan, Geoff O'Connor, Graham Clarke, Sandy Lightfoot, Chris Day, and the photographer of the department Paul Smith.

Finally, the author would like to thank the British Railways Board and ABB British Wheelset Ltd. who supplied the rail and wheel materials used during this work. The financial support of Mu'tah University of Jordan and The British Council is also appreciated.

CONTENTS

	<i>Page</i>
PREFACE	I
NOMENCLATURE	i
CHAPTER 1: INTRODUCTION	1.1
CHAPTER 2: LITERATURE REVIEW	2.1
2-1. TRIBOLOGY OF THE WHEEL-RAIL SYSTEM	2.1
2-1-1. Contact mechanics	2.1
2-1-2. Contact of elastic bodies	2.1
2-1-3. Contact of cylindrical bodies (line contact)	2.4
2-1-4. Rolling contact	2.6
2-1-5. Wheel rail contact	2.7
2-1-5-1. Operating conditions	
2-2. RAIL DETERIORATION DUE TO WHEEL-RAIL CONTACT	2.10
2-2-1. Introduction	2.10
2.2.2. Rail wear	2.10
2-2-2-1. Wear types in general	2.10
2-2-3. Rail wear classification	2.13
2-2-4. Rolling contact fatigue of rail	2.13
2-2-5. Effect of operating conditions on rail deterioration	2.14
2.2.6. Closing remarks	2.18
2-3. RAIL STEELS	2.19
2-3-1. Rail steel selection criteria	2.19
2-3-2. Pearlitic rail steels	2.19
2-4. WEAR AND ROLLING CONTACT FATIGUE TESTING	2.21
2-4-1. Introduction	2.21
2-4-2. Simulation techniques	2.22
2-4-3. Rolling contact fatigue failure criteria	2.23
REFERENCES	2.25
CHAPTER 3: TEST EQUIPMENT, MATERIALS, PROCEDURE AND CONDITIONS	3.1
3-1. LEICESTER UNIVERSITY ROLLING-SLIDING TESTING MACHINE	3.1
3-2. TEST MATERIALS AND SPECIMENS	3.3
3-3. TEST PROCEDURE	3.4
3-3-1. Prior testing	3.4
3-3-2. During testing	3.5
3-3-3. After testing	3.6
3-4. TEST GENERAL CONDITIONS	3.6
REFERENCES	3.8
CHAPTER 4: THE STEADY STATE WEAR BEHAVIOUR OF BS11 RAIL STEEL	4.1
4-1. INTRODUCTION	4.1

4-2. TEST RESULTS	4.2
4-2-1. Number of rolling cycles to establish steady state wear rate	4.2
4-2-2. Strain hardening behaviour	4.4
4-2-3. Accumulated plastic strain	4.4
4-2-4. Coefficient of traction	4.5
4-3. DISCUSSION	4.5
4-3-1. Weight loss and plastic flow	4.5
4-3-2. Measurement of the accumulated plastic strain	4.5
4-3-3. Ratchetting failure	4.6
4-3-4. Traction coefficient	4.10
4-4. CONCLUSIONS	4.11
REFERENCES	4.13
CHAPTER 5: EFFECT OF ROLLING DIRECTION REVERSAL ON THE WEAR BEHAVIOUR OF BS11 RAIL STEEL	5.1
5-1. INTRODUCTION	5.1
5-2. RESULTS	5.1
5-2-1. Common features	5.2
5-2-2. Unidirectional rolling	5.3
5-2-3. Tests under conditions of single rolling direction reversal	5.4
5-2-4. Tests under conditions of multiple rolling direction reversal	5.6
5-3. DISCUSSION	5.7
5-3-1. Reliability of results	5.7
5-3-2. Other factors affecting the wear behaviour	5.7
5-3-3. Effect of manganese sulphide inclusions	5.9
5-3-4. Effect of strain hardening on deformation morphology and wear behaviour	5.9
5-3-5. Effect of rolling direction reversal regime	5.10
5-4. SUMMARY	5.11
5-5. CONCLUSIONS	5.11
REFERENCES	5.13
CHAPTER 6: ROLLING CONTACT FATIGUE OF RAIL STEELS	6.1
6-1. INTRODUCTION	6.1
6-2. BOWER'S ROLLING CONTACT FATIGUE CRACK PROPAGATION MECHANISM	6.1
6-3. PERFORMANCE OF BS11 AND MILL HEAT TREATED STEELS UNDER ROLLING CONTACT FATIGUE CONDITIONS	6.3
6-3-1. Test conditions	6.4
6-3-2. Test results and discussion	6.4
6-4. CONCLUSIONS	6.9
REFERENCES	6.10

CHAPTER 7: EFFECT OF ROLLING DIRECTION REVERSAL ON ROLLING CONTACT FATIGUE CRACK PROPAGATION AND MORPHOLOGY	7.1
7-1. INTRODUCTION	7.1
7-2. RESULTS	7.1
7-3. DISCUSSION	7.4
7-3-1. The variable crack face friction mechanism	7.5
7-4. SUMMARY	7.8
7-5. CONCLUSIONS	7.9
REFERENCES	7.10
CHAPTER 8: EFFECT OF DRY ROLLING-SLIDING ON ROLLING CONTACT FATIGUE	8.1
8-1. INTRODUCTION	8.1
8-2. RESULTS	8.1
8-2-1. Coefficient of friction	8.3
8-2-2. Hardness below the contact surface	8.4
8-3. DISCUSSION	8.4
8-3-1. A physical model	8.4
8-3-2. The role of ratchetting	8.6
8-3-3. The effect of dry-wet cycling	8.9
8-4. CONCLUSIONS	8.12
REFERENCES	8.13
CHAPTER 9: GENERAL DISCUSSION AND CONCLUSIONS	9.1
9-1. INTRODUCTION	9.1
9-1-1. Interaction between wear and rolling contact fatigue	9.1
9-2. GENERAL CONCLUSIONS	9.2
REFERENCES	9.4
CHAPTER 10: AREAS OF FURTHER RESEARCH	10.1
APPENDICES	

NOMENCLATURE

X, Y, Z	Rectangular co-ordinates
A, B, C	Constants
R_1, R_2	Radii of curvature of contacting bodies 1 and 2, respectively
T_1, T_2	Distant points on contacting bodies 1 and 2, respectively
$\bar{U}_{z_1}, \bar{U}_{z_2}$	Surface displacements of bodies 1 and 2, parallel to contact load
p	Contact pressure
p_0	Maximum contact pressure
r	Distance from the contact centre
a	Semi-contact width
E	Modulus of elasticity
ν	Poisson's ratio
R	Equivalent radius of curvature, $\frac{1}{R} = \frac{1}{R_1} + \frac{1}{R_2}$
E^*	Contact modulus of elasticity, $\frac{1}{E^*} = \frac{1-\nu_1^2}{E_1} + \frac{1-\nu_2^2}{E_2}$
δ	Approach of distant points in two solids in contact
W	Contact load
p_m	Contact mean pressure
P	Contact load per unit length
$\sigma_x, \sigma_y, \sigma_z$	Contact stresses in X, Y, and Z directions
τ	Principal shear stress
RCF	Rolling contact fatigue
L	Rolling contact fatigue life
g	Percentage creepage
S	Interlamellar spacing in pearlite
MHT	Mill heat treated pearlitic rail steel
R_T, R_B	Radii of top (braking) and bottom (driving) test discs, respectively
N_T, N_B	Revolution counts of top and bottom discs, respectively
ϵ	Shear strain
γ	Shear angle

τ_{xz}	Shear stress in X-Z-co-ordinates
k	Shear yield strength
μ	Friction coefficient
RDR	Rolling direction reversal
SRDR	Single rolling direction reversal
MRDR	Multiple rolling direction reversals
f	Traction coefficient
$q(x)$	Surface traction at a distance x from the contact centre
$p(x)$	Normal pressure distribution as a function of x
RF	Reversal factor
C_r	Number of cycles per reversal
L_u	RCF life in unidirectional rolling
N_{eff}	Effective number of cycles ($\mu > 0.25$)
μ_{eff}	Effective friction coefficient
μ_{fin}	Friction coefficient at the end of the test
k_{eff}	Effective shear yield strength
k_0	Shear yield strength of the unstrained material
H_0	Bulk hardness
H_{eff}	Effective hardness
P_{eff}	Effective ratchetting load
P_s	Plastic shakedown limit
P_r	Severity of loading above the shakedown limit
Rd	Total ratchetting strain

Chapter 1

INTRODUCTION

The cost of the attention paid to the different forms of rail deterioration caused by wheel/rail contact forms a substantial proportion of the overall cost of track maintenance. Wear is the main criterion for rail replacement. Efforts to minimise wear rates through wheel and rail profile design, selection of material and improving the operating conditions never stop. The use of lubricants has reduced rail wear rates significantly. However, this reduction has not been achieved without a price. The introduction of fluid lubricants to the wheel-rail contact area has given rise to another serious kind of rail deterioration, that due to rolling contact fatigue. This phenomenon has been given considerable attention since its potential to develop transverse rail fracture and cause derailments remains a real threat.

Since both wear and rolling contact fatigue are two forms of deterioration caused by the same contact, it is thought that an interaction may exist between the two phenomena. The work presented in this thesis is aimed at investigating the areas where wear and rolling contact fatigue may interact, and has been focused on pearlitic rail steels, these being the most widely used material for rail application.

The results obtained, which are directly focused at the wheel-rail contact in particular, can also be beneficial for other counter-conformal loaded contact applications, where the contact conditions are akin to those of the wheel-rail system such as gears, chains, overhead crane railing systems and wheel-sprocket systems. Certainly the difference in loading and other operating conditions has to be taken into consideration in this case.

Despite the results being obtained under laboratory conditions, where only a selection of operating conditions, rather than the whole range, could be investigated during a particular test, these results have contributed in providing a clearer insight to the mechanisms of rail deterioration due to wheel-rail contact. These contributions have been the subject of four papers, three of which have already been published in *TRIBOLOGY INTERNATIONAL* and *WEAR* while one is awaiting final review, APPENDICES 1 to 4.

The thesis chapters are arranged in such a way that each chapter forms an independent unit for those who are interested in a particular aspect. Each chapter contains all the information needed including references, which are quoted in superscript

parenthesis, and figures and tables, the identification of which are quoted in ordinary parenthesis. However, different chapters are also inter-linked so that a logical and smooth transition is felt between the consequent chapters. In total, the thesis consists of ten chapters. Chapter 1, this chapter, is the introduction to the thesis, while chapter 2 is a summary of the literature reviewed by the author and considered relevant to the thesis subject. Chapter 3 describes the experimental materials, procedure and equipment used throughout the project. The five chapters following chapter 3, chapters 4 to 8, are the core of the thesis in which the experimental results and their explanation have been discussed. Chapter 4 describes the steady state wear behaviour of pearlitic rail steel, in which ratchetting has been proposed as a wear mechanism. This mechanism has been confirmed in chapter 5, where the effect of rolling direction reversal on the wear rate and wear mechanism of pearlitic rail steel has been studied. The two chapters following chapter 5, chapters 6 and 7, were then focused at studying the rolling contact fatigue behaviour of rail steels under conditions identical to those used in chapters 4 and 5, except that the rolling contact fatigue tests were water lubricated. In chapter 6, general performance of the steels used have been investigated, while in chapter 7, the effect of rolling direction reversal on rolling contact fatigue and cracking morphology have been studied.

After devoting four chapter to studying wear and rolling contact fatigue independently, chapter 8 is an integrating chapter, focused at studying the interaction between the two phenomena by studying the effect of initial wear (dry cycling) on the subsequent rolling contact fatigue life of pearlitic rail steel.

Chapter 9 focuses on general discussion and conclusions, arising from the interaction of results discussed in the different preceding chapters. Finally, chapter 10 has been devoted to highlight some of the areas where the author feels that further research is needed.

Chapter 2

LITERATURE REVIEW

2.1. TRIBOLOGY OF THE WHEEL RAIL SYSTEM

2.1.1. Contact mechanics

The science of contact mechanics may be said to have started in 1882, after the publication of Hertz's theory of contact, which he developed during experiments on the effect of elastic deformation on the optical interference between glass lenses in contact⁽¹⁾. When two bodies are brought into contact, and subjected to a normal load, they first touch through an area known as the area of contact. If one or both of those bodies are curved, the elastic deformation of their interface gives rise to the contact area. If this area is small, in comparison with the bodies' surface radii of curvature, the contact is said to be non-conformal.

The Hertzian contact geometry is always bounded by an ellipse, whose minor to major axes ratio lies between zero (line contacts) and unity (circular contacts). This axis ratio is a function of both body geometry and the orientation of the principal radii of curvature, while the length of the semi-axis is a function of the material properties and the applied load. The hypothesis that the area of contact is always of an elliptical shape was first made by Hertz. He also simplified the conditions of the contact analysis by regarding each body as a half space loaded over a small region of its surface.

2.1.2. Contact of elastic bodies

Figure (2.1) shows two bodies of general shape in contact. By taking the point of first contact O as the origin of a rectangular co-ordinate system, in which the X-Y plane is the common tangent to the surfaces, and the Z axis lies along the common normal with its positive direction towards the lower body, the profile of each surface in the region near the contact origin can be expressed by⁽¹⁾:

$$Z = A X^2 + B Y^2 + C XY \quad 2.1$$

where A, B and C are constants whose values depend on the geometry of the surfaces, and

higher orders in X and Y are neglected. By the choice of a suitable set of axes the term in XY vanishes and for two bodies of revolution of R_1 and R_2 radii of curvature

$$A = B = \frac{1}{2} \left(\frac{1}{R_1} + \frac{1}{R_2} \right) \quad 2.2$$

The contours of separation between the two bodies before loading are circles of origin O, and the contact area is also circular.

To study the elastic deformation of the contact, consider two bodies of solids of revolution, shown after deformation in figure (2.2). During compression, distant points in the two bodies, T_1 and T_2 , move towards the contact origin O along the Z axis by displacements δ_1 and δ_2 , respectively. Due to the contact pressure the surface of each body is displaced parallel to OZ by an amount \bar{U}_{z_1} and \bar{U}_{z_2} relative to the distant points T_1 and T_2 . The pressure which is exerted between two frictionless elastic solids of revolution in contact is given by Hertz theory as;

$$p = p_0 \left\{ 1 - \left(\frac{r}{a} \right)^2 \right\}^{1/2} \quad 2.3$$

where p_0 is the maximum contact pressure, r is the distance from the contact centre and a is the semi-contact width. From the theory of elasticity expressions for \bar{U}_{z_1} and \bar{U}_{z_2} are given as;

$$\bar{U}_{z_1} = \frac{1 - \nu_1^2}{E_1} \frac{\pi p_0}{4a} (2a^2 - r^2), \quad r \leq a \quad 2.4$$

$$\bar{U}_{z_2} = \frac{1 - \nu_2^2}{E_2} \frac{\pi p_0}{4a} (2a^2 - r^2), \quad r \leq a \quad 2.5$$

The radius of the contact circle is given by;

$$a = \frac{\pi p_0 R}{2E^*} \quad 2.6$$

In this case E^* is given by;

$$\frac{1}{E^*} = \frac{1-\nu_1^2}{E_1} + \frac{1-\nu_2^2}{E_2} \quad 2.7$$

ν_1 and ν_2 being Poisson's ratio of bodies 1 and 2, respectively.

R is given by,

$$\frac{1}{R} = \frac{1}{R_1} + \frac{1}{R_2} \quad 2.8$$

where R_1 and R_2 are the radii of curvature of bodies 1 and 2.

The approach of distant points in the two solids is given by

$$\delta = \frac{\pi p_0 a}{2E^*} \quad 2.9$$

and the maximum contact pressure is given by

$$p_0 = \frac{3/2 p}{\pi a^2} = \frac{3}{2} p_m \quad 2.10$$

where W is the contact load and p_m is the mean pressure.

Substituting for p_m from equation 2.10 in equations 2.6 and 2.9

$$a = \left(\frac{3WR}{4E^*} \right)^{1/3} \quad 2.11$$

and

$$\delta = \left(\frac{9W^2}{16RE^{*2}} \right)^{1/3} \quad 2.12$$

p_0 is then given by

$$p_0 = \frac{3W}{2\pi a^2} = \left(\frac{6WE^{*2}}{\pi^3 R^2} \right)^{1/3} \quad 2.13$$

2.1.3. Contact of cylindrical bodies (line contact)

In the case of two cylinders of radii R_1 and R_2 in contact, with their axes parallel to the Y axis, A and B of equation 2.1 are given by

$$A = \frac{1}{2} \left(\frac{1}{R_1} + \frac{1}{R_2} \right), \quad B = 0 \quad 2.14$$

If the two cylinders are pressed by a load P per unit length, they make a contact over a narrow strip of length l and width $2a$. In this case the load P can be expressed by;

$$P = \frac{\pi a^2 E^*}{4R} \quad 2.15$$

This expression is valid only within the contact area. From equation 2.15 an expression for a can be written as;

$$a^2 = \frac{4PR}{\pi E^*} \quad 2.16$$

The maximum pressure p_0 is equal to $(2P / \pi a)$. Substituting for a from 2.16, we get;

$$p_0 = \left(\frac{PE^*}{\pi R} \right)^{1/2} \quad 2.17$$

For two elastically similar steel cylinders, Tomeshinko and Goodier's⁽²⁾ form of equation 2.17 is:

$$p_0 = 0.418 \left(\frac{PE}{R} \right)^{1/2} \quad 2.18$$

where P is the contact load per unit contact length, E is Young's modulus of steel and R is given by equation 2.8. At the contact interface $\sigma_x = \sigma_y = -p(x)$, and outside the contact region all stress components at the surface are zero, and the principal stresses along the Z axis are;

$$\sigma_x = -\frac{P_0}{a} \{ (a^2 + 2Z^2)(a^2 + Z^2)^{-1/2} - 2Z \} \quad 2.19$$

$$\sigma_z = -\frac{P_0}{a} (\alpha^2 + Z^2)^{-1/2} \quad 2.20$$

$$\tau = -\frac{P_0}{a} \{Z - Z^2 (\alpha^2 + Z^2)^{-1/2}\} \quad 2.21$$

for which ;

$$\tau_{\max} = 0.3(p_0), \quad \text{at } Z = 0.78\alpha \quad 2.22$$

The variation of these stresses below the surface is shown in figure (2.3)⁽¹⁾.

Unlike most engineering components, such as beams and shafts, the stress state beneath the contact is highly compressive in character, as seen in equations 2.19-2.21. More precisely, the spherical stress component is usually very negative and the magnitude of the deviatoric stress components is quite small by comparison. This character of the contact stresses has the following effects⁽³⁾:

- a. The tendency of the contacting bodies' material to yield is quite small. As a result, a substantial pressure may be sustained before the onset of plasticity.
- b. Deformation is very ductile and even normally brittle materials show considerable ductility.
- c. The likelihood of brittle fracture is small as all the three principal stresses are negative (compressive).

It can be seen that Hertz theory of contact is based on a number of assumptions and simplifications, which can be summarised by the following^(4,5).

- a. The two bodies are isotropic, which means that the theory is not applicable to bodies with varying elastic properties across their dimensions.
- b. The contacting bodies are linearly elastic. This implies that the theory is not applicable in plastically loaded contacts, such as heavily loaded wheel-rail contacts where the contact surface is plastically deformed⁽⁶⁾.
- c. The dimensions of the contact area are small compared with the radii of curvature of the undeformed bodies.

d. The geometry of the surfaces adjacent to the contact zone can be described accurately by equation 2.1.

e. The two bodies in contact are frictionless.

f. The two surfaces are clean and unlubricated (despite e above).

After the publication of the Hertz theory, most of the research in the field of contact mechanics was concentrated on extending the theory beyond these restrictions of assumptions and simplifications. For example, the introduction of the effect of tractional loading⁽⁵⁾, surface roughness⁽⁷⁾, strain hardening⁽⁸⁾, plastic loading⁽⁴⁾ and lubrication⁽⁹⁾.

2.1.4. Rolling contact

In many applications, such as the railway wheel-rail system, the contacting bodies are in continuous rolling motion and are required to transmit torque. A high coefficient of friction in this case is vital for system efficiency. The tractional force between the two contacting bodies results in changing the stress state proposed by Hertz according to the assumption of frictionless bodies. This may suggest that any rolling situation should be analysed from three stand-points, where any of the following situations may take place⁽¹⁰⁾:

a- Pure or free rolling: when the rolling occurs without sliding or spin, the motion is often referred to as pure rolling. However, this term is ambiguous, since the absence of apparent sliding does not exclude the transmission of a tangential force of magnitude less than the limiting friction. So, the term free rolling will be used to describe motions in which the tangential force is zero.

b- Tractive rolling: this term is used to describe the situation where a tangential force accompanies the rolling motion.

c- Rolling with regions of slip in the contact zone: this type of rolling is necessitated by the geometry of the system, as in the case of a ball-groove system, where the contact is conformal.

If the rolling bodies are loaded there will be tangential strains. If the two bodies exhibit different strains a slip motion can take place, particularly when the two bodies are designed to transmit tangential traction. This slip motion is commonly known as creep. The

way in which creep arises may be better understood by the example of a deformable wheel rolling on a relatively rigid plane surface. If, due to the elastic deformation, the tangential strain in the wheel is tensile, the surface of the wheel is stretched where it is in sticking contact with the plane. The wheel then behaves as though it had an enlarged circumference, and in one revolution it moves forward a distance greater than its undeformed perimeter by a fraction known as the creep ratio. If the tangential strain in the wheel is compressive, the effect is the reverse.

It is now clear that Hertz theory of contact is not applicable to most of the contact problems. However, in the absence of a reliable elastic-plastic analysis the theory represents a useful approximation. For plastically loaded contacts the shakedown analysis has recently received more attention, as will be discussed later.

2.1.5. Wheel-rail contact

Figure (2.4) shows a typical wheel-rail system. The geometry of the wheel/rail contact appears, at the first sight, to be that of a narrow disc on a cylinder, as illustrated in figure (2.5). However, in reality the contact is much more complicated due to the following:

a- The wheel tread is coned to prevent the wheel flange from making contact with the rail head, and to create the forces needed for steering.

b- The rails are usually laid with the rail table inclined towards the centre of the track.

c- On curves the outer rail is higher than the inner rail.

d- Due to wear and occasional grinding, the cross-sectional profiles of the rail and wheel change continuously.

f- On curves, the outer wheel has to travel a longer distance than the inner wheel, and in case of worn wheel profile one of them has to slide to compensate for this difference.

g- In addition to the flange forces, the wheel rail contact is subjected to three forms of loading:

1. Normal load due to the axle load.
2. Tangential load parallel to the rail length.
3. Tangential load parallel to the wheel axis.

From the above discussion, it can be seen that Hertz theory of contact is not readily applicable to the wheel/rail contact. However, the problem can be simplified by considering the contact geometry, as shown in figure (2.6), of a cone and a cylinder, where the relative radii of curvature can be calculated. The Engineering Study Data Unit (ESDU 78035)⁽¹¹⁾ gives a step by step procedure to calculate the wheel-rail contact stresses.

An important step in finding the stresses and strains associated with the contact is the determination of the contact area. Researchers have suggested different methods to find this area. Johnson⁽¹²⁾ used rubber balls and wheels in contact with a transparent plate to view the contact area directly. Roberts and Johnson⁽¹³⁾ took optical interferograms of the contact. A number of indirect methods have also been used to determine the contact area. Halling⁽¹⁴⁾ applied grease, measured the track width of a ball rolling on a plate, and thus calculated the contact area. Similar techniques were used to determine the shape and area of wheel rail contact. Labrijn⁽¹⁵⁾ used carbon paper between the wheel and the rail to measure the contact area variation with pressure. Kalousek⁽¹⁶⁾ used aluminium foil to measure the tread and flange contact areas on a small scale wheel/rail wear apparatus. Poole⁽¹⁷⁾ used a low pressure air passing through 1 mm diameter holes drilled into a wear test block, monitoring those holes being blocked by the wheel contact. The advantage of this method was that it could be used under dynamic conditions. For a maximum contact pressure of 1200 MPa, which represents a typical maximum pressure caused by the axle load of a stationary locomotive in British Rail, Barwell⁽²⁹⁾ estimated the wheel-rail contact area to be 1.2 cm². However, the maximum contact pressure and the contact area due to the same axle load are also a function of the profiles used.

2.1.5.1. Operating conditions

a. Axle load: The effect of axle load on wheel-rail adhesion has been discussed in the previous section. High locomotive axle load is necessary to obtain higher tractional force. If the weight of the locomotive is not enough to give the required axle load dummy weights, sometimes in the form of heavy concrete blocks, are added to increase the axle

load. On the other hand, higher axle load causes higher contact stresses and faster deterioration of wheel and rail lives, as will be discussed later. Luden⁽¹⁹⁾ has shown that for a static axle load of 22.5 tonnes this contact pressure is 1475 MPa. The axle load of a typical British Rail stationary locomotive results in a maximum contact pressure of about 1200 MPa⁽¹⁸⁾. However, these values are also a subject of the rail and wheel profiles.

b. Wheel and rail profiles: The main aim of the wheel and rail profile design is to provide a wheel guidance tool. However, these profiles play an important role in determining the magnitude and distribution of the wheel-rail contact stresses. In service both the profiles change continuously, due to wear, rail grinding and wheel reprofiling. More conformal profiles, caused by wear, results in larger contact area, and as a result, lower contact stresses. In the contrary rail grinding and wheel reprofiling results in a less conformal contact and higher stresses. Recently, reduction of contact stresses started to play an important role in the design of wheel and rail profiles. Marich et al⁽²⁰⁾ suggested different actions to extend the rail life among which is the introduction of new wheel profiles. Garg and Singh⁽²¹⁾ studied the effect of wheel conicity on the flange force and showed that this force increases with the conicity angle of the wheel. DiBrito et al⁽²²⁾ have studied the important role of wheel and rail profiles in creating contact geometries that adversely affect wheelset steering.

c. Rail contamination: the wheel-rail contact area can be contaminated either artificially, by the application of lubricants to the wheel flange and rail gauge face to reduce wear, or by the surrounding environmental conditions such as rain and tree leaves. Rail surface contamination with such foreign materials can reduce wheel-rail adhesion by reducing substantially the coefficient of friction from a typical value of 0.4-0.6 to only 0.1 or less⁽²³⁾. The coefficient of friction controls the location of the maximum orthogonal shear stress. The effect of the presence of fluid lubricants on wear and RCF will be discussed later.

d. Creepage: Creepage between wheel and rail arises mainly from the contact geometry and lateral forces, as well as, the driving and braking forces between wheel and rail. These conditions can cause three types of creepage:

i- Longitudinal creepage, in the direction of train movement.

ii- Lateral creepage perpendicular to the rail long axis and caused by the lateral movement of the wheel.

iii- Spin creepage caused by the rotation of the wheel about an axis perpendicular to the rail surface.

The relationship between creepage and adhesion is shown in figure (2.7)⁽²⁴⁾. It can be seen that the maximum adhesion is achieved when creepage is about 1%.

2.2. RAIL DETERIORATION DUE TO WHEEL-RAIL CONTACT

2.2.1. Introduction

The cost of the attention paid to the different forms of rail deterioration caused by wheel/rail contact forms a substantial proportion of the overall cost of track maintenance. Wear is the main criterion for rail replacement. It was estimated that the North American Railroads was spending \$ 600 million annually for the replacement of deteriorated rails in the early eighties⁽²⁵⁾. This figure does not include the cost of direct labour, maintenance equipment or loss of revenue as a result of line closure for rail replacement. Two of the most significant forms of damage caused by the wheel-rail contact are initiated within the contact area. Friction that results from wheel flange contact with the rail gauge face during negotiating curves has always been a cause for wear of rail as well as wheel⁽²⁶⁾. The serious problem of rolling contact fatigue cracks⁽²⁶⁾, which are known in British Rail as squats are of great concern due to their potential to develop fracture. Subsurface initiated defects similar to squats appear on wheel treads and rail heads are known as shellings^(27, 28).

Other forms of deterioration, such as corrugations⁽²⁹⁾, wheel burns, or wheel flats, can aggravate wear and RCF. For example wheel burns caused by the failure to start a train from rest become favoured locations for surface initiated RCF crack^(30,31). Wheel flats caused by wheel skid adds a dynamic augment to the contact stresses and accelerates other forms of rail deterioration^(32,33). However, these forms of deterioration will not be discussed here, attention being focused at wear and RCF.

2.2.2. Rail wear

2.2.2.1 Wear types in general

It seems specialists do not agree on a single definition of wear. Some define wear as

the progressive loss of material when two surfaces undergo relative motion under load. A committee of the Institution of Mechanical Engineers decided to define wear as: the progressive loss of substance from the surface of a body, brought about by mechanical action⁽³⁴⁾. Neither definition is perfect, since the first appears to eliminate spark erosion, and the second perhaps places too much emphasis on fatigue effects in wear.

Wear can be classified into four main types⁽¹⁰⁾. Those are:

i. Adhesive wear

When two surfaces are in contact, they first touch through relatively few isolated asperities, even with microscopically smooth surfaces. As the load is increased, the local contact pressure at the asperities becomes extremely high. When the yield pressure is exceeded, the asperities continue to deform plastically until the real contact area becomes sufficiently large to support the load. In the absence of surface films, the two surfaces adhere together. However, the presence of any amount of contaminant prevents this adhesion. Relative tangential motion acts to disperse the contamination film, and to cause cold welding of junction. Continued sliding shears these junctions and forms new ones. According to this mechanism, the coefficient of friction is equal to the shear strength divided by the yield strength of the material. The amount of wear in this case depends on the position at which the junction is sheared. If shear takes place at the position of the interface the wear is zero, whereas, if shear takes place away from the interface, the metal is transferred from one surface to the other. With further rubbing, some of the transferred material is detached to form a loose wear particle.

ii. Abrasive wear.

Abrasive wear is the kind of wear in which ploughing-out of the soft surface material takes place. It is caused by either a hard rough surface sliding against a softer one, as in the grinding process, or loose hard particles sliding between two rubbing surfaces, as in paste polishing. This type of wear has been largely eliminated in modern equipment due to the great awareness of the importance of surface finish⁽¹²⁾ and maintenance of clean lubricants.

iii. Fatigue wear

It has been shown that for abrasive and adhesive wear to take place there must be direct contact between the two surfaces, as well as relative motion between coincident points on the two surfaces. If the two surfaces can be separated by a clean lubricating film,

the mechanism for adhesive and abrasive wear cannot operate. This is the case of rolling bearings in which, although direct contact does not occur, the opposing surfaces experience large stresses transmitted through the lubricating film during the rolling motion. The nature and magnitude of these stresses was discussed earlier, where it was shown that, although the maximum compressive stress is at the surface, the maximum shear stress is below the surface, as in the example of rolling cylinders, equation 2.22 and figure (2.3). As rolling proceeds, the direction of the shear stresses for any element changes to create a state of cyclic stress, which can cause a fatigue failure, which is dependent on the amplitude of the cyclic stress as well as the number of cycles. If in rolling contact, these are above the endurance limit of the material, failure will occur.

Tractional rolling motion will have two effects; first, the location of the maximum shear stress moves towards the surface. Second, the amplitude of the shear stress component increases. Finally, tractional rolling means higher coefficient of friction and lower shakedown limit⁽³⁵⁾.

Since fatigue wear is a fatigue failure, it is characterised, like other fatigue failures, by a crack which initiates after a critical number of stress cycles. This crack may propagate to form comparatively large wear fragments which detach from the surface to form a pit or a spall. Prior to this stage, the amount of wear is negligible. However, it has transpired from laboratory experiments that the surface fatigue cracks do not propagate to form a deep fatigue pit or spall without the presence of a lubricating fluid⁽³⁶⁾.

Fatigue wear can also take place in sliding contact. When sliding bodies make contact via asperities without adhering or abrading, they can pass each other leaving one or both asperities plastically deformed. After a critical number of such passes, an asperity would fail due to fatigue⁽³⁷⁾.

iv. Fretting wear

Fretting wear is a form of adhesion wear, but is often treated separately since it occurs under specific conditions, that of two metal surfaces loaded against each other under low amplitude vibratory motion. The normal load causes adhesion between asperities, and the vibratory motion causes the rupture of those asperities as described earlier. Fretting is mostly combined with corrosion. The corrosion product in air is oxide, and due to the close fit of the two surfaces, the hard oxide particles cannot readily escape. Instead, they become trapped between the two surfaces and act as an abrasive agent.

2.2.3. Rail wear classification

Rail head wear is usually classified into three types which are related to locations, rather than wear mechanisms. Each of the three types, which are schematically illustrated in figure (2.8)⁽³⁸⁾, may involve a number of wear mechanisms. They can be summarised as follows⁽³⁸⁾:

a. Gauge corner (side cutting) wear of the inside edge of the higher rail on curved track. It is considered to be adhesive wear caused by the sliding motion between the wheel flange and the rail gauge face. The loss of material due to this kind of wear is high such that flange lubricators are used to lubricate the contact area between the wheel flange and the rail gauge face⁽³⁹⁾. In addition to being the main reason for rail replacement, this kind of wear can cause derailment due to the incipient danger of the wheel flange mounting the rail head.

b. Plastic flow of rail edges of curved track. although material may not detach from the rail head, plastic flow can be considered a form of wear since the deformed material is lost from the contact area, figure (2.8). Bower et al⁽⁴⁰⁾ described this type of flow as extrusion of slivers from the corners of the rail head, particularly from the field side corner of the low rail and the gauge corner of the high rail.

c. Spalling and shelling: which are also sometimes classified as fatigue failures since they are caused by rolling contact fatigue (RCF). Shelling is caused by cracks initiate at the surface of the gauge corner and propagate into the running surface of the rail head, whereas shelling is the detachment of thick portions of the gauge corner by subsurface initiated RCF cracks. The role of this type of failure in developing transverse rail fracture will be discussed later.

2.2.4. Rolling contact fatigue

Rolling contact fatigue (RCF) of rails is a term used to describe fatigue failures caused by the wheel/rail contact stresses. The initiation of RCF cracks, which can either be surface or subsurface, appears to be similar to that of delamination wear⁽²⁶⁾. In rails, these cracks are characterised by a main crack propagating in the forward direction with respect to traffic. They branch downwards at a depth of 3-4 mm below the surface to produce a transverse defect⁽²⁶⁾, figure (2.9) shows such a defect caused by a subsurface initiated RCF crack⁽⁴¹⁾

Like other fatigue failures, RCF occurs in two stages:

a. Crack initiation: which is less understood than crack propagation. Initiation sites can be divided into surface and subsurface. Subsurface initiated cracks are thought to be due to the presence of inclusions, while surface cracks could initiate from microscopic flaps of metal forming over the surface irregularities⁽⁴²⁾.

b. Crack propagation: the initiated cracks propagate, generally, in the direction parallel to the lines of plastic flow. One feature of RCF crack propagation is that it does not take place without the presence of a fluid lubricant. The role of liquid lubricant in crack propagation was first described by Way⁽⁹⁾. He explained this role in terms of hydraulic pressurisation of the crack tip by the fluid which is forced to the crack cavity in the slower moving roller during RCF laboratory tests. The mechanism will be discussed further in chapter 4.

2.2.5. Effect of operating conditions on rail deterioration

The operating environment effect on wear and rolling contact fatigue of rail steels can be classified into:

a. Track geometry: the geometrical parameters of the track plays an important role in the deterioration caused by the wheel-rail contact. The main geometrical parameter in this regard is the wheel and rail profiles and the position of the rail in relation to the curve in curved tracks. Smallwood et al⁽⁴³⁾ have shown that the maximum contact stress on the rail is dictated by the lateral wheelset shift. Using a vehicle dynamic software package they concluded that the maximum contact pressure on the outer (high) rail is more than that on the inner rail. The situation is more aggravated by the direction of the creepage force, caused by steering forces⁽⁴⁴⁾ which has been found to oppose the load movement direction on the outer rail and match it on the inner rail. This may explain the reason behind the outer rail being more prone to rolling contact fatigue failure which favours a traction opposite to the load movement. Figure (2.10) shows an example of a curving diagram obtained by Smallwood et al⁽⁴³⁾, who suggested a more conformal rail profile to reduce contact stresses. The arrows on the diagram indicate the direction and magnitude of the contact forces. Figure (2.11) is a prediction of the maximum contact stress due to leading wheelset of figure (2.10).

b. Mechanical environment

b.1. Axle load and creepage

It has been shown in equations 2.18-2.22 that the normal load is one of the main factors which governs the level of contact stresses, mainly the maximum contact pressure p_0 . Dikshit and Clayton⁽⁴⁵⁾ showed that, for eutectoid steels, the relationship between the maximum contact pressure p_0 and RCF life L is a power function of the form $L = A (p_0)^{-B}$, where A and B vary with material properties, creepage and type of lubricant. Different researchers have attached different values to the constants A and B . Ollerton and Morey⁽⁴⁶⁾ have shown that, for a water lubricated test with zero creepage $L \propto (p_0)^{-1}$, whereas Akoka and Hirasawa⁽⁴⁷⁾ used a mineral oil lubricant and a creepage of 11% and suggested $\alpha(p)^{-1.5}$. More recently, Beynon et al⁽⁴⁸⁾ have studied the effect of loading on the RCF life of different rail steels, under rolling-sliding water lubricated line contact, and suggested a set of formulae to relate RCF life to creepage under different contact pressures. Those formulae are of the form $L = A (g)^B$, where g is the percentage creepage and A and B are constants whose values are dependent on contact pressure and material properties. It was also shown in this study that it is unreasonable to suggest a single formula to relate RCF to creepage and load for the different rail steels.

As far as the effect of the load and creepage on the wear rate of rail steels is concerned, Devanathan and Clayton⁽⁴⁹⁾ studied the effect of the maximum contact pressure on the steady state wear rates of different rail steels and found that the wear rate increases with increasing p_0 . Bolton et al⁽⁵⁰⁾ showed similar results. Garnham and Beynon⁽⁵¹⁾ have studied the dry rolling-sliding wear behaviour of different rail steels and have shown that the steady state wear rate increases in a non-linear fashion with the product of contact pressure and creepage $p_0.g$. Eyre⁽⁵²⁾ also showed similar results.

b.2. Cyclic loading

In wheel-rail contact, the loading takes the form of repeated cycles. The response of material to cyclic loading, in this case, can take four different forms, as listed below and illustrated in figure (2.12)⁽⁵³⁾:

- Perfectly elastic behaviour if the load does not exceed the elastic limit during any load cycle, figure (2.12a).
- Elastic shakedown, where plastic deformation takes place during the early cycles

but, due to the development of residual stresses and the strain hardening of some materials, such as steel, the steady state behaviour is perfectly elastic, see figure (2.12b). The load below which this is possible is referred to as the elastic shakedown limit.

- Plastic shakedown, in which the steady state is a closed elastic-plastic loop but with no net accumulation of plastic deformation. This behaviour is sometimes referred to as cyclic plasticity, figure (2.12c), and the corresponding load limit is called the plastic shakedown limit or the ratchetting threshold.

- Above the ratchetting threshold, the steady state consists of an open elastic-plastic loops and the material accumulates a net unidirectional strain during each cycle, a process known as ratchetting; shown in figure (2.12d). Ratchetting is sometimes referred to as incremental collapse.

Recently, this type of analysis has received great attention and has been employed to explain the wear behaviour of different materials⁽⁵³⁻⁵⁵⁾. Figure (2.13) shows a shakedown map as a function of contact pressure, coefficient of friction and the shear yield strength of the material⁽³⁾. This subject will be discussed further in chapter 4 onwards.

c. Material parameters

c.1. material mechanical properties

Heller et al⁽⁵⁶⁾ have indicated that material mechanical properties have a significant effect on the rolling contact fatigue life of rail steels. They have shown that reverse bending fatigue strength increases in a linear fashion with the tensile strength of the material. Damage by RCF can therefore be reduced by using materials of higher tensile strength.

As far as material hardness is concerned, it is suggested that there is an optimum mating material hardness combination to give the highest RCF life. For rolling bearings application this optimum is obtained when the rolling part element hardness is 10% higher than that of the race way⁽⁵⁷⁾. Similar results were obtained for the case of wheel/rail contact⁽⁵⁸⁾. More recently, and after the introduction of the shakedown analysis, the shear yield strength of the material has been shown to play a very important role in determining the shakedown limits, and as a result, the type of response the material exhibits when subjected to cyclic loading (in the case of wheel/rail contact the repeated rolling-sliding motion). The shakedown limits of low shear yield strength materials can be easily exceeded, and as a result, those materials exhibit higher wear rates⁽⁵⁶⁾.

c.2. Inclusions

Inclusions play an important role in subsurface rolling contact fatigue cracking, as well as wear rate⁽⁵⁹⁻⁶¹⁾. Their effect depends mainly on their composition, size and distribution. Although soft inclusions like calcium and manganese sulphides are thought to be less harmful⁽⁶²⁾, inclusions in general act as stress raisers. Beynon et al⁽⁶³⁾ have shown that manganese sulphide inclusions can act as crack formation sites in the braking disc during tests under rolling-sliding conditions. Similar observations have been reported by Laufer et al⁽⁶⁴⁾. To minimise the effect of inclusions, steel manufacturers are capable of producing steels with negligible inclusion content. For example, British Steel plc uses a strict quality control procedure to detect inclusions during the production of rails. A sixteen probe ultrasonic machine is used to test all produced rails for micro-inclusions⁽⁶¹⁾. The introduction of new steel melting techniques, such as vacuum and double-vacuum melting process resulted in the production of high quality steels and lead to substantial increase in RCF life and wear resistance.

b.3. microstructure

Up to date pearlitic steel is the most widely used material for rail applications. Pearlitic microstructure is found desirable for both wear resistance and RCF prevention⁽⁶²⁾. Slack quenched very fine pearlitic head hardened rails showed a promising future in Japan National Railways⁽⁶²⁾. The superiority of pearlitic steel as a wear resistant material is thought to be due to cementite lamellae which deform parallel to the wear surface to form a mosaic like arrangement and as a result increase the area fraction of the hard cementite exposed to the contact surface⁽⁵⁵⁾. During experiments on the performance of four different types of rail steels, Park and Fletcher⁽⁶⁵⁾ found that pearlitic head hardened steel rails have a performance which is superior to that of ordinary carbon steels or even Cr-V and Cr-Mo steels. Perez-Unzueta and Beynon⁽⁶⁶⁾ have shown that wear resistance of pearlitic rail steel increases with lower interlamellar spacing between the cementite lamellae.

In studying their effect on RCF life and wear resistance, material properties effect can not be separated from microstructural effects. Different microstructures of the same material may exhibit different levels of RCF resistance⁽⁵⁸⁾. Operating conditions may cause microstructural modifications which may lead to a better or worse performance. An example of a preferential modification is the realignment of cementite lamellae mentioned earlier.

d. External environment

d.1. Rail contamination

Wheel/rail contact patch can be contaminated either artificially, by the lubricant from the flange lubricators used to reduce gauge face wear⁽⁶⁷⁾ and train rolling resistance⁽⁶⁸⁾, or naturally, mainly by rain. The presence of the fluid lubricant in the contact area may have two main effects:

- it reduces the traction coefficient between wheel and rail, and as a result increases the shakedown limit of the material and leads to lower wear rates⁽⁵⁵⁾.

- the presence of the fluid lubricant is, as suggested by Way⁽⁹⁾, essential for RCF crack propagation by the pressurising mechanism. This mechanism has been further improved by Bower⁽⁶⁹⁾ who analysed the role of the fluid lubricant in mode I crack propagation due to the pressure of the liquid entrapped in the crack cavity. He also introduced the concept of crack face friction and the role of the fluid lubricant in reducing this friction to allow relative motion between the two faces of the crack, causing mode II crack propagation. The mechanism will be discussed in greater detail in chapters 6.

2.2.6. Closing remarks

The discussion presented in this section shows how difficult it is to design the wheel rail contact system. It is interesting to notice that while some design features are favoured to achieve a certain requirement they have, at the same time, an adverse effect on another design requirement. As examples:

- Higher axle load is required to obtain higher traction, see section 2.1.5.1. At the same time higher axle load means higher contact stresses, see equation 2.17, and higher rolling resistance.

- High coefficient of friction is required for effective wheel-rail adhesion. However, it reduces the shakedown limit of the material and affects the location of the maximum orthogonal shear stress.

- High modulus of elasticity is favoured to reduce the rolling resistance but not favoured from the viewpoint of contact pressure, equation 2.18.

- Lubricants are recommended to reduce wheel flange and rail gauge face wear but they are known to promote RCF failure.

Research in these areas can help decision making during the design stages by giving understanding of the mechanisms of rail deterioration due to wheel contact. This can lead to models and quantified arguments on the effect of the different service and material parameters.

2.3. RAIL STEELS

2.3.1. Rail steel selection criteria

Material selection for rail application is a major decision in rail design. In addition to the economical factor, a successful selection must take in consideration the interaction between the track geometry, the material parameters, the environment and the service conditions, discussed earlier in section 2.2.5. Furthermore, since most of the railway rails are laid continuously welded, weldability must also be taken in consideration. Despite the fact that wear resistance is the most significant material property for rail application⁽²⁵⁾, improvement of this property should be achieved without sacrificing the material resistance to other forms of rail deteriorations, such as rolling contact fatigue.

It is clear that it is difficult to obtain a material which can satisfy all the ultimate requirements including cost. However, it remains possible to achieve an optimum balance between properties and cost. Among the different types of rail steels used, fully pearlitic rail steels are still enjoying the maximum share. More recently, head hardened rails have started to show a promising future in some railways⁽⁶²⁾.

2.3.2. Pearlitic rail steels

Pearlite is a lamellar product of eutectoid composition which can form in steel during transformation under isothermal, continuous cooling or forced velocity (directional) growth conditions⁽⁷⁰⁾. It consists of ferrite (α) iron and cementite (Fe_3C). The nucleation sites of pearlite could be either ferrite or cementite. On an austenite grain boundary in hypereutectoid steel cementite nucleates first, whereas, in hypoeutectoid steel it is the ferrite which nucleate first during the diffusion-controlled austenite decomposition in the eutectoid region of the phase diagram shown in figure (2.14)⁽⁷⁰⁾.

The interlamellar spacing in pearlite S , defined in figure (2.15), has a significant effect on the mechanical properties of pearlitic rail steel.

Kaveshe⁽⁷¹⁾ has shown the strength parameters of pearlitic steel are inversely related to interlamellar spacing. The influence of this spacing on rotating shaft fatigue has been

investigated by Gray et al⁽⁷²⁾ who showed that the endurance limit of pearlitic steel can be increased significantly by decreasing the interlamellar spacing. In addition to this spacing, the thickness of the cementite lamellae also can affect the mechanical properties. Laufer et al⁽⁶⁴⁾ have shown that thinner cementite lamellae can deform, rather than break, resulting in a better hardening behaviour of the deformed surface.

Alloying elements, such as Mn, Ni, Cr, Mo and Ti, can slow down the pearlitic reaction by lowering the transformation temperature⁽⁷⁰⁾. The resistance to wear and plastic flow of fully pearlitic microstructures made them favourable for rail application.

Pearlitic rail steel is produced in large basic oxygen steel-making vessels and is vacuum degassed prior to being continuously cast into large blooms. Vacuum degassing permits very tight control over chemical composition and inclusions. After casting, the blooms are slowly cooled at a rate of about 1 °C per hour. This slow cooling rate reduces the hydrogen level in the finished product. The blooms are then reheated and rolled to the finished rail profile. Depending upon the properties required, the rails are either cooled in air or subjected to higher cooling rate to obtain higher strength. Before cutting them to the required length, non-destructive testing techniques are used to monitor inclusions, external defects and flatness of the rail running table⁽⁶¹⁾.

Rail steels are usually classified into three types, based on their tensile strength⁽⁷³⁾. These types are:

a. Normal grades, with a minimum tensile strength of about 700 MPa. Typical examples of these grades are BS11: 1978 and UIC 860-0 Grade 70. The normal grades are those used in normal service conditions in many railways. The majority of British Rail tracks and London underground is laid in BS11 Normal Grade. The chemical composition of these grades is 0.4-0.6% C, 0.05-0.35% Si, and 0.8-1.25% Mn.

b. Wear-resistant grades, with a tensile strength of about 880 MPa. These grades are characterised by a hardness higher than that of the normal grades. This is achieved by refining the interlamellar spacing through increasing the carbon and manganese content. Typical examples of these grades are BS11 Wear-Resisting Grade A and BS11 Wear Resisting Grade B. Both have the same tensile strength, 880 MPa, However, BS11 Wear-Resisting Grade B is harder since it contains higher percentage of manganese, 1.3-1.7%, and as a result, a refined pearlite lamellae. The wear resistant grades are used for heavy haul railway routes and in tightly curved tracks.

c. High-strength grades, with a minimum tensile strength of 1080 MPa. For very high axle loads and extremely tight curved track, higher tensile strength and further refinement of the pearlitic structure is needed. Most steel makers produced such steel by adding 1% Cr to the basic C-Mn composition⁽⁷⁴⁾. Addition of chromium increases, significantly the rail hardness and the wear resistance⁽⁷⁵⁾. The replacement of joint bolted rails by continuously welded rails brought about the need for adequate level of weldability, a property not satisfied with the addition of 1% Cr⁽⁷³⁾. An alternative method of producing high strength rails was introduced. In-line cooling is now used to give high quality head hardened rails⁽⁷⁶⁾. The rate of cooling in this case has to be accurately controlled so that a sufficiently high cooling in the centre of the rail head is achieved without cooling the head surface at a rate which could lead to the formation of bainite or martensite. Using this method, the hardness can be controlled within a narrow range across the rail head.

Under conditions of extremely high wear rate, a very high manganese steel, around 12% Mn, can be used for high wear resistance⁽⁷⁷⁾. The mechanical properties of such steel are characterised by a high tensile to yield strength ratio. That means its work hardening rate is very high such that its hardness is almost doubled, to an appreciable depth, after a short period in service. This type of steel is used in points, crossings and other locations where the extended life can justify its cost compared with other steels.

2.4. WEAR AND ROLLING CONTACT FATIGUE (RCF) TESTING

2.4.1. Introduction

The effect of operating conditions on rail deterioration has been discussed in section 2.2.5. It has been shown that there are many variables which can affect this deterioration. The objective behind any testing in this field is to give quantitative and/or qualitative statements about the effect of a single or a group of operating conditions on the rail deterioration behaviour. This includes the possible interaction between the different phenomena associated with the rail deterioration. For example the effect of the pearlitic microstructure modification on wear and RCF, or the effect of oxidation on the surface layer deformation, or even the interaction between wear and RCF. A number of testing strategies may be followed to achieve these tasks. Those strategies have been classified by Zum Gahr⁽⁵⁹⁾ into six categories: field, bench, subsystem, simplified component and model tests. For wheel rail contact, those categories are schematically represented in figure (2.16). Field tests could be the most informative, however, they do not represent an

attractive option due to their high cost, long duration, and the difficulty in isolating or selecting the test conditions and environment. This may explain the reasons behind using the model tests where the wheel/rail contact is simulated in laboratory by a model test. Since most of the rail damage occurs in the wheel flange-rail gauge face area, it is the motion in this area which has to be simulated. As discussed in section 2.1.5.1, creepage in this area is two types, longitudinal and lateral. Beagley⁽⁷⁸⁾ has shown that the value of this creepage is a function of track curvature and that the longitudinal creepage component is significantly higher than that of the lateral. The motion in this case can be simulated by a rolling motion with a longitudinal sliding component. However, the relationship between adhesion and creepage, shown in figure (2.7), indicates that the limiting value of adhesion, which is a function of traction coefficient, is achieved after a creepage of 1%. In this case, any simulation which can result in such traction coefficient may be used, keeping in mind the other parameters, such as the contact pressure, the contact environment and material. This is supported by the work of Bolton and Clayton⁽⁷⁹⁾ who found that the wear rate is independent of creepage once the limiting friction is achieved. However, researchers have used different simulation techniques and testing machines to study the wear behaviour of rail steels. These are discussed below:

2.4.2. Simulation techniques

2.4.2.1. *Pure sliding tests*: where test are conducted under full slip motion. Different machines and configuration are used. The main difference between the different designs is the configuration of the test specimens. A pin with a spherical end is run against a rotating disc in the pin-on-disc machine⁽⁸⁰⁾, as illustrated in figure (2.17a), or against a rotating cylinder as in Archard's⁽⁸¹⁾ pin-on-ring machine, figure (2.17b). The main disadvantage of these machines is the continuous change in the contact area due to the change in the contact geometry caused mainly by the pin wear. This can result in difficulties in controlling the contact pressure as the contact becomes a conformal rather than a Hertzian contact.

2.4.2.2. *Rolling-sliding tests*: where creepage can be controlled. A variety of machines and specimen configurations are used. These can range from machines where the specimens take a small scale wheel and rail configuration, such as the 1/8 scale dual disc-on-disc machine used by Kalausek⁽⁸²⁾, to the most widely used twin disc machine, the Amsler machine, schematically shown in figure (2.18)⁽⁸³⁾. The machine consists of a single

drive and two gear train connected to two parallel shafts. The gear ratio between the two gear trains is designed to give 10% creepage if the diameters of both the test discs are equal. Creepage ratios higher or lower than 10% can be achieved by using discs of unequal diameters. The main disadvantages of the Amsler design can be summarised by the following:

- i. The non-standard test disc diameters needed to achieve the required creepage. Each set of specimens is suitable only for tests under a particular creepage value.
- ii. The limited choice of test speeds
- iii. The limited maximum loading capacity which can be applied without reducing the width of test discs. Using narrower discs increases the edge effect caused by the contact pressure drop at the edges.
- iv. The open type unlubricated gear boxes used causes high vibration noise level.

These disadvantages have been eliminated in the design of Leicester university Rolling Sliding (Leros) twin disc machine⁽⁸⁴⁾ which has been used during this research project. The machine is capable of applying contact pressures up to 3000 MPa on disc specimens of 10 mm track width. This well above the maximum wheel-rail contact pressure experienced in service, see section 2.1.5.1. This high pressure can be achieved while the width of the test discs is maintained sufficiently large to reduce the edge effect. The independent test disc drives utilised enables accurate creepage control and the use of standard disc dimensions. In addition, the machine is equipped with a control system capable of controlling and monitoring almost all the test parameters. However, the machine has some disadvantages, such as the artificial cooling system of the test discs, the long time needed to warm up the hydraulic loading system and the rigidity of the specimen holding arrangement. These are areas where there is still room for improvements. The machine will be described in further detail in chapter 3.

2.4.3. RCF failure criteria

It has been shown in sections 2.2.3 and 2.2.4 that RCF cracking can result in different forms of damage, mainly, pits, spalls, shells or even detailed fracture. A question arises: what is the definition of failure in this case? Is it the appearance of the first pit, spall or shell, and if yes, of what size? Could it be a certain pitting or spalling degree measured as a percentage area of the test surface? Finally, what about the initiation of RCF cracks as

a failure criteria? Many questions but, no clear answers. The crack initiation, as a failure criteria, may be an attractive candidate if a clear definition of initiation is known, and if on-line detection of this initiation is possible. These difficulties, along with the lack of a standardised definition of RCF life, have lead researchers to use different RCF failure criteria^(36,84). As a result, RCF lives reported by different workers are difficult to compare, unless they are reported as comparison between materials or conditions.

A failure criterion which has been widely used is the degree of spalling, measured by using vibration accelerometers^(36,69). Tests were run until a network of cracks was sufficient for material to spall from the test disc surface to trigger the accelerometers. Garnham and Beynon⁽⁸⁵⁾ have shown that this method suffers from some drawbacks, which can be summarised by:

- a. Spalling is not always the sole RCF failure. Deep cracks can propagate below the surface before any material has spalled from that surface.
- b. Under certain test conditions, surface flakes develop well before spalling occurs, those flakes may also register on the accelerometer.
- c. Due to the extent of damage seen by the surface material before the test is stopped, this method handicaps the possibility of determining whether a particular feature of the surface material is responsible for forming or propagating the early cracks.

These drawbacks have lead researchers to use other on-line crack detection systems, such as photothermal radiometry⁽⁸⁵⁾ and the eddy current system used during this project which will be described in chapter 3.

REFERENCES:

1. K. L. Johnson, *Contact Mechanics*, Cambridge University Press (1985).
2. Timoshenko S P and Goodier D N, *Theory of Elasticity*, McGraw-Hill, 1970.
3. D. A. Hills, D. Nowell and A. Sackfield, *Mechanics of Elastic Contacts*, Butterworth Heinemann, 1993.
4. H. Krause and G. Poll, The Influence of Tangential Traction at the Surface on the Stresses in contacting Bodies During Rolling Sliding Contact, *Wear*, 88, (1981), 221-232.
5. K. L. Johnson, Non-Hertzian Contact of Elastic Spheres, *Proc. of the Symp. on the Mechanics of the Contact Between Deformable Bodies*, Enchede, Netherlands, (1975), 27-41.
6. R. Steele, The Effect of Metal Removal, Steel Cleanliness and Wheel Load on the Fatigue Life of Rail, *Wear*, 144, (1991), 71-87.
7. Greenwood J. A, Johnson K. L and Matsubara E, A Surface Roughness Parameter in Hertz Contact, *Wear*, 100, (1984), 47-57.
8. A. Bower and K. L. Johnson, Plastic Flow and Shakedown of the Rail Surface in Repeated Wheel-Rail Contact, *Wear*, 144, (1991), 1-18.
9. Way S, Pitting due to rolling contact, *Trans. ASME, Journal of Applied Mechanics*, Vol. 2, (1935), pp A49-A58.
10. J. Halling, *The Principles of Tribology*, Macmillan Education Ltd., (1989).
11. Contact Phenomena I: Stress, Deflection and Contact dimensions of Normally Loaded Unlubricated Elastic Components, *Engineering Science Data Unit (ESDU)*, 78035, I Mech E, (1988).
12. K. L. Johnson, Tangential Traction and Microslip in Rolling Contact, *Proc. Symp. In Rolling Contact Phenomena*, Elsevier, (1962), 260
13. P. Robert and K. L. Johnson, Lubrication of a Rubber Ball Rolling With Spin, *Wear*, 27, (1974), 225-235.
14. J. Halling, The Rolling of a Ball Subjected to Normal and Tangential Loads, *Wear*, 7, (1965), 516-534.

Wear, 7, (1965), 516-534.

15. P. Labrijn, Wheel and Rail, *Bull. International Railway Congress*, 1951

16. J. Kalousek, *Establishment of a Quantitative Wear and Fatigue Model For Railway Wheel Subjected to Heavy Traffic Conditions and Different Lubrication Regimes*, National Research Council, Canada, Report TR-WE-42, (1984).

17. W. Poole, The Measurement of the Contact Area Between Opaque Objects Under Static and Dynamic Rolling Conditions, *Proc. of the 2nd International Symp. on Contact Mechanics and Wear of Rail/Wheel Systems*, University of Rhode Island, WU Press, (1987), 59-72.

18. F. T. Barwell, The Tribology of Wheel on Rail, *Tribology International*, Aug. (1974), 146-150.

19. R. Lunden, Contact Region Fatigue of Railway Wheel Under Combined Mechanical Pressure and Thermal Brake Loading, *Wear*, 144, (1991), 57-70.

20. S. Marich, G. Tew and R. Mitchell, Procedures for Extending the Rail Life To at Least 1000 MGT-The Mt. Newman Mining Experience, *Proc. of Railway Engineering Conf.*, Adelaide, Australia, (1991), 60-66.

21. V. Garg and S. Singh, Dynamic Curve Negotiation Behaviour of a Freight Car, *Heavy Haul Railways Conf.*, Perth, Australia, (1978).

22. D. DiBrito, S. Mace and N. Wilson, Effect of Wheel/Rail Contact Geometry on Wheelset Steering Forces, *Preliminary Proc. Contact Mechanics and Wear of Rail/Wheel Systems*, Vancouver Canada, (1994), Edited by J. Kalousek.

23. N. Kumagaya, H. Ishikawa, K. Haga and T. Kigawa, Factors of Wheel Flats Occurrence and Prevention Measures, *Wear*, 144, (1991), 277-288

24. J. Greenwood, The Contact of Real Surfaces, *Proc. International Symp. of Contact Mechanics and Wear of Wheel/rail Systems*, University of British Columbia, Vancouver, Canada, (1982), 21-37.

25. W. Jamison, Wear of Steel in Combined Rolling and Sliding, *ASLE Trans.*, 25, 1, (1980), 71-78.

26. P. Clayton, M. Allery and P. Bolton, Surface Damage Phenomena in Rails, *Proc. International Symp. of Contact Mechanics and Wear of Wheel/rail Systems*, University of

British Columbia, Vancouver, Canada, (1982), 419-441.

27. K. Hirakawa, K. Toyama and M Yamamoto, Fundamental Study of Shelling in Railway Wheel Materials, *Proc. of The 8th Wheelset Congress*, Madrid, Spain, (1985), V.4/1-V.4/41.

28. Question D173, Rolling Contact Fatigue, Review of Rolling Contact Fatigue in Rails, Report No. 1, *European Railway Research Institute(ERRI)*, (1990).

29. J. Alias, Characteristics of Wave Formation in Rails, *Rail International*, November, (1986), 17-23.

30. F. T. Barwell, Wheel to Rail Adhesion, *Proc. of The First Symp. on Contact Mechanics and Wear of Rail/Wheel Systems*, University of British Columbia, Vancouver, Canada, (1982), 503-523.

31. M. C. Purbrick, The Use Of Rails in British Railways, *Proc. Second Heavy Haul Railway Conference*, Colorado, USA, (1982), 380-387.

32. Y.Cheng D. Chen and F. Fogate, Fatigue Behaviour of Rail Steel Under Low and High Loading Rates, *Fatigue Fract. Engrg. Mat. Struct.*, 17, 1, (1994), 113-118.

33. W. Partington, Wheel Impact Load Monitoring, *Proc. Instn. Civ. Engrs. Trans.*, 100, (1993), 239-243.

34. A. D. Sarker, *Friction and Wear*, Academic Press, 1980.

35. H. Krause and G. Poll, The Effect of tangential Traction at the surface on Stresses in Contacting Bodies During Rolling-Sliding Contact, *Wear*, 88, 221-232.

36. 40. P. Clayton and D. Hill, Rolling Contact Fatigue of a Rail Steel, *Wear*, 117, (1987), 319-334.

37. J. M. Challen, P. L. Oxley and B. S. Hockenhull, Prediction of Archard's Wear Coefficient for Metallic Sliding Friction Assuming Low Cycle Fatigue Wear Mechanism, *Wear*, 111, (1986), 275-288.

38. K. Kilburn, An Introduction to Rail Wear and Lubrication Problem, *Wear*, 7, (1965), 155-269.

39. J. Kalousek, Wear and Contact Fatigue Model for Railway Rail, *National Research Council*, Canada, Report No. TR-WE-50.

40. A. Bower, K. L. Johnson and J. Kalousek, A Ratchetting Limit for Plastic Deformation of a Quarter-Space Under Rolling Contact Loads. *Proc. of the 2nd International Symp. on Contact Mechanics and Wear of Rail/Wheel Systems*, University of Rhode Island, WU Press, (1987), 117-131.
41. P. Clayton, Tribological Aspects of Wheel/Rail Contact: A Review of Recent Experimental Results, *Preliminary Proc. Contact Mechanics and Wear of Rail/Wheel Systems*, Vancouver Canada, (1994), Edited by J. Kalousek.
42. P. Clayton, Metallurgical Aspects of Surface Damage Phenomena in Rails, *Canadian Metallurgical Quarterly*, 21, 1, (1982), 31-46.
43. R. Smallwood, J. Sinclair and K. Sawley, An Optimisation Technique to Minimise Rail Contact Stresses, *Wear*, 144, (1991), 373-384.
44. H. I. Andrews, *Rail Traction*, Elsevier, (1986).
45. V. Dikshit and P. Clayton, A Simple Material Model for Water Lubricated Rolling Contact Fatigue of Eutectoid Steels, *Proc. STLE/ASME Tribology Conf.* Missouri, USA, (1991), 1-29.
46. E. Ollerton and J. Morey, Fatigue Strength of a Rail Steel in Rolling Contact, *Proc. of Fatigue in Rolling Contact Symp.*, London, (1963)
47. J. Akoka and K. Hirakawa, Fatigue Phenomena Under Rolling Contact Combined With Sliding, *Bulletin of Japanese Society of Mechanical Engineers*, 2, 5, (1959), 43-50.
48. J. Beynon, J. Garnham and K. Sawley, Rolling Contact Fatigue of Four Pearlitic Rail Steels, II: Effect of Loading, *To appear*.
49. R. Devanathan and P. Clayton, Rolling-sliding Wear Behaviour of Three Bainitic Steels, *Wear*, 148, (1991), 255-267.
50. P. Bolton, P. Clayton and McEwen, Wear of Rail and Tire Steel Under Rolling-Sliding Conditions, *ASLE Trans.*, 25, 1, (1987), 17-24.
51. J. Garnham and J. Beynon, Dry Rolling-Sliding of Bainitic and Pearlitic Steels, *wear*, 157, (1992), 81-109.
52. T. Eyre, Wear of Pearlitic Steel, *Proc. 2nd Heavy Haul Railway Conf.*, Colorado, USA, (1982), 277-281.

53. K. L. Johnson, Aspects of Contact Mechanics, *Proc. International Conf. of Tribology-Friction, lubrication and wear, Fifty Years On*, I Mech E, (1987), c246/87.
54. A. Kapoor, Plastic Ratchetting as a mechanism of Metallic Wear, *Proc. R. Society, A*, 445, (1993), 367-381.
55. A. Kapoor, Shakedown Limit in Sliding Contact of Surface-Hardened Half-Space, *Wear*, 172, (1994), 197-206.
56. W. Heller, R. Schweitzer and L. Weber, Modern Developments in Rail Steel Metallurgy and Production, *Canadian Metallurgical Quarterly*, 21, 1, (1982), 3-15.
57. D. Scott, *Contact Fatigue*, Treatises of Material Science and Technology, 13, Academic Press, (1987).
58. M. Akama and M. Shinsaka, Wear Characteristics of Wheel and Rail Steels, *J. of JSLE*, 131, 2, (1986), 876-882.
59. K. Zum-Gahr, *Microstructure and Wear of Materials*, Tribology Series, 10, Elsevier, (1987).
60. D. Brooksbank and K. Andrews, Stress Field Around Inclusions and Their Relation to Mechanical Properties, *Proc. International Conf. of Production and Application of Clean Steels*, Hungary, (1970), 186-195.
61. W. Hodgson and R. Peterson, *Production Processes to Yield Superior Steel*, Transportation Research Record 1174, 43-56.
62. K. Sugino, H. Kamagaya and H. Masumoto, Development of a weldable High Strength Steel Rails, *Proc. 2nd International Heavy Haul Railway Conf.*, Colorado, USA, (1982), 187-197.
63. J. Beynon, J. Garnham and K. Sawley, Rolling Contact Fatigue of Four Pearlitic Rail Steels, I: Early Crack Formation, *To appear*.
64. E. Laufer, D. Fegredo and J. Kalousek, The Effect of Microstructure on Wear in Standard and Head-Hardened Rails in Heavy-Haul Service, *Proc. 3rd International Heavy Haul Railway Conf.*, Vancouver, Canada, (1986), I*-16-1-I*16-17.
65. Y. Park and F. Fletcher, Fatigue Behaviour and Fracture Toughness of Standard Carbon and High Strength Rail Steels, *Proc. 2nd International Heavy Haul Railway Conf.*, Colorado, USA, (1982), 199-206.

67. H. Ghonem, J. Kalousek, D. Stone and D. Dibble, Observations of Rail wear on Heavy Haul Railway Lines, *Proc. International Conf. on Contact Mechanics and Wear of Wheel/Rail Systems*, Vancouver, Canada, (1982), 249-268.

68. M. Roney, Economics of the Wear of Rail on Canadian Railways, *Proc. International Conf. on Contact Mechanics and Wear of Wheel/Rail Systems*, Vancouver, Canada, (1982), 271-291.

69. A. Bower, The Influence of Crack Face Friction and Trapped Fluid on Surface Initiated Rolling Contact Fatigue Cracks, *Trans. ASME, J. of Tribology*, 110, (1988), 704-711.

70. A. Sinha, *Ferrous Physical Metallurgy*, Butterworth Heinemann, 1989.

71. F. Kavishe and T. Baker, Effect of Prior Austenite Grain and Pearlite Interlamellar Spacing on Strength and Fracture Toughness of a Eutectoid Rail Steel, *Mat. Scie. and Tech.*, 2, (1986), 816-822.

72. G. Gray, A. Thompson and J. C. Williams, Influence of Microstructure on Fatigue Crack Initiation in Fully Pearlitic Steels, *Metallurgical Transactions*, 16A, (1985), 753-759.

73. D. T. Liewellyn, *Steel Metallurgy and Application*, Butterworth Heinemann, 1992.

74. W. Heller and R. Schweitzer, Hardness, Microstructure and Wear Behaviour of Rail Steels, *Proc. 2nd International Heavy Haul Railway Conf.*, Colorado, USA, (1982), 282-286.

75. A. Moser and G. Prskawetz, New Rail Manufacturing Technology at Voest-Alpine Schienen Ges.M.B.H., *Proc. of The International Symposium on Rail Steels-Development, Manufacture and Performance*, Montreal, Canada, (1992), 3-10.

76. B. Bramfitt, Accelerated cooling of Rails, *Iron and Steel Making*, June, (1991), 33-41.

77. Hans Bern and Hans-Georg Frank, Effect of Hard Phases on the Abrasive Wear Resistance of Austenitic Manganese Steel, *Stahl u. Eisen*, 18, (1986), 122-123.

78. T. Beagley, Severe Wear of Rolling/Sliding Contact, *Wear*, 36, (1976), 317-335.

79. P. Bolton and P. Clayton, Rolling-Sliding Wear Damage in Rail and Tyre Steels,

78. T. Beagley, Severe Wear of Rolling/Sliding Contact, *Wear*, 36, (1976), 317-335.
79. P. Bolton and P. Clayton, Rolling-Sliding Wear Damage in Rail and Tyre Steels, *Wear*, 93, (1984), 145-165.
80. E. Robinowics, Wear Coefficients-Metals, in *Wear Control Handbook*, edited by M. Peterson and W. Winer, ASTM, (1980), 475-506.
81. J. Archard, Contact and Rubbing of Flat Surfaces, *J. Appl. Phys.*, 24, (1953), 981-988.
82. J. Kalousek, Development of a 1/8 Scale Dual Disc-on-Disc Rail/Wheel Wear Testing Facility, *Canadian Metallurgical Quarterly*, 21, 1, (1982), 67-72.
83. J. Garnham, J. Brightling and J. Beynon, Rolling-Sliding Dry Wear Testing-a Vibration Analysis, *Wear*, 124, (1988), 45-63.
84. J. Garnham and J. H. Beynon, The Early Detection of Rolling-Sliding Contact Fatigue Cracks, *Wear*, 144, (1991), 103-116.
85. J. Bodnar, C. Menu and M. Egee, Detection of Wear Cracks By Photothermal Radiometry, *Wear*, 144, (1991), 590-592.

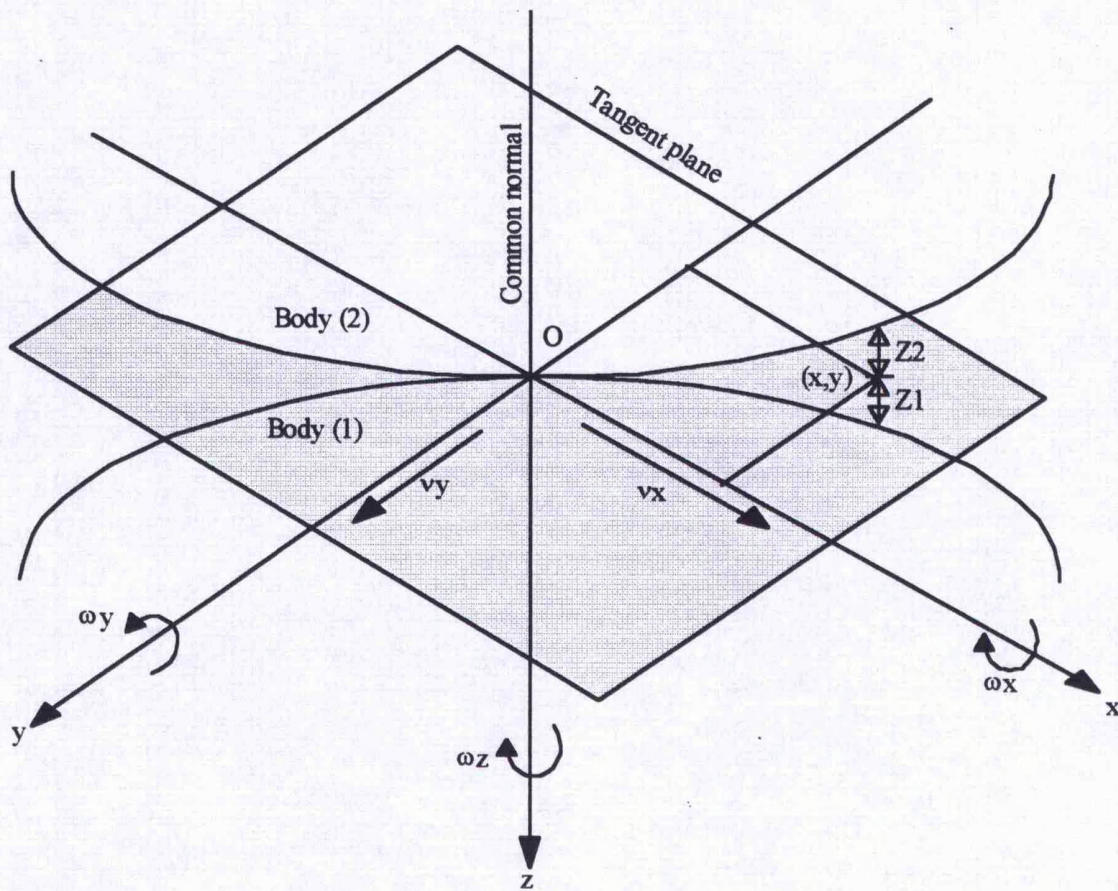


FIGURE (2.1): FIRST CONTACT OF NON-CONFORMAL SURFACES (AFTER JOHNSON⁽¹⁾)

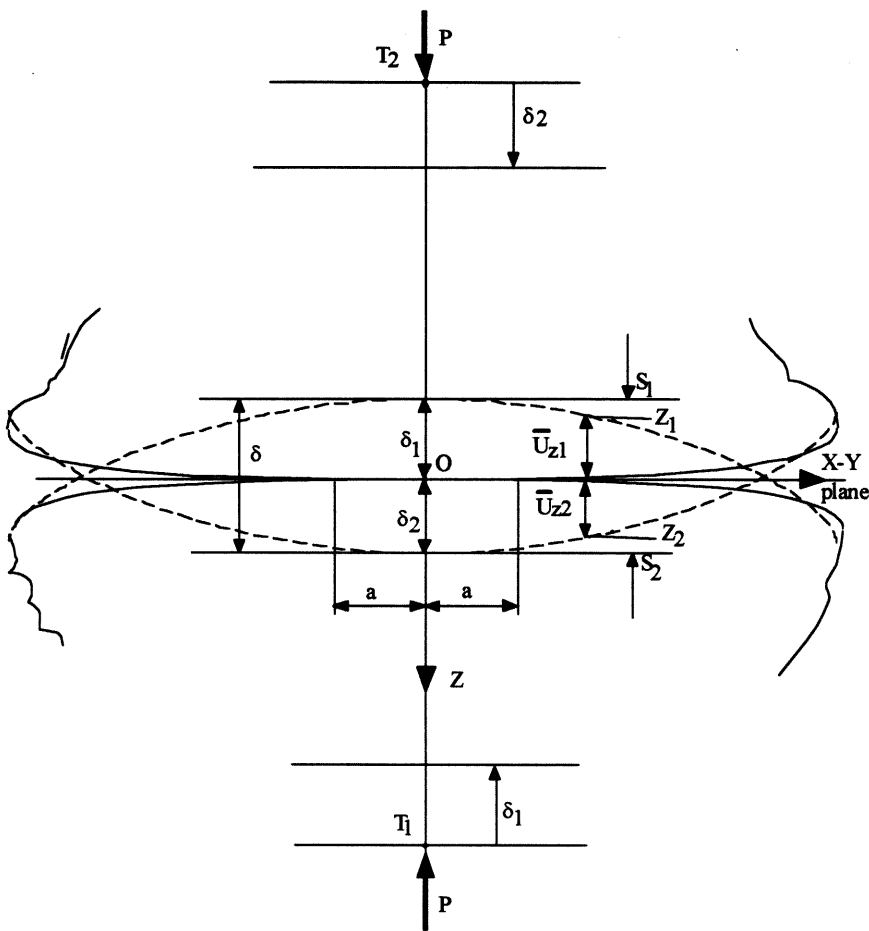


FIGURE (2.2): THE CONTACT OF NON-CONFORMAL SURFACES AFTER LOADING (AFTER JOHNSON⁽¹⁾)

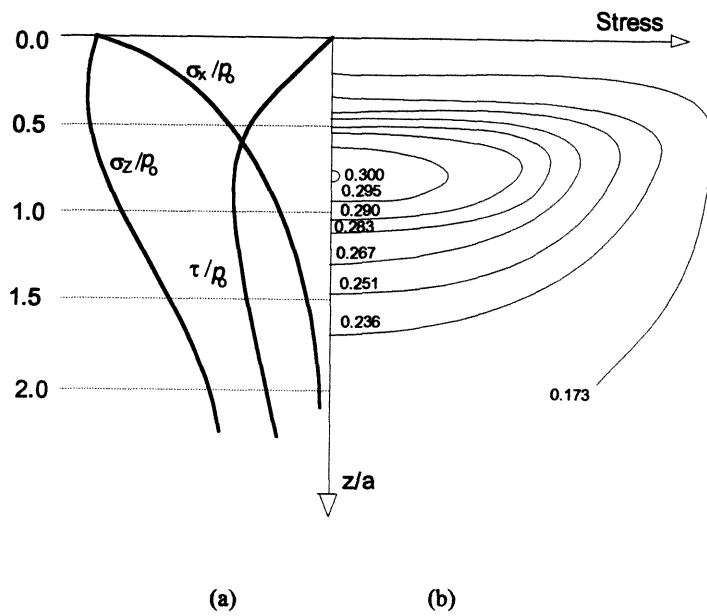


FIGURE (2.3): CONTACT STRESSES (a) VARIATION ALONG THE Z AXIS
(b) CONTOURS OF PRINCIPAL SHEAR (AFTER JOHNSON⁽¹⁾)

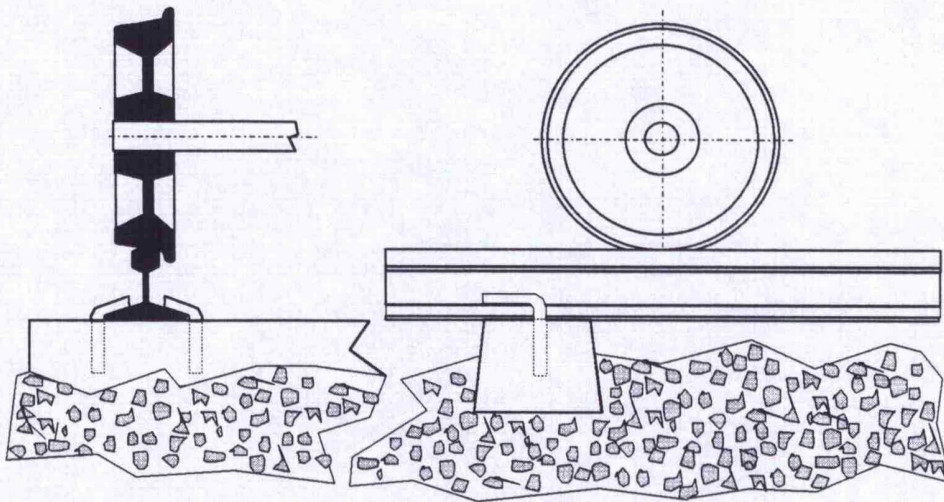


FIGURE (2.4): A TYPICAL WHEEL/RAIL SYSTEM

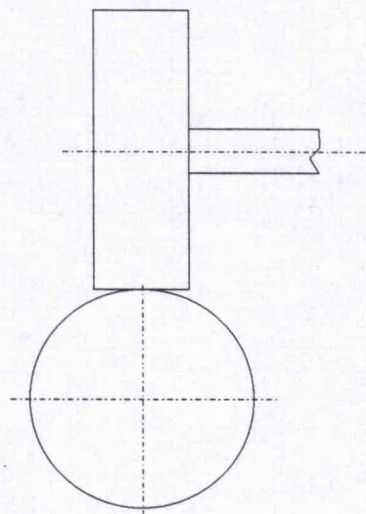


FIGURE (2.5): APPARENT WHEEL RAIL CONTACT GEOMETRY

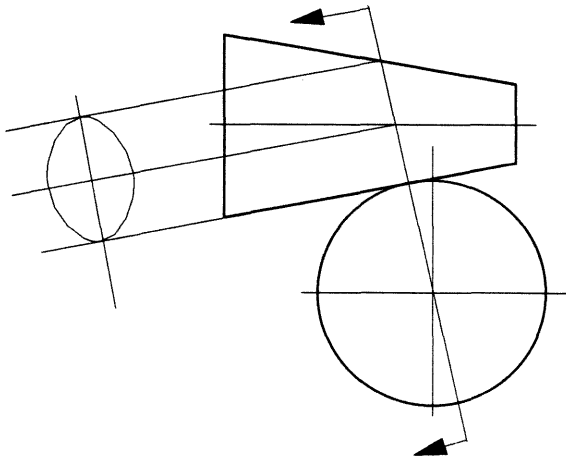


FIGURE (2.6): ACTUAL WHEEL-RAIL CONTACT GEOMETRY (AFTER ESDU⁽¹¹⁾)

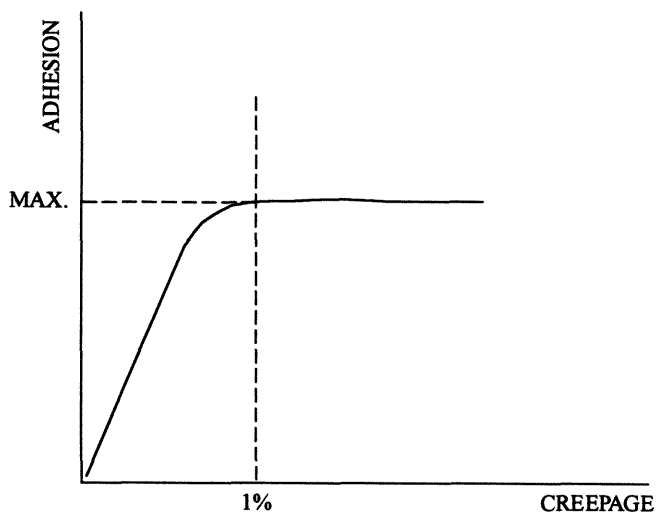


FIGURE (2.7): RELATIONSHIP BETWEEN CREEPAGE AND ADHESION (AFTER GREENWOOD⁽²⁴⁾)

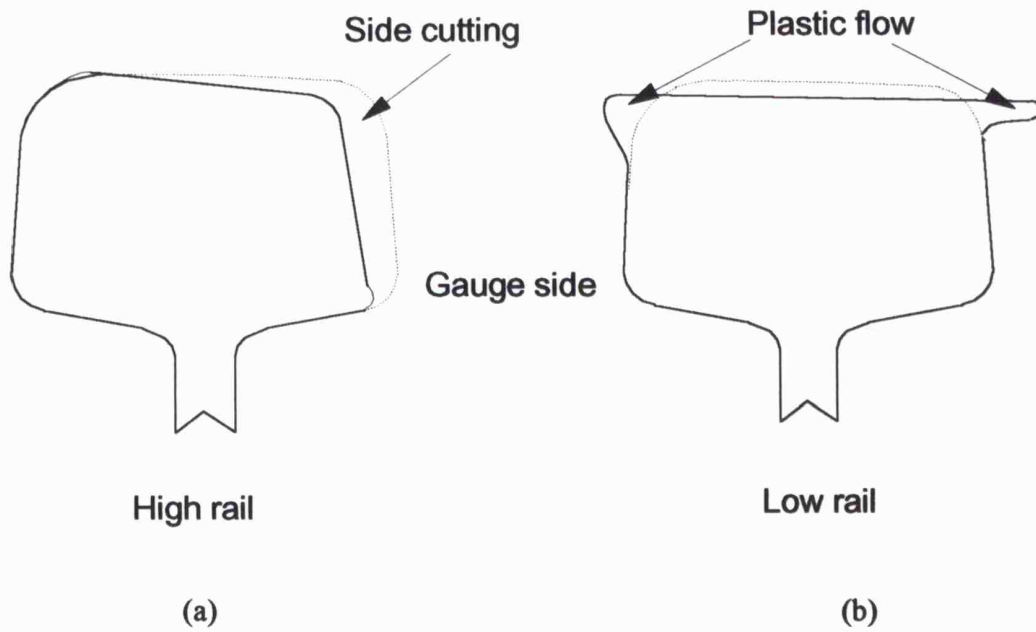


FIGURE (2.8): RAIL WEAR (AFTER KILBURN⁽³⁸⁾)

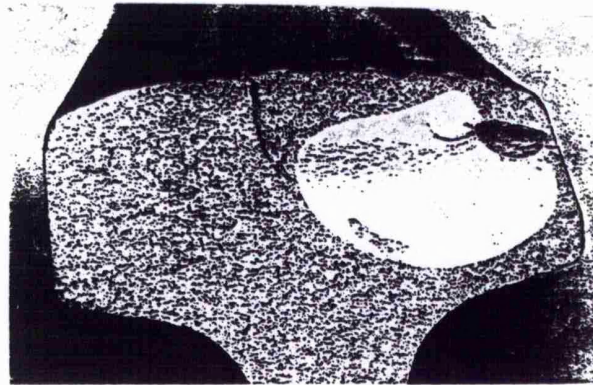


FIGURE (2.9): A DETAILED RAIL FRACTURE CAUSED BY SUBSURFACE INITIATED ROLLING CONTACT FATIGUE CRACK⁽⁴¹⁾

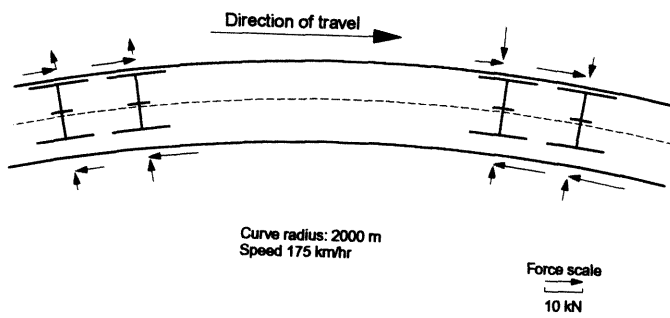


FIGURE (2.10): CURVING DIAGRAM FOR A VEHICLE ON STANDARD BRITISH RAIL TRACK⁽⁴³⁾

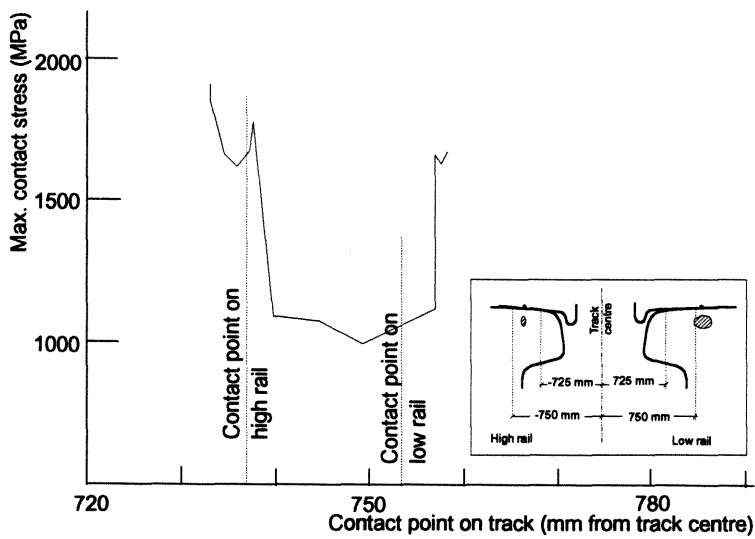


FIGURE (2.11): PREDICTED CONTACT STRESS ON HIGH AND LOW RAIL FOR A LEADING WHEELSET ON A STANDARD BRITISH RAIL PROFILE (FOR THE CONDITIONS IN FIGURE (2.10))⁽⁴³⁾

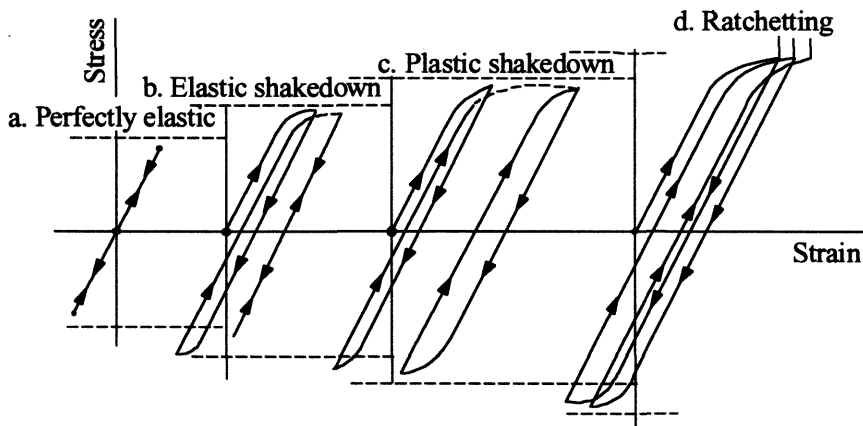


FIGURE (2.12): MATERIAL RESPONSE TO CYCLIC LOADING (AFTER JOHNSON⁽⁵³⁾)

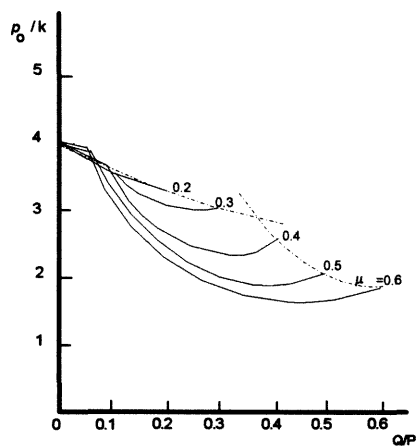


FIGURE (2.13): SHAKEDOWN LIMITS FOR TRACTIVE ROLLING OF TWO ELASTICALLY SIMILAR CYLINDERS ASSUMING ELASTIC PERFECTLY PLASTIC BEHAVIOUR (AFTER HILLS et al⁽⁵⁾)

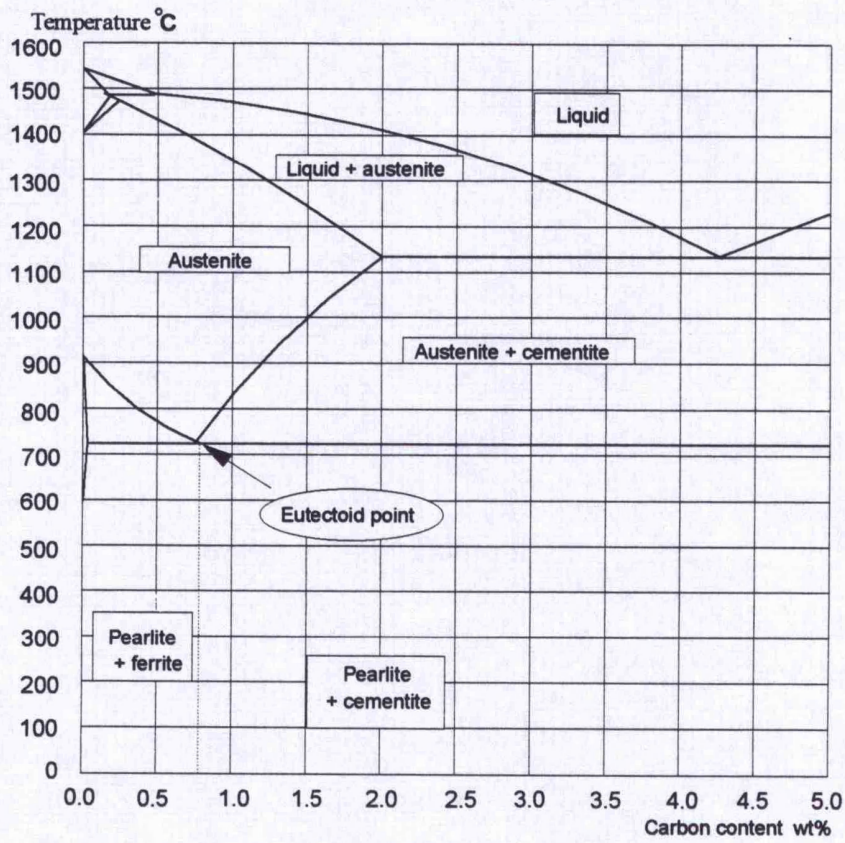


FIGURE (2.14): THE IRON-CARBON PHASE DIAGRAM (AFTER SINHA⁽⁷⁰⁾)

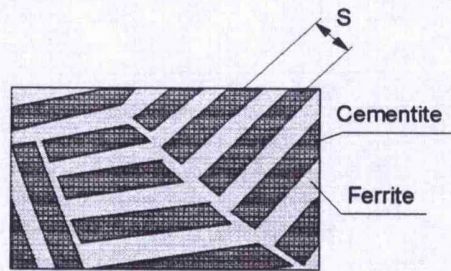
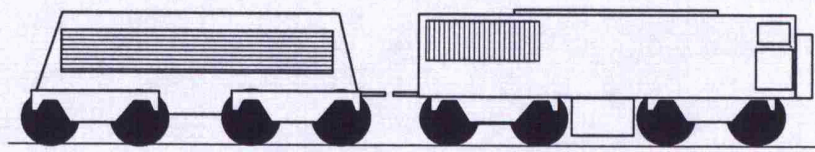
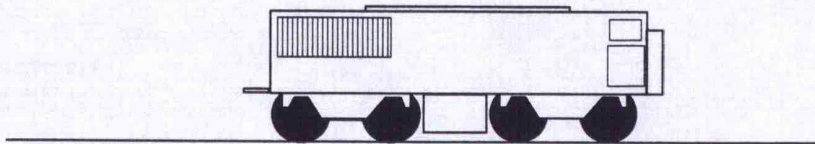


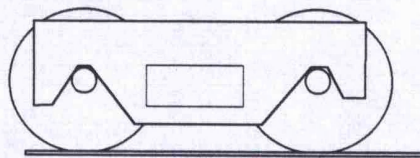
FIGURE (2.15): SCHEMATIC REPRESENTATION OF THE DEFINITION OF INTERLAMELLAR SPACING



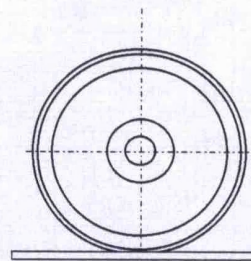
(a): Field test



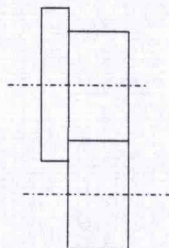
(b): Bench test



(c): Sub-system test



(d): Component test

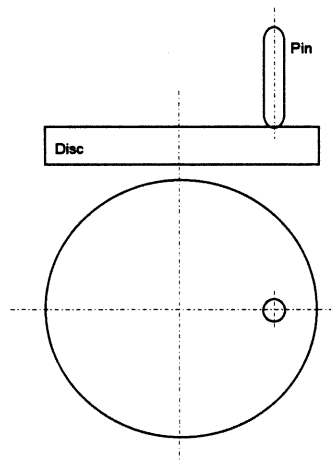


(e): Simplified component

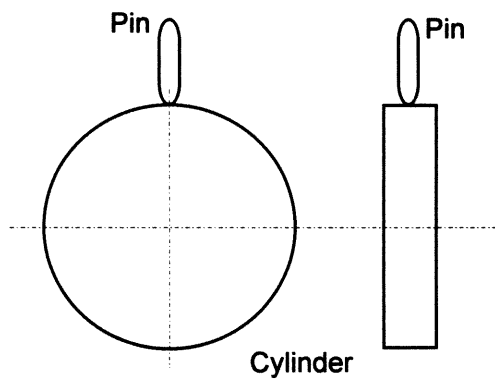


(f): Model test

FIGURE (2.16): SCHEMATIC REPRESENTATION OF TEST CLASSIFICATION
(AFTER ZUM GAHR⁽⁵⁹⁾)



(a): THE PIN-ON-DISC WEAR TEST SET-UP (AFTER ROBINOWSIC⁽⁸⁰⁾)



(b): ARCHARD'S PIN-ON-RING SET-UP (AFTER ARCHARD⁽⁸¹⁾)

FIGURE (2.17): SCHEMATIC REPRESENTATION OF THE PURE SLIDING WEAR TESTS

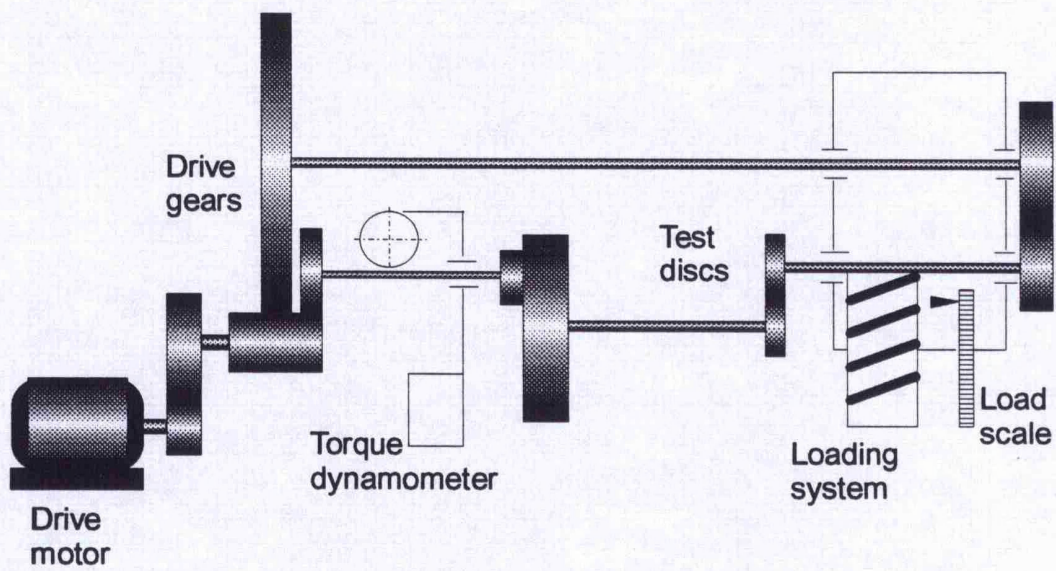


FIGURE (2.18): SCHEMATIC REPRESENTATION OF THE AMSLER WEAR TESTING MACHINE (AFTER GARNHAM et al⁽⁸³⁾)

Chapter 3

TEST EQUIPMENT, MATERIALS, PROCEDURE AND CONDITIONS

3.1. LEICESTER UNIVERSITY ROLLING-SLIDING (LEROS) TESTING MACHINE

Learning from the limitations and disadvantages of readily available test equipment normally used to simulate and investigate rail deterioration due to wheel-rail contact, such as the Amsler machine discussed in section 2.4.2, the research group working on wear and RCF at Leicester University have designed a new machine, LEicester university ROLLING-Sliding (LEROS) wear testing machine. The machine has an improved loading system, accurate creep control, a reliable RCF crack detection system and many other features⁽¹⁾. The large number of previous wear and RCF tests obtained by others^(2,3) using the machine produced a pool of comparable and reproducible test results. The LEROS machine and its related equipment is schematically illustrated in figure (3.1). The machine is basically a Colchester Mascott 1600 lathe modified to suit the purpose; figure (3.2) is a photograph of the machine. A 4 kW DC motor is mounted on the tail stock end of the machine bed. A drive shaft consisting of universal joints and splines, powered by the DC motor through an interchangeable gear box with a 5:1 gear ratio, was used throughout this work. The other end of the drive shaft is fitted with a machine tool arbor, supported through a pivoted bearing assembly with a counter weight. The wheel disc specimen (driving disc) is bolted to the end of the arbor. This assembly can swing by the action of a hydraulic jack powered by an electric motor driven hydraulic pump to facilitate the loading mechanism. The rail material disc (slower, or braking, disc) is secured to an arbor at the end of another drive shaft supported between a fixed bearing housing and the lathe chuck. The mid-section of this drive shaft is a torque transducer, which enables measurement of the tractional torque between the two discs, figure (3.3). The torque signal is fed to a chart recorder which records the change in torque with time, the torque is then converted into tractional force from which the coefficient of traction is calculated. The recorded traction is expected to be slightly higher than that between the two discs since a small proportion of the torque is

contributed by the fixed bearing assembly, located between the test discs and the torque transducer. The centre lines of the two drive shafts are parallel when discs are loaded, figure (3.4) shows a close-up view of the two discs in position. The required slip ratio (creepage) is achieved by selecting the test speed of the rail disc, using the lathe gear selector, and adjusting the rotational speeds of the DC motor which drives the wheel disc.

The machine is equipped with manual, as well as computer creepage control through a number of shaft encoders, transducers and a computer interface. Contact load is easily applied and controlled by electronically adjusting the opening of the hydraulic control valve that passes the oil to the jack, which in turn raises the bottom shaft bearing assembly which secures the wheel disc. Using a hydraulic control valve to adjust the load is prone to hysteresis loss during loading and unloading. The loading system can be improved by changing the load measuring device from a hydraulic valve to a load cell measuring device. A 10 kN load cell was used occasionally in this work to confirm the hydraulic valve load reading. The hydraulic loading system enables loads up to 29 kN to be applied. Assuming, for the sake of illustration, a Hertzian elastic contact, for the dimensions of disc specimens used in the present work this represents a maximum contact pressure of 3000 MPa. This feature of the machine results in minimising the disc track edge effect since wider track discs can be accommodated while maintaining contact pressures well above those experienced in the field. However, at loads higher than 1500 MPa, uniformity of the load distribution across the track width of the test discs is thought to be affected. This could be due to the accumulation of the fixed bearing assembly clearances to one side, resulting in a higher load at the lathe side of the contact area.

The idea of using a machine tool arbor as a specimen holder was to standardise this part so that it can be replaced with a readily available one. However, due to some modifications to the in-house built arbor housing, even new arbors have to be modified to suit this housing. To decrease the effect of the accumulation of clearances and to increase the stiffness of the test disc holding assembly, it is suggested that in future the arbor assembly be replaced with a single part to suit the purpose.

To detect RCF cracks, a computer controlled non-contact eddy current crack scanning and detection system (Elotest B1, manufactured by Rohmann (UK) Ltd.) is used. This scanning system represents a reliable method in which a signal level can be adjusted to activate an alarm when RCF cracking reaches a certain stage. It also enables the defect

area to be located with sufficient accuracy for further sectioning and investigation. One of the other advantages of the system is its ability of giving an idea about the propagation rate of the crack. This is possible by monitoring the rate of growth of the signal amplitude with number of cycles. Furthermore, in addition to the maximum signal which indicates the maximum crack depth, the cracking intensity can also be monitored by monitoring the number of signals above a certain level. This gives an idea whether the failure is due to single or a network of cracks. This is illustrated in figure (3.5) which shows a signal due to a single crack and another due to a network of cracks of different depths. The disadvantage of the system is its high sensitivity of the signal to the instrument settings including the lift off distance, which is the distance between the test probe tip and the track surface of the test disc.

The maximum contact pressure p_0 [MPa] is calculated using equation 2.18⁽⁴⁾. The creepage or slip ratio is calculated by the formula:

$$g(\%) = \frac{200(R_T N_T - R_B N_B)}{R_T N_T + R_B N_B} \quad (3.1)$$

where R_T and R_B are the radii of the top (braking) and the bottom (driving) disc, and N_T and N_B are the revolution counts of the top and bottom discs, respectively.

To maintain a relatively stable temperature, normally about 1 to 2 °C above room temperature, and to isolate the test discs from the external environment, an environment chamber which seals the test discs from the surrounding atmosphere is used. The chamber has two air nozzles supplying dry pressurised air to the running track of each disc. The debris generated during wear testing is removed by ensuring a slight negative pressure in the environment chamber using an industrial type vacuum cleaner. Debris can be collected in a filter for further analysis. The environment chamber is not used during RCF testing, since discs are cooled by the lubricating water needed during such testing. A simple gravity dripping system, where the supply of water is controlled by adjusting vales has been found to be the most reliable.

3.2. TEST MATERIALS AND SPECIMENS

It has been shown in chapter 2 that pearlitic steel is still the most widely used material for rail application. This may justify why this research project has focused on pearlitic rail steels. Most of the experiments have been carried out using BS11 Normal

Grade steel. High Strength Grade rail steel, sometimes referred to as Head Hardened (HH) or Mill Heat Treated (MHT), has also been used, mainly to study the deterioration of rolling contact fatigue life of rail steels due to dry-wet contact. All rail discs were run against W8A wheel steel discs. The chemical composition and the mechanical properties of the different disc materials are given in tables (3.1). For the purpose of this thesis the BS11 Normal Grade will be referred to as BS11 and the High Strength Grade as MHT.

Rail and wheel test materials have been kindly supplied by British Railways Board and ABB Wheelset Ltd., respectively. Disc specimens were machined in the Engineering main workshop to the dimensions shown in figure (3.6). The 47 mm disc diameter is the maximum obtainable from the rails supplied. All cutting and machining operation were chosen such that the original properties and microstructure were maintained. The orientation of the wheel disc specimens in relation to the wheel rim is shown in figure (3.7a). To ensure uniform properties of the rail discs, all the BS11 and some MHT discs were cut with their axis parallel to the rail long axis as in figure (3.7b). However, since the hardness of the MHT rail head varies with depth below the surface, as in figure (3.8), some MHT discs were cut with their axis perpendicular to the rail table, figure (3.7c).

3.3. TEST PROCEDURE

Detailed test procedure is, in general, dictated mainly by the objectives of that test. However, there are certain steps which were followed during all tests. The special procedure required for each set of tests aiming at studying a particular phenomenon will be discussed in the relevant chapters. The general procedure can be divided into three stages: prior to testing, during testing and after testing.

3.3.1. Prior to testing

Prior to every test, discs were engraved with an identification code, examined for surface defects and checked for dimensional accuracy. To ensure roundness and concentricity, roundness profiles of disc track and bore were recorded using a Talyrond 200 profilometer (Rank Taylor Hobson Ltd.), figure (3.9) shows the format of this record. The surface roughness of the disc running track was then recorded. The measuring stylus was run across the disc track perpendicular to the grinding marks (disc circumference), using a sampling range of 4 mm in the middle of the disc track. Discs were then cleaned in an ultrasonic bath of isopropanol, and their original weight was recorded using an

analytical balance (Sartorius R300S) of 0.0001 g resolution.

3.3.1.1. LEROS machine preparation

Two hours before starting the test the LEROS machine and related equipment, described in section 2.4.2, were switched on, allowing the hydraulic oil of the loading system to warm up and reach a steady temperature. The settings of the power supply to the torque transducer were checked before calibration. Using a loading lever and static weights, the torque transducer output was calibrated, the calibration plots were then converted into a relationship between the transducer output [mV] and the coefficient of traction. For the two loads used during this project this relationship is shown in figure (3.10). In case the planned test was a wear test, the air compressor and the air dryer were switched on and the pressure was adjusted to 1 kg/cm². The vacuum cleaner was also started to ensure that while the test discs were cooled by the air flow, a negative pressure sufficient to suck out the wear debris was maintained inside the environment chamber. For RCF testing air cooling was not needed since the discs were cooled by the water lubrication system described earlier. Water flow rate was adjusted to approximately one drop per second. The crack detection system (eddy current unit) was then calibrated using artificial cracks spark eroded to the surface of a calibration disc. The unit adjustments were then saved, using the unit memory, so that they could be used during all other similar tests. The lift-off distance (the gap between the disc track surface and the detection probe tip) was adjusted to 0.2 mm. Test discs were then firmly secured in position and the rotational speeds of the two shafts were set to give the required creepage, see equation 2.33. Before the two discs were brought to contact, the required load was set by raising the swinging bearing housing against the stop bolt. The calibration of the loading system was continuously checked using a 10 kN load cell.

3.3.2. *During testing*

With all preparations completed, the two test discs were loaded while rotating at the required speeds. simultaneously, the revolution counters were started and the chart recorder which records the torque was also enabled. Care was taken at the initial stages of tests to maintain the required creepage, since the torque transmitted between the two discs tends to slow the driving disc and speed up the braking disc. The crack detection scanning system was also started in case of RCF testing. Tests were then run either to a certain number of revolutions, in the case of wear testing, or to failure for RCF testing.

3.3.2.1. Locating RCF cracks

When the signal triggers the pre-set gates on the eddy current screen, the scanning mechanism was locked to that position using the computer scanning control system. Since the detection system is dynamic, response can be obtained only if the disc is rotating. Using the micrometer adjustment, the position of the scanning probe was adjusted to obtain the maximum signal amplitude. A hard copy of the signal and the settings was then printed, figure (3.11). Those settings were those used during calibration. Reducing the rotational speed of the disc to 20 rpm enabled marking a line along the circumference of the disc track opposite to the probe tip. The crack at this stage is known to be at any point on that line. Using the audible signal facility while watching the test disc rotation, the radial location could be roughly known by marking the radial position of the probe when the signal is heard. Accurate location of the crack could be achieved by stopping the disc and using the eddy current unit filter adjustment to set the frequency to 0.4 Hz and the by pass filter to 1 MHz. This increased sensitivity of the equipment to respond to any rotational movement of the disc. By manual back and forth rotation of the disc within the roughly marked area the crack could be located to within 1 mm accuracy. This feature enabled optimum sectioning of each test disc through the crack for further analysis.

3.3.3. After testing

At the end of each test, discs were dismantled and the after-test diameter and track width recorded. The running track roundness profile was also recorded. Discs were then cleaned in an ultrasonic bath of isopropanol and dried before their after-test weight was recorded. All discs were then sectioned, specimens were mounted, ground and polished before microhardness profiles below the contact surface were recorded. Specimens were then etched, using 2% concentration nitric acid in alcohol (nital), to reveal the microstructural features.

3.4. TEST-GENERAL CONDITIONS

It was shown in section 2.2.5 that there is a large number of variables affecting the rail deterioration due to wheel/rail contact. Test conditions used during this project were chosen to represent the service conditions of British Railways. Only two contact pressures, 1200 and 1500 MPa, were used. These represent the range of typical maximum contact pressures observed in service, see section 2.1.5.1. All tests were conducted with a

creepage of 1%, the value which is known to result in maximum coefficient of traction between wheel and rail, see section 2.1.5.1. Water lubrication was used during RCF testing since it is the dominant lubricant in many climates. Particular test conditions will be discussed in relevant chapters.

REFERENCES:

1. J. E. Garnham and J. H. Beynon, The Early Detection of Rolling-Sliding Contact Fatigue Cracks, *Wear*, 144, (1991), 103-116.
2. A. Perez-Unzueta, Ph. D. Thesis, University of Leicester, (1992).
3. J. E. Garnham and J. H. Beynon, Dry Rolling-Sliding of Bainitic and Pearlitic Steels, *wear*, 157, (1992), 81-109.
4. S. P. Timoshenko and D. N. Goodier, *Theory of Elasticity*, McGraw-Hill, (1970).

Material	Rail		Whee l
	BS11	MHT	W8A
Specification			
Chemical composition (wt %)			
C	0.52	0.72-0.82	0.64
Si	0.2	0.10-0.60	0.23
Mn	1.07	0.80-1.10	0.71
Ni	0.03		0.17
Cr	<0.01		0.18
Mo	<0.01		0.03
S	0.018	0.02 max.	0.041
P	0.013	0.03 max.	0.023
Mechanical properties			
Average hardness (HV500g)	240-250	385	275
Ultimate tensile strength (MPa)	781	1250	857
Yield strength (MPa)	406	724	325
Total plastic elongation (%)	21.9		20.3
Young's modulus (GPa)	209	210	199

TABLE (3.1): CHEMICAL COMPOSITION AND MECHANICAL PROPERTIES OF THE TEST MATERIALS

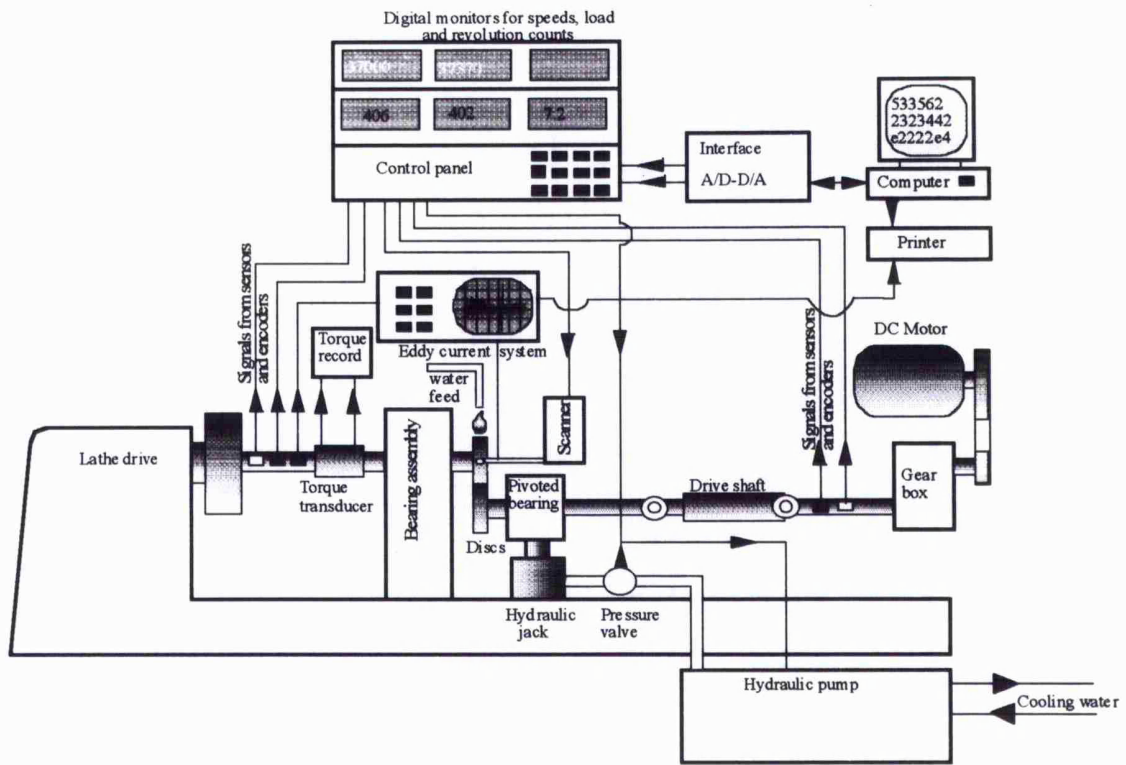


FIGURE (3.1): SCHEMATIC REPRESENTATION OF THE LEROS MACHINE AND THE TEST SET-UP

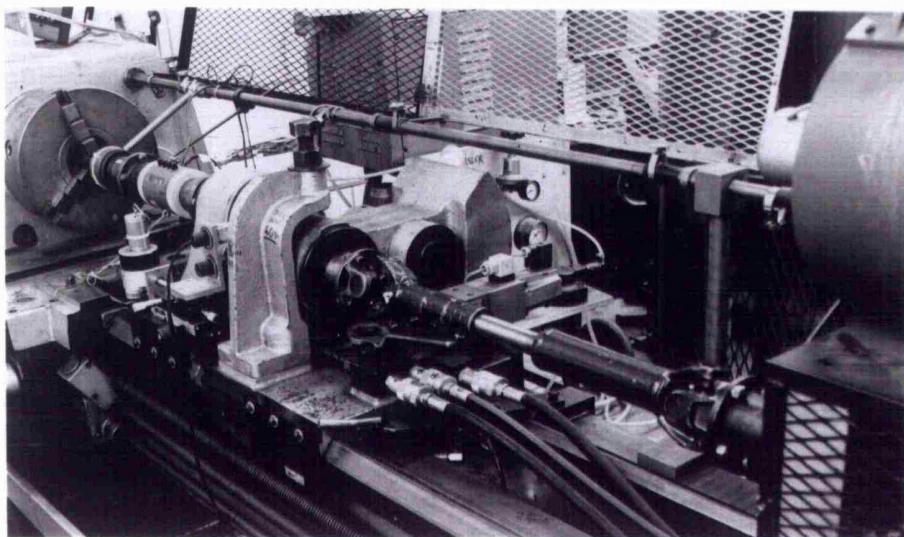


FIGURE (3.2): THE LEROS TESTING MACHINE

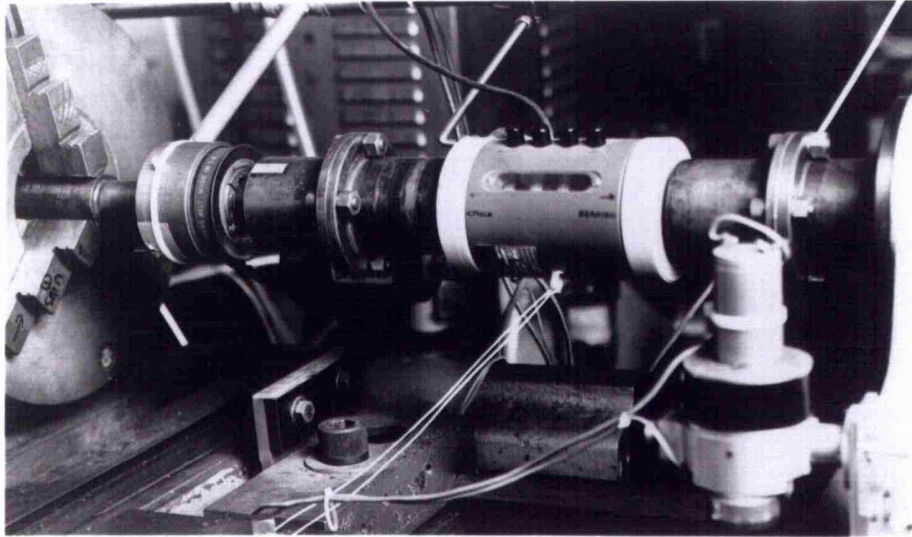


FIGURE (3.3): THE TORQUE TRANSDUCER USED TO MONITOR THE TRACTION TRANSMITTED BETWEEN THE TWO TEST DISCS

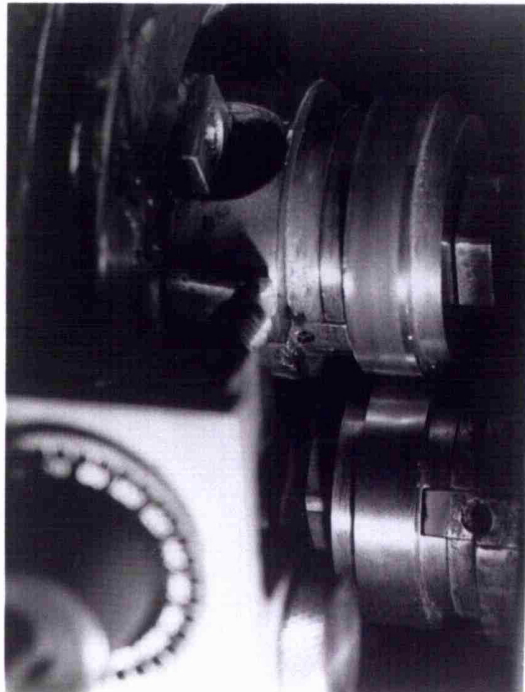
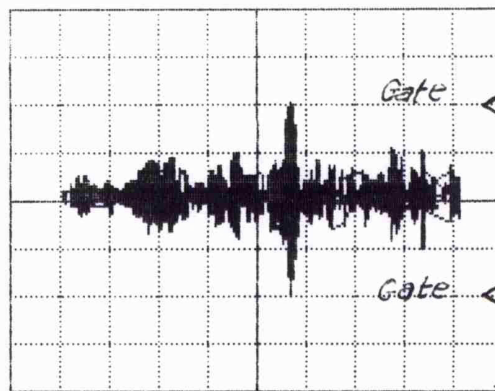
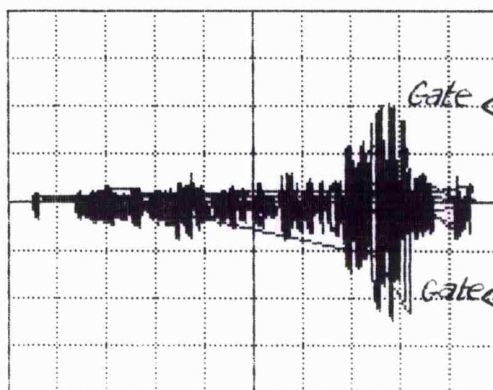


FIGURE (3.4): A CLOSE-UP VIEW OF THE TWO TEST DISCS IN POSITION

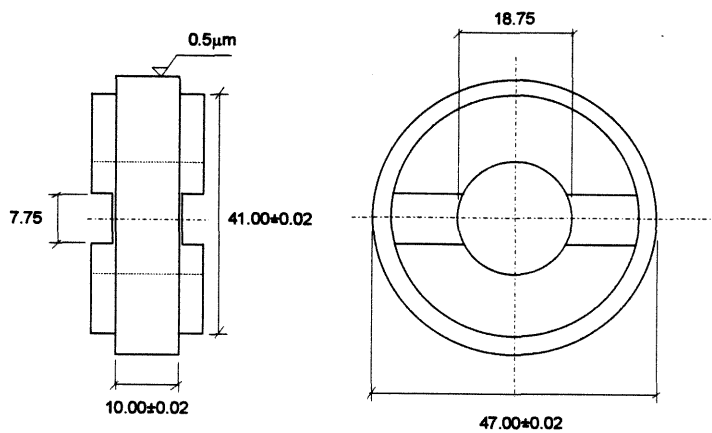


(a): SINGLE CRACK



(b): A NETWORK OF CRACKS

FIGURE (3.5): EDDY CURRENT CRACK DETECTION SYSTEM SIGNALS



ALL DIMENSIONS ARE IN (mm)

FIGURE (3.6): DIMENSIONS OF THE TEST DISCS

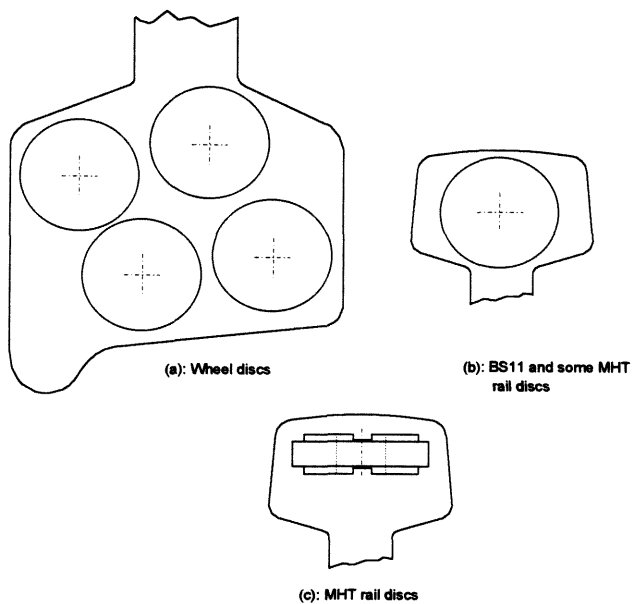


FIGURE (3.7): THE ORIENTATION OF THE TEST DISCS IN RELATION TO THE WHEEL RIM AND RAIL SECTION

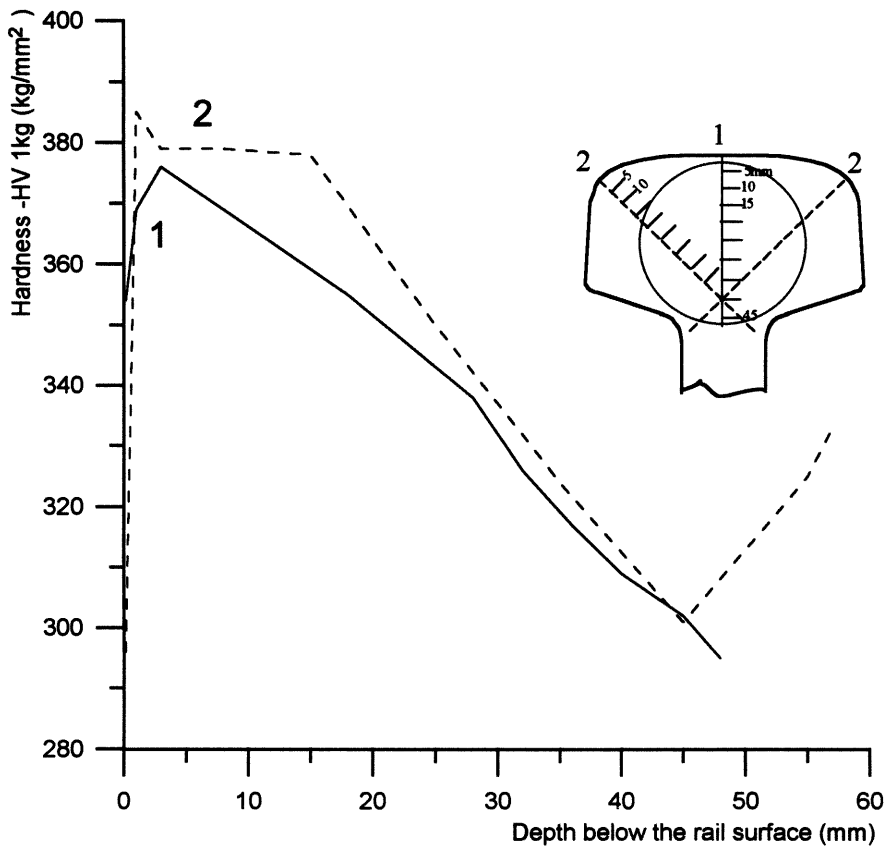


FIGURE (3.8): THE CHANGE IN HARDNESS WITH DISTANCE FROM THE SURFACE OF THE MHT RAIL HEAD

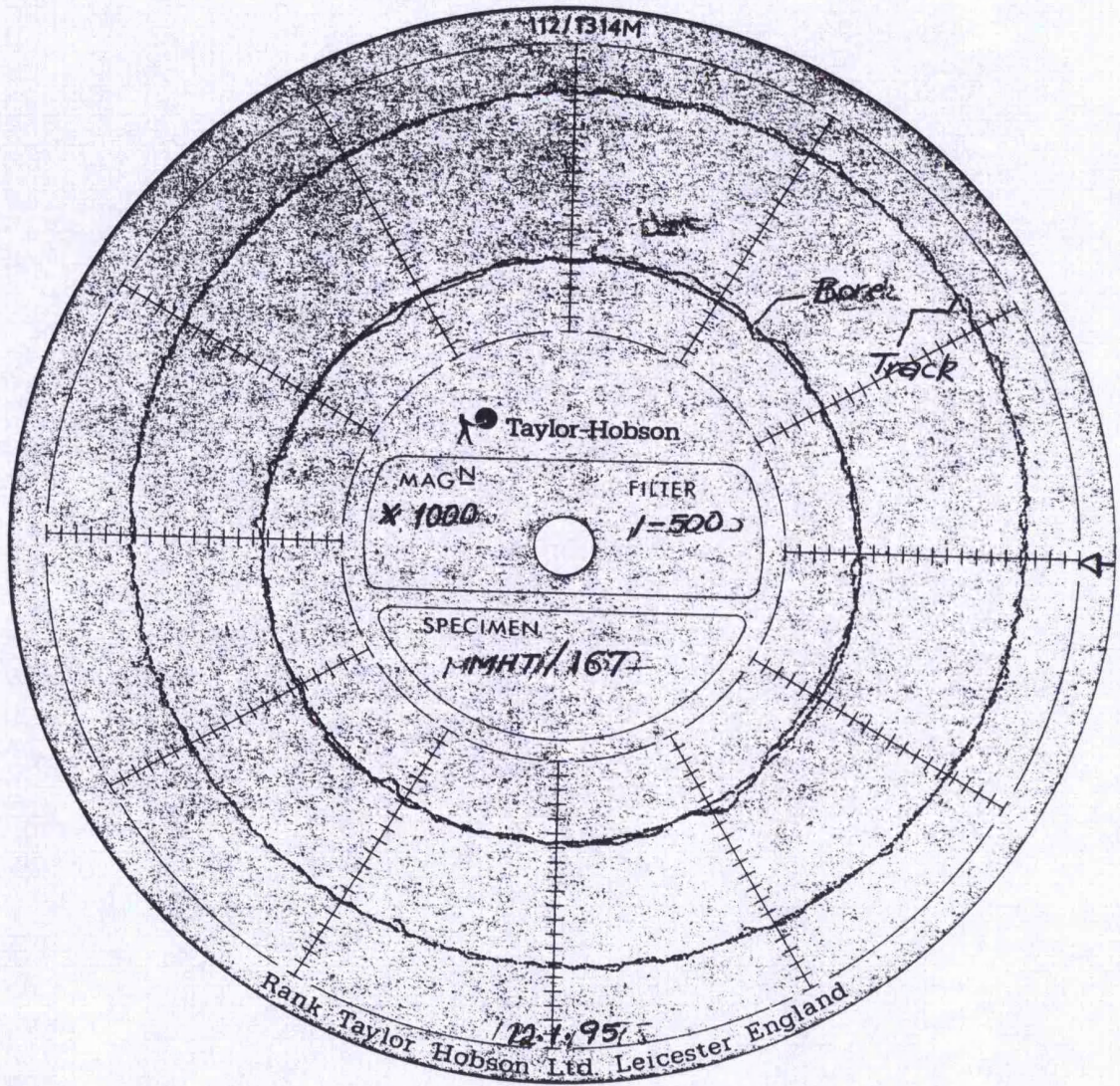


FIGURE (3.9): THE FORMAT OF THE DISC PROFILOMETRY RECORDING SYSTEM

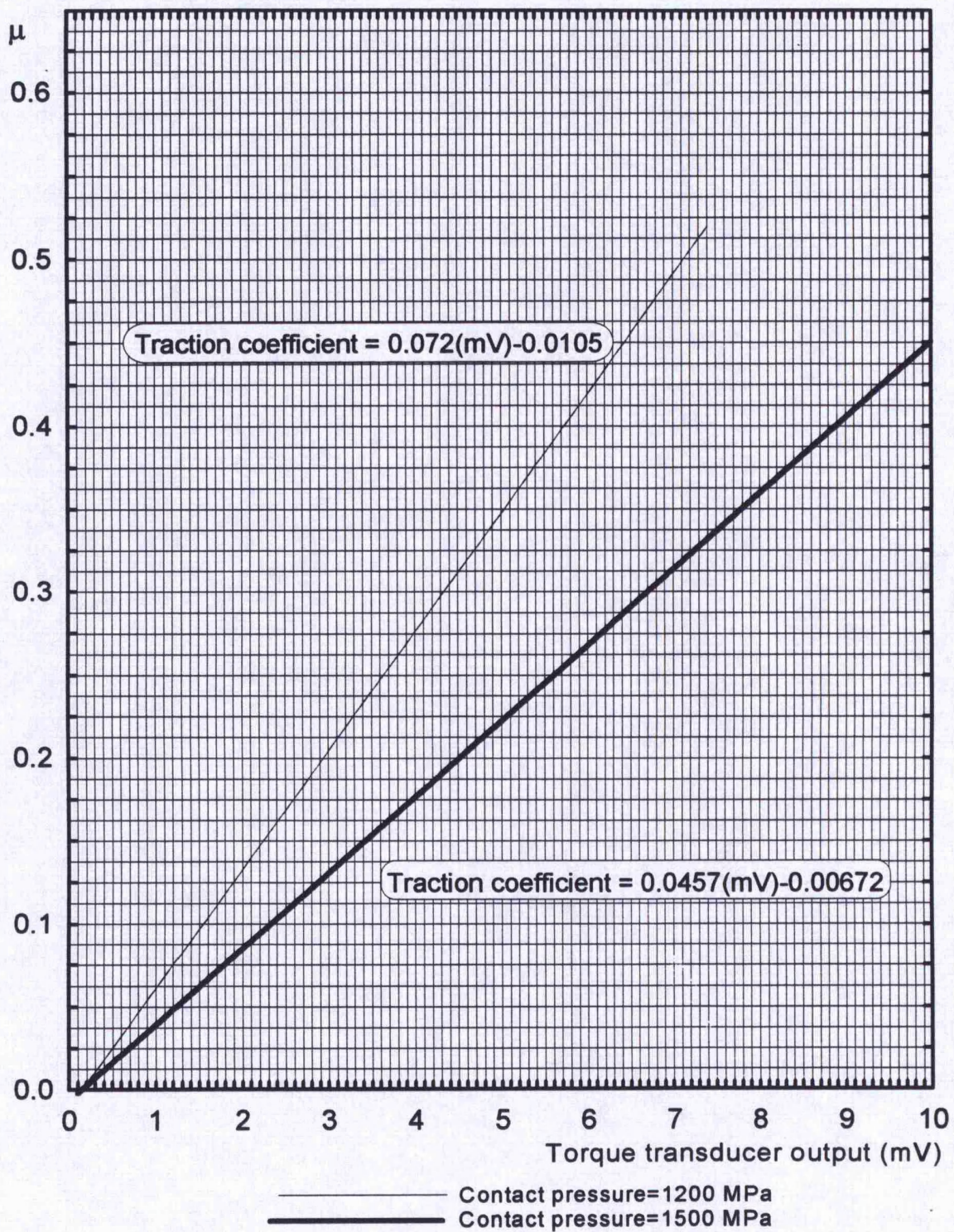


FIGURE (3.10): THE RELATIONSHIP BETWEEN THE TORQUE TRANSDUCER OUTPUT AND THE TRACTION COEFFICIENT

EDDY CURRENT R.C.F. CRACK DETECTION

LEICESTER UNIVERSITY ENGINEERING DEPARTMENT TRIBOLOGY LABORATORY
Test No:.....Date:.....Machine:L/A/.....
Material:()Top:.....()Bottom:.....(x disc tested)
Max. Contact Stress (MPa):.....Creepage (%):.....
Top / Bottom disc rpm:.....Top / Bottom disc revs:.....
Lubrication:.....Av. Friction Coefficient:.....

Elotest B1.3 DM Version 1.09 Serial Number 87119

SETTINGS:
Frequency : 1.0 MHz
Bandwidth : HF
Preamplifier : 24dB
Gain Y/X : 46dB/ 41dB
Phase : 5 degrees
Dot Position Y/X : 0/ 0
Filter : Highpass 350 Hz BP:3.4

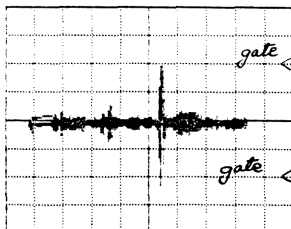


FIGURE (3.11): SETTINGS OF THE EDDY CURRENT CRACK DETECTION FACILITY

Chapter 4

THE ONSET OF STEADY STATE WEAR BEHAVIOUR OF PEARLITIC RAIL STEEL UNDER DRY ROLLING-SLIDING CONTACT CONDITIONS

4.1. INTRODUCTION

The mechanism by which material is lost from the contact surface during dry rolling-sliding is an area of scientific debate. Different workers have different views and theories by which they explain the contact surface failure mechanism in this case. Those theories can be summarised by :

a. The elastic fatigue failure mechanism which explains the formation of wear particles in terms of elastic fatigue. Kraghelsky⁽¹⁾ argued that even when the initial contact is plastic, it soon changes to elastic with repeated loading. The material in this case fails due to elastic fatigue.

b. The delamination mechanism proposed by Suh⁽²⁾, in which he explained the formation of wear particles in terms of dislocation pile-ups at finite depth below the contact surface. These result in formation of voids which, with repeated loading, coalesce to form cracks. When these cracks grow to a critical length they produce sheet like particles.

c. The low cycle fatigue mechanism: plastic flow of the surface layer material during repeated contact loading have lead some workers to try to explain wear in this case in terms of low cycle fatigue. This explanation has been used by Challen et al⁽³⁾, Lacey and Torrance⁽⁴⁾ and more recently by Kopalinsky and Oxley⁽⁵⁾.

d. Ratchetting mechanism: which explains wear by the accumulation of unidirectional plastic strain above a certain critical limit. Kapoor⁽⁶⁾ has recently shown that ratchetting and low cycle fatigue are competitive and that the material fails by whichever is satisfied in the shorter number of cycles.

In view of the above discussion, it is difficult to verify which of these mechanism can explain the wear behaviour of rail steel under service conditions. To throw more light on

this subject, experiments under conditions akin to those experienced in service have been conducted; aimed at studying the mechanism by which material is lost from the surface of the rail (braking) test disc when subjected to dry rolling-sliding repeated contact conditions. Attention has been focused on the period which leads to steady state wear behaviour. The results have been the subject of a paper published in 1994 in *Wear*, a copy is attached as appendix (I). The test procedure was that described in chapter 3. BS11 rail discs were run against W8A wheel discs; see tables (3.1) for chemical composition and mechanical properties. All tests were conducted under a maximum contact pressure of 1500 ± 5 MPa and a creepage of -1 ± 0.01 %. Test conditions are summarised in table (4.1). All tests but one were non-stop tests, only test number 130 was stopped every 2500 cycles to monitor the wear rate at different stages of the rolling-sliding process.

4.2. RESULTS

The test results are summarised in table (4.2). Hardening is calculated as the percentage ratio between the hardened material and that of the bulk. Wear rates are presented as total weight loss of the test disc. Disc track width gain due to the lateral plastic flow at the free sides, as well as loss in disc diameter, are also reported. Strains are estimated by measuring the shear angle (γ) between the tangent to the deformed grain boundaries or lamellar deformed pearlite and the normal to the contact surface; figure (4.1) shows a schematic representation of this method. Shear strains are then calculated by:

$$\varepsilon = \tan(\gamma) \quad (4.1)$$

Coefficient of traction is calculated and presented as maximum as well as end-of-test values. It is derived from the chart record by which the torque transmitted between the two test discs is monitored.

4.2.1. Number of rolling-sliding cycles to establish steady state wear rate

Measuring the weight loss of the discs of test number 130 at regular intervals of 2500 cycles enabled the wear behaviour to be monitored as the rolling-sliding proceeded. Accumulated weight loss of the rail disc is plotted in figure (4.2) against number of rolling-sliding cycles. The plot reveals a slow wear rate at the early stages of the test, beyond

which the relationship appear to be linear, except for a slight change in the wear behaviour, in the form of a small kink corresponding to nearly 17500 cycles. To study the significance of this behaviour, weight loss per cycle of the rail disc is plotted in figure (4.3) against number of rolling cycles. It can be seen that the wear rate is almost negligible during the first 2500 cycles, thereafter increasing with number of rolling cycles until around 17500 cycles, where it stabilises at around 18 μg per cycle for the remainder of the test. This reveals that the kink on the plot of figure (4.2), described earlier, is not an experimental error but a significant change in the wear behaviour.

The running track appearance indicates that the mechanism by which the rail disc loses material prior to the steady state stage is mainly oxidative wear, where the disc track was observed to be covered by a thin, grey oxide layer. However, during steady state the track appearance is characterised by a shiny flaked surface. The transition to steady state is characterised by the gradual loss of the oxide layer and the exposure of the disc material to the surface. At the same time, fine surface cracks start to appear on the running track. These cracks are thought to be the origins of the flakes noticed during the steady state stage. These surface features are shown in figure (4.4), which is a low magnification photograph of the rail disc running track after different numbers of rolling cycles. The similar oxidised surface features after 500 and 1000 cycles may indicate a similarity in the wear mechanism. Likewise, it is difficult to differentiate between the tracks of the discs tested for 17500 and 40000 cycles. Both are characterised by a shiny flaked surface of similar scale. In this case the wear rates are also at the same level. Moreover, regardless of the initial surface roughness of the disc pairing, measurement of the after-test track surface roughness revealed identical values after 500 and 1000 cycles. In both the cases this roughness was Ra 0.26 μm , whereas it was around Ra 8 μm after 5000 cycles, see table (4.2). Surface roughness after 17500 and 40000 cycles appeared to be higher than that after 5000 cycles. However numerical values could not be obtained since the size of the flakes was too large compared with the sampling range of the available measuring equipment.

In all but one case the driving (wheel) disc wear rate was higher than that of the driven (rail) disc. A comparison between the wear rates of the two discs from test 130 is shown in figure (4.5). No attempt has been made to study the strains and the strain

hardening behaviour of the wheel disc material, attention being focused on the rail disc.

4.2.2. Strain hardening behaviour

Measurement of the hardness at and very near to the worn contact surface does not give accurate results. At a shallow depth below the contact surface, hardness values are affected by the existence of flake roots, subsurface cracks and by the directionality in the properties of the heavily deformed layer where, due to the shear stress, a lamellar structure is dominant. To reduce the influence of these features, hardness at depths less than 0.2 mm below the contact surface was measured with the indenter perpendicular to the disc axis. Progressive grinding and polishing of the disc wear track enabled this kind of measurement to be carried out. Hardness profiles below the contact surface are shown in figure (4.6) for different test cycles. These profiles indicate that the material is hardening in a non-linear manner, where hardening rate is highest during the initial stages of the test. No further hardening is noticed beyond 17500 cycles. This is better revealed in figure (4.7), where the percentage hardening at 0.2 mm below the contact surface is plotted against number of rolling cycles. The depth 0.2 mm was chosen for the reasons mentioned at the beginning of this section. The maximum percentage hardening, 86% above the bulk material hardness, is established after 17500 cycles. However, almost 30% hardening is achieved during the first 500 cycles. The hardening rate decelerates with number of rolling cycles until it becomes zero beyond 17500 cycles; (no measurements were taken between 10000 and 17500 cycles). The degree of strain hardening is maximum at the contact surface. At steady state, the rail disc surface hardness reaches a value 2.5 times that of the bulk material.

4.2.3. Accumulated plastic strain

It was shown in section 3.2 that most of the hardening is established during the initial stages of the rolling process. The deformed structure due to the different cycling distances indicates that most of the shear strain is also accumulated during the early rolling cycles. To quantify this accumulation, shear strains after the different number of rolling cycles used were measured using the method described earlier, see figure (4.1). Figure (4.8) shows the shear strains, measured at 0.2 mm below the contact surface, plotted as a function of number of rolling cycles. The plot reveals a high strain accumulation rate during the initial stages. This rate decelerates with number of rolling cycles until it is zero

after 17500 cycles, where the accumulated strain achieves its maximum value. No further strains were observed beyond these cycles. This is illustrated in figure (4.9) which shows the deformation of the pearlitic structure after different numbers of rolling cycles. The similarity of the deformation after 17500 and 40000 cycles is very close.

4.2.4. Coefficient of traction

Recording the torque transmitted between the two test discs during a non-stop test of 40000 cycles enabled the behaviour of traction coefficient to be monitored as the rolling process proceeded. This coefficient is plotted in figure (4.10) as a function of number of rolling cycles. The plot reveals that the coefficient of traction starts to increase with number of cycles and reaches its maximum, 0.441, after around 2000 cycles before it starts to fall again. The rate of fall decelerates slowly until it sustains a constant fall rate after around 15000 cycles. After 40000 cycles, the traction coefficient drops to 0.268. No attempt has been made to investigate the traction coefficient behaviour beyond 40000 cycles. The same behaviour was noticed during all other non-stop tests.

Cleaning the test discs prior to weighing, as in test number 130 where the test was being stopped every 2500 cycles, affected the traction coefficient. After each cleaning, nearly 500 cycles were required to raise the traction to its pre-cleaning level before it exceeded that level and then drifted downward again, see figure (4.10).

4.3. DISCUSSION

4.3.1. Weight loss and side plastic flow

During rolling-sliding testing, material is lost from the contact surface by detachment of wear flakes as well as by plastic flow into lips to the sides of the test disc track. Table (4.2) shows that the diameter loss of the disc specimens is more than what could be contributed by the weight loss. It also shows the track widening due to the formation of lips at the sides of the track, schematically exaggerated in figure (4.11). Although track widening increases the apparent contact area, it may not affect the contact stresses since the extra area is in the form of lips which may not support load. That is why this type of flow can be considered as wear. The same type of flow is also noticed on the gauge face of curved rails, see figure (2.11) in chapter 2. However, the term 'wear' will be used here to

describe the weight loss only. No attempt will be made to discuss the effect of plastic side flow.

The steady state wear rate of 18 $\mu\text{g}/\text{cycle}$, mentioned in section 3.1, corresponds to 1.54 nm per cycle depth loss, assuming all the metal is lost and no plastic lip is formed. Since such a lip does form, the diameter loss will actually be larger. From the measurements of diameter change, the depth loss is about 80% more than that calculated from the weight loss alone. Thus just under 3 nm per cycle is lost from the surface. Such small amounts are not found in the debris, where flakes of the order of 3-10 μm thick are observed. Thus the process of metal loss by flaking must be a discrete event occurring periodically rather than a continuous process. However, this discrete event gives a fairly uniform weight loss curve, rather than a discrete stair shaped curve, since it happens at different places on the running track surface of the disc.

4.3.2. Measurement of the accumulated plastic strain.

The method used to measure the accumulated unidirectional plastic strains reported in section 3 may not be very accurate to measure strains at or very near to the contact surface, where a small change in the shear angle corresponds to a significant increase in the shear strain. However, at depths of 0.2 mm and deeper below the contact surface the method gives a reasonably accurate measure of the strain. The method is similar to that used by Bower and Johnson⁽⁷⁾ who used spark eroded slots filled with dental amalgam to measure surface displacement during sliding wear tests. A similar technique has also been used by Bhargava et al⁽⁸⁾. Zhang and Alpas⁽⁹⁾ used a marker platelet inserted to the test piece surface to visualise and measure displacement during sliding contact testing.

4.3.3. Ratchetting failure

The contact pressure ($p_0 = 1500 \text{ MPa}$) and the coefficient of friction ($\mu > 0.3$) in the case of this work are known to cause a shear stress (τ_{xz}) higher than the shear yield strength of the material (k). In this case two failure mechanisms may be considered. If the cyclic straining of the material does not result in accumulation of plastic strain, the surface layer fails by low cycle fatigue^(3,10). Alternatively, if the surface layer accumulates unidirectional plastic strain with number of cycles, the material may fail due to an

alternative failure mechanism, 'ratchetting failure', in which failure takes place when the material accumulates unidirectional plastic strain equal to its critical strain to failure⁽¹¹⁾.

It has been shown in figure (4.8) that the test conditions of the present work have resulted in strain accumulation with number of rolling cycles. Accordingly, the failure mechanism is expected to be that of ratchetting. As a wear mechanism, ratchetting implies that material should start to detach from the surface (fail) after accumulating plastic strain equal to its critical strain to failure. Consequently, the material has to be subjected to a certain number of rolling-sliding cycles before the first weight loss can be observed. In these experiments, wear rate increases gradually before the steady state is observed, see figure (4.3). This behaviour can be explained by arguing that:

(a) Ratchetting is not the only wear mechanism operating during rolling-sliding contact. Oxidative wear is dominant during the initial stages. Under the test conditions of this work oxidative wear was observed to prevail during the first 5000 cycles

(b) Every time material is removed from the surface, a new layer of a different accumulated strain history is exposed to contact surface.

The argument in (b) may be better understood if we consider three material elements at different depths below the contact surface, with the first element at the surface. The three elements will be subjected to different shear stress levels according to their depth below the surface, where the surface element will be subjected to the maximum shear stress. These shear stresses will have two main effects:

1. With each passage of the load they produce a shear strain which decreases with the depth. The surface element will see the maximum strain.

2. This leads to strain hardening, the maximum of which is also at the surface.

At the beginning of the test, the shear yield strength of the material (k) is constant over the depth below the surface, figures (4.6) and (4.12a). The distribution of the shear stress (τ_{xz}) divides the material below the surface into two regions. Down to a certain depth, point s on figure (4.12), the shear stress is higher than (k). Since the surface element has not strain hardened and is still relatively soft, its strain rate will be higher. This explains the high hardening and straining rates during the initial stages of the test, see

figures (4.7) and (4.8) respectively. As the rolling continues, this element strain hardens, figure (4.12b) and, as a result, the strain accumulated per cycle decreases. As deformation proceeds, the surface element reaches a stage where further strain is not possible due to the exhaustion of ductility, figures (4.8) and (4.12c). The material of the element would be expected to fail when it accumulates plastic strain equal to its critical strain to failure. This failure is the detachment of metal from the surface as a flake.

Once the surface element detaches from the surface, the second element will be exposed to the contact. However, the difference between the two is that the second element will reach the surface partially damaged (partially strained with part of its ductility already exhausted while it was still below the surface). This implies that it requires fewer subsequent cycles to fail by ratchetting. This may explain the increase in wear with number of rolling cycles before the steady state.

As far as the third, deepest, element is concerned, it is expected to reach the surface with greater previous damage than that of the second element and it should fail even earlier leading to a yet higher wear rate.

If the same argument is applied to more elements, a stage will be reached where all the material reaching the surface will have the same prior history of accumulated strain and loss of ductility as its predecessor. The steady state wear rate is expected when the first of the layers of such material reaches the surface. In the case of the present work this stage starts after about 17500 cycles.

The diameter loss corresponding to a test of 17500 cycles duration, number 138 in table (4.2), is 85 μm , or just over 40 μm loss in radius. It is interesting to observe in figure (4.6) that this is very close to the surface compared with the depth of penetration of the plastic deformation. Thus steady state conditions do not require the feeding through of the subsurface material from below the fully work hardened layer.

The above argument is supported by the measurements of the accumulated plastic strain, plotted in figure (4.8) as a function of number of rolling cycles. It shows that after a certain number of rolling cycles, in this case about 17500 cycles, further strain accumulation ceases and no further strain accumulation is observed up to the end of the test, (40000 cycles). Similar behaviour of rail steel can be seen in figure (4.12b) of Bower

and Johnson⁽⁷⁾ under conditions of dry sliding contact. Likewise, between 17500 and 40000 cycles no additional hardening could be observed, see figure (4.7). Similar results have been obtained by Zhang and Alpas⁽⁹⁾, who reported a work hardening rate close to zero near the surface of Al-7% Si alloy tested under sliding conditions.

It can be concluded that steady state wear behaviour is established when material elements of the same strain hardening and accumulated plastic strain history start to reach the surface. This is evident in figure (4.13) where the percentage strain hardening, the accumulated unidirectional plastic strain and the wear rate are plotted against number of rolling cycles. Further evidence is the similarity of the deformed structure and the test disc running track appearance after 17500 and 40000 cycles, figures (4.9a) and (4.9b), respectively.

The complexity of the stress state and the hardening behaviour during rolling-sliding contact conditions has led some researchers to simplify these conditions. Controlled cycling tests under conditions of tension-compression, tension-torsion and compression-torsion^(7,13,14), at different mean stress levels and cycling regimes have been aimed at quantifying the hardening and ratcheting behaviour under rolling-sliding conditions.

The hardening behaviour observed in this work could not be correlated with the results of those studies. This could be due to the following factors:

(a) As it approaches the contact surface, deformed pearlitic steel exhibits directionality in its mechanical properties⁽¹⁵⁾. As a result, the assumption of isotropic material properties in studying the near-surface stress state is not appropriate.

(b) The simulations used to represent the rolling-sliding stress state mentioned above do not include the element of wear and the consequent continuous changes of the stress state of the near-surface layer as this layer approaches the contact surface.

(c) Studying the coefficient of traction recorded under the test conditions adds further complications to the surface layer stress state. The plastic strains are governed by the difference between the operating contact pressure and the shakedown limit of the material⁽⁷⁾. Since the plastic shakedown limit of the material is a function of the coefficient of traction, any change in this coefficient results in a new strain cycle. In studying the

hardening behaviour under rolling-sliding conditions, researchers usually assume a constant traction coefficient with each cycle. However, figure (4.10) shows a significant difference between the maximum and the end-of-test traction coefficients, 0.441 and 0.268 respectively. This difference cannot be ignored.

(d) The high hydrostatic pressure, caused by the contact load, enhances the ductility of the material. This is evident in figure (4.9) where severe deformation of the surface layer can be observed.

To summarise, it has been shown that if pearlitic rail steel is subjected to the rolling-sliding conditions used during this work, steady state wear is established when material layers of the same previous history of strain hardening and unidirectional plastic strain are exposed to the contact surface. There, material reaches its critical strain to failure and fails by detaching from the surface. This allows the next layer to be exposed to the contact surface to face the same end result.

4.3.4. Traction coefficient

It is preferable to refer to the ratio between the tractional and normal forces between the two discs as the 'coefficient of traction' rather than the coefficient of friction. According to Amonton's laws of friction the coefficient of friction is a constant and is determined only by the material pairing. This implies that friction is not a function of rolling distance. The plot in figure (4.10) shows that the traction coefficient does change with number of rolling cycles. Similar behaviour has also been reported by others⁽¹⁶⁾. No attempt has been made to study the effect of surface layer deformation on the traction transmitted between the two discs. However, there is evidence that the mechanical and chemical properties of the surface layer of the disc change with number of rolling cycles^(17,18). A study of the relationship between the coefficient of traction and the changes to the surface layer was conducted by Krause and Demerci⁽¹⁷⁾ who showed that the behaviour of the traction coefficient under dry rolling-sliding conditions is affected by the structural changes to the deformed surface layer, such as the changes to the crystal orientation and subgrain size.

The effect of cleaning the test discs on the traction behaviour could be explained by arguing that cleaning involves the removal of the oxide layer, mainly off the wheel disc where it is more prevalent. This oxide is known to act as a lubricant between the two discs.

The sharp peaks observed after every cleaning, figure (4.10), supports this argument. The traction coefficient drop after the initial peak coincides with the formation of a new oxide layer.

4.4. CONCLUSIONS

4.4.1. If pearlitic rail steel is subjected to rolling-sliding loads above its ratchetting threshold it exhibits a steady state wear rate, characterised by a constant weight loss per rolling cycle, after a certain number of rolling cycles. Under the conditions used in this work, this number is around 17500 cycles.

4.4.2. The steady state wear rate is established when material of the same history of strain hardening and accumulated unidirectional plastic strain reaches the surface and the unidirectional plastic strain limit to failure is reached.

4.4.3. Strain accumulation and strain hardening rates are maxima at the beginning of the rolling-sliding process and decrease in a non-linear fashion to cease after a certain number of cycles.

4.4.4. During the initial stages of the rolling-sliding process, oxidative wear is the main mechanism by which material is lost from the surface of the pearlitic rail steel.

4.4.5. The coefficient of traction is a function of rolling distance and cannot be assumed to be constant since it changes significantly with number of rolling cycles. Interrupting the test to clean the test discs affects the coefficient of traction by increasing it momentarily. This increase is due to the removal of the oxide layer, mainly off the wheel disc, which acts as a lubricant between the two discs.

4.4.6. A good method to prove that ratchetting, not low cycle fatigue, is the dominant failure mechanism under the test conditions, is to conduct wear experiments under conditions of rolling direction reversal. Since low cycle fatigue is not sensitive to strain direction, while ratchetting is, a drop in the wear rate due to strain direction reversal is a significant indication that accumulation of unidirectional plastic strain (ratchetting) is the contact surface failure mode in this case. It is interesting that very recently this verification method has been suggested by Kopalinsky and Oxley⁽⁵⁾ to support the low cycle fatigue argument. They wrote: “ *then a problem arises in explaining wear for*

conditions where direction of sliding is reversed. Such a reversal would be expected to act to cancel out unidirectional strain already put into the surface and in this way to reduce wear. This might be the case, but it certainly needs testing. This is one reason for using the effective strain in calculating changes in flow stress resulting from strain hardening in complex stress situations". This will attempted in chapter 5.

REFERENCES:

1. I. V. Kraghelsky, *Friction and Wear*, Butterworths, (1959).
2. N. P. Suh, The Delamination Theory of Wear, *Wear*, 25, (1973), 111-124.
3. J. M. Challen, P. L. Oxley and B. S. Hockenhull, Prediction of Archard's Wear Coefficient for Metallic Sliding Friction Assuming Low Cycle Fatigue Wear Mechanism, *Wear*, 111, (1986), 275-288.
4. P. Lacey and A. A. Torrance, The Calculation of Wear Coefficients For Plastic Contacts, *Wear*, 145, (1991), 367-383.
5. E. M. Kopalinsky and P. L. Oxley, Investigation of the Deformation and Damage Sustained by a Wearing Surface in Sliding Metallic Contact, *Trans. ASME, J. Tribology*, 49, (1994), 1-6.
6. A. Kapoor, A Re-evaluation of the Life to Rupture of Ductile Metals by Cyclic Plastic Strain, *Fatigue Fract. Engng. Mater. Struct.*, 17,2, (1994), 201-219.
7. A. F. Bower and K. L. Johnson, The Influence of Strain Hardening on Cumulative Plastic Deformation in Rolling and Sliding Line Contact. *J. Mech. Phys. Solids*, 37, 4, (1989), 471-493.
8. V. Bhargava, G. T. Hahn and C. A. Rubin, Analysis of Rolling Contact with Kinematic Hardening for Rail Steel Properties, *Wear*, 122, (1988), 267-283.
9. J. Zhang and A. T. Alpas, Delamination Wear in Ductile Materials Containing Second Phase Particles, *Material Science and Engineering*, A160, (1993), 25-35.
10. L. F. Coffin and J. R. Schenectady, A study of the Effect of Cyclic Thermal Stresses on a Ductile Metal, *Transactions of the ASME*, Aug., (1954), 931-950.
11. P.P. Benham and H. Ford, Low Endurance of a Mild Steel and an Aluminium Alloy, *J. Mech. Engg. Sci.*, 3, 2, (1961), 119-132.
13. A. F. Bower, Cyclic Hardening Properties of Hard-Drawn Copper and Rail Steel, *J. Mech. Phys. Solids*, 37, 4, (1989), 455-470.
14. H. Sehitoglu and R.Y. Jiang, Cyclic Ratchetting Behaviour of 1070 Steel and Experimental Simulation of Rolling Contact, (1992), *American Association of Railroads Progress Report No. 5*, University of Illinois.

15. G. Langford, Deformation of Pearlite, *Metallurgical Transactions*, 8A, (1977) 861-875.
16. H. Krause and H. Lehna, Investigation of the Tribological Characteristics of Rolling-Sliding Friction Systems by Means of Systematic Wear Experiments Under Well-Defined Conditions, *Wear*, 119, (1987), 153-174.
17. H. Krause and H. Demirci, Factors Influencing the Real Trend of the Coefficient of Friction of Two Elastic Bodies Rolling Over Each Other in Presence of Dry Friction, *The Mechanics of Contact Between Deformable Bodies*, (1975), Delft University Press, Eds. A. D Pater and J. J. Kalker.
18. B. I. Kostas, The Structural-Energetic Concept in the Theory of Friction and Wear (Synergism and Self-Organisation), *Wear*, 159, (1990), 1-15.

TEST CONDITIONS	TEST NUMBER						
	134	136	137	136	138	130	139
Disc material	Top (Rail)			Bottom (Wheel)			
Initial surface roughness (Ra, µm)	Rail			Wheel			
Maximum contact pressure (MPa)	0.10			0.44			
Percentage creepage (%)	0.12			0.14			
Test speed: [Rail-Wheel] (RPM)	1500						
Orientation of rail disc specimen relative to the rail section	-1						
Total number of cycles [Rail]	406-410						
Test environment	 Dry, air cooled						

* Test stopped every 2500 cycles for weight loss measurements.

TABLE (4.1): TEST CONDITIONS

RESULTS	TEST NUMBER									
	134	136	137	135	138	130	139	134	136	137
Total number of cycles	500	1000	5000	10000	17500	40000	40000	500	1000	5000
Coefficient of traction :	0.405	0.432	0.441	0.441	0.441	0.441	0.441	0.405	0.432	0.441
End of test	0.405	0.432	0.386	0.322	0.300	0.340	0.268	0.405	0.432	0.441
Contact area (mm ²)	6.11									
Total disc weight loss (g):	0.0005	0.0029	0.0348	0.1341	0.2490	0.6520	0.6198	0.0005	0.0029	0.0348
Wheel	0.0005	0.0001	0.0382	0.1694	0.6320	1.3650	1.6732	0.0005	0.0001	0.0382
Total disc diameter loss (mm):	n.m	0.005	0.005	0.045	0.085	0.200	0.200	n.m	0.005	0.005
Wheel	n.m	0.005	0.005	0.030	0.162	0.330	0.400	n.m	0.005	0.005
Total disc track width gain (mm):	n.m	0.130	0.220	0.385	0.720	1.060	1.145	n.m	0.130	0.220
Wheel	n.m	0.080	0.170	0.215	0.485	0.960	0.675	n.m	0.080	0.170
Accumulated shear strain at 0.2 mm below the contact surface of rail disc	2.0	2.4	4.3	5.7	11.4	11.4	n.m	2.0	2.4	4.3
Total strain hardening at 0.2 mm below the contact surface of rail disc (%)	29.2	37.9	69.6	80.8	88.8	88.8	n.m	29.2	37.9	69.6
End of test surface roughness: Rail Ra (µm)	0.26	0.26	7.3	8.11	n.m	n.m	n.m	0.26	0.26	7.3

n.m: Value not measured due to the limitation of the measuring equipment.

TABLE (4.2): TEST RESULTS

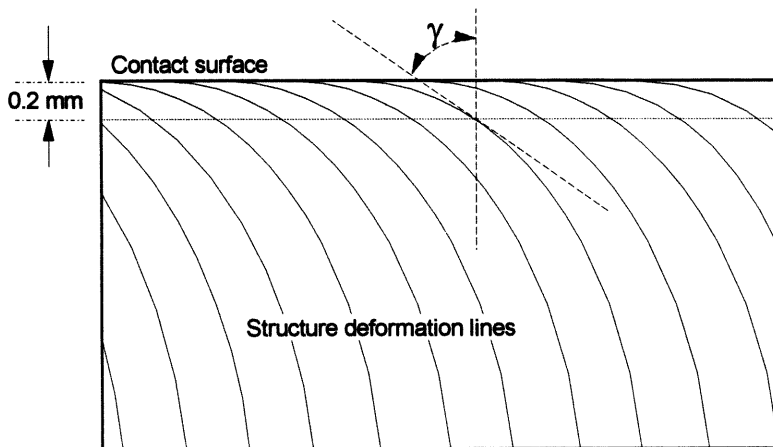


FIGURE (4.1): SCHEMATIC REPRESENTATION OF THE METHOD USED TO MEASURE THE SHEAR STRAIN

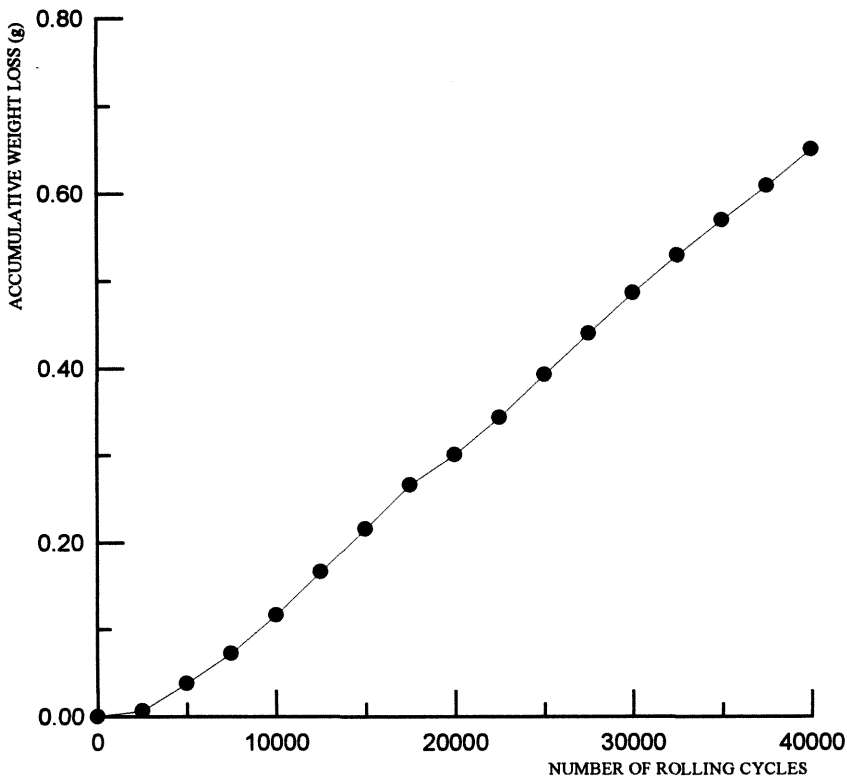


FIGURE (4.2): WEAR OF THE RAIL DISC REPRESENTED AS ACCUMULATED WEIGHT LOSS (TEST 130)

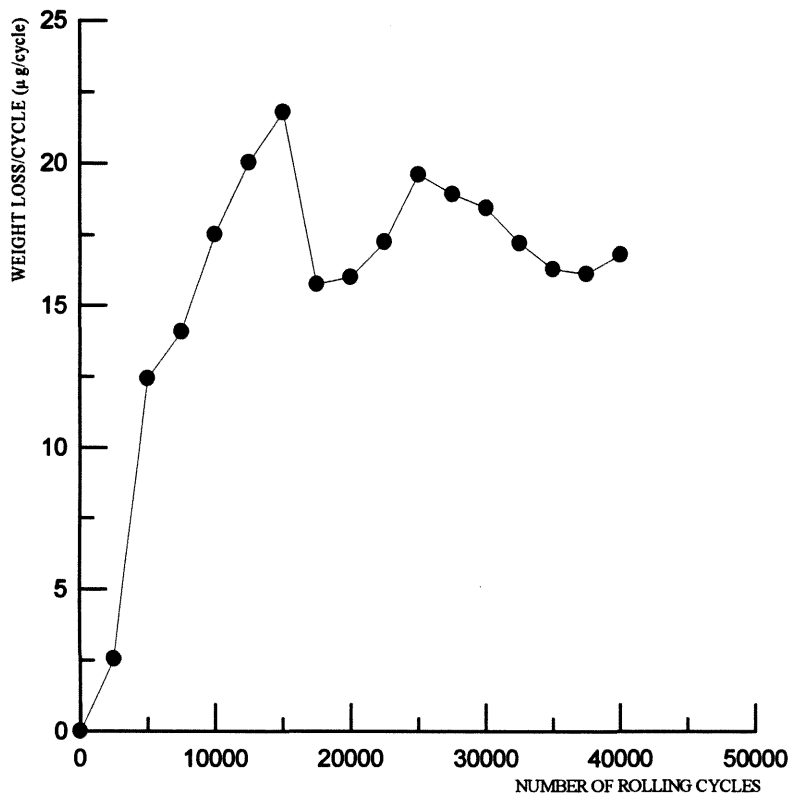
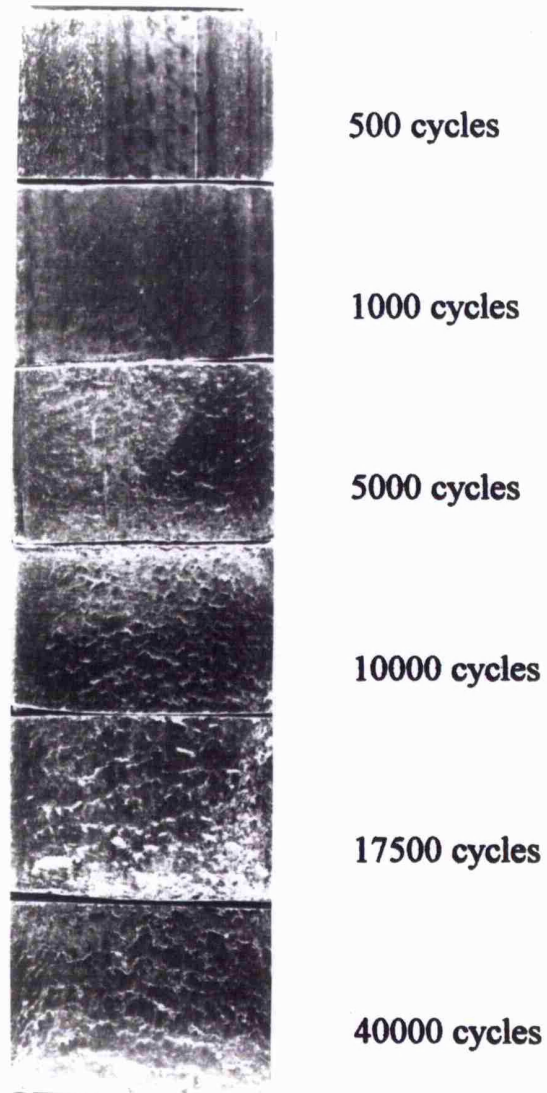


FIGURE (4.3): RELATIONSHIP BETWEEN THE WEAR RATE OF THE RAIL DISC, EXPRESSED AS WEIGHT LOSS PER ROLLING CYCLE AND NUMBER OF ROLLING CYCLES



**FIGURE (4.4): RAIL DISC RUNNING TRACK APPEARANCE AFTER
DIFFERENT ROLLING DISTANCES**

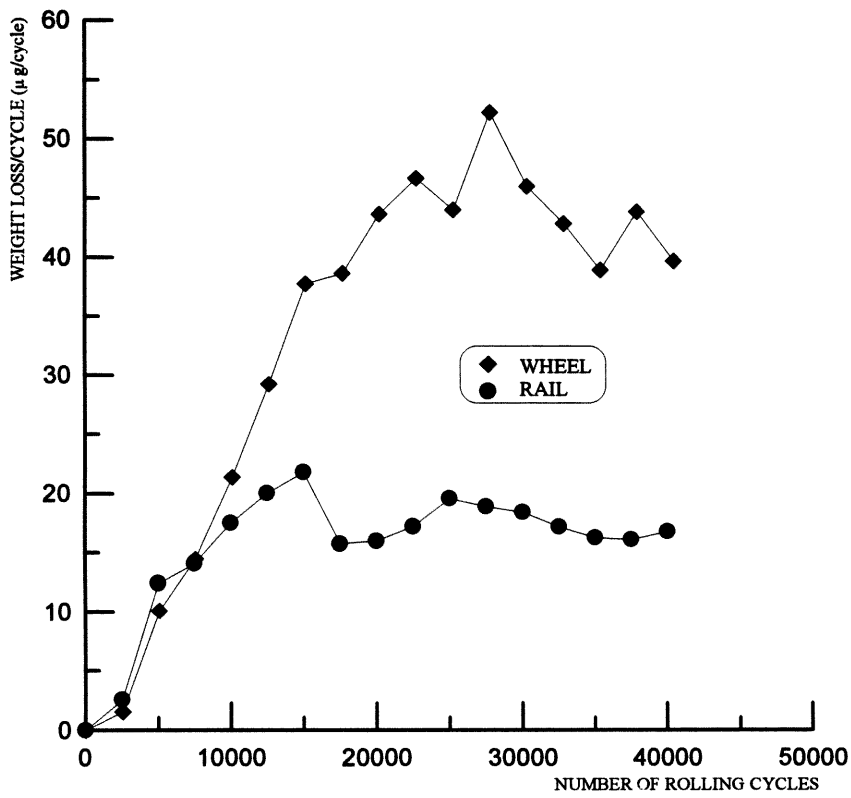


FIGURE (4.5): A COMPARISON BETWEEN THE WEAR RATES OF THE RAIL AND WHEEL TEST DISCS (TEST 130)

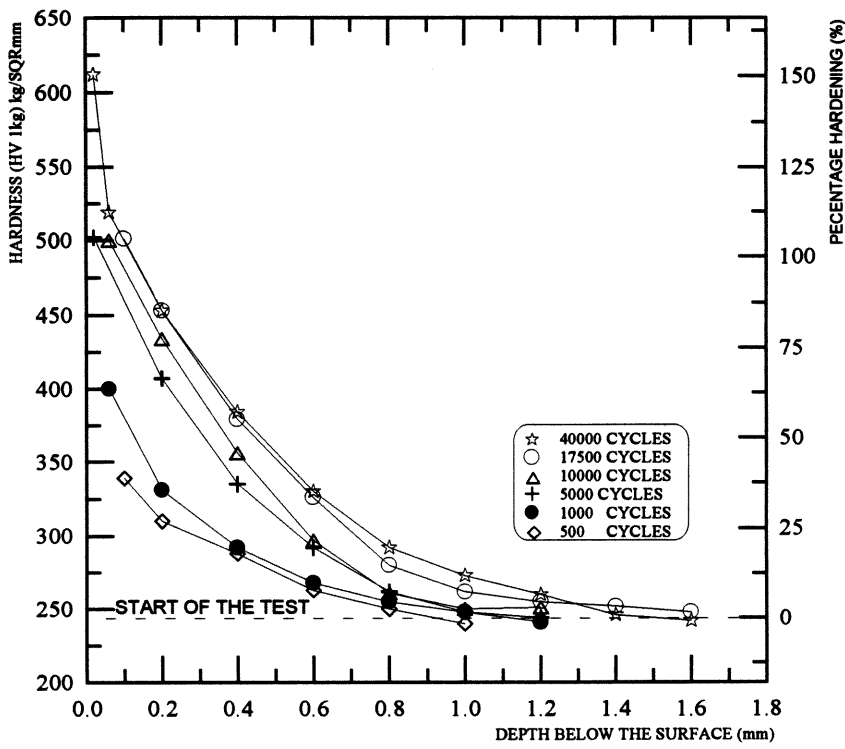


FIGURE (4.6): HARDNESS PROFILE BELOW THE CONTACT SURFACE OF THE RAIL DISC AFTER DIFFERENT ROLLING DISTANCES

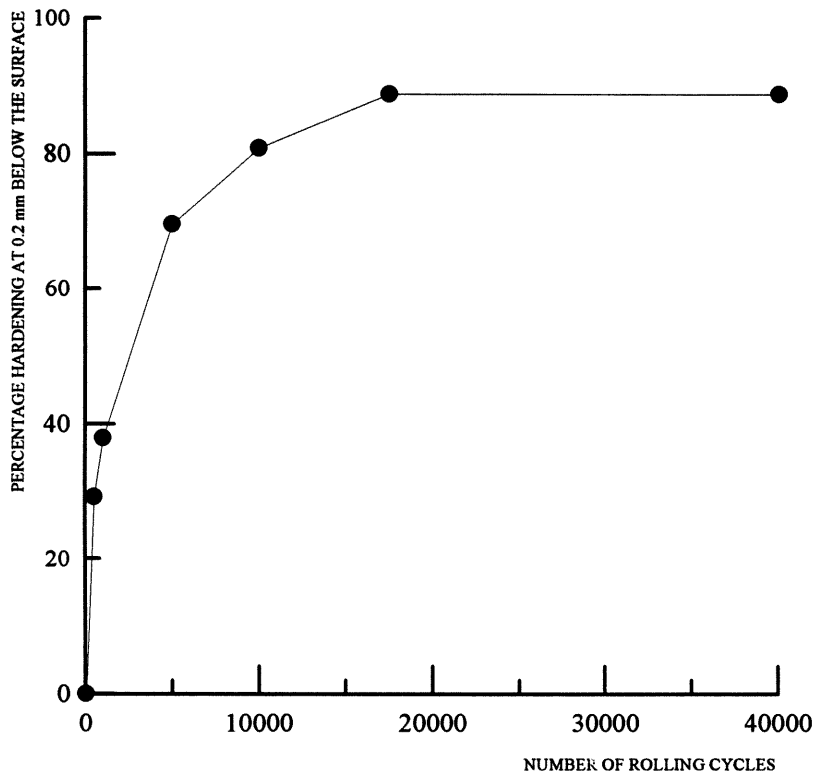


FIGURE (4.7): PERCENTAGE HARDENING OF THE RAIL DISC MATERIAL AT 0.2 mm BELOW THE SURFACE AS A FUNCTION OF TEST DURATION

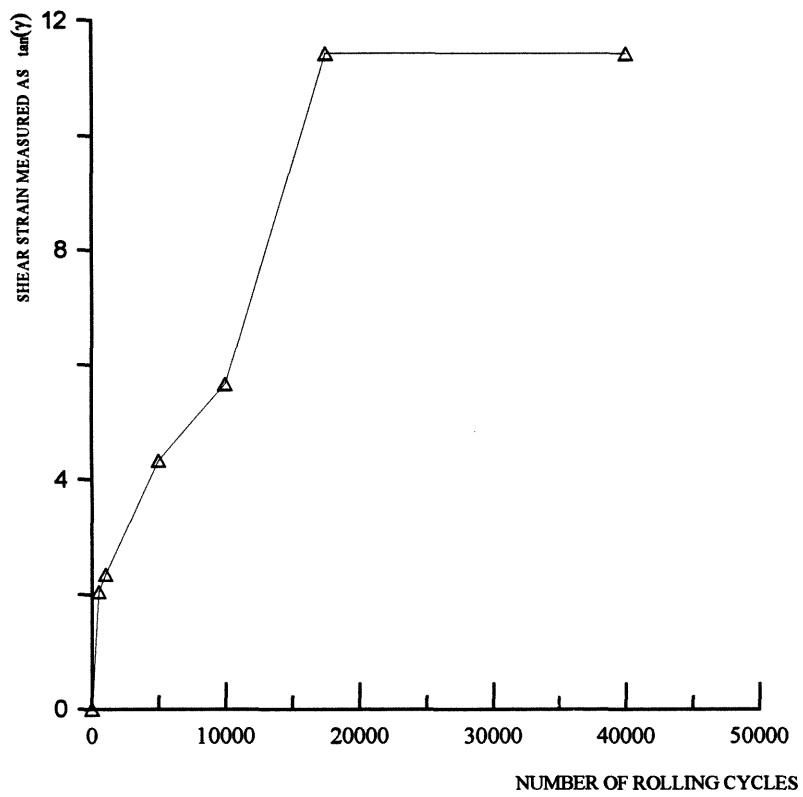


FIGURE (4.8): ACCUMULATED SHEAR STRAIN AT 0.2 mm BELOW THE CONTACT SURFACE OF THE RAIL DISC AS A FUNCTION OF ROLLING CYCLES



(a) AFTER 17500 CYCLES (TEST 138)



(b) AFTER 40000 CYCLES (TEST 130)

FIGURE (4.9): DEFORMED STRUCTURE BELOW THE CONTACT SURFACE OF THE PEARLITIC RAIL STEEL DISC AFTER 17500 AND 40000 CYCLES

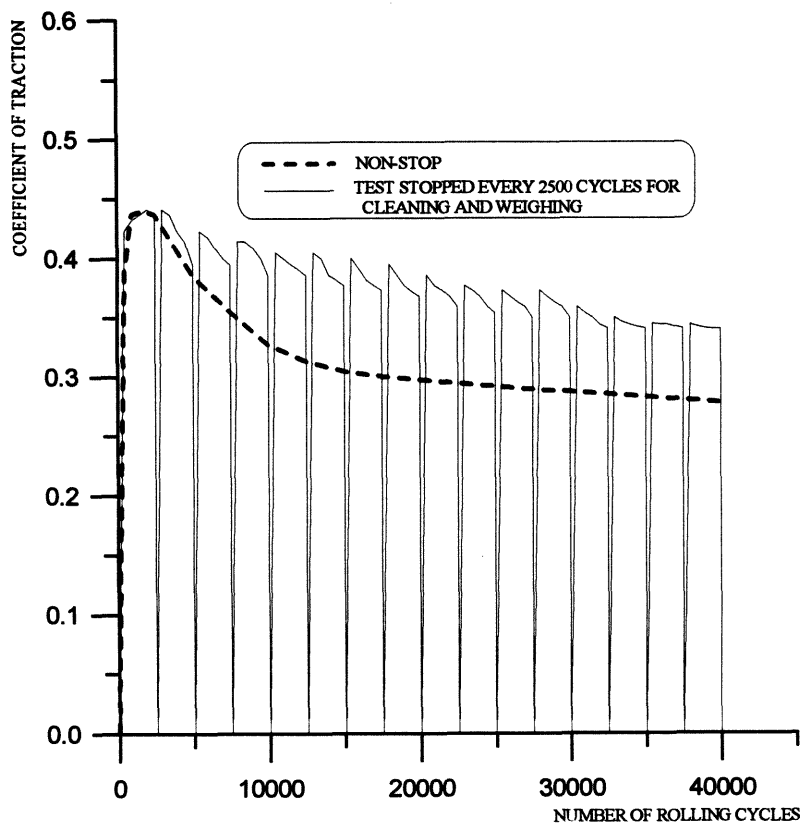


FIGURE (4.10): EFFECT OF ROLLING CYCLES AND TEST DISC CLEANING ON THE TRACTION COEFFICIENT

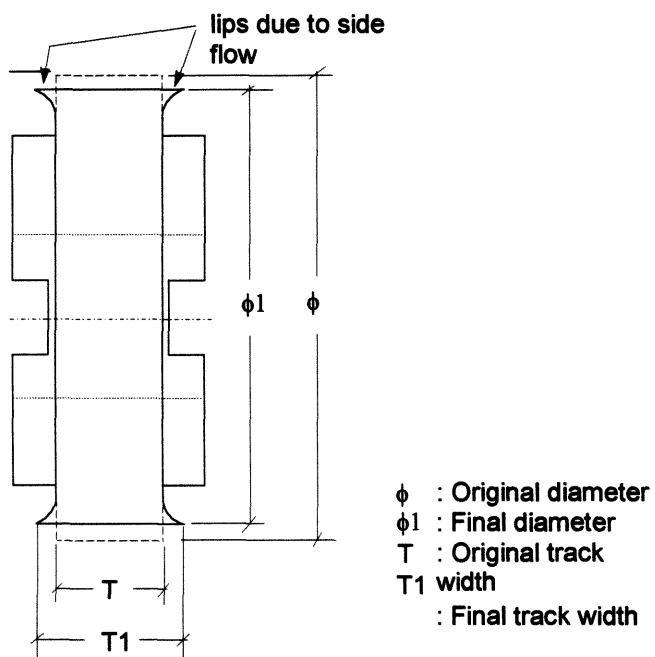


FIGURE (4.11): PLASTIC FLOW AT THE EDGES OF THE CONTACT AREA OF THE TEST DISC (T1 IS EXAGGERATED FOR CLARITY)

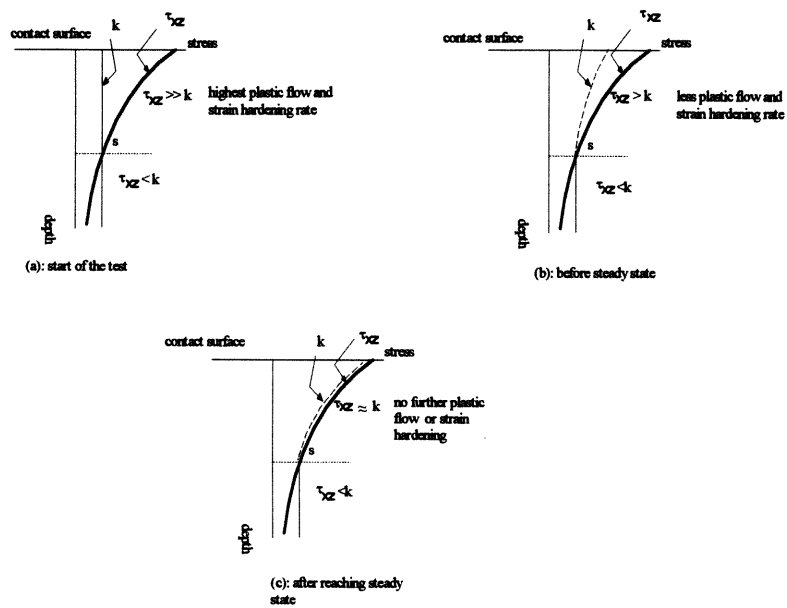


FIGURE (4.12): SCHEMATIC ILLUSTRATION OF STRAIN HARDENING AND DAMAGE ACCUMULATION DURING THE DIFFERENT STAGES OF THE ROLLING SLIDING PROCESS

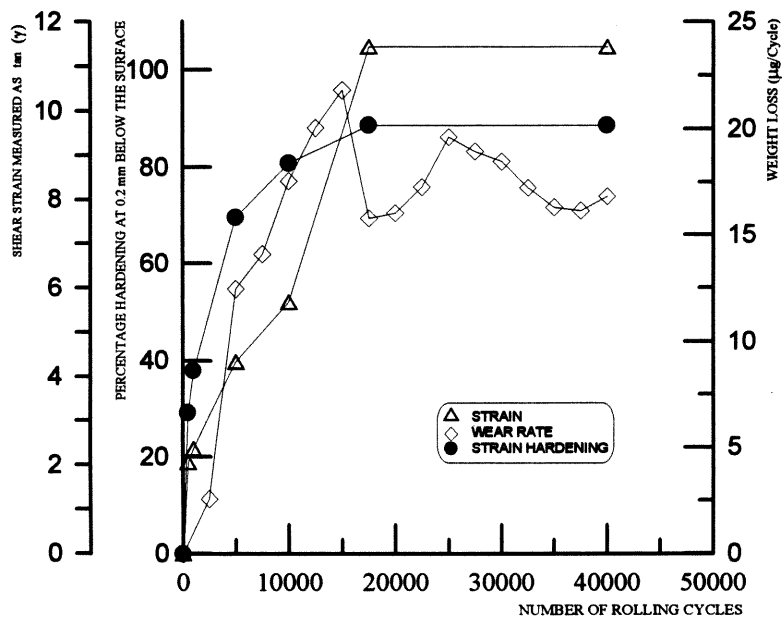


FIGURE (4.13): EFFECT OF ROLLING DISTANCE ON THE ACCUMULATED SHEAR STRAIN, PERCENTAGE HARDENING AND WEAR RATE OF RAIL DISC

Chapter 5

THE EFFECT OF ROLLING DIRECTION REVERSAL ON THE WEAR RATE AND WEAR MECHANISM OF PEARLITIC RAIL STEEL

5.1 INTRODUCTION

As concluded in section 4.5.6 and suggested by Kopalinsky and Oxley⁽¹⁾, the work presented in this chapter is aimed at confirming that, under the unlubricated wheel-rail contact conditions simulated on LEROS, the dominant wear mechanism is the failure of the surface layer of the rail by ratchetting (accumulation of unidirectional plastic strain beyond a critical limit). This confirmation can be achieved by conducting rolling-sliding experiments under conditions of rolling direction reversal (RDR). The main experimental procedures were those described in chapter 3. To ensure comparability, test conditions were identical to those used in chapter 4, except for the rolling direction which, in the case of the work presented in this chapter, was reversed at pre-determined numbers of rolling-sliding cycles. Reversal has been made possible by flipping the rail disc in such a way that the outer face of the disc, adjacent to the fixing bolt, became the inner face, adjacent to the drive shaft. Two main reversal regimes were used, single rolling direction reversal (SRDR) after a certain number of cycles and multiple rolling direction reversals (MRDR) with each test having a different number of cycles per reversal. All tests were stopped every 2500 cycles (the minimum number of cycles per reversal used) for disc weight loss measurement. Test conditions are summarised in table (5.1).

The results obtained and their interpretation were the subject of a paper published in *Tribology International*, 27, 6, (1994), 401-412, appendix (2)

5.2 RESULTS.

A summary of test results is shown in table (5.2). Wear rates are presented as total weight loss and as diameter loss of the rail disc. Although the wear rates were different under different rolling direction reversal regimes, there are some features which were found to be common for all the tests; these will now be described.

5.2.1. Common features.

5.2.1.1. Coefficient of traction.

Rolling direction reversal appears to have no effect on the coefficient of traction between the two discs. It can be seen from table (5.2) that this coefficient, which is calculated as a time average value, remained in the range of 0.370-0.374 for the whole series of tests. The initial surface roughness of the disc pairs did not affect this value, even at the very early stages of the rolling-sliding contact. However, the traction behaviour after cleaning the discs for weight loss measurement was different, as described in section 4.2.4 and shown in figure (4.10).

5.2.1.2. Hardness below the contact surface.

Measurements of the hardness below the contact surface of the rail disc revealed maximum hardening at the contact surface. The bulk hardness is reached at about 1.3 mm below the worn surface. Rolling direction reversal appears to have little effect on the hardening behaviour of the disc specimens. Figure (5.1) reveals that the hardness profiles due to the different rolling direction reversal (RDR) regimes are very similar.

As discussed in section 4.2.2, measurement of the hardness very near to the contact surface with the indenter parallel to the disc axis proved to be tricky, since the indenter can cause interlaminar cracking parallel to the contact surface, resulting in an indentation larger than that representing the actual hardness, figure (5.2a). Figure (5.2b) shows a satisfactory indentation. To avoid such a condition, hardness was also measured with the indenter perpendicular to the disc axis. Progressive grinding of the disc track surface enabled hardness measurements at progressive depths. Figure (5.3) shows the hardness profile below the contact surface of the rail disc of test number 130 measured in both the directions mentioned above. The profile in both is nearly identical except very near to the surface, where the hardness value measured perpendicular to the disc axis shows a value lower than that measured parallel to the disc axis at the same depth. This behaviour is due to the delamination cracking mentioned earlier. Even at deeper indentation locations short cracks were noticed near the indentation corners in the direction of structure deformation, figure (5.4). This behaviour will be discussed in more detail below.

5.2.1.3. Formation of wear particles.

The mechanism by which material is lost from the contact surface has been discussed

in chapter 4. The formation of wear particles or flakes can be explained by the delamination cracking due to ratchetting. Surface, as well as subsurface, cracks were noticed at and below the contact surface, opposite to the direction of traction, parallel to the deformed structure, as shown in figures (5.5a) and (5.5b). The cracks appear to propagate between the laminates parallel to the contact surface. Cracks propagating at different levels of the laminar structure can join only if they can break through the laminates perpendicular to the direction of deformation, as shown in figure (5.6). Figure (5.7) shows a number of such cracks propagating at different levels of the stacked structure without joining, even though they are only few microns apart. Flakes are formed when a laminate breaks to the contact surface. Debris are formed by these flakes detaching from the disc surface.

Metallographic sections cut at a tangent to the worn surface show that the cracks propagate along the laminate borders even when those are corrugated. This is shown in figure (5.8), which shows a micrograph of the deformed structure of the rail disc of test number 130, sectioned parallel to the disc axis, looking down on wear track but on a section cut at a tangent to it.

5.2.1.4. *Wheel disc wear rate.*

Reversal of the rail disc rolling direction appears to have no significant effect on the wear rate of the wheel disc regardless of the reversal regime. The wear rate of the wheel disc was always higher than that of the rail. The wear mechanism in this case was oxidative. Prior to cleaning a grey oxide layer, which is easy to remove, was found to cover the running track of the wheel disc. The number of cycles required to establish steady state was around 17500 cycles, which is identical to that of the rail disc, see figure (4.3) in chapter 4. However, neither the steady state behaviour nor the wear mechanism of the wheel disc appears to be affected by the rail disc rolling direction reversal.

5.2.2. *Unidirectional rolling*

Test number 130 was run under conditions of unidirectional rolling in order to establish a reference for comparison with the remainder of the tests.

The wear rate due to unidirectional rolling has been discussed in chapter 4. It has been shown that the wear behaviour is characterised by a relatively low rate during the first few thousand cycles before it starts to increase rapidly to reach a constant steady state rate

which prevails to the end of the test, arbitrarily chosen here to be 40000 revolutions of the rail disc, see figure (4.3).

Since the test was conducted under dry conditions, the maximum plastic shear stress and, as a result, the maximum deformation are expected at the contact surface, as seen in figure (5.9). The structure very near to the surface is deformed parallel to the rolling direction. Scanning electron microscopy (SEM) spot analysis on the dark parallel lines seen below the surface showed that they are stringered manganese sulphide inclusions. The result of this analysis is shown in figure (5.10). Those flattened inclusions may have an important role in the structure deformation and crack initiation, as will be discussed later. The deformed structure just below the contact surface appears as a multi-layer stack of cementite laminates separated by layers of flattened ferrite. The border between the adjacent laminates is a straight line parallel to the contact surface, as seen in figure (5.9). Indentation in the direction parallel to those laminates showed that they can separate easily, see figure (5.3a).

Sections parallel to the disc axis, such as that of figure (5.8), show another view of the deformed structure. It can be noticed that the flake root cracks follow the deformation lines of the structure. Multi-layered delamination flakes were also noticed at the contact surface, figure (5.11).

5.2.3. Tests under conditions of single rolling direction reversal [SRDR]

Three tests were conducted under conditions of different SRDR regimes. The results of these tests are shown under numbers 124, 128 and 129 of table (3). Under the test conditions used, it was found that RDRs have a significant effect on the wear rate of the pearlitic rail steel discs. Figure (5.12) shows a comparison between the different wear rates obtained under the three different SRDR regimes and that obtained under unidirectional rolling conditions, plotted as accumulated rail disc weight loss per cycle against number of cycles rolled. It can be seen that the wear rates were nearly equal before the RDR. Upon reversal, those rates drop suddenly to a significantly lower level. This is better revealed in figure (5.13) where rail disc wear is presented as disc weight loss per cycle against number of rolling cycles.

The behaviour after the RDR depends on the number of cycles before reversal. If

reversal is carried out after a relatively low number of cycles, as in test number 129 where the rolling direction was reversed after the first 2500 cycles, the effect is to lower the wear rate temporarily, leading to an extension of the period required to establish a steady state wear rate from around 17500 cycles during the unidirectional rolling, test number 130, to around 22500 cycles during test 129, as revealed in figure (5.13). On the other hand, if RDR is carried out after a higher number of cycles, the wear rate drops suddenly from the unidirectional steady state wear level, which is in the range of 15-18 $\mu\text{g}/\text{cycle}$, to a significantly lower level of around 7 $\mu\text{g}/\text{cycle}$ as in test numbers 128 and 124 where reversal was carried out after 10000 and 20000 cycles, respectively.

It appears from figure (5.13) that the wear rate well after reversal depends mainly on the number of cycles rolled in the first direction. In test number 128, RDR was carried out after the first 10000 cycles before continuing the test for another 50000 cycles in the opposite direction to examine whether the wear rate would recover its pre-reversal level. It was found that the minimum weight loss/cycle is achieved directly after the reversal. This wear rate then starts to increase slowly. However, even after 50000 cycles in the reversed direction, the wear rate is barely half way back to its pre-reversal level. On the other hand, when the rolling direction was reversed after only 2500 cycles before continuing for another 37500 cycles in the reversed direction, as in test number 129, the wear rate was lower than that of the unidirectional rolling up to 22500 cycles, after which the wear rate was at a steady state level, slightly higher than that for the unidirectional condition.

The micrographs of the deformed structures of test number 124, 128 and 128, which were run under conditions of single RDR after 20000, 10000 and 2500 cycles, respectively, are shown in figures (5.14a), (5.14b) and (5.14c). When the initial phase was 20000 cycles and equal to the reversal period, as in figure (5.14a), the deformation shows some recovery back to an apparently undeformed arrangement. This recovery is incomplete in spite of the equal number of cycles in each direction. Strain hardening is thought to hinder full undoing of the deformation by reversal. Similarly, when 10000 cycles is followed by 30000 cycles in the reversed direction, as in figure (5.14b), the deformation is confined to a shallow depth below the contact surface. This is further evidence that an accumulated deformation caused by a certain number of rolling cycles needs a higher number of cycles in the other direction to realign it. A reversal regime of 2500 cycles followed by 37500 cycles in the reverse direction, figure (5.14c), shows no trace of

deformation due to the first 2500 cycles.

5.2.4. Tests under conditions of multiple rolling direction reversals.

Three tests were conducted under conditions of multiple reversals using three different reversal regimes. Test numbers 125, 126A and 127A were reversed every 15000, 10000 and 2500 cycles, respectively. The wear rate as accumulated weight loss of the rail disc due to the different MRDRs is shown in figure (5.15). Figure (5.16) shows the same wear rates but expressed as weight loss per cycle against number of rolling cycles. It can be seen that upon the first reversal the wear behaviour is identical to that obtained under single RDR of the same cycle interval. The effect of further reversals depends on the cycle interval. The first reversal in the multiple reversal regime of 15000 cycles per reversal had a dramatic effect on the weight loss per rolling cycle. However, the effect of the second reversal, after 30000 cycles, is barely distinguishable. The second reversal during test number 125, in which the rolling direction was reversed every 10000 cycles, produced a slight reduction in wear rate followed by a small increase, whereas, the third reversal, at 30000 cycles, showed a higher reduction which was more sustained, figure (5.16).

The average wear rates after the first RDR are nearly equal under the three multiple reversal regimes, figure (5.16). All of the three multiple reversal regimes used brought about a significant reduction in the wear rate.

The effect of multiple RDR on the deformation of the microstructure below the contact surface is shown in figure (5.17a), (5.17b) and (5.17c) (contrast differences are due to different amounts of etching during metallographic preparation). Test number 127A, in which the reversal interval was only 2500 cycles, resulted in a complicated wavy structure adjacent to the worn surface, figure (5.17c). In contrast, the longer cycle interval of test number 126A produced a deformation pattern similar to that of unidirectional rolling, figure (5.17a). It is remarkable that such different deformation patterns have such similar wear rates.

Comparison between the effect of single and multiple reversal on the wear rate under the 10000 and the 2500 cycle interval regimes is shown in figures (5.18) and (5.19), respectively. It can be seen that the difference between single and multiple reversal rates increases as the number of cycles per reversal is reduced.

5.3. DISCUSSION.

5.3.1. Reliability of results

Despite of the extreme care taken during disc cleaning and weighing, the wear rate data expressed as disc weight loss per rolling cycle against number of rolling cycles in figures (5.13) and (5.16) show slightly scattered patterns. This scatter is more during the unidirectional test and tests of a high number of cycles in a certain direction. This behaviour could be related to the larger flake size and longer pitch between the flakes, where during cleaning the effect of an extra flake detaching from the surface will be significant to the weight loss measurement.

5.3.2. Other factors affecting the wear behaviour

It has been proposed in chapter 4 that, under the test conditions used, ratchetting is the failure mode by which material is lost from the contact surface of the rail disc specimen. However, there are other factors which may affect the rate of ratchetting.

Many researchers⁽²⁻⁴⁾ have shown that the strength parameters are not the only factors affecting the wear rates. Grozier and Bucher⁽²⁾ showed that although there is a good correlation between the wear behaviour and the strength of the material, very little correlation exists between wear rate and work hardening or wear rate and unidirectional-axial fracture properties. Clayton⁽³⁾ showed a good inverse relationship between wear rate and total plastic strain obtained in a tensile test. These findings may indicate that the wear rate is a function of many factors including the material composition and microstructure.

During a study of the deformation of pearlitic steels, Langford⁽⁴⁾ described the deformation as an interlamellar slip, the analogy being a deck of cards, which takes place when a highly stressed slip system in the ferrite is nearly parallel to the plane of cementite lamellae. Figure (5.8) shows the deformed structure of the pearlitic rail steel disc near to the surface layer caused by the unidirectional rolling-sliding motion, and reveals that the type of deformation prevailing under such conditions becomes like a deck of cards: one where the deformed structure is parallel to the direction of maximum shear stress. Under such loading conditions, where the traction coefficient is above 0.25, the surface layer will suffer the maximum strain⁽⁵⁾. This strain falls gradually with the depth below the contact surface. Although the stress level caused by a certain rolling-sliding loaded contact at any particular circumferential location in the rail disc is assumed to be constant, it is still

possible to increase the total plastic strain by cyclic increments^(3,6). This has been shown in chapter 4 where, after a certain number of unidirectional rolling-sliding cycles, the accumulated plastic strain exceeds the critical unidirectional plastic strain and fracture results. This fracture is expected to be within the surface layer of the disc. However, material deficiencies, such as inclusions, may encourage subsurface cracking similar to these shown in figure (5.5). Such cracks were also reported by Suh⁽⁷⁾ and Jahanmir et al⁽⁸⁾.

The deformed structure caused by unidirectional rolling and shown in figure (5.9) appears to exhibit directional properties near the contact surface. Crack propagation in a direction perpendicular to the structure laminates proved to be difficult. Indentation parallel to the laminates, at a depth of less than 50 μm below the contact surface caused laminar separation cracks, figure (5.2a). Even when the indenter corner was very near to the free surface, no cracking towards the surface was noticed. The indentation mark shown in figure (5.2a) revealed that the indenter caused a separation of a significant width without the separated layer breaking through to the surface. This can be noticed from the indentation mark border line nearer to the surface, which indicates that the separation crack has closed back, but not completely, after releasing the indenter. This directionality in mechanical properties was also reported by Bucher⁽⁹⁾ during a study of the effect of inclusions on the brittle fracture of hot rolled steel. Indentation in the bulk material, away from the deformed structure, showed no evidence of directional properties, as revealed from the indentation borders and corners shown in figure (5.2b).

Perez-Unzueta and Beynon⁽¹⁰⁾ showed that the wear rate of pearlitic rail steel decreases with shorter cementite interlamellar spacing. Clayton⁽³⁾ demonstrated a strong correlation between wear rate of pearlitic steel and the mean free path in ferrite. This path is defined as the average distance a dislocation can travel in any direction before encountering an obstacle, whether a carbide plate or a grain boundary. Shorter interlamellar spacing leads to a shorter free path in ferrite. During unidirectional rolling sliding contact the pearlitic microstructure nearer to the surface is deformed in such a way that both the carbide lamellae and the grain boundaries are aligned parallel to the contact surface, as shown in figure (5.9). In this case the unit length in the direction parallel to the surface contains the minimum number of obstacles facing the mobile dislocation. On the other hand, perpendicular to the contact surface the obstacle density is a maximum and increases with shorter interlamellar spacing, as shown schematically in figure (5.20). This

argument may partially explain the cracking parallel to the contact surface shown in figure (5.7) where subsurface cracks are propagating at different levels of the laminar structure without joining, despite the very short distance separating them.

5.3.3 Effect of manganese sulphide inclusions

The manganese sulphide inclusions are thought to be suitable sites for crack initiation and propagation and, as a result, they could increase the wear rate^(11,12). The role of these inclusions in assisting fracture could be explained by arguing that since they are known to be soft inclusions, their strength is less than that of the bulk material. This can result in a higher localised plastic strain in and around the inclusions. This argument is supported by the work of Krause and Schroelkamp⁽¹²⁾ who detected such inclusions within a crack. Bucher⁽⁹⁾ also reported flat voids around the stringered manganese sulphide inclusions in hot rolled steel sections. Crack initiation at local deformation bands ahead of an inclusion and due to decohesion of the inclusion-matrix interface have recently been reported for four-point bending fatigue of rail steels⁽¹³⁾. It should be noted though, that the MnS inclusion content of the steels used in this work is too low for the wear to be dominated by such a mechanism, table (3.1).

5.3.4. Effect of strain hardening on deformation morphology and wear behaviour

Deforming strain hardened materials is easier before they establish their full hardening. This is evident in figure (4.8) of chapter 4. Krause et al⁽¹⁴⁾ reported similar strain hardening behaviour. This hardening could be the reason behind the structure morphology caused by a single RDR at half the total number of rolling-sliding cycles and shown in figure (5.14a). This is a micrograph of the deformed structure of test number 124 which was run for 20000 cycles in each direction. It can be seen that while the first cycle interval caused the structure to deform parallel to the rolling direction, the duration of the reversed cycle interval was not enough fully to reverse the structure deformation to the other direction. Only that part of structure nearest to the surface, where the shear stress is at a maximum, is reversed. The single reversal appears to have two effects on the structure morphology. First, the transition region between the two directions of the deformation moves down below the contact surface as the ratio between the number of cycles in the second direction and that of the first increases. Second, recovery of the deformation

caused by the first rolling interval is also noticed. Figure (5.14) shows the structural changes below the rail disc surface caused by the three different single reversal regimes of tests number 124, 128 and 129. A complete reversal of the direction of deformation is noticed in test number 129 where, compared with the other two tests, the ratio of the first to the second cycle interval is very low. In this case the deformed structure is very similar to that of unidirectional rolling shown in figure (4.3), chapter 4. This similarity in the deformed structure is associated with a nearly similar wear rate nearer to the end of the two tests, see figure (5.13).

5.3.5 Effect of rolling direction reversal regime

5.3.5.1. Single reversal

Among the three single RDR regimes, that of test number 124 in which reversal was carried out after 20000 cycles, resulted in the minimum wear rate after 40000 cycles. According to the maximum unidirectional plastic strain and the free path in ferrite criteria, such behaviour is expected since reversal appeared to have delayed the critical plastic strain limit in addition to its effect in reducing the free path in ferrite. On the other hand, the maximum wear rate is that of test number 129, where the rolling direction was reversed after the first 2500 cycles. This behaviour is also expected since the number of rolling cycles after reversal was enough to recover fully the deformation caused by the first cycle interval and to accumulate plastic strain in the opposite direction.

4.3.5.2. Multiple reversals

The above arguments can be used to explain the wear behaviour under multiple RDR. The approximately equal wear rates after reversal shown in figure (5.16) could be related to two factors:

- a. Multiple RDR can result in reducing the plastic strain accumulated in one particular rolling direction.
- b. Multiple RDR can produce a structure deformation morphology which is more complicated than that of the single RDR, resulting in additional obstacles to dislocation movement and leading to a smaller flake size.

Both arguments are supported by figure (5.21) which shows low magnification scanning electron micrographs of the running track of the three rail discs tested under

different multiple reversal regimes. It can be noticed that the minimum flake size, figure (5.21c), corresponds to the multiple RDR regime of minimum number of cycles per reversal (in this case 2500 cycles per reversal).

5.4. SUMMARY

To summarise, under the test conditions used, the mechanism by which rolling direction reversal reduces the wear rate of pearlitic rail steel is thought to operate as follows:

It has been shown in chapter 4 that the wear rate is a function of the accumulated plastic strain and its direction. The strain in this case is dictated by the maximum contact pressure, the shear yield strength, the hardening behaviour of the material and the traction coefficient between the two test discs. The test conditions used during the work presented in this chapter have been conducted using material and loading conditions identical to those of chapter 4 except for the rolling direction. RDR had no effect on the maximum contact pressure, the shear yield strength or the hardening and traction behaviour. As a result, this reversal should have no effect on the low cycle fatigue behaviour of the material since this behaviour is not sensitive to strain direction. In this case the drop in the wear rate due to RDR reversal cannot be explained in terms of low cycle fatigue, whereas it is explicable in terms of ratchetting. Strain accumulated in a certain direction would be expected to be lower under RDR conditions since upon reversal many cycles will be consumed to undo the deformation due to the previous rolling direction. In addition, this reversal produces a complicated structure morphology which hinders the dislocation movement and the interlamellar slip.

5.5. CONCLUSIONS

1. Under the test conditions used, ratchetting (accumulations of unidirectional plastic strain) can explain the drop in the wear rate due to rolling direction reversal.
2. Rolling direction reversal proved to have a beneficial effect on the wear rate of pearlitic rail steel.
3. The morphology of the deformed pearlitic structure plays an important role in the wear mechanism and wear rate. Multiple reversals at short cycle intervals gave the minimum wear rate.

4. The mechanism by which wear particles are generated appears to be that of delamination caused by accumulated unidirectional plastic strain.

5. Rolling direction reversal of the rail disc has no effect on the wear behaviour of the wheel disc.

REFERENCES

1. E. M. Kopalinsky and P. L. Oxley, Investigation of the Deformation and Damage Sustained by a Wearing Surface in Sliding Metallic Contact, *Trans. ASME, J. Tribology*, 49, (1994), 1-6.
2. Grozier J D and Bucher J H. Correlation of Fatigue Limit with Microstructure and Composition of Ferrite-Pearlite Steels. *Journal of Materials*, 2, 2,(1967), 393-407.
3. Clayton P. The Relations Between Wear Behaviour and Basic Material Properties for Pearlitic Steels, *Wear*, 60, (1980), 75-93.
4. Langford G. Deformation of Pearlite, *Metallurgical Transactions*, 8A, (1977), 861-875.
5. K. Zum-Gahr, *Microstructure and Wear of Materials*, Tribology Series, 10, Elsevier, (1987).
6. Garnham J E and Beynon J H. Dry Rolling-Sliding Wear of Bainitic and Pearlitic Steels, *Wear*, 157, (1992), 81-109.
7. N. P. Suh, The Delamination Theory of Wear, *Wear*, 25, (1973), 111-124.
8. Jahanmir S J, Suh N P and Abrahamson E P. Microscopic Observations of the Wear Sheet Formation by Delamination. *Wear*, 28, (1974), 235-249.
9. Bucher J. H. The effect of Inclusions on the Brittle Fracture of Hot Rolled Steel. *Journal of Materials*, 2, 2, (1967), 432-445.
10. Perez-Unzueta A and Beynon J H. Microstructure and Wear Resistance of Pearlitic Rail Steels. *Wear*, 162-164, (1993), 173-182.
11. Steel R K and Stone D H. Developments in Railroad Rails. *Proc. of The American Railway Engg. Assoc.*, 87, (1986), 311-358.
12. Krause H and Schroelkamp C. Influence of Non-Metallic Inclusions on the Wear Behaviour of Ferrous Metals in Nominally Dry Friction Systems, *Wear*, 120, (1987), 353-367.
13. Lui C D, Bassim M N and Lawrence S St. Evaluation of Fatigue Crack Initiation at Inclusions in Fully Pearlitic Steels. *Materials Science and Engineering*, A167, (1993), 107-113.

14. Krause H and Demirci H. Factors Influencing the Real Trend of the Coefficient of Friction of Two Elastic Bodies Rolling Over Each Other in Presence of Dry Friction, *The Mechanics of Contact Between Deformable Bodies*, (1975), Delft University Press.
Eds. Pater A. D and Kalker J. J.

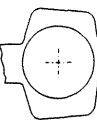
Test conditions		Test number							
		124	125	126A	127A	128	129	130	
Disc material	Top (Rail)	BS11 W8A							
	Bottom (Wheel)								
Initial surface roughness (Ra, μm)	Rail	0.37	0.46	0.46	0.51	0.44	0.39	0.16	
	Wheel	0.31	0.4	0.44	0.53	0.41	0.39	0.16	
Maximum contact pressure (MPa)		1500							
Percentage creepage (%)		-1							
Orientation of rail disc specimen relative to the rail section									
Test speed: [Rail-Wheel] (RPM)		406-410							
Wear measurement intervals		Every 2500 cycles							
Total number of cycles		40000	40000	45000	40000	60000	40000	40000	
Reversal regime		Single	Multiple	Multiple	Multiple	Single	Single	None	
Number of cycles/reversal		20000	10000	15000	2500	10000	2500	40000	
Test environment		Dry, air cooled							

TABLE (5.1): TEST CONDITIONS.

Results	Test number									
	124	125	126A	127A	128	129	130			
Total number of cycles	40000	40000	45000	40000	60000	40000	40000			
Coefficient of friction	0.370	0.370	0.371	0.371	0.370	0.374	0.373			
Contact area (mm ²)	6.11									
Total rail disc weight loss (g):	Rail	0.422	0.287	0.472	0.270	0.559	0.660	0.652		
	Wheel	1.285	1.022	1.451	1.249	1.562	1.294	1.366		
Total rail disc diameter loss (mm):	Rail	0.150	0.125	0.180	0.160	0.150	0.150	0.200		
	Wheel	0.300	0.200	0.310	0.230	0.280	0.350	0.330		
Total rail disc track width gain (mm):	Rail	0.990	0.860	1.100	1.020	0.990	1.050	1.060		
	Wheel	0.610	0.670	0.345	0.700	0.760	0.810	0.900		

TABLE (5.2): TEST RESULTS

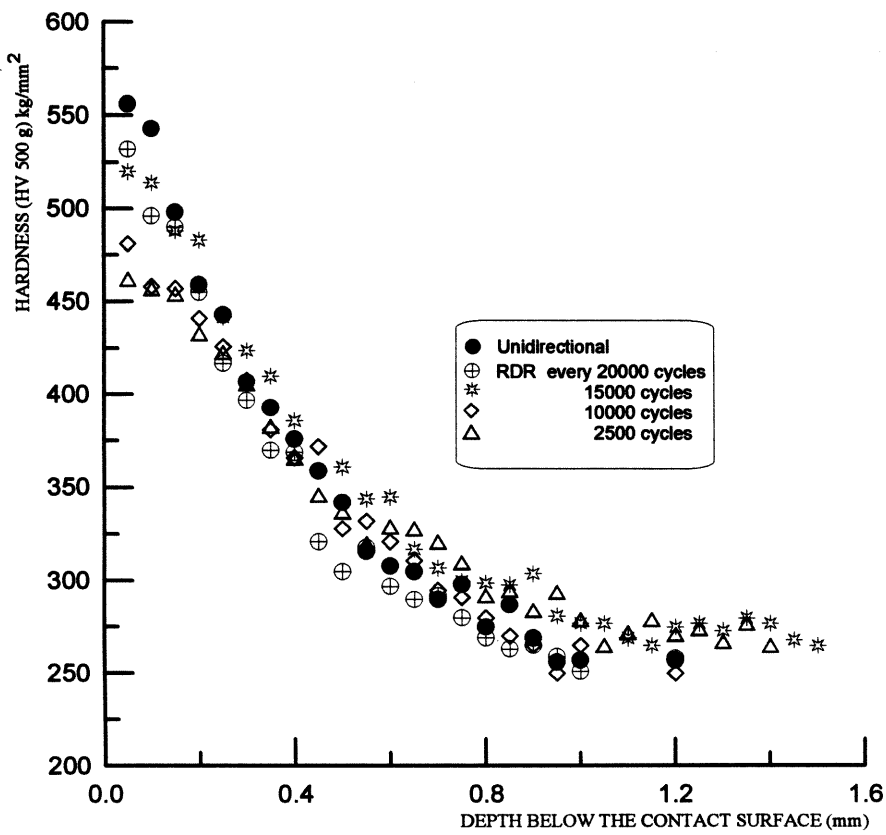


FIGURE (5.1): HARDNESS PROFILES BELOW THE CONTACT SURFACE OF THE RAIL DISCS AFTER DIFFERENT RDR REGIMES

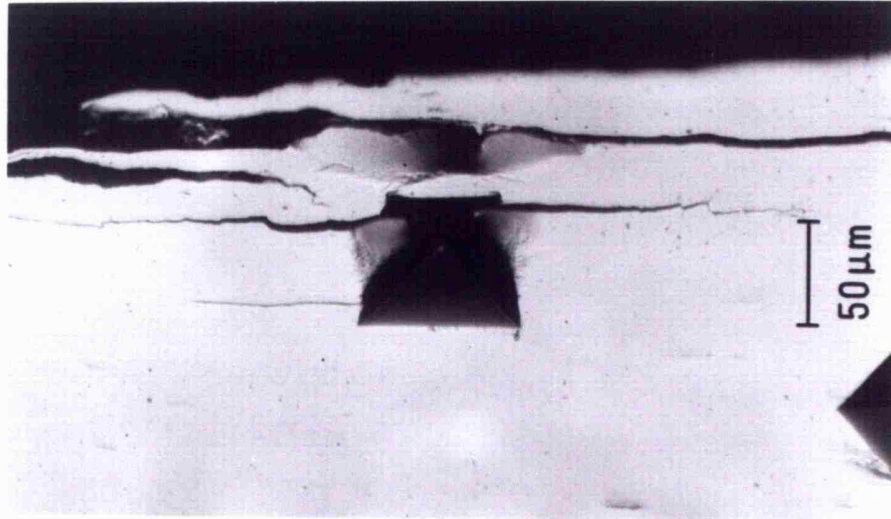


FIGURE (5.2a): DELAMINATION CRACKING DUE TO INDENTATION NEAR THE RAIL DISC SURFACE

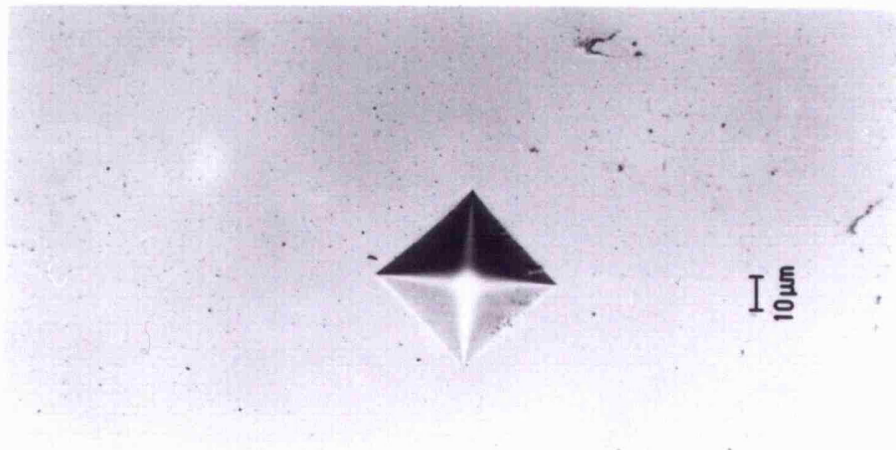


FIGURE (5.2b): INDENTATION MARK AWAY FROM THE DEFORMED STRUCTURE

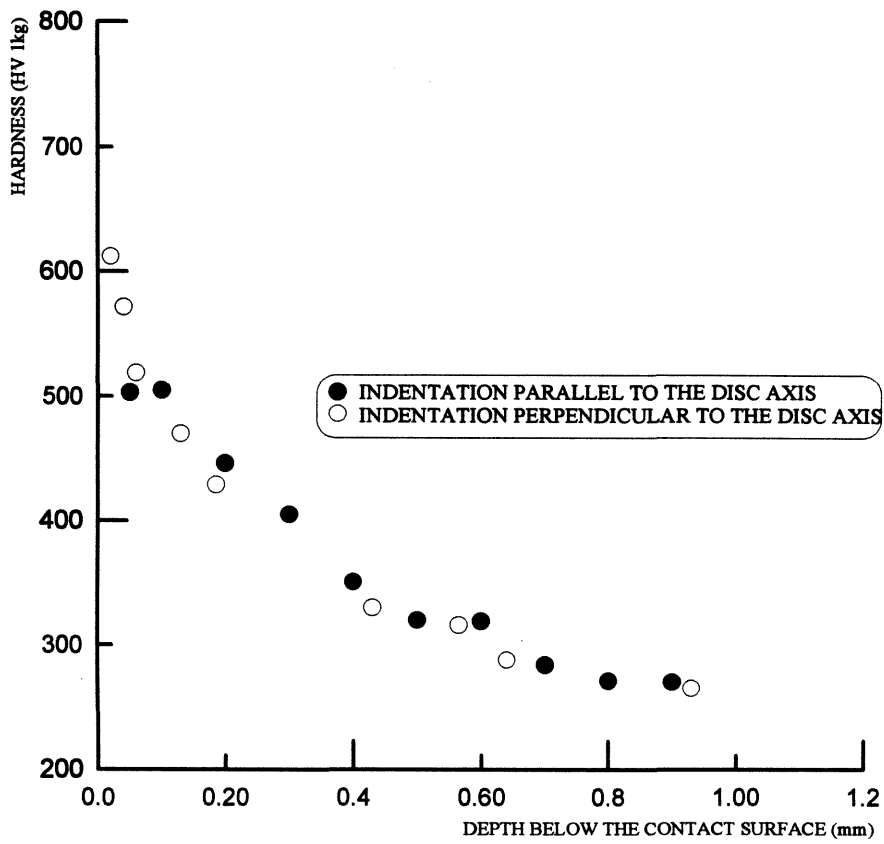


FIGURE (5.3): HARDNESS PROFILE BELOW THE RAIL DISC CONTACT SURFACE AFTER 40000 CYCLES OF UNIDIRECTIONAL ROLLING

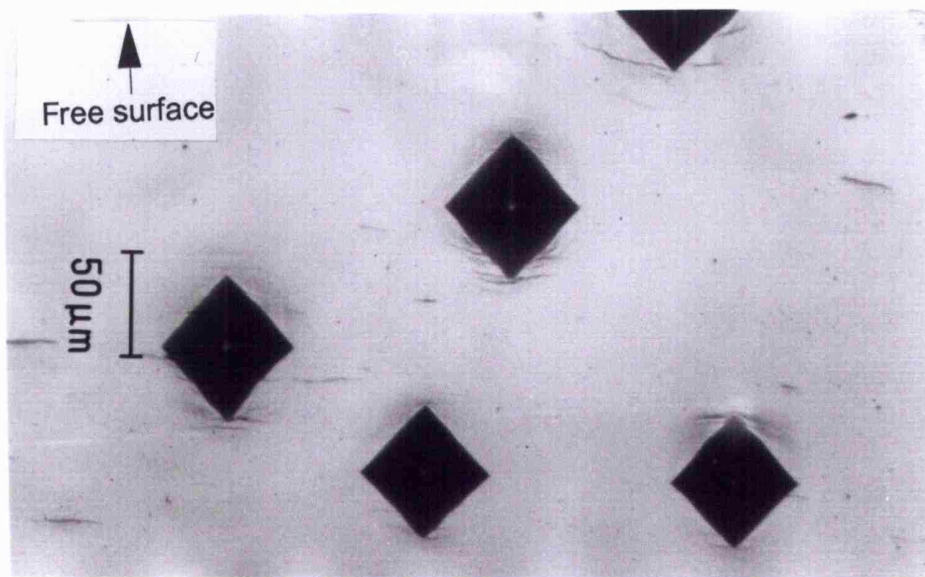
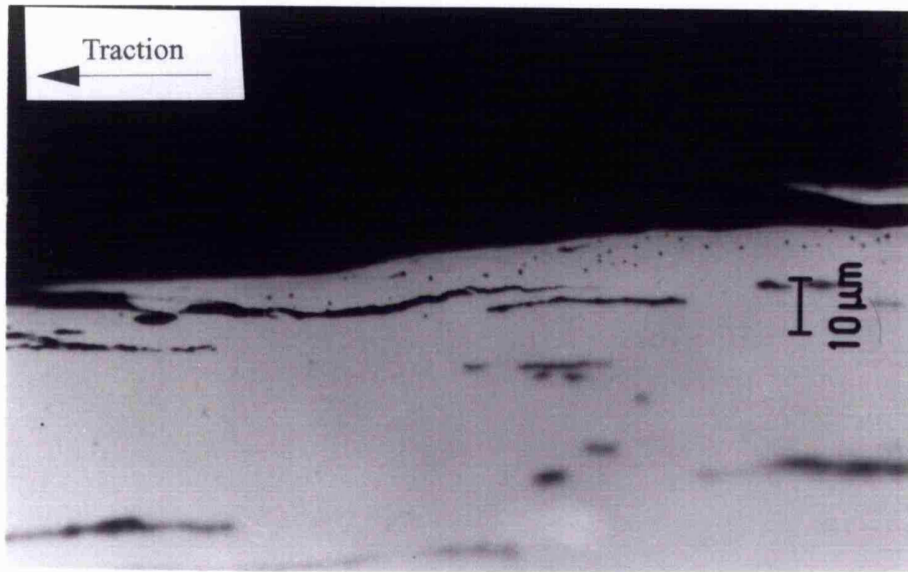
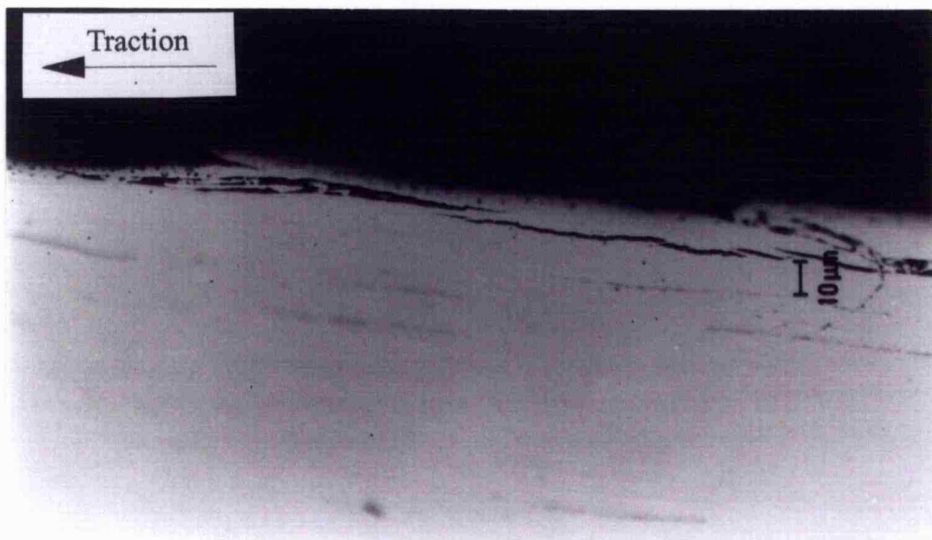


FIGURE (5.4): CRACKING CAUSED BY INDENTATIONS AT DIFFERENT DEPTHS BELOW THE CONTACT SURFACE



(a)



(b)

FIGURE (5.5): DELAMINATION CRACKS UNDER UNIDIRECTIONAL ROLLING CONDITIONS

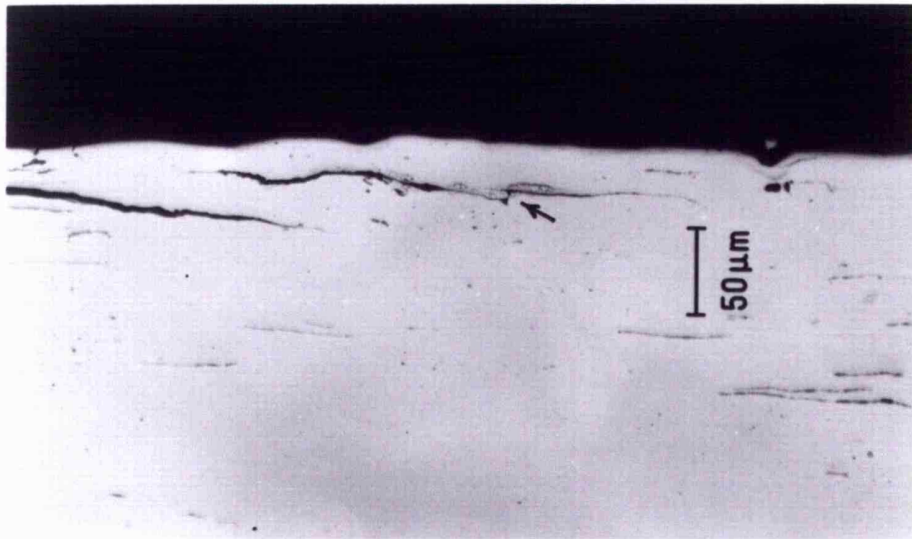


FIGURE (5.6): CRACK PROPAGATION THROUGH THE LAMINATES.

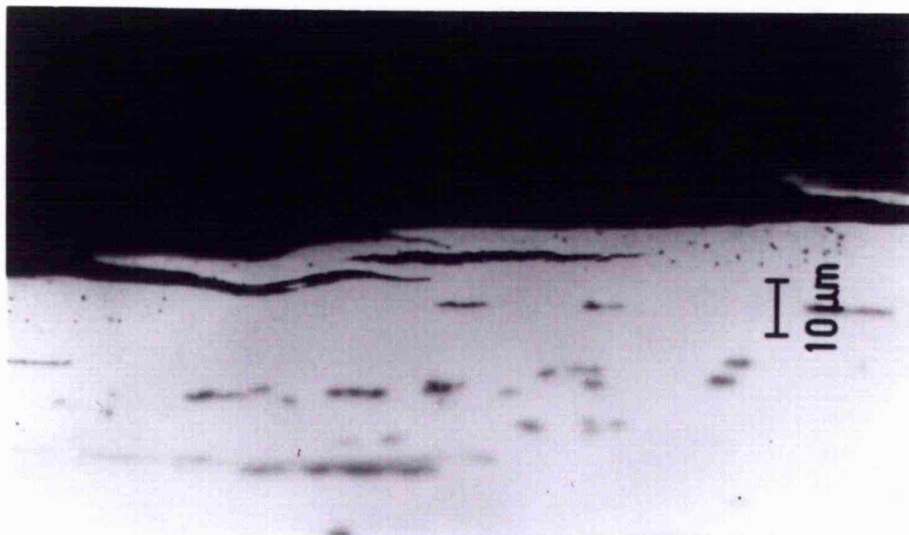


FIGURE (5.7): CRACK PROPAGATION AT DIFFERENT LEVELS OF THE STACKED STRUCTURE WITHOUT JOINING TOGETHER

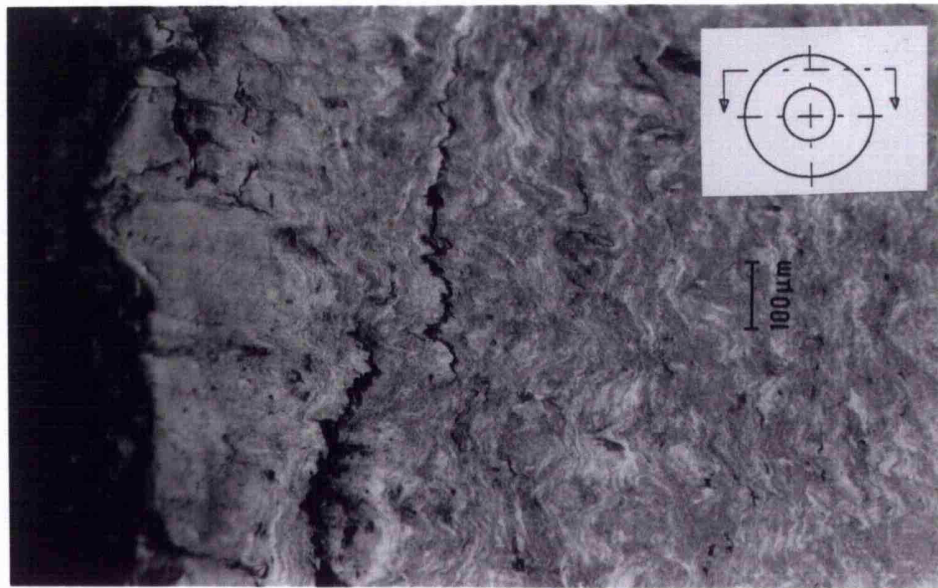


FIGURE (5.8): DEFORMED STRUCTURE OF THE RAIL DISC AFTER 40000 UNIDIRECTIONAL ROLLING CYCLES (DISC SECTIONED PARALLEL TO THE DISC AXIS)

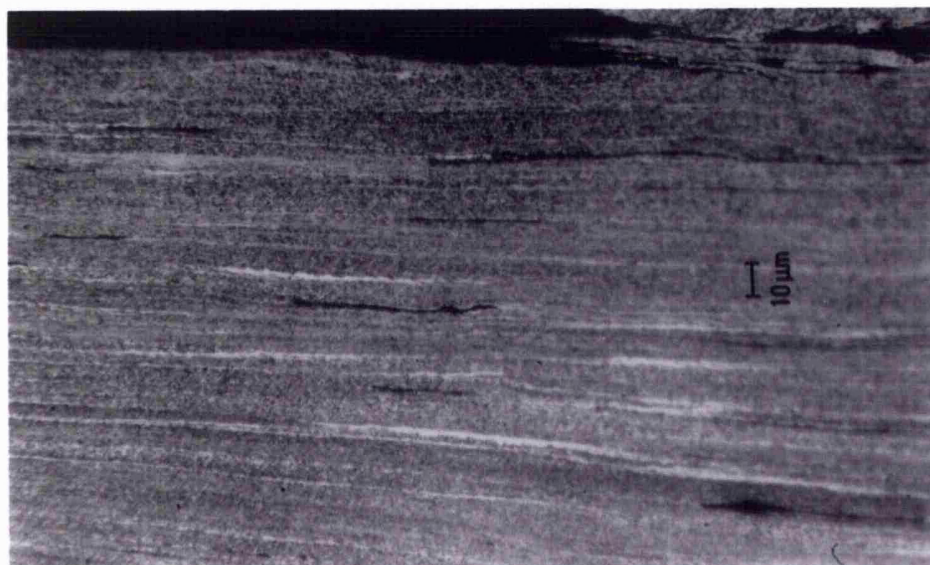


FIGURE (5.9): THE STRAIGHT PARALLEL BORDERS BETWEEN THE LAMINATES OF THE DEFORMED STRUCTURE BELOW THE CONTACT SURFACE OF THE RAIL DISC AFTER 40000 UNIDIRECTIONAL CYCLES

SPT 6279	BEARING	
WSI	1664- 1812 EV	448 COUNTS
WS	2229- 2383 EV	7701 COUNTS
WN	5798- 5998 EV	7129 COUNTS
WFE	6300- 6496 EV	3113 COUNTS

SPECTRUM LABEL

BEARING

SPECTRUM

BEARING

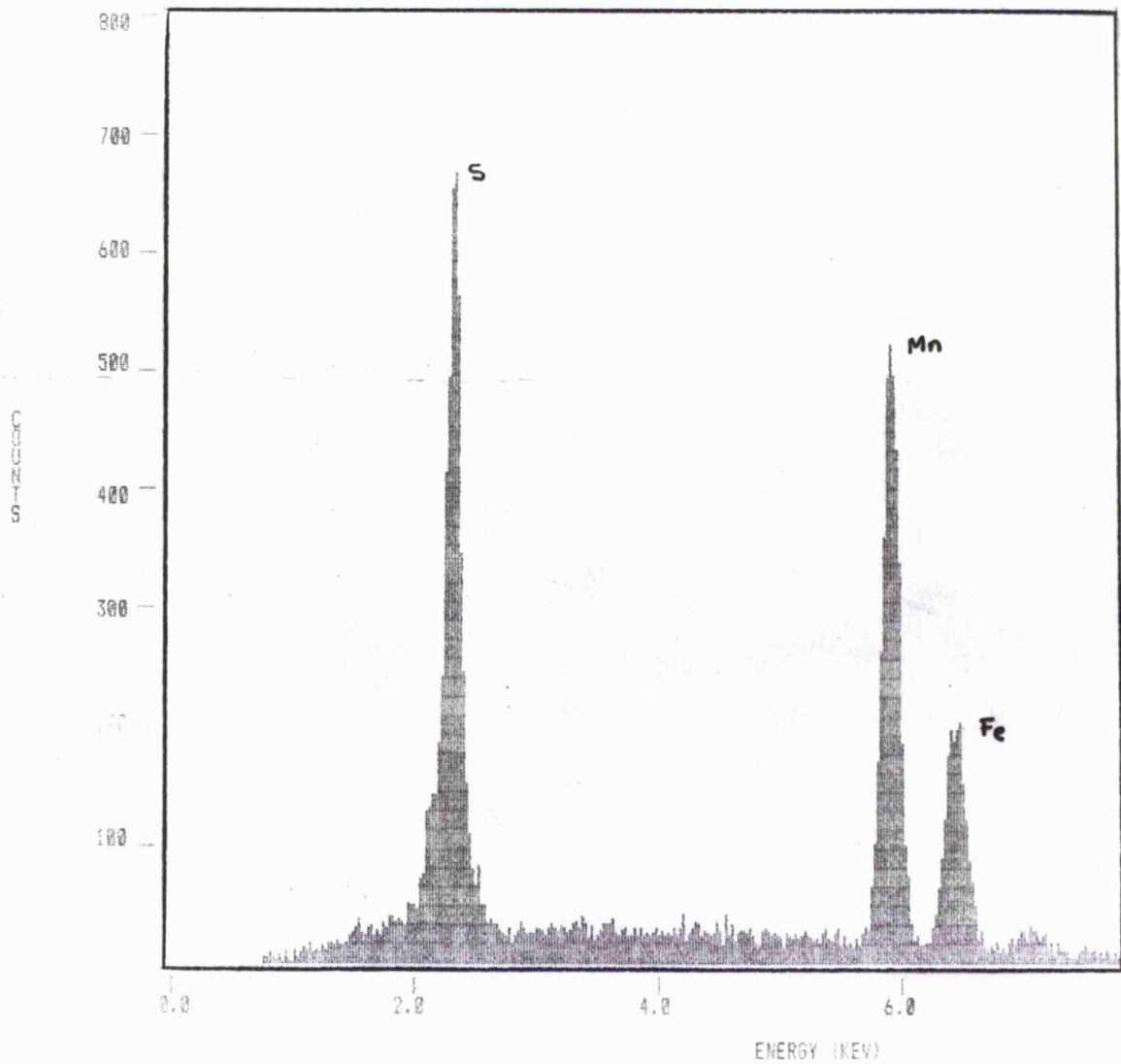


FIGURE (5.10): RESULTS OF THE SEM SPOT ANALYSIS ON THE DARK LINES SHOWN IN FIGURE (5.9)

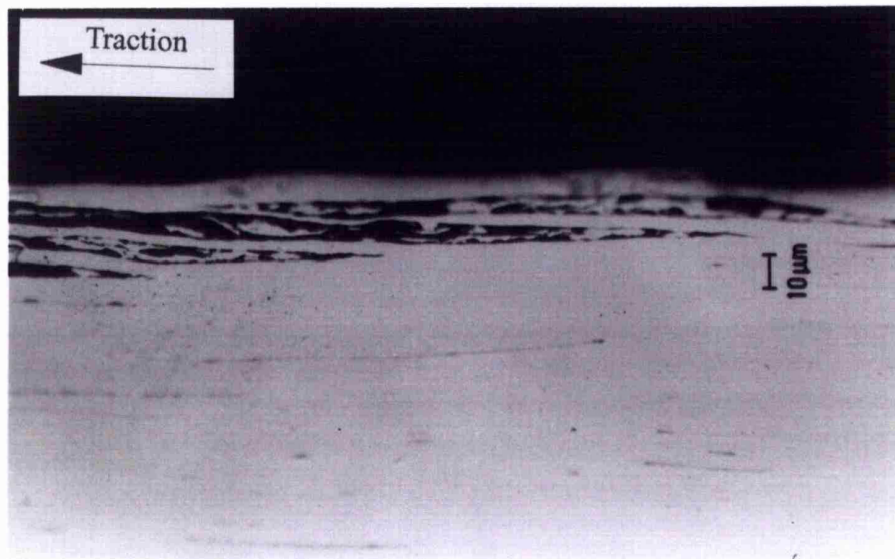


FIGURE (5.11): MULTI-LAYER DELAMINATION OF THE RAIL DISC
SURFACE OF TEST NUMBER 130

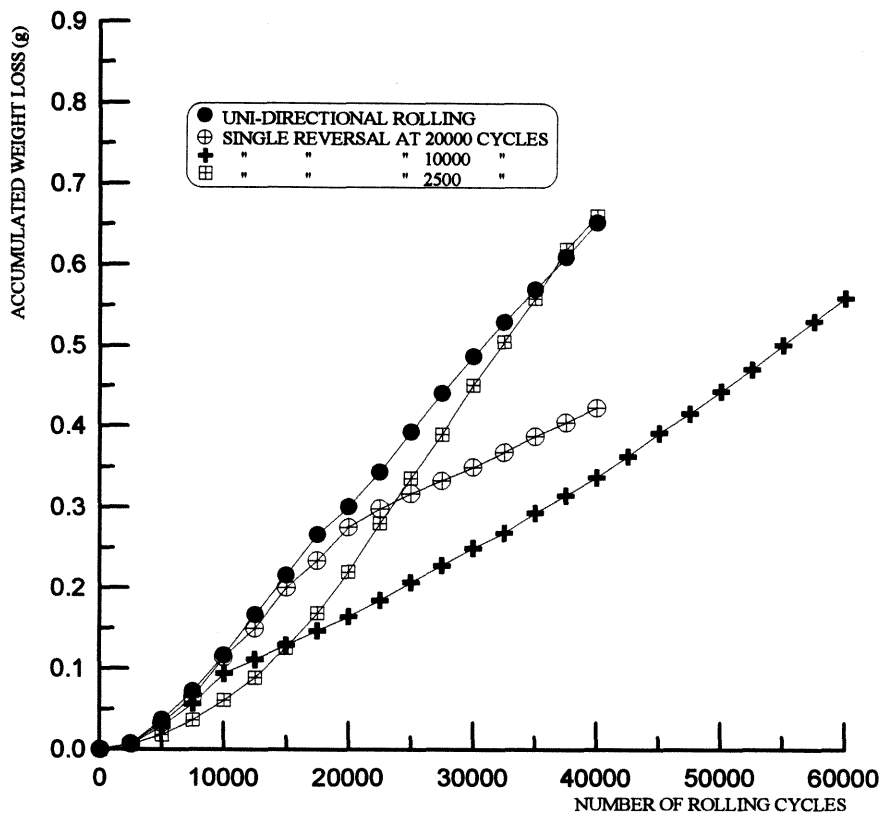


FIGURE (5.12): ACCUMULATED WEAR DUE TO THE DIFFERENT SINGLE ROLLING DIRECTION REVERSAL REGIMES

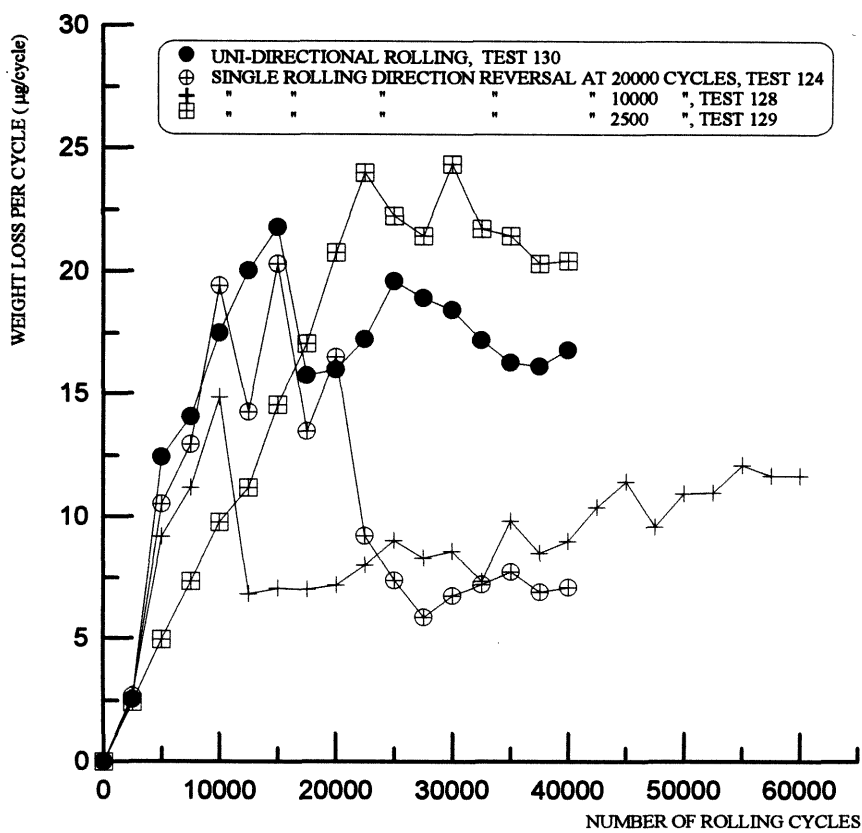
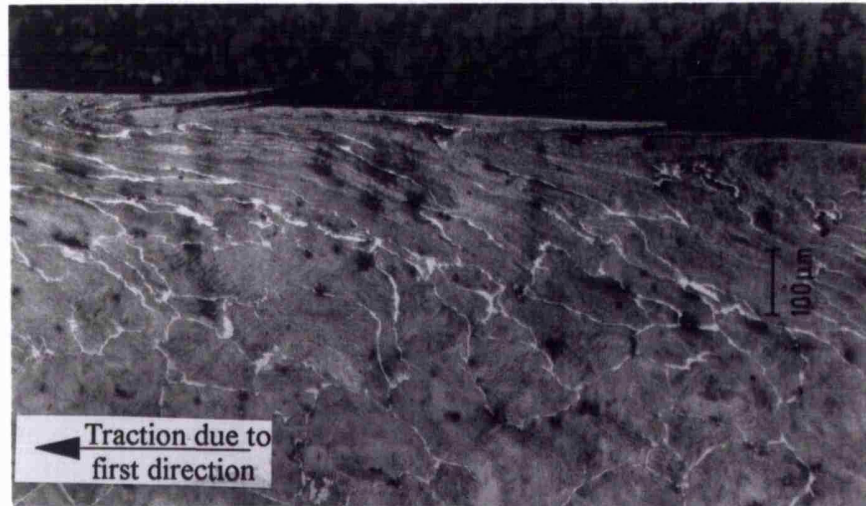
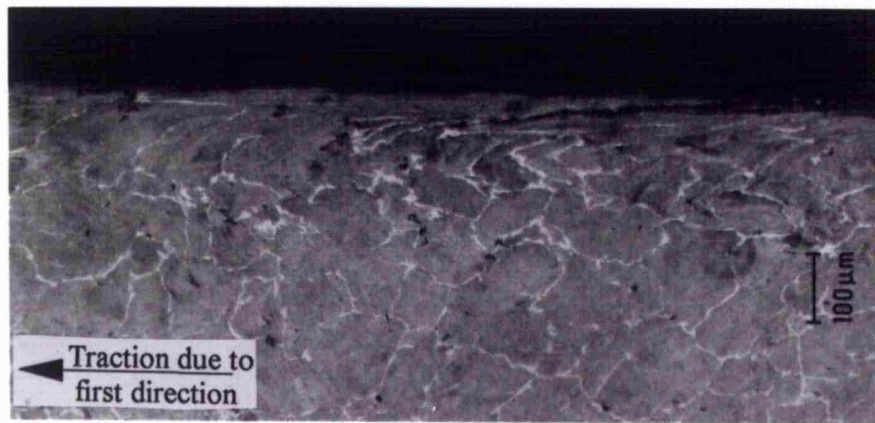


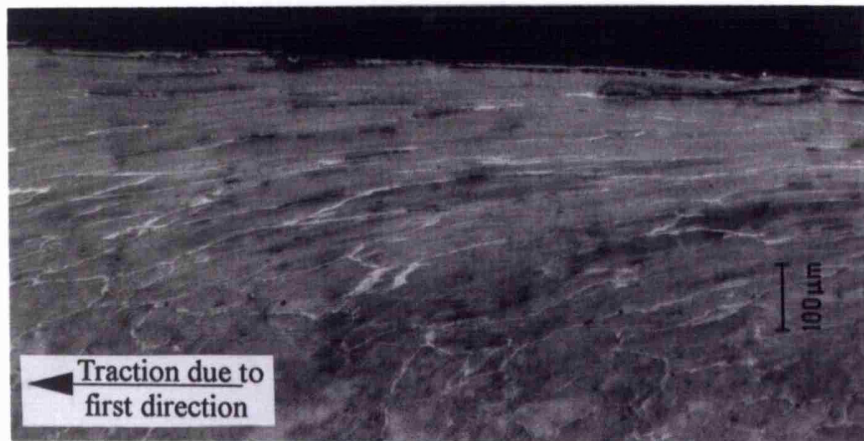
FIGURE (5.13): EFFECT OF SINGLE REVERSAL ON THE RAIL DISC WEIGHT LOSS PER ROLLING CYCLE



(a): REVERSAL AFTER 20000 CYCLES.



(b): REVERSAL AFTER 10000 CYCLES.



(c): REVERSAL AFTER 2500 CYCLES.

FIGURE (5.14): DEFORMED STRUCTURE OF THE RAIL DISC SURFACE LAYER CAUSED BY DIFFERENT SINGLE REVERSAL REGIMES

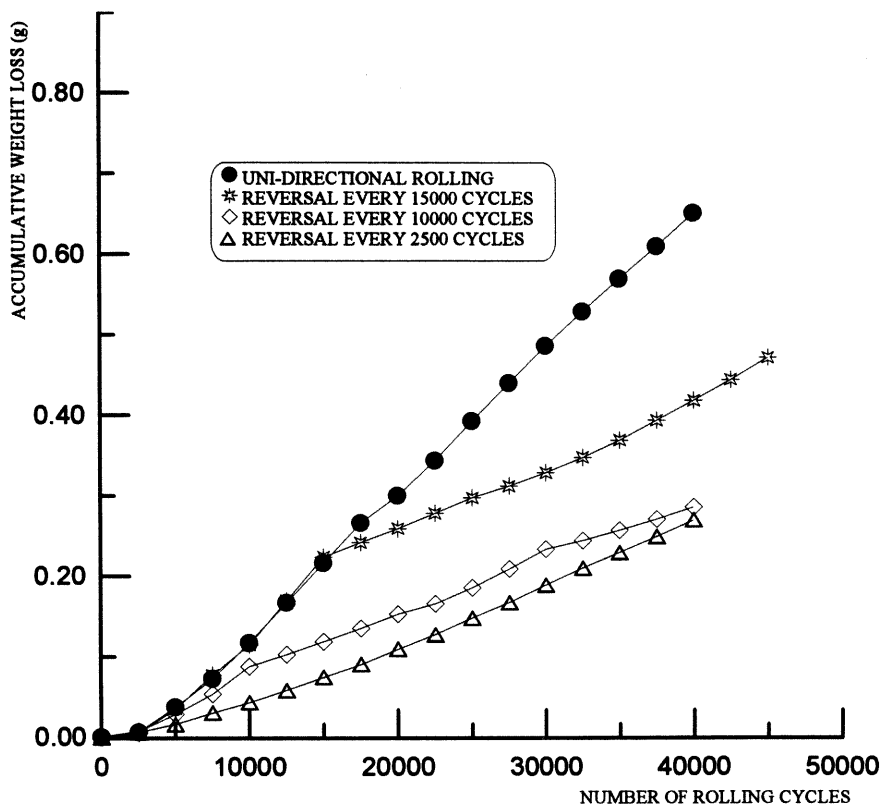


FIGURE (5.15): WEAR RATE AS ACCUMULATED WEIGHT LOSS OF THE RAIL DISC DUE TO THE DIFFERENT MULTIPLE RDRs

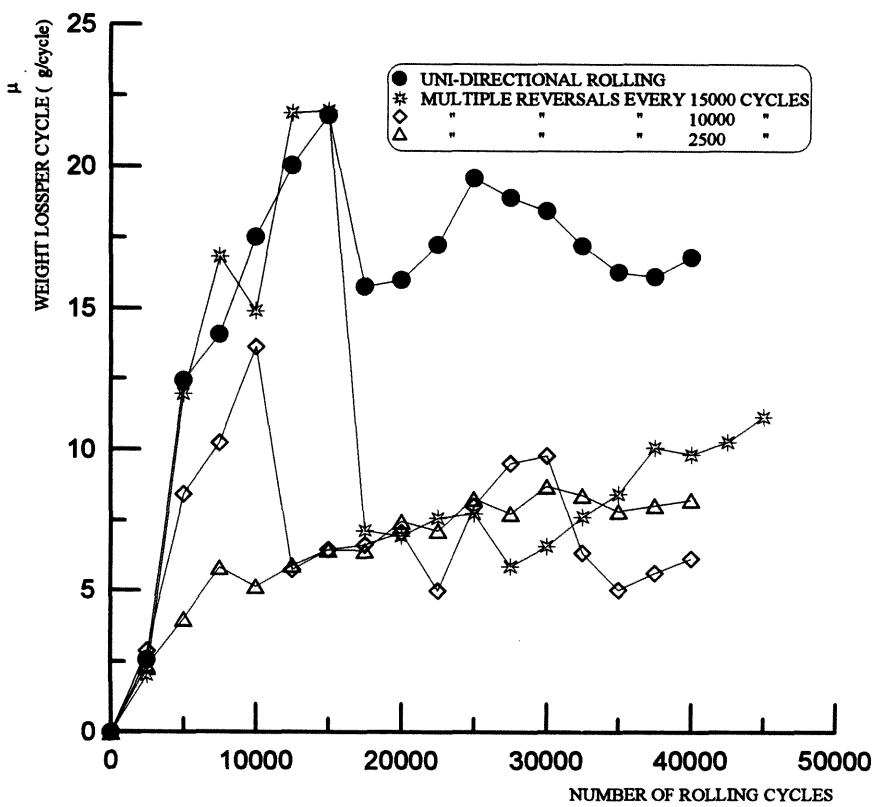
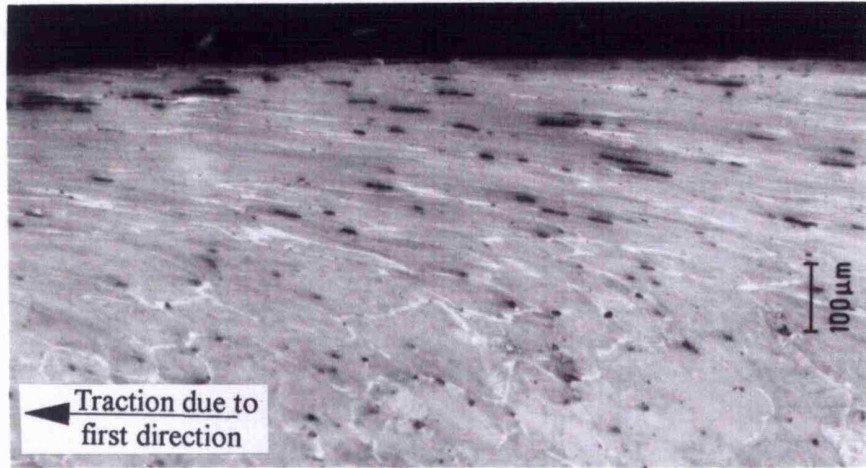
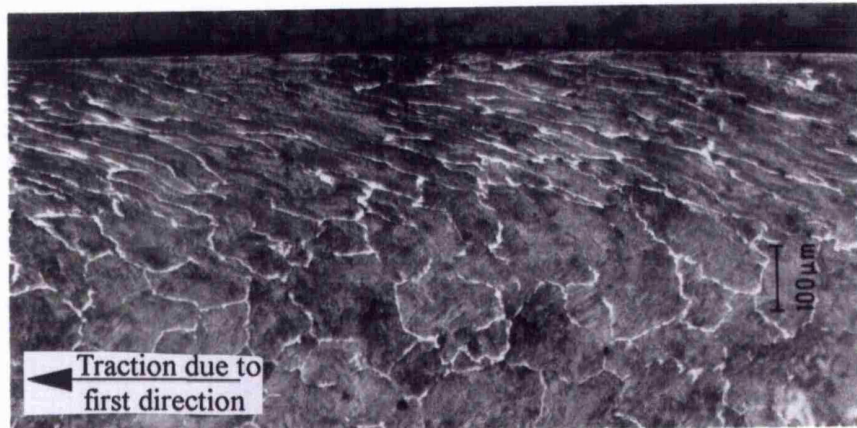


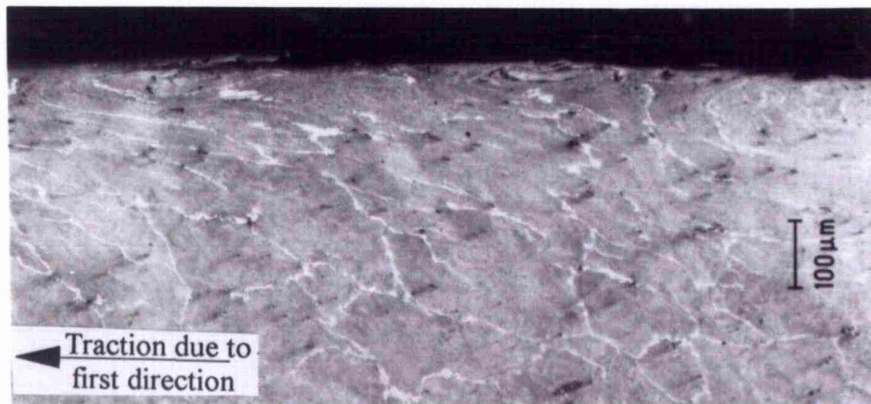
FIGURE (5.16): EFFECT OF MULTIPLE ROLLING DIRECTION REVERSAL ON THE RAIL DISC WEIGHT LOSS PER ROLLING CYCLE



(a): EVERY 15000 CYCLES.



(b): EVERY 10000 CYCLES.



(c): EVERY 2500 CYCLES

FIGURE (5.17): STRUCTURE DEFORMATION DUE TO MULTIPLE ROLLING DIRECTION REVERSAL

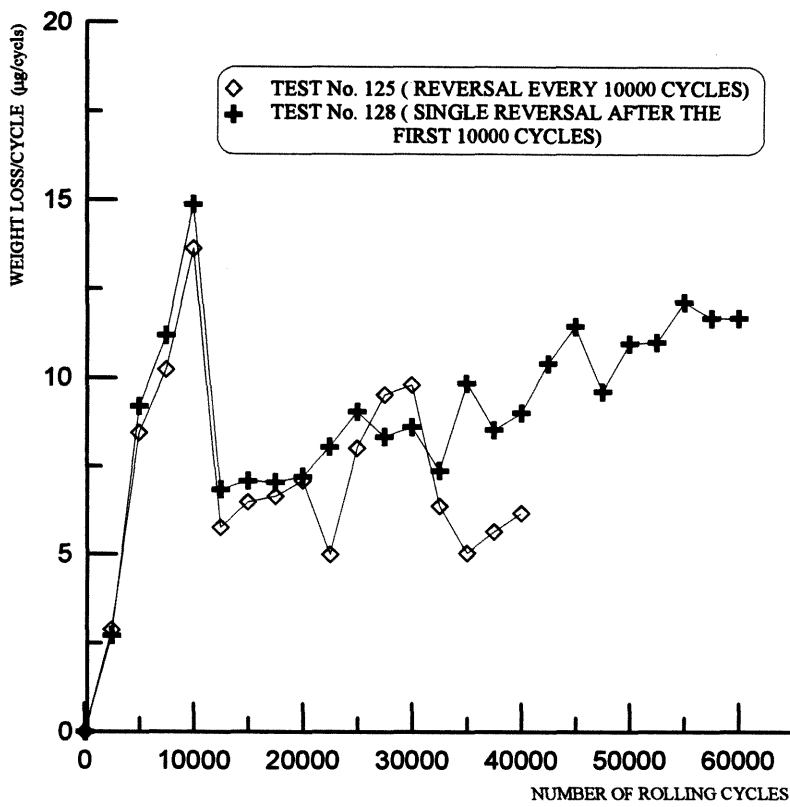


FIGURE (5.18): COMPARISON BETWEEN THE EFFECT OF SINGLE AND MULTIPLE ROLLING DIRECTION REVERSAL UNDER A CYCLE INTERVAL OF 10000 CYCLES

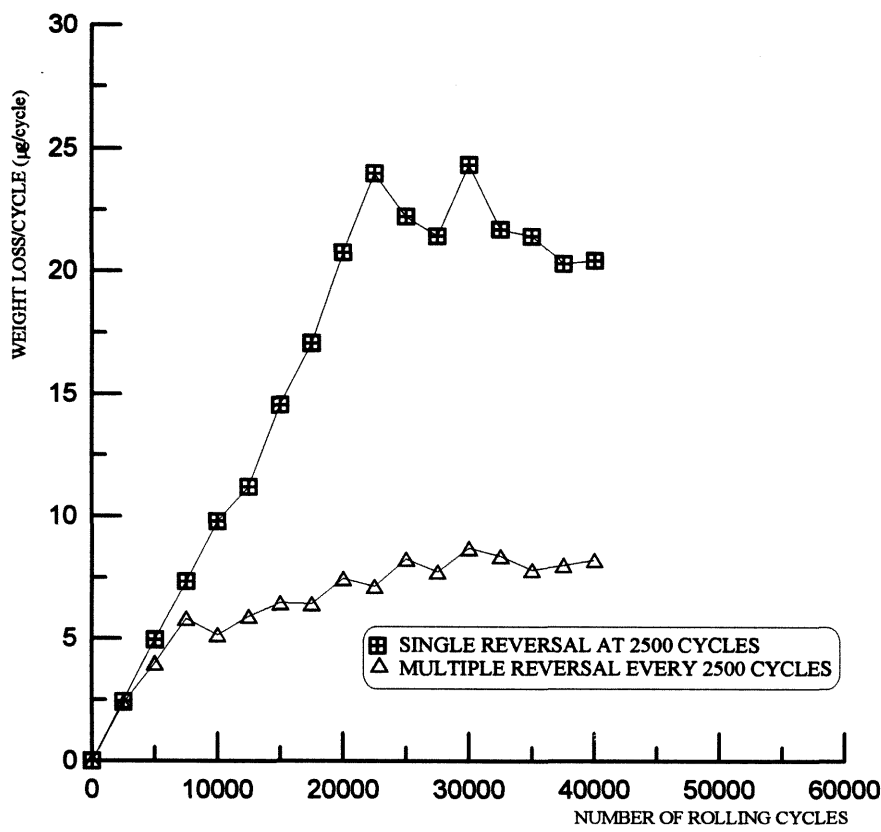


FIGURE (5.19): COMPARISON BETWEEN THE EFFECT OF SINGLE AND MULTIPLE ROLLING DIRECTION REVERSAL UNDER A CYCLE INTERVAL OF 2500 CYCLES

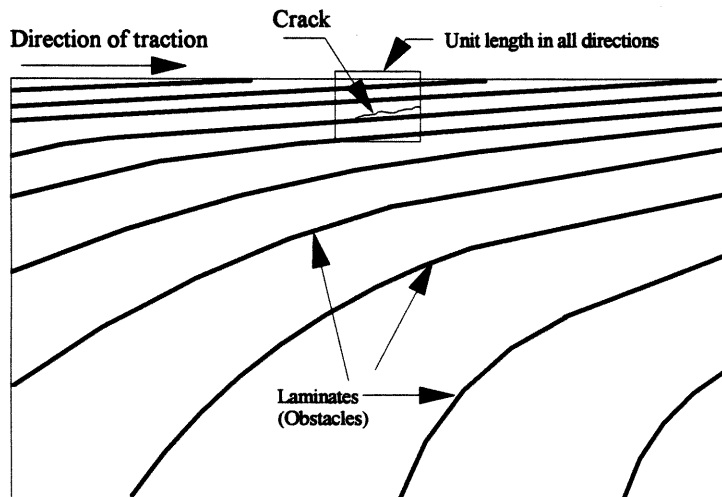
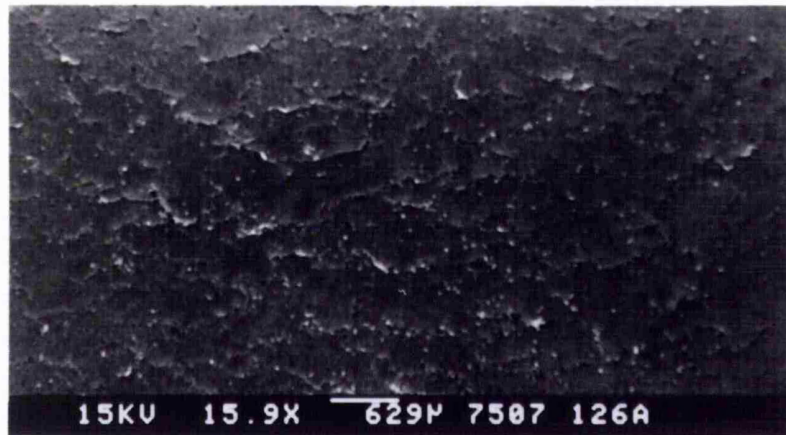
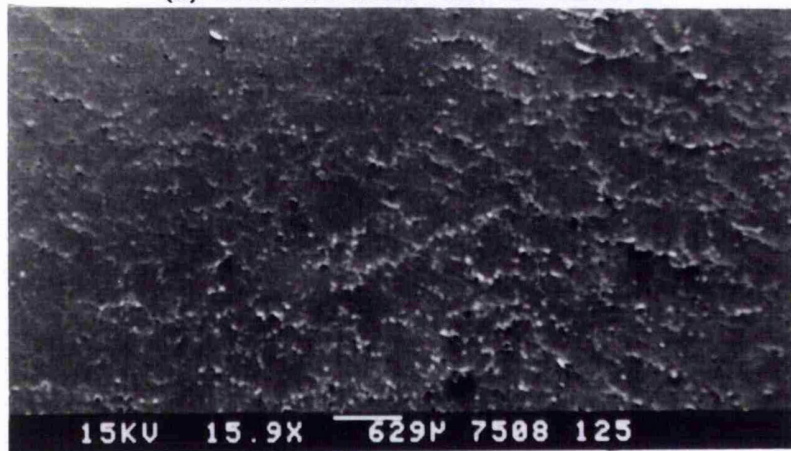


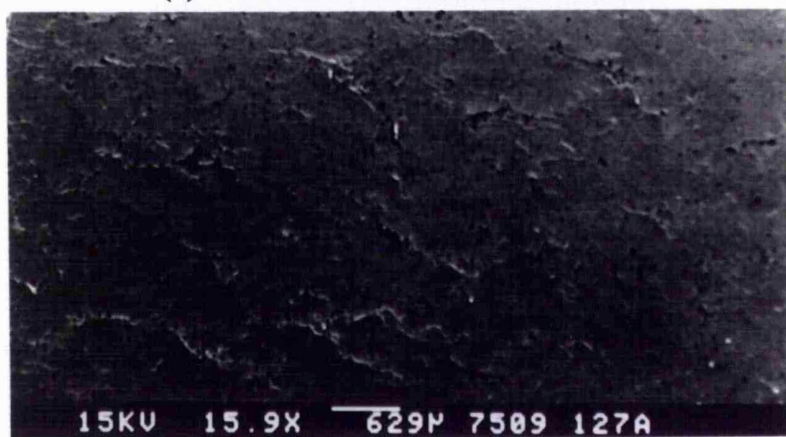
FIGURE (5.20): SCHEMATIC REPRESENTATION OF THE LAMELLAR OBSTACLES FACING THE DISLOCATION MOVEMENT IN A PEARLITIC DEFORMED STRUCTURE



(a): 15000 CYCLES PER REVERSAL.



(b): 10000 CYCLES PER REVERSAL.



(c): 2500 CYCLES PER REVERSAL.

FIGURE (5.21): RUNNING TRACK OF THE THREE RAIL DISCS TESTED UNDER DIFFERENT MULTIPLE REVERSAL REGIMES

Chapter 6

ROLLING CONTACT FATIGUE OF RAIL STEELS

6.1 INTRODUCTION

As discussed in section 2.2.4 of chapter 2, rolling contact fatigue (RCF) failure can be either surface or subsurface initiated. Subsurface initiation is often associated with the presence of non-metallic inclusions in regions of maximum shear stress⁽¹⁾. Both surface and subsurface cracks can continue their growth to form either a shell or spall, or to result in detailed fracture of the rail. It has also been shown that the initiation of RCF cracks is less understood than their growth⁽¹⁾. Since the presence of a liquid lubricant has been found to be essential for RCF failure to take place, any explanation which does not take the role of the fluid lubricant in consideration will not be convincing. However, the models in which the role of lubricant is accounted for, fail to explain the crack initiation. They focus only on the mechanism of propagating a pre-existing crack from a certain crack length.

6.2. BOWER'S ROLLING CONTACT FATIGUE CRACK PROPAGATION MECHANISM

The first attempt to produce RCF failure under laboratory conditions is due to Way⁽²⁾, who was the first to explain crack growth in terms of the liquid lubricant pushed inside the crack cavity by the rolling action to generate hydrostatic pressure and cause mode I stress intensity at the crack tip. This pressurising mechanism has been the basis for most of the recent models⁽³⁻⁷⁾. According to these models, the fluid lubricant has one or more of the following effects on RCF crack propagation.

- a. If it enters the crack cavity, the fluid lubricant can be trapped and pressurised to pull apart the two faces of the crack causing mode I stress intensity at the crack tip.
- b. It lubricates the two faces of the crack and, as a result, reduces the coefficient of friction and allows easier relative motion between the two faces causing mode II stress intensity at the crack tip.
- c. The lubrication effect of the fluid lubricant reduces the coefficient of friction between the two contacting bodies and, as a result, reduces the surface traction $q_{(s)}$, which is a function of the traction coefficient f and the Hertzian pressure $p_{(s)}$, the three quantities

are related by⁽⁸⁾:

$$q_{(x)} = f p_{(x)} \quad 6.1$$

Among the different models which explain the role of the fluid lubricant in RCF crack propagation, Bower's model⁽⁶⁾ appears to be the most widely accepted. It is basically an extension of the two dimensional model developed by Keer and Bryant⁽³⁾ to include the effect of the crack face friction. According to Bower's model, which is schematically illustrated in figure (6.1), the crack is pulled open by the load just before the load reaches the crack mouth and, as a result, the liquid lubricant enters the crack cavity by capillary action, figure (6.1a). As the load approaches the crack mouth, the fluid inside the crack cavity is trapped by the contact area sealing the crack mouth and by the load closing the upper part of the crack, figure (6.1b). However, since the fluid is reasonably assumed to be incompressible, part of the crack will remain open by the action of the pressure inside the crack cavity. As the load moves further, the fluid is pushed towards the crack tip while its pressure rises to balance the hydrostatic pressure due to the applied load. This pressure causes mode I stress intensity at the crack tip, figure (6.1c). When the pressure inside the crack cavity exceeds the contact pressure around the crack mouth, the crack opens to allow some of the pressurised liquid to escape keeping the two faces of the crack apart and allowing relative motion between them. This relative motion causes mode II crack propagation, figure (6.1d).

Using this model, Bower calculated the mode I and II stress intensities in the form of a cycle, repeated every time the load passes over the assumed crack. Different conditions and various crack face friction coefficients were tried. A typical result for the mode II stress intensity of the crack shown in figure (6.2a) is illustrated in figure (6.2b).

Bower's model is based on the following assumptions:

- a. The initial crack is sufficiently large for linear elastic fracture mechanics to be applied.
- b. The coefficient of friction between the two lubricated faces of the crack is 0.1.

The main limitations of the model can be summarised by the following:

- i. It ignores the initiation stage of cracking.
- ii. It does not predict the crack direction and/or rate of propagation.

- iii. It fails to explain the crack branching or change in direction of propagation.
- iv. It cannot explain the propagation of subsurface initiated RCF cracks.

Despite these limitations, and in the absence of other reliable models, Bower's model remains the most attractive to explain the role of lubricant in RCF failure. Researchers have been trying to extend the model beyond these limitations. Recently, Cheng et al⁽⁹⁾ have studied the initiation stage of RCF cracking. Using a micromechanics model of dislocation pile-up, they have shown that crack initiation does not require the presence of a liquid lubricant and that surface initiation starts at lower dislocation density compared with subsurface initiation. Bold and Brown⁽¹⁰⁾ have tried to add a branching criterion to the model. They have conducted biaxial fatigue tests on cruciform specimens by applying a sequential stress cycle of mode I followed by mode II, as suggested by Bower and illustrated in figure (6.3). They found that the combination of mode I and II loading did produce coplanar crack growth, *i.e.* growth which was both perpendicular to the maximum tensile stress of the first part of the cycle (mode I) and in the direction of maximum shear stress for the subsequent mode II part of the overall cycle. The direction of growth was found to depend on the ratio between the mode I and mode II stress intensities. If the mode I stress intensity range dropped below about one-half of the mode II intensity range, then branch crack growth occurred.

Bower's model implies that the crack would not grow if the rolling direction is reversed. Upon reversal the crack tip enters the Hertzian pressure region before the mouth, leading to the gradual closure of the crack cavity starting from the tip. In this case no fluid will be pressurised inside the crack cavity. Instead, even the fluid which has entered the cavity during the first direction will be expelled and mode I propagation will be disabled. Furthermore, upon further cycling, the two faces of the crack will lose the lubrication effect of the fluid, resulting in disabling mode II propagation. Disabling both mode I and II will prevent crack propagation. This implication, which has been theoretically concluded by Bower⁽⁷⁾, will be investigated in chapter 7, where the effect of rolling direction reversal on rolling contact fatigue will be studied. However, before considering rolling direction reversal, the unidirectional RCF behaviour needs to be considered.

6.3. PERFORMANCE OF BS11 AND MILL HEAT TREATED STEELS UNDER ROLLING CONTACT FATIGUE CONDITIONS

In the following sections, the behaviour of both BS11 and Mill Heat Treated (MHT)

steels under rolling contact fatigue conditions will be investigated. The aim of this investigation is to determine the fatigue lives of these steels under unidirectional rolling-sliding conditions. Due to the difficulties in defining RCF life under these conditions, discussed in section 2.4.3 of chapter 2, RCF life will be defined as the number of rolling-sliding cycles required to initiate and propagate a RCF crack deep enough to trigger a pre-set alarm level on the eddy current flow detection system described in section 3.1. This alarm level has been set by using a calibration disc, in which an artificial crack has been spark eroded to a certain depth below the contact surface, at 45° to the disc surface, in the direction of load movement.

6.3.1. Test conditions

General test conditions have been discussed in section 3.4. Other conditions are summarised in table (6.1). Both BS11 and MHT rail steels have been tested against W8A wheel steel discs under the two maximum contact pressures, 1200 and 1500 ± 5 MPa, used during this project and calculated using equation 2.18. All tests were conducted under a rail disc creepage of $-1 \pm 0.01\%$, equation 3.1. Orientation of rail discs was those shown in table (6.1). BS11 rail discs were machined with their axes parallel to the long axis of the rail. MHT rail discs were machined using two different orientations, as shown in table (6.1). As shown in figure (3.9), the hardness varies across the MHT steel rail head. As a result the orientation shown under test numbers 154 and 149 resulted in discs with varying hardness at different circumferential locations of the disc track. Using this orientation may not represent the contact conditions experienced in the field by the MHT rail, where the rail surface has the maximum hardness, which is relatively uniform within the zone affected by the contact stresses. The aim of studying the RCF life using such an orientation was to establish a reference fatigue life to be utilised when the effect of initial damage, caused by dry cycling, will be investigated. This investigation will be the subject of the chapter 8.

6.3.2. Test results and discussion

Table (6.2) summarises the test results. Crack dimensions are reported as maximum crack depth below the contact surface and maximum length. Wear of the test discs is presented as total disc weight loss as well as total loss in disc diameter. Track width gain is also reported. The maximum crack depth should be equal since the same failure criterion (*i.e.*, eddy current trip level) has been used during all the tests. However, the values shown

in table (6.2) shows some scatter. This could be explained by arguing that RCF crack propagates below the surface with a elliptical tip⁽⁴⁾ of a relatively small radius. To reveal the maximum crack depth/length, sectioning must be made at the centre of the crack, otherwise only part of the crack can be seen in the section. The width of the crack at the disc surface is normally less than 2 mm and the width of the tip is expected to be less. With these small crack dimensions it becomes difficult to ensure sectioning exactly at the crack centre. This argument is schematically illustrated in figure (6.4)

Before discussing the RCF behaviour of each steel, there are common features noticed in all tests. These are discussed below.

6.3.2.1. Common features

a. Behaviour of traction coefficient

The traction coefficient, which was monitored throughout each test, was characterised by a sharp rise at the start of the test to reach about 0.06 before the rising rate decelerated. It reached a maximum value of about 0.15 to 0.2 after a certain number of cycles. This number has been found to vary during different tests. After reaching its maximum value, the traction coefficient gradually drops again. After about 10000 cycles it starts to rise again slowly but steadily to reach another maximum, which is lower than the first one, after about 25000 cycles. Figure (6.5) shows the overall behaviour of traction coefficient until the end of test number 164 as a function of rolling-sliding cycles, whereas figure (6.6) shows the traction coefficient during the initial stages of the test. This type of behaviour, which has been observed by others^(11,12), makes it difficult to report a single value to represent the traction coefficient during the test. Instead, two values are reported in table (6.2), the maximum and the end-of-test.

b. Crack location.

Crack location relative to the disc running track is reported as the location of the maximum eddy current signal relative to the disc edge near the drive shaft. In all tests, maximum cracking was found in the midsection of the track. The same observation has been reported by Garnham⁽¹³⁾, and could be related to the drop of the contact stresses at the disc edges. The cracked area has been found to be associated with undulations in the roundness profile recorded after each test. Figure (6.7) shows a comparison between the original and after-test roundness profiles of test number 164 as an example of such

undulations. It is difficult to identify whether these undulations are a cause or a consequence of RCF cracking. However, if they are formed before crack initiation they could cause high localised contact stresses as suggested by Cheng et al⁽¹⁴⁾, who studied the initiation of RCF cracks near transverse furrows, introduced to the test discs by electric discharge machining. They showed that the rise in the local contact pressure at the furrows' edges can be much higher than the overall maximum contact pressure.

c. Maximum strain hardening

The traction coefficient between the two discs dictates the location of the maximum orthogonal shear stress and, as a result, the location of maximum strain hardening⁽¹⁵⁾. Traction coefficients of less than 0.25 cause subsurface strain hardening. Table (6.2) shows that the maximum traction coefficient during these tests did not exceed 0.25. Even if this happens, it is only for a short period, compared with the overall number of cycles of the test. Figure (6.8) shows the hardness profile below the contact surface of the BS11 rail disc of test 114, as an example of subsurface maximum strain hardening, where the maximum hardness is at about 0.25 mm below the contact surface.

e. Wear and plastic deformation

Since tests were run non-stop until failure, it was not possible to monitor the wear behaviour with number of rolling-sliding cycles. The end-of-test weight loss reported in table (6.2) may not be a good measure of the wear rate since it corresponds to different numbers of rolling-sliding cycles. However, the plastic flow in the form of lips at the edges of the disc, also reported in table (6.2) as disc track width gain, shows that despite the higher number of cycles, the MHT discs showed less deformation compared to the BS11 discs tested under the same loading conditions. This was expected, since the shear yield strength of the MHT steel, which is a function of the yield strength in tension, is much higher, as shown in table (3.1) of chapter 3.

6.3.2.2. Rolling contact fatigue (RCF) of BS11 rail steel

Under a maximum contact pressure of 1500 MPa the fatigue life of the BS11 rail steel was 37422 cycles, whereas this life was 96879 cycles under a maximum contact pressure of 1200 MPa. The morphology of the crack which triggered the eddy current detection system during test number 114, tested under 1500 MPa contact pressure, is shown unetched in figure (6.9). The crack propagated in the direction of load movement,

opposite to the direction of traction, in a straight fashion, parallel to the deformed structure. It also branched upwards in many locations to form branched cracks perpendicular to the main crack. A close-up view of part of the crack is shown in figure (6.10). It reveals that the main crack prefers to propagate in the softer (ferrite) phase of the structure, either in the elongated ferrite islands or between the stacked cementite layers. The softer ferrite phase is expected to demonstrate lower tensile/shear strength. According to the propagation mechanism proposed by Bower⁽⁶⁾ and discussed earlier, crack propagation is due to both mode I and II intensities. Lower tensile strength will ease mode I crack propagation, whereas lower shear strength will result in easier mode II propagation. Furthermore, the hard cementite layers act as obstacles to crack propagation⁽¹⁶⁾. This argument has been discussed in section 5.3.2 and illustrated in figure (5.20).

The difference between the main and branch cracks in their morphology and propagation angle may indicate that they are due to two different propagation modes, as discussed in section 3.1 and suggested by Bold et al⁽¹⁰⁾. Figure (6.11) shows the crack caused by 1200 MPa maximum contact pressure. The morphology of the crack in general is similar to that caused by 1500 MPa, shown in figure (6.9). The initiation of the main crack under both loads appears to be on the surface. This is in agreement with the work of Cheng et al⁽⁹⁾, who have shown that surface crack initiation starts at lower dislocation density compared with subsurface initiation. This may be supported by the subsurface crack shown in figure (6.12). This crack appears to have initiated from the edge of a stringered manganese sulphide inclusion in the rail disc of test number 144. Despite the presence of the inclusion this crack is still much smaller compared with the surface initiated crack which has caused the failure. This may suggest that the surface crack has initiated at an earlier stage.

Despite the similarity in the crack morphology under the two loads, the following differences are worth mentioning.

- i. The crack angle, measured between the contact surface and the main crack, was wider under the lower contact pressure. It has been shown earlier that a crack prefers to propagate in the direction of the deformed structure lines which are at a wider angle under lower loads.

ii. The crack mouth opening, revealed after sectioning, is larger under the higher load.

6.3.2.3. RCF of MHT rail steel

MHT rail steel has been tested using two different disc orientations. Discs machined with their axes parallel to the long axis of the rail have been tested under 1200 and 1500 MPa, test numbers 154 and 149, while the rail disc used in test number 164 was machined with its axis perpendicular to the rail surface. This was done in order to establish reference RCF lives to be used during the part of the project in which the effect of initial dry cycling on RCF will be studied, this will be discussed in chapter 8.

As seen in table (6.2), MHT rail steel showed better resistance to RCF under both the loads. The disc orientation relative to the rail section during tests numbers 154 and 164 resulted in varying strengths at different circumferential locations of the disc, see table (6.1) and figure (3.9). This may not represent the field contact conditions where only a shallow depth below the rail surface is subjected to the contact stresses. However, the minimum hardness of the MHT rail disc remained higher than the hardness of the BS11. This may explain the general trend of higher RCF life for the MHT steel. The same observation has been reported by others⁽¹⁷⁾.

Unlike the straight main crack with upward branches observed in BS11 rail steel, RCF cracks of MHT rail steel are characterised by a network of cracks. It is difficult to define which is a main crack and which is a branch. Figure (6.13) shows the deepest crack found in the MHT rail disc of test 149. The specimen has been slightly etched to improve the visibility of the cracks and to reveal some of the microstructural features. Despite the high contact pressure, the deformation is confined to a very shallow depth, about 30 μm below the contact surface. This may explain the formation of a network, rather than a main crack parallel to the deformed structure. The absence of the stacked lamellar structure with a preferential propagation between the laminates, seen in the BS11 deformed structure in figure (6.9), causes the crack to take other directions. Furthermore, the pearlitic structure of the MHT steel is very fine compared with that of the BS11. As a result, the obstacles to crack propagation are not as aligned as in the deformed BS11 structure.

A reasonable comparison between the RCF lives of BS11 and MHT rail steels can be concluded from tests 114 and 164. Both were conducted under a maximum contact pressure of 1500 MPa. In addition, the orientation of the discs in both the tests represents

the field conditions more accurately. A simple comparison shows that, under the test conditions, the RCF life of MHT rail steel was almost 1.75 times that of the BS11.

6.4. CONCLUSIONS

i. Mill Heat Treated (MHT) rail steel resists RCF more than the BS11 rail steel.

ii. In addition to the material strength parameters used in most of the mechanisms by which RCF crack propagation is explained, the structural features play an important role in crack propagation.

iii. In the absence of other mechanisms by which RCF crack initiation can be explained, the micromechanics model of Cheng et al⁽⁹⁾ in which the presence of a liquid lubricant is not essential for RCF initiation may be accepted.

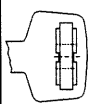
iii. The morphologies of RCF cracks in BS11 and MHT rail steels are different. This could be related to the different strength and structural parameters. Crack propagation is easier parallel to the laminates of the deformed BS11 steel structure. This conclusion could be confirmed by conducting RCF tests under conditions of rolling direction reversal to obtain a structure which is less aligned than that obtained during unidirectional rolling.

iv. In addition, rolling direction reversal may give a reliable method to investigate experimentally one of the implications of Bower's model⁽⁶⁾ which predicts that an existing crack will cease propagation upon reversing the direction of rolling. Such an investigation will be presented in chapter 7.

REFERENCES

1. P. Clayton, Metallurgical Aspects of Surface Damage Phenomena in Rails, *Canadian Metallurgical Quarterly*, 21, 1, (1982), 31-46.
2. S. Way, Pitting due to rolling contact, *Trans. ASME, Journal of Applied Mechanics*, Vol. 2, (1935), A49-A58.
3. Keer L M and Bryant M D. A Pitting Model for Rolling Contact Fatigue. *Transactions of ASME, Journal of Lubrication Technology*, 105, (1983), 198-205.
4. M. Kaneta, Y. Murakami and H. Yatsuzuka, Propagation of surface cracks in rolling line contact, *Proceedings of the JSLE International Tribology Conference*, Tokyo, Japan, (1985), 911-916.
5. M. Kaneta, H. Yatsuzuka and Y. Murakami, Mechanics of Crack Growth in Lubricated Rolling/Sliding Contact, *ASLE Transactions*, 28, 3, (1985).
6. A. F. Bower, The Influence of Crack Face Friction and Trapped Fluid on Surface Initiated Rolling Contact Fatigue Cracks. *Transactions of ASME, Journal of Tribology*, (1988), 110. 704-711.
7. A. Bower, Some Aspects of Plastic Flow, Residual Stresses and fatigue Cracks Due to Rolling and Sliding Contact, PhD Thesis, *Cambridge University*, (1987).
8. K. L. Johnson, *Contact Mechanics*, Cambridge University Press (1985).
9. W. Cheng, H. Cheng, T. Mura and L. Keer, Micromechanics Modelling of Crack Initiation Under Contact Fatigue, *Transactions of ASME, J. Tribology*, 116, (1994), 2-8.
10. P. E. Bold, M. W. Brown and R. J. Allen, A Review of Fatigue Crack Growth in Steels Under Mode I and Mode II Loading, *Fatigue Fracture of Engineering Materials and Structures*, 15, (1992), 965-977.
11. H. Krause and H. Demirci, Factors Influencing the Real Trend of the Coefficient of Friction of Two Elastic Bodies Rolling Over Each Other in Presence of Dry Friction, *The Mechanics of Contact Between Deformable Bodies* (1975), Delft University Press, Eds. A. D. Pater and J. J. Kalker.
12. A. F. Bower and K. L. Johnson, The Influence of Strain Hardening on Cumulative Plastic Deformation in Rolling and Sliding Line Contact, *J. Mech. Phys. Solids*, 37, 4 (1989) 471-493.

13. J. E. Garnham, Crack Initiation in Rolling Contact Fatigue, *University of Leicester, engineering Dept., Internal Report*, Feb., (1991).
14. W. Cheng, H. Cheng, L. Keer and X. Ai, Surface Crack Initiation Under Contact Fatigue: Experimental Observation and Contact Analysis, *Trans. ASME, J. Tribology*, 115, (1993), 658-665.
15. K. L. Johnson, *Contact Mechanics*, Cambridge University Press (1985).
16. W. Tyfour and J. H. Beynon, The Effect of Rolling direction Reversal on the Wear Rate and Wear Mechanism of Pearlitic Rail Steel, *Tribology International*, 27, 6, (1994), 401-412
17. V. Dikshit, P. Clayton and D. Christensen, Investigation of Rolling Contact Fatigue in Head Hardened Rail, *Wear*, 144 (1991) 89-102.

<i>Test Conditions</i>	<i>Test Number</i>				
	114	144	154	164	149
Disc material Rail wheel	BS11 ^(a) W8A ^(b)	BS11 W8A	MHT W8A	MHT W8A	MHT W8A
Maximum contact pressure, eq. 2.18 (MPa)	1500	1200	1500	1500	1200
Percentage creepage, eq. 3.1 (%)	-1				
Test speed (RPM)	402/406				
Initial surface roughness (Ra, µm)	Rail/Wheel 0.38/0.39	Rail/Wheel 0.44/0.47	Rail/Wheel 0.19/0.27	Rail/Wheel 0.26/0.32	Rail/Wheel 0.29/0.37
Lubrication	Water, one drip per second				
Orientation of rail disc specimens in relation to rail section ^(b)					

^(a) For mechanical properties and chemical composition see table (3.1) in chapter 3.
^(b) The orientation of the wheel disc specimen in relation to the wheel rim is the same for all tests, see figure (3.7a).

TABLE (6.1): TEST CONDITIONS

<i>Test results</i>	<i>Test number</i>				
	114	144	154	164	149
Number of cycles to failure (cycles)	37422	96879	59623	64347	230263
Crack location (mm from the disc edge nearer to the drive shaft)	3.7	5.6	4.6	5.5	4.2
Maximum crack length (µm)	586	550	550	630	915
Maximum crack depth (µm)	600	320	260	340	420
Traction coefficient, Maximum	0.137	0.161	0.167	0.162	0.204
End-of-test	0.112	0.115	0.125	0.112	0.104
Total weight loss (g)	Rail 0.0547 Wheel 0.0101	0.1070 0.0247	0.0636 0.1247	0.0665 0.0806	0.1100 0.1192
Diameter loss (mm)	Rail 0.025 Wheel 0.005	0.015 0.010	0.005 0.025	0.005 0.020	0.015 0.015
Track width gain (mm)	Rail 0.18 Wheel 0.11	0.16 0.02	0.05 0.03	0.07 0.16	0.03 0.06

TABLE (6.2): TEST RESULTS

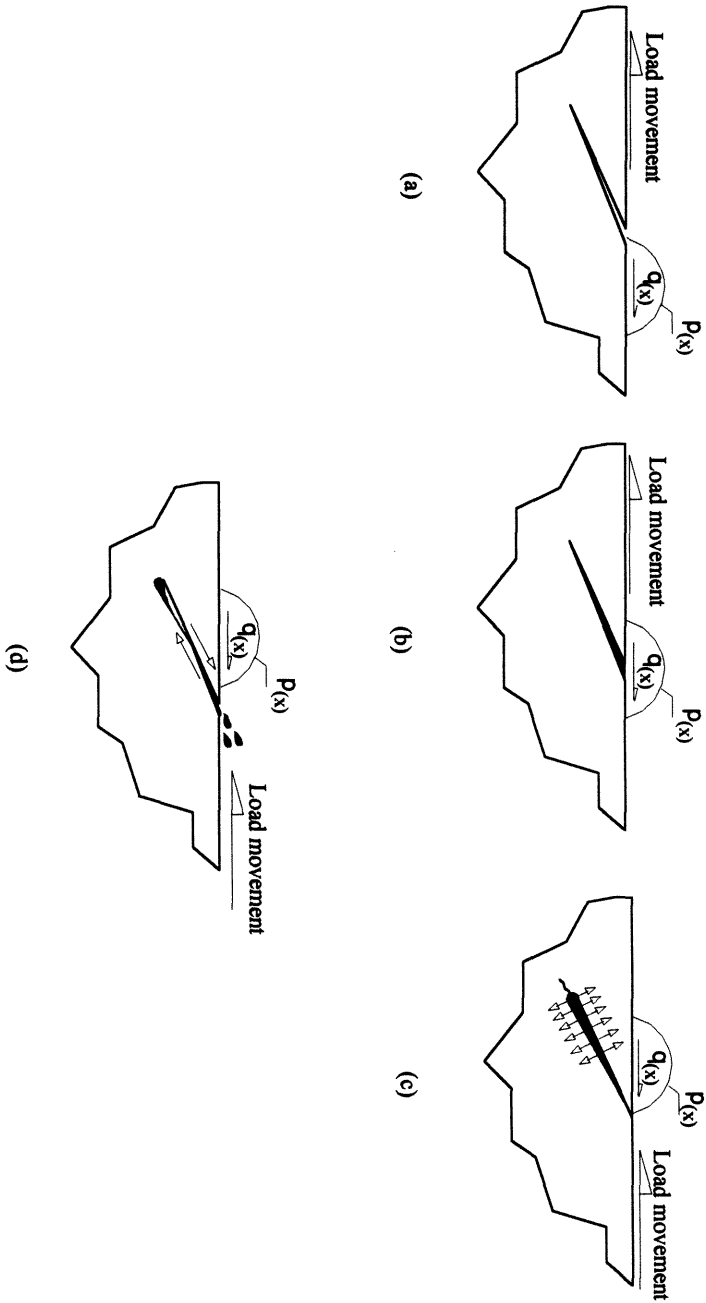


FIGURE (6.1): SCHEMATIC REPRESENTATION OF CRACK PROPAGATION BY THE ENTRAPPED FLUID MECHANISM (AFTER BOWER⁽⁷⁾)

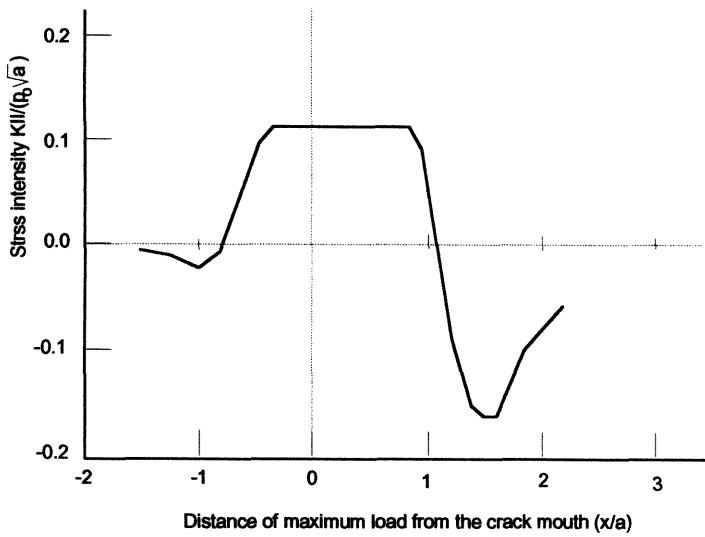
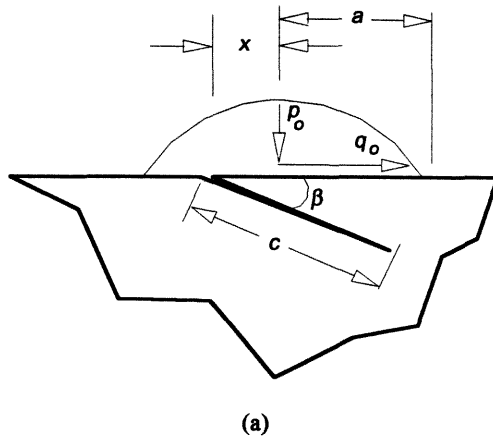


FIGURE (6.2): THE MODE II STRESS INTENSITY CYCLE FOR THE CRACK SHOWN IN (a) ABOVE, UNDER LUBRICATED ROLLING-SLIDING CONDITIONS (AFTER BOWER⁽⁷⁾)

(Crack face friction coefficient = 0.25, $\beta = 25^\circ$, $q_o/p_o = 0.05$, $c/a = 0.5$)

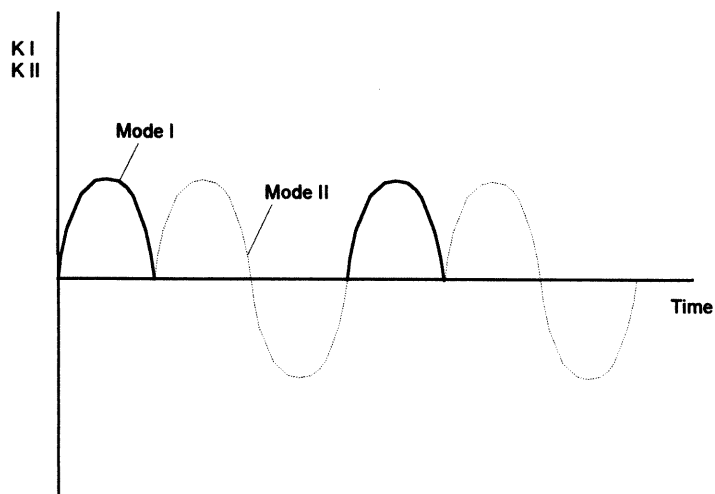


FIGURE (6.3): THE SEQUENTIAL MODE I AND MODE II STRESS CYCLE USED BY BOLD et al ⁽¹⁰⁾ TO PRODUCE COPLANAR CRACK GROWTH

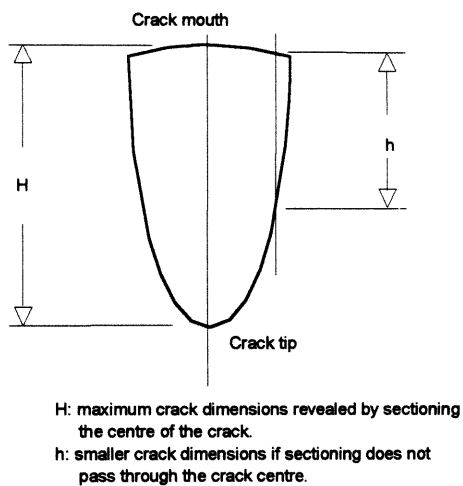


FIGURE (6.4): SCHEMATIC REPRESENTATION OF THE EFFECT OF OFF-CENTRE SECTIONING ON MEASURED CRACK DIMENSIONS

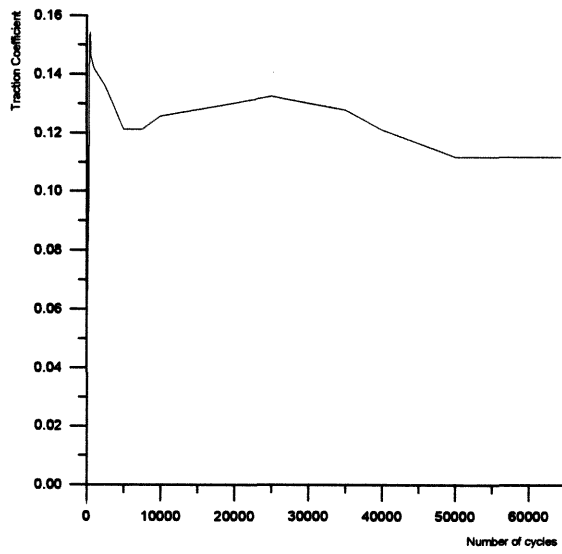


FIGURE (6.5): TRACTION COEFFICIENT AS A FUNCTION OF NUMBER OF CYCLES, TEST NUMBER 164

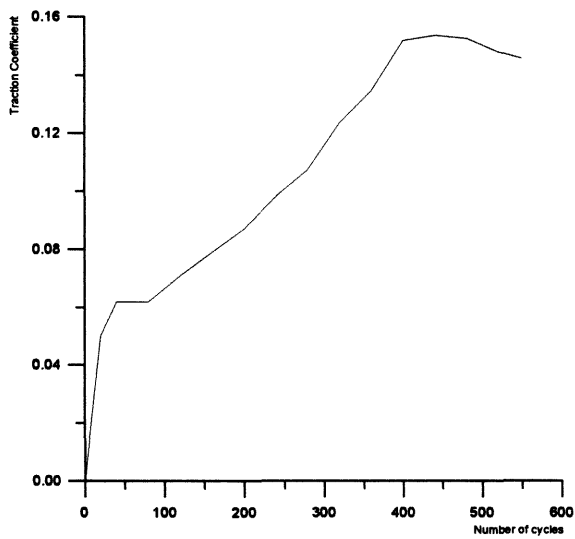
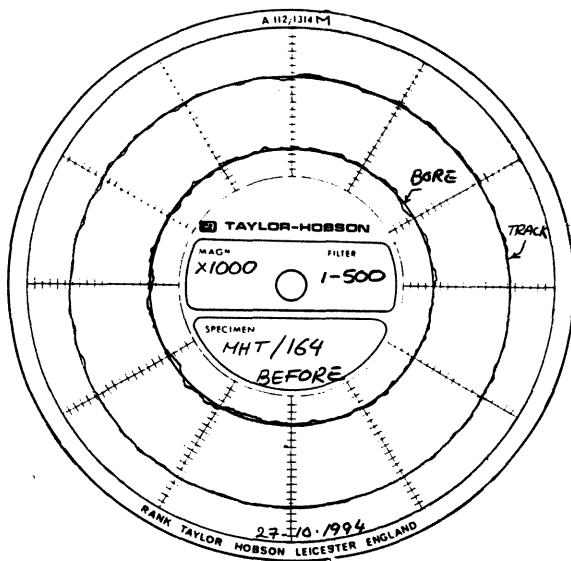
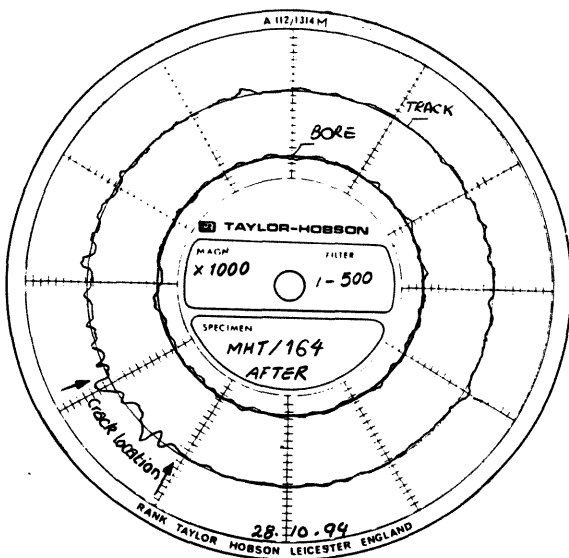


FIGURE (6.6): TRACTION DURING THE INITIAL STAGES OF ROLLING-SLIDING, TEST NUMBER 164



(a): BEFORE TEST



(b): AFTER TEST

FIGURE (6.7): ROUNDNESS PROFILE UNDULATIONS IN THE REGION OF RCF CRACKING, TEST NUMBER 164

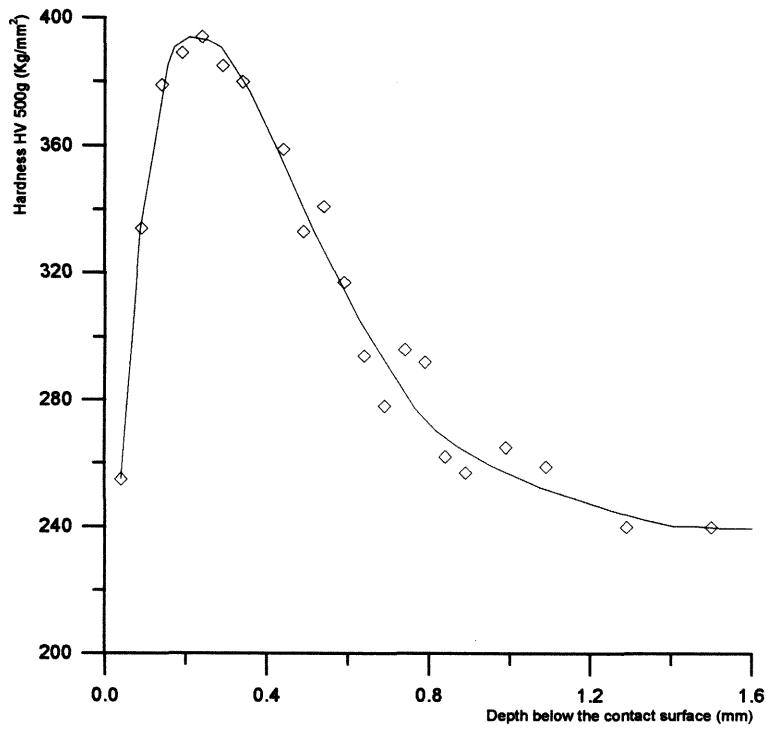


FIGURE (6.8): HARDNESS PROFILE BELOW THE CONTACT SURFACE OF THE BS11 RAIL DISC, TEST NUMBER 114

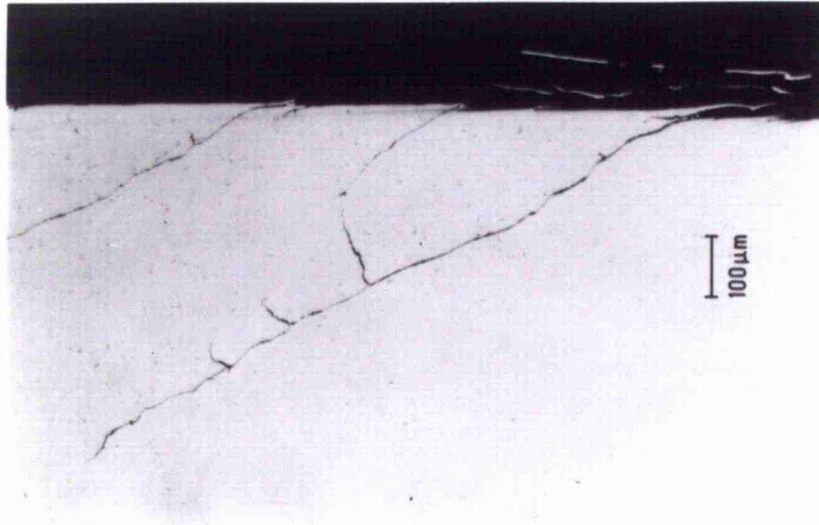


FIGURE (6.9): RCF CRACK OF BS11 RAIL STEEL DISC TESTED UNDER A MAXIMUM CONTACT PRESSURE OF 1500 MPa, TEST NUMBER 114



FIGURE (6.10): RCF PROPAGATION THROUGH THE SOFT FERRITE PHASE, TEST NUMBER 114

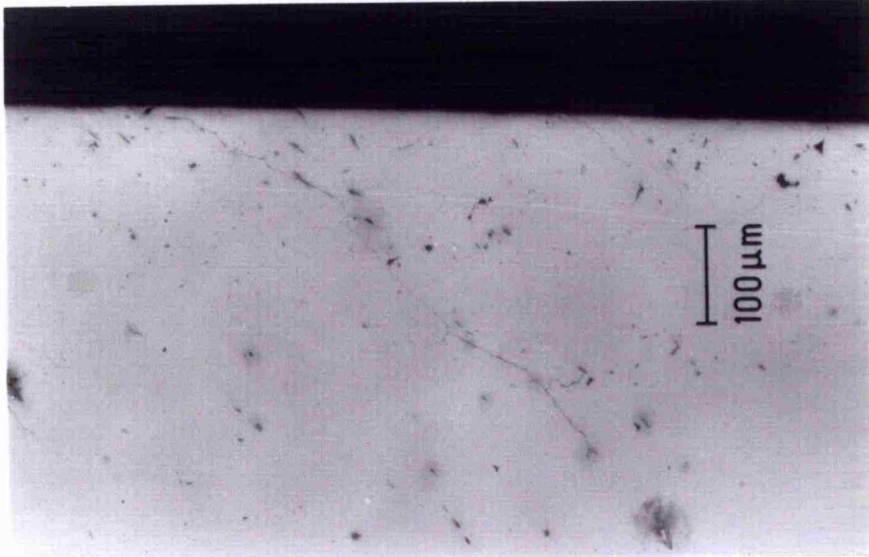


FIGURE (6.11): RCF CRACK OF BS11 RAIL STEEL DISC TESTED UNDER A MAXIMUM CONTACT PRESSURE OF 1200 MPa, TEST NUMBER 144

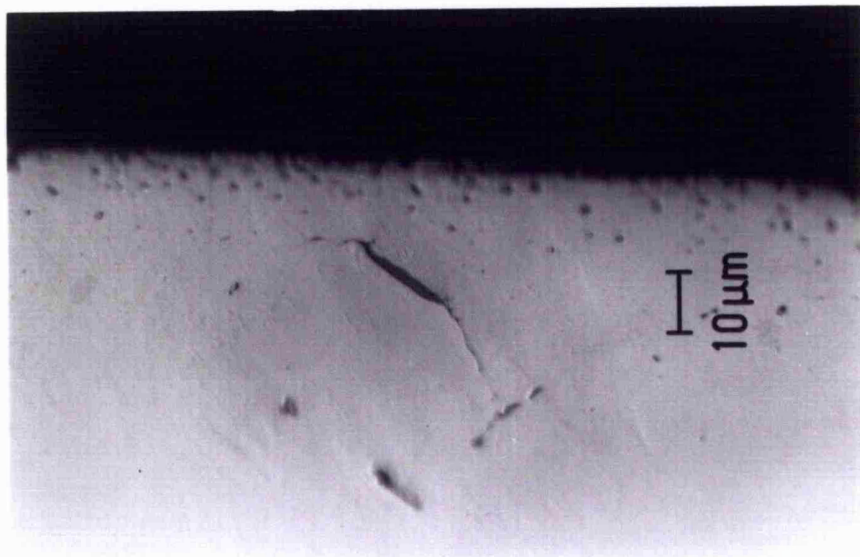


FIGURE (6.12): SUBSURFACE CRACK INITIATED FROM THE EDGE OF A STRINGERED MANGANESE SULPHIDE INCLUSION, TEST NUMBER 144

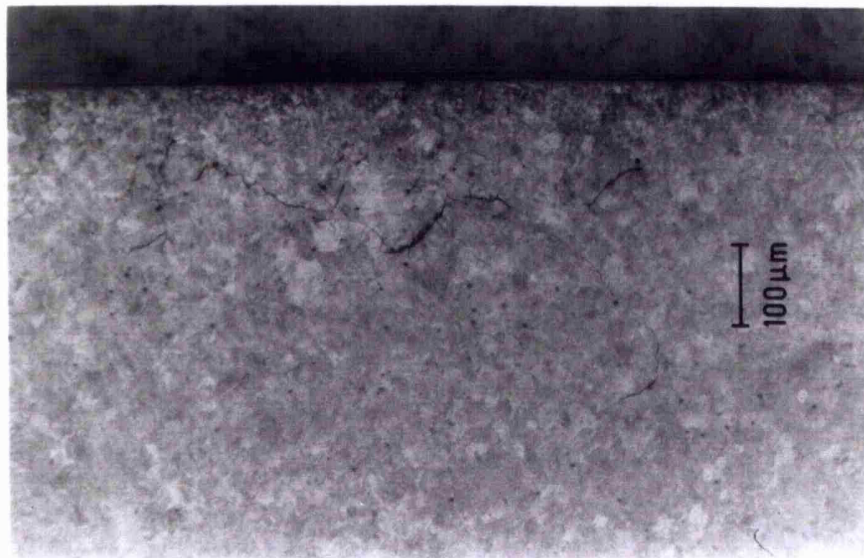


FIGURE (6.13) RCF CRACKING IN MHT RAIL STEEL, TEST NUMBER 149

Chapter 7

THE EFFECT OF ROLLING DIRECTION REVERSAL ON FATIGUE CRACK MORPHOLOGY AND PROPAGATION

7.1. INTRODUCTION

It has been suggested in section 6.4 of chapter 6 that rolling direction reversal [RDR] could be a reliable test method to confirm that, in addition to the strength parameters, the structural features play an important role in dictating the cracking morphology in RCF. At the same time, RDR gives the opportunity to investigate the possibility of the RCF crack ceasing its propagation once the rolling direction is reversed, as suggested by Way⁽¹⁾ and analysed by Bower's entrapped fluid mechanism of RCF crack propagation⁽²⁾.

The general test procedure was that discussed in section 3.4, and the reversal procedure was as described in section 5.1. Test conditions are shown in table (7.1). The non-dimensional term 'reversal factor' is used during this work to define the regime of rolling direction reversal for the rail disc and is defined by:

$$RF = \frac{C_r}{L_u} \quad 7.1$$

where C_r is the number of rolling cycles per reversal, and L_u is the number of rolling cycles to cause RCF failure in a unidirectional rolling test under the same conditions of load and creepage.

The work presented in this chapter has been the subject of a paper published in *TRIBOLOGY INTERNATIONAL*, 24, (1994), 273-282, and can be found in appendix 3.

7.2. RESULTS

A summary of the test results is shown in table (7.2). The non-dimensional term 'life factor' is introduced to evaluate the change in RCF life under conditions of different reversal factors. It is defined as the ratio of fatigue life due to any reversal regime and that due to unidirectional rolling. A life factor of more than unity means an increase in the RCF life, over that obtained in the unidirectional test, and vice versa.

Crack location is the distance of the maximum signal from the track edge nearest to its drive shaft. Crack dimensions are reported for all cracks over 180 microns deep and are

presented as average values, except for the crack length, where the maximum length is also presented. The term 'crack direction competition factor' [CDC factor] is introduced to evaluate the direction for the crack propagation. It is defined as the ratio between crack depth, measured radially from the track surface, and the crack circumferential length measured parallel to the surface between the mouth and the tip of the crack, as illustrated in figure (7.1). This method of reporting the crack morphology was preferred since it takes into consideration the crack branching and changing direction.

The behaviour of traction coefficient was not affected by RDR. It was similar to that obtained under unidirectional rolling and discussed in section 6.3.2.1 of chapter 6.

The effect of rolling direction reversal on the RCF life of pearlitic rail steel is shown in figure (7.2), in which the reversal regime is represented by the reversal factor, and the change in RCF life by the life factor. It can be seen from the plot that any reversal regime has a beneficial effect on the RCF life of pearlitic rail steel. This effect ranges from +10.5% for a reversal factor of 0.75 to +87% for 0.267. The maximum RCF life improvement appears to be achieved between reversal factors of 0.267 and 0.375.

The relationship between the life factor and the crack direction competition [CDC] factor is shown in figure (7.3). Although the data are scattered, they still show a trend of higher life factor with higher CDC factor.

Figure (7.4) shows the relationship between the reversal factor and the CDC factor, where it can be seen that the CDC factor is at its maximum value when the reversal factor is between 0.267 and 0.375. Superimposing this relationship on that between life factor and reversal factor shows that the optimum life factor and the maximum CDC factor are coincident and obtained under the same reversal factor.

Optical microscopy of sections perpendicular to the rotation axis of the disc through the crack face reveals different crack morphologies under different reversal regimes. RCF cracks in the rail specimen run unidirectionally in test number 114 have been discussed in chapter 6. The crack which resulted in the maximum signal on the detection system has been shown in figure (6.10). For easier comparison with other cracks obtained under reversal conditions, figure (6.10) is shown again in figure (7.5).

Unlike the straight cracks in the disc tested unidirectionally, the cracks in the specimen run under a reversal factor of 0.267 (10000 cycles/reversal), which gave the maximum life factor during test number 115, are of a quite different morphology. They can

be classified into two types: first the 'branched' type, which is characterised by a primary crack propagating to a shallow depth below the contact surface before it diverts its direction to the opposite sense. It then branches parallel to the initial direction to produce a two branch crack as shown in figures (7.6a) and (7.6b). The second type is the 'double' cracking type, which is characterised by two cracks of different initiation points and of opposite sense of directions, as shown in figure (7.7). The angle between the two cracks is very close to that between the two branches of the branched type.

Figure (7.8) shows a crack of the branched type, with a longer primary crack, found in the rail test disc of test number 116 which was conducted under a reversal factor of 0.5 (18711 cycles/reversal). Cracks in test discs run under a reversal factor of 0.053, which represents the lowest reversal factor used and corresponds to 2000 cycles/reversal, were similar to those of the unidirectional test number 114, except that the crack line is slightly wavy, as shown in figure (7.9). All cracks studied during the present work were observed to originate from either a pit or a flake root. A summary of the different crack morphologies under conditions of different reversal factors is schematically represented in figure (7.10), which shows a braking elastic half space subjected to a driving load travelling in the x - y plane in the direction of the box arrows. $p(x)$ and $q(x)$ are the pressure and traction distributions, respectively, at a distance x from the centre of the contact. The arrows within the half space represent the direction of load movement under which the marked portion of the crack has propagated.

The relationship between the microhardness and the depth below the contact surface for the rail discs is shown in figure (7.11). It appears that reversal has no effect on the depth or magnitude of maximum hardening. Kopalinsky and Oxley⁽³⁾ showed that strain hardening is a function of the effective strain rather than the unidirectional strain. It seems that the number of rolling cycles during any of the tests was enough to cause maximum hardening. This is in agreement with the suggestion that most strain hardening takes place during the initial stages of the rolling-sliding process^(4,5).

Wear rates were measured at the end of each test and reported as weight loss/cycle. Similarly, diameter loss and track width gain are also presented. No significant trend could be found between reversal factor and these values since the total weight loss was negligible in all tests, between 0.035 and 0.055 g.

7.3. DISCUSSION

The results presented in the previous section suggest that rolling direction reversal has a beneficial effect on RCF life of pearlitic rail steel. They also indicate that reversal affects the morphology of RCF cracking.

Several researchers have indicated similar effects⁽⁶⁻⁸⁾. Fujita et al⁽⁶⁾ carried out oil lubricated rolling direction reversal experiments on carbon steel under a reversal regime of just a single reversal after varying number of cycles and reported significant improvements in RCF life.

Ichinose et al⁽⁷⁾ also indicated an extended fatigue life and suggested that if the rolling direction is reversed the cracks formed in the primary direction cease to propagate.

The mechanism by which the rolling direction reversal improves the RCF life may be better understood if it is possible to understand the effect of reversal on crack propagation. Crack propagation in unidirectional rolling has been the subject of considerable attention by researchers using the theory of fracture mechanics to study the stress field around the tip of a propagating RCF crack^(2,9-11). This has been discussed in chapter 6, where it has been shown that, if the rolling direction is reversed, the crack tip enters the contact pressure zone between the two discs before the mouth. In this case no fluid is expected to be trapped since the crack cavity is gradually closed starting from the crack tip, while the crack mouth is still open. As a result the RCF crack formed in the preceding rolling direction is not expected to propagate in mode I when the rolling direction is reversed. Similarly, in the absence of the lubricant, the compressive load will increase the frictional force between the two faces of the crack and will reduce the mode II propagation.

The implication of Bower's analysis⁽²⁾ was that the primary RCF crack would not divert or branch upon reversal of the rolling direction, nor would it grow significantly during the reversal period. In the present work, cracks have clearly demonstrated that they branch and continue to grow in a different direction to the primary crack during the reversal.

RCF cracks propagate in the braking part of rolling/sliding system in a 'preferential direction' which is the direction of the driving load movement as shown in figure (7.12). Upon reversal, many parameters in the stress cycle are affected.

7.3.1. The Variable Crack Face Friction Mechanism

The following descriptive mechanism is proposed to explain the crack propagation under rolling direction reversal conditions and will be referred to as *The Variable Crack Face Friction Mechanism*. No attempt will be made to explain the initiation or early propagation of the primary crack.

First, it is assumed that the primary crack propagates in the direction of load movement to a certain length during a certain cycle interval. Upon reversing the rolling direction, the crack tip will start to enter the Hertzian pressure dominated area before the mouth, leading to the gradual closure of the crack starting from the tip. The coefficient of the friction between the crack faces is expected to be at its maximum value nearest to the crack tip and to decrease gradually towards the crack mouth. Lower crack face friction nearer to the crack mouth can be explained by one or more of the following arguments:

- i. The lubrication effect of the residual fluid which is assumed to have entered the crack during the preceding rolling direction cycles.
- ii. Reduction of crack face surface roughness due to the plastic deformation of the crack faces caused by the rubbing action. Such a rubbing action was reported by Ichinose et al.⁽⁷⁾
- iii. The chemical changes of the crack surfaces caused by the exposure to the environment, notably oxidation. The role of oxidation in reducing the coefficient of friction, and subsequently the torque between the two discs during the running-in period, has been mentioned earlier in section 4.3.4. A similar effect of oxidation between the two faces of the crack has been reported by Kalousek⁽¹²⁾.

It is expected that the maximum effect of these actions will be in that part of the crack which is nearest to the mouth, since it is this part of the crack which has been subjected to a higher number of rolling cycles, is nearer to the surrounding environment and has a wider opening. This leads to the conclusion that freedom of the crack faces to slide relative to each other decreases with distance from the crack mouth. As a result, at a certain distance from the crack mouth, the crack is expected to lock up, and mode II propagation can no longer operate at the crack tip. The point of the crack corresponding to this lock up will be subjected to tensile stresses in a plane perpendicular to the direction of the relative motion between the two surfaces. This type of loading causes the crack to

branch from that point and to start propagation by mode I. This argument is supported by the work of Smith⁽¹³⁾, who tried to propagate mode II cracks while they were under compressive loading and found that under such conditions the crack branches to propagate in mode I.

In modelling the mechanism by which RCF cracks propagate, most workers assume a constant coefficient of friction over the whole crack length^(2,9-11). They also show that mode II crack propagation is very sensitive to crack face friction. Smith⁽¹³⁾ suggested that crack face friction is the main reason for mode II crack branching and that friction can lock up the crack tip and reduce the difference in mode II stress intensity factor (ΔK_{II}) to zero. Under such conditions, mode II crack growth will be arrested. If a mode II crack is arrested by friction, it would start to grow again only if a much higher load is applied after it had branched to mode I⁽¹⁴⁾. This may partially explain the improvement in life factor if the rolling direction is reversed.

The question remains as to how a particular reversal regime results in maximum RCF life. The effect of rolling direction reversal on crack initiation is beyond the scope of the present work and no attempt will be made to discuss this effect. Instead discussion will be focused on the effect of three reversal regimes on the RCF life according to the variable crack face friction mechanism. Tests with reversal factor of 0.053 and 0.5 represent two regimes below and above the optimum reversal factor of 0.267.

a. Reversal under a reversal factor of 0.053 (test number 121).

The crack morphology in this case is shown in figure (7.9) and schematically represented in figure (7.10b). Comparing this morphology with that of the unidirectional rolling crack of figure (7.5) reveals that the crack of the 0.053 reversal factor is not as straight as that of unidirectional rolling. It is suggested that the wavy shape of the crack in this case is due to the rolling direction reversal. According to the proposed crack propagation mechanism, the short reversal intervals were not enough to cause complete crack direction inversion or branching. Instead, it seems that the cycle reversal was being carried out just after the beginning of the crack direction diversion. These small diversions which are schematically shown in figure (7.10b), should slightly increase the angle of the crack to the free surface. However, the angle in this case is found to be slightly less than that of the unidirectional case shown in figure (7.10a). This behaviour can be explained by arguing that RCF crack observed under unidirectional rolling conditions do not keep an

exact prevailing propagation angle. This angle can vary slightly for tests conducted under the same conditions due to material microstructural heterogeneities.

The improvement in life factor in this case could be related to the arrest of mode II propagation by crack face friction during the cycle interval when the direction of the crack is opposite to that of the load movement. This action is supported by the work of Smith⁽¹³⁾, which has been mentioned earlier. The evidence clarifying crack propagation under a regime of reversals becomes clearer at larger reversal factors, as will now be discussed.

b. Reversal under a reversal factor of 0.267 (test number 115)

Figures (7.6) and (7.10c) show the crack of the maximum life factor, caused by a reversal factor of 0.267, which corresponds to 10000 cycles/reversal. It can be seen that the cracks in both the micrographs of figure (7.6) are of nearly an identical geometry. Each has diverted its direction by nearly 90 degrees in relation to the primary crack and then branched later in a direction parallel to the primary crack. This diversion and branching is thought to be caused by crack face friction variations as described earlier. The angle between the secondary branches and the free surface is bigger than that of the unidirectional crack shown in figure (7.5). The improvement in life factor in this case is greater than with a reversal factor of 0.053. In addition to the arrest of mode II propagation mentioned in *a* above, the large angle between the crack and the free surface also reduces both mode I and II stress intensities^(2,9-11). It seems that the cycle interval in this case was long enough to divert the crack in the first reversal after the crack initiation and branch it during the next reversal from a point nearer to the surface than the tip of the original crack. This branching point corresponds to the onset of the crack lock up where tensile stresses encourage branching under mode I. The new branch will consume a proportion of the cycle interval to merely reach the depth of the main crack (figure 7.10c).

The argument that RCF cracks such as those shown in figure (7.6) are hard to propagate and that rolling direction reversal arrests the cracks formed during a previous opposite rolling direction, is supported by the cracking morphology shown in figure (7.7) which shows two cracks of nearly the same angle to the surface but of opposite direction. This morphology suggests that only one crack - which is in the direction of load movement - is propagating during each cycle interval. If this were the only mechanism, such a cracking morphology should result in a life factor of 2. Figure (7.2) shows that at the optimum reversal factor between 0.267 and 0.375 this factor of 2 is almost reached,

indicating that there is little propagation of cracks which are not favourably oriented to the prevailing loading direction. This must apply whether the cracks are branching, as in figure (7.10 c1 & c2), or growing separately, as in figure (7.10 c3).

c. Reversal under a reversal factor of 0.5 (test number 116)

Figure (7.8) is a micrograph and figure (7.10d) a schematic representation of the cracking of a rail specimen tested under a reversal factor of 0.5, which corresponds to a change in rolling direction every 18711 cycles. It is noticed that the primary crack has propagated to a relatively deeper distance as a unidirectional RCF crack before it starts to branch from the tip. The large branch seen above the tip is not expected to be due to reversal. It may have taken place in a similar mechanism to that of the unidirectional crack branching shown in figure (7.5), since in both cases the branching is upwards. In addition, such a branch may cause a pit rather than a transverse defect. The branch at the tip is expected to be caused by the reversal. However, it seems that the cycle interval in this case was long enough to propagate the crack almost to failure. The failure appears to have been delayed by the reversal which, according to the proposed mechanism, arrested mode II propagation by the high friction at the crack tip before leading to mode I propagation. This may explain why the improvement in life factor in this case is not as large as for the optimum reversal strategy.

7.4. SUMMARY

To summarise, the different mechanisms by which RCF crack propagation is explained^(2,9-11,15) were found to be unable to predict the type of crack morphology and propagation prevailing under conditions of repeated rolling direction reversal.

The proposed variable crack face friction mechanism, discussed in part 3 above, predicts crack branching or direction inversion at the lock up point of the crack. In the reversed cycle interval, where the crack tip reaches the pressure zone before the mouth, the lock up point in the part of the crack which is nearest to the crack tip. Crack face friction rises from a minimum at the crack mouth to a maximum nearest to the tip, leading to each long crack having a slip and a stick crack face region. A crack locks up at the transition point between the two regions, giving rise to tensile stresses and encouraging mode I propagation in a direction perpendicular to the crack faces. The assumption that the crack face friction increases away from the mouth, rather than remaining constant as suggested by others⁽⁷⁻¹⁰⁾, has a sound foundation which has been discussed earlier.

Finally, it is expected that the variable crack face friction mechanism proposed in this chapter to explain the effect of rolling direction reversal, may be extended in future to explain the branching of unidirectional RCF cracks. However this beyond the scope of this project.

7.5. CONCLUSIONS

1. Rolling direction reversal has a beneficial effect on the RCF life of pearlitic rail steel. The life factor is almost doubled when the reversal is repeated in cycle intervals of 25% to 37% of the unidirectional RCF life.
2. Cracks formed in the preceding rolling direction do not cease their propagation upon reversal as predicted by the various RCF crack propagation mechanisms.
3. Cracking morphology is affected by the rolling direction reversal. The degree of this effect depends on the reversal factor.
4. The variable crack face friction mechanism can explain the improvement in rolling contact fatigue life under rolling direction reversal conditions
5. Rolling direction reversal has no effect on the magnitude or the location of maximum strain hardening. After a certain number of cycles, hardening reaches it peak and further cycling has no effect.

REFERENCES

1. S. Way, Pitting due to rolling contact, *Trans. ASME, Journal of Applied Mechanics*, Vol. 2, (1935), A49-A58.
2. A. F. Bower, The Influence of Crack Face Friction and Trapped Fluid on Surface Initiated Rolling Contact Fatigue Cracks, *Transactions of ASME, Journal of Tribology*, 110,(1988), 704-711.
3. E. M. Kopalinsky and P. L. Oxley, Investigation of the Deformation and Damage Sustained by a Wearing Surface in Sliding Metallic Contact, *Trans. ASME, J. Tribology*, 49, (1994), 1-6.
4. K. Fujita and Y. Yoshida, The Effect of Changing Rolling Direction on the Rolling Contact Fatigue Life of Annealed and Head Hardened Steel Rollers, *Wear*, 43, (1977), 315-327.
5. W. R. Tyfour, J. H. Beynon and A. Kapoor, The Steady State Wear Behaviour of Prealitic Rail Steel Under Dry Rolling-Sliding Contact Conditions, *Wear*, To appear.
6. K. Fujita and Y. Yoshida, The Effect of Changing Rolling Direction on the Rolling Contact Fatigue Life of Annealed and Head Hardened Steel Rollers, *Wear*. 43, (1977), 315-327.
7. H. Ichinose, J. Takehara , N. Iwasaki and M. Ueda, An Investigation on Contact Fatigue and Wear Resistance Behaviour in Rail Steels, *Heavy Haul Railway Conference, Perth, Australia*, Sept. (1987).-British Library Bound Copy.-,1-10
8. M Kaneta and Y. Murakami, Effect of Oil Hydraulic Pressure on Surface Crack Growth in Rolling/Sliding Contact, *Tribology International*, 20, (1987), 210- 217.
9. L. M. Keer and M. D. Bryant, A Pitting Model for Rolling Contact Fatigue. *Transactions of ASME, Journal of Lubrication Technology*, 105, (1983), 198-205.
10. D. A. Hills, A. Sackfield , and A. R. Uzel, Stress Concentration in Tractive Rolling, *Proceedings of the 12th Leeds-Lyon Symposium on Tribology*, Lyon, France. (1985), 171-177.
11. M. Kaneta, Y. Murakami and H. Yatsuzuka, Propagation of Surface Cracks in Rolling Line Contact, *Proceedings of the JSLE International Tribology Conference*,

Tokyo, Japan, (1985), 911-916.

12. J. Kalousek, General discussion, *Third International Conference on Contact Mechanics and Wear of Rail/Wheel Systems*, Cambridge, UK July, 1990. *Wear*, 144, (1991), 385-393.

13. E. W. Smith and K. J. Pascoe, The Behaviour of Fatigue Cracks Subjected to Biaxial stress: A Review of the Experimental evidence, *Fatigue Fracture of Engg Materials and Structures*, 6, (1983), 201-224.

14. P. E. Bold, M. W. Brown and R. J. Allen. A Review of Fatigue Crack Growth in Steels Under Mode I and Mode II Loading, *Fatigue Fracture of Engg Materials and Structures*, 15, (1992), 965-977.

15. M. Kaneta, H. Yatsuzuka and Y. Murakami, Mechanics of Crack Growth in Lubricated Rolling/Sliding Contact, *ASLE Transactions*, 28, (1985), 407-414.

Test conditions	Test number						
	113	114	115	116	119	120	121
Disc material Top (rail) Bottom (wheel)	BS11 W8A						
Rail disc orientation in relation to rail section							
Maximum contact pressure (MPa)	1500						
Percentage creepage (%)	1						
Lubrication	Water (one drip per second)						
Test speed (RPM) Rail/wheel	402/406						
Initial surface roughness, Ra (µm), Rail/wheel	0.38/0.47	0.38/0.39	0.28/0.37	0.32/0.33	0.20/0.21	0.20/0.19	0.21/0.32
Number of cycles per reversal (rail)	5000	37422 ^a	10000	18711	28066	14033	2000
Reversal factor ^b	0.133	1 ^a	0.267	0.5	0.75	0.375	0.0534

^a: Unidirectional test.

^b: Reversal factor is the ratio between the number of rolling cycles per reversal and the number of cycles to RCF failure during unidirectional rolling.

TABLE (7.1): TEST CONDITIONS

Test results	Test number								
	113	114	115	116	119	120	121		
RCF life (rail disc revolutions)	55000	37422	70000	52119	41365	69123	50980		
Life factor ^a	1.469	1.000	1.870	1.392	1.015	1.847	1.362		
Crack location (axial distance from the disc edge nearer to the drive shaft (mm))	3.7	4.5	4	5.2	5.7	4	5		
Maximum crack length (µm)	586	1226	276	920	n.m	920	908		
Average crack length (µm)	536.9	881	276	759	n.m	893	908		
Average crack depth (µm)	296	410	180	445	n.m	585	403		
Crack direction competition factor ^b	0.65	0.57	0.85	0.71	n.m	0.85	0.53		
End -of-test traction coefficient	0.132	0.112	0.123	0.125	0.125	0.132	0.148		

^a: Life factor is the ratio of the life cycles of the rail disc tested under reversal conditions and those obtained under unidirectional conditions.

^b: Crack direction competition (CDC) factor is the ratio of crack propagation length in the radial direction and that in the circumferential direction.

n.m: Not measured, specimen was damaged during sectioning

TABLE (7.2): TEST RESULTS

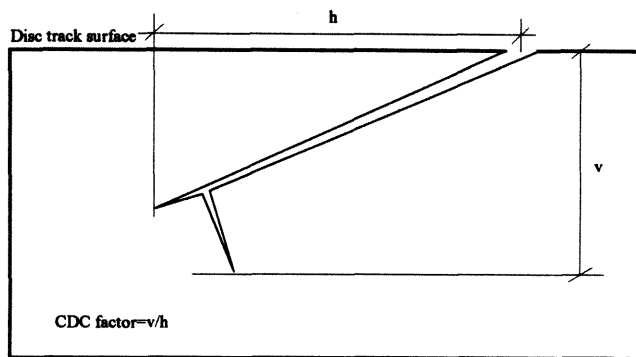


FIGURE (7.1): SCHEMATIC ILLUSTRATION OF THE DEFINITION OF CRACK DIRECTION COMPETITION FACTOR

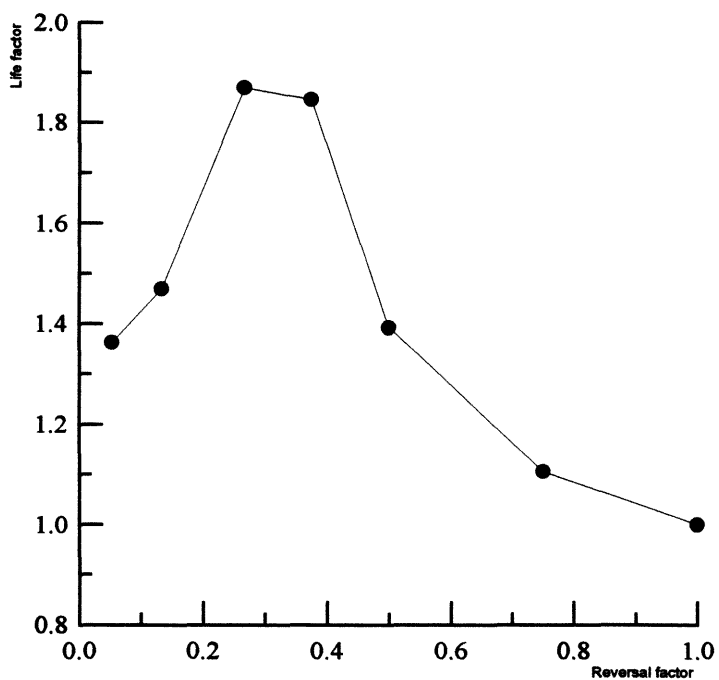


FIGURE (7.2): EFFECT OF ROLLING DIRECTION REVERSAL ON ROLLING CONTACT FATIGUE LIFE AS A RELATIONSHIP BETWEEN LIFE FACTOR AND REVERSAL FACTOR

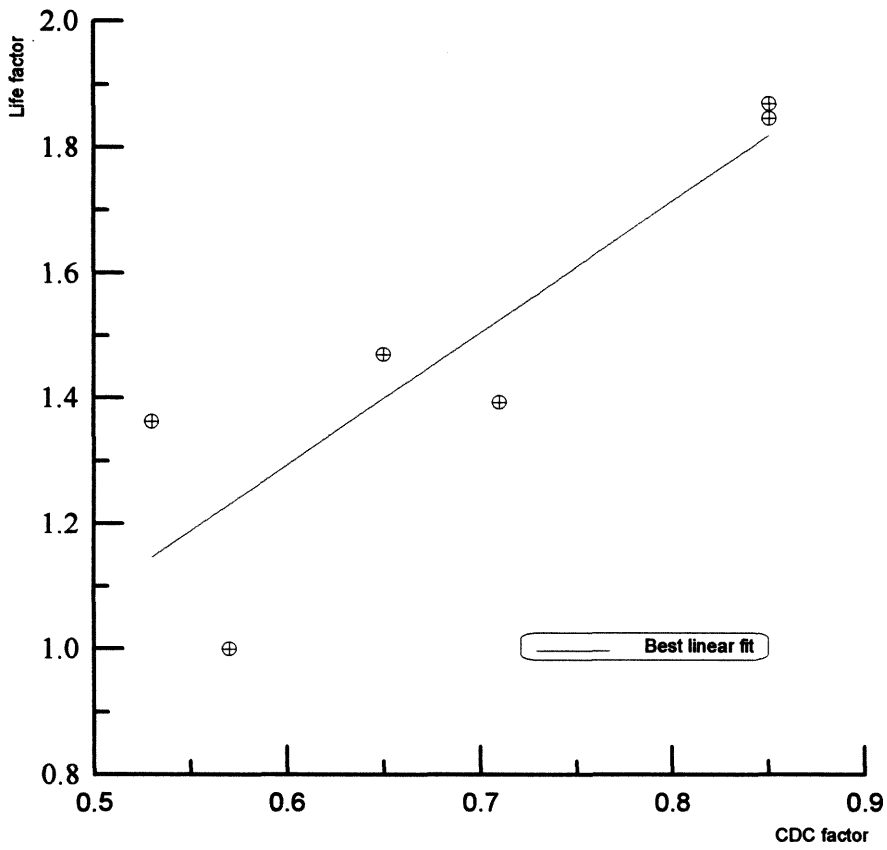


FIGURE (7.3): LIFE FACTOR AS A FUNCTION OF CRACK DIRECTION COMPETITION FACTOR

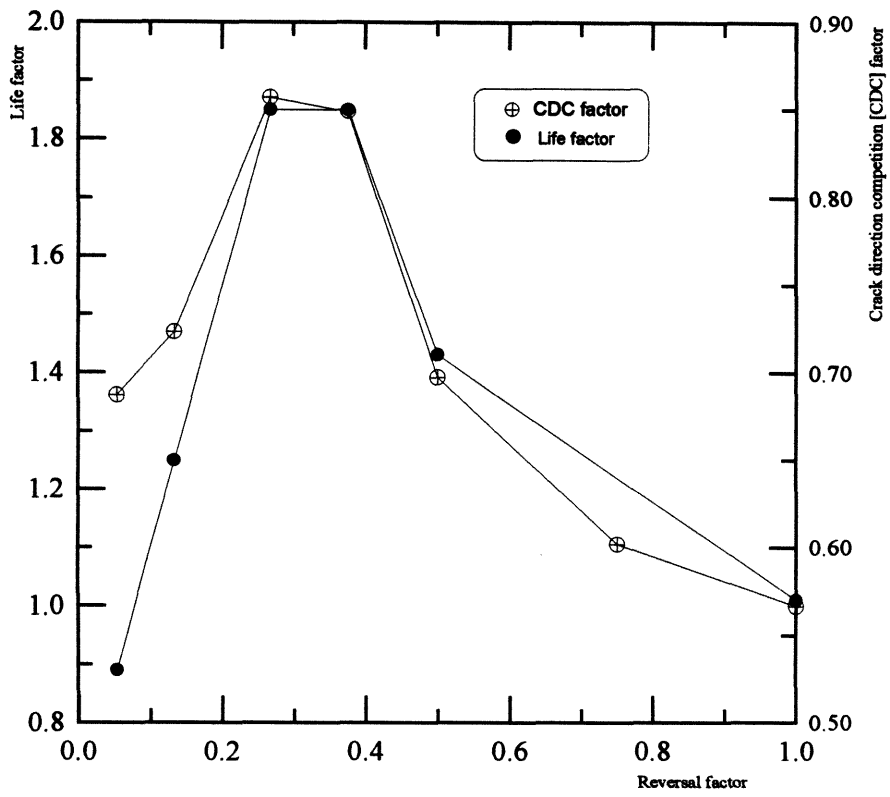


FIGURE (7.4): RELATIONSHIP BETWEEN REVERSAL FACTOR AND CRACK DIRECTION COMPETITION FACTOR

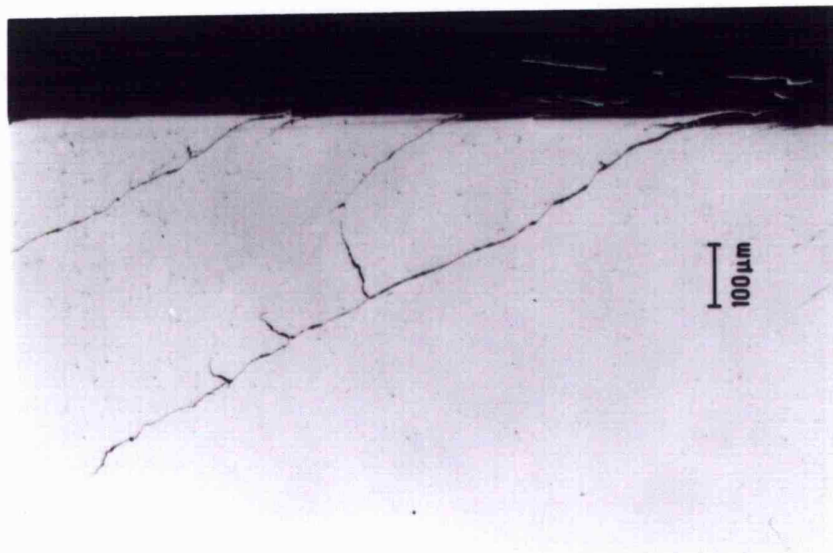
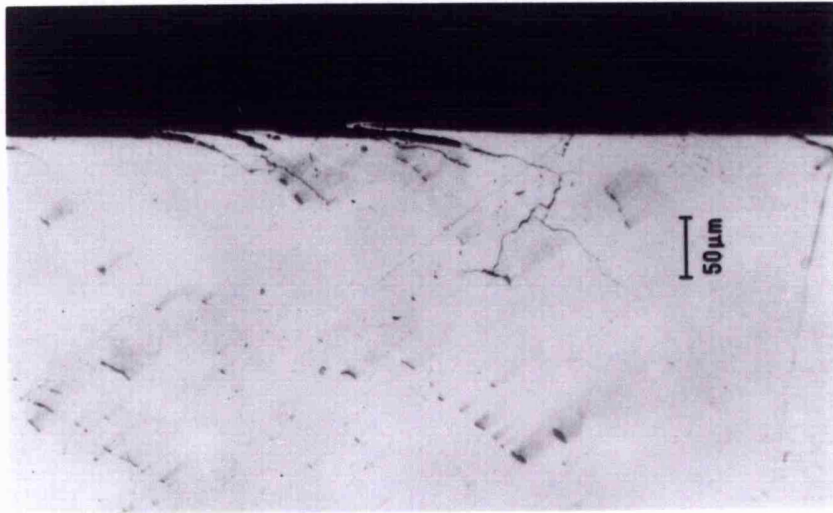
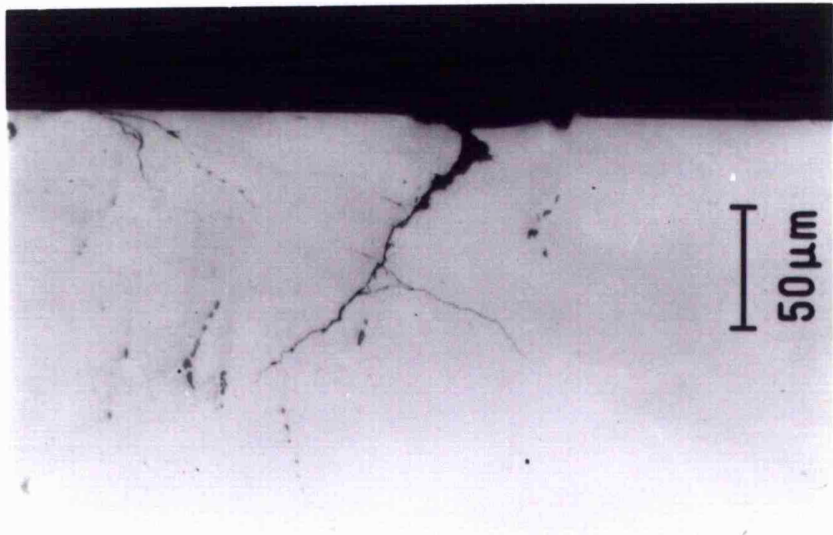


FIGURE (7.5): CRACKING MORPHOLOGY DUE TO UNIDIRECTIONAL ROLLING-SLIDING



(a)



(b)

FIGURE (7.6): BRANCHED TYPE RCF CRACKING UNDER A REVERSAL FACTOR OF 0.267, TEST NUMBER 115



FIGURE (7.7): DOUBLE RCF CRACKING UNDER A REVERSAL FACTOR OF 0.267, TEST NUMBER 115



FIGURE (7.8): RCF CRACKING UNDER 0.5 REVERSAL FACTOR, TEST NUMBER 116

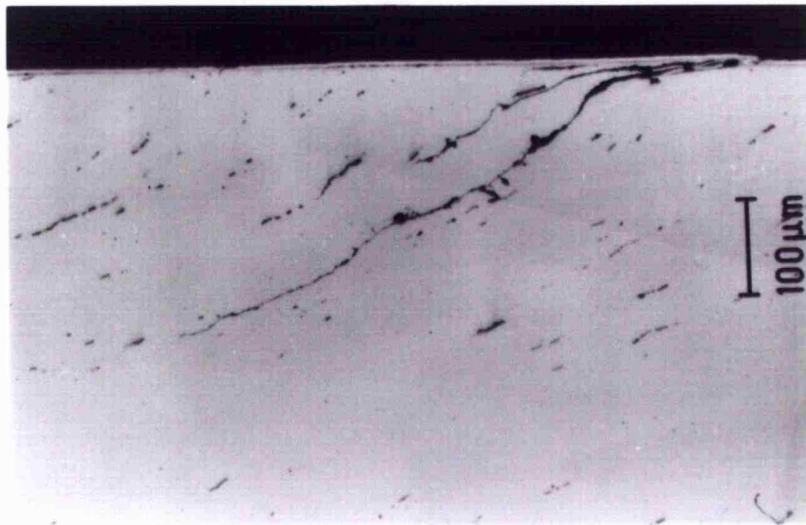


FIGURE (7.9): THE WAVY RCF CRACKING UNDER A REVERSAL FACTOR OF 0.053, TEST NUMBER 121

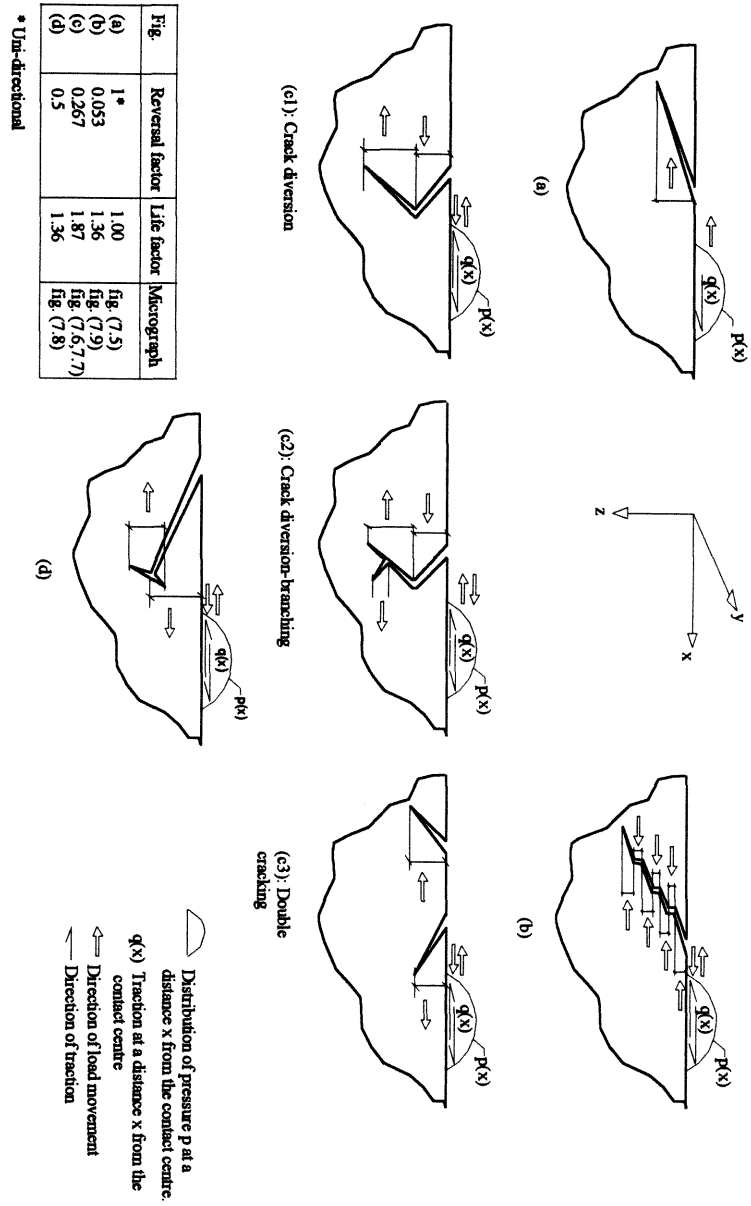


FIGURE (7.10): SCHEMATIC REPRESENTATION OF THE VARIOUS CRACKING MORPHOLOGIES DUE TO THE DIFFERENT REVERSAL REGIMES

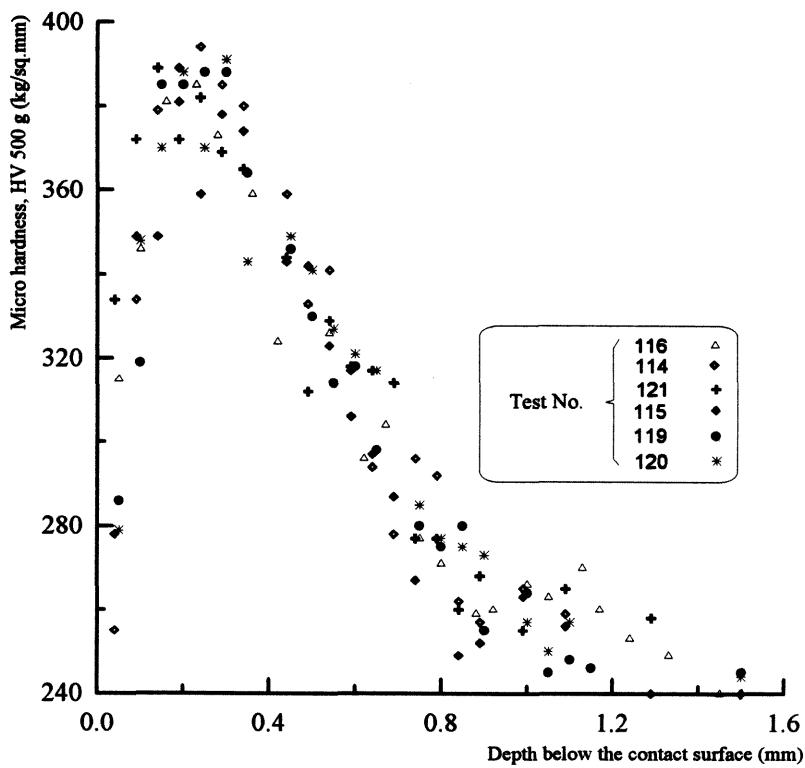


FIGURE (7.11): STRAIN HARDENING BELOW THE CONTACT SURFACE OF THE RAIL DISCS TESTED UNDER DIFFERENT REVERSAL REGIMES

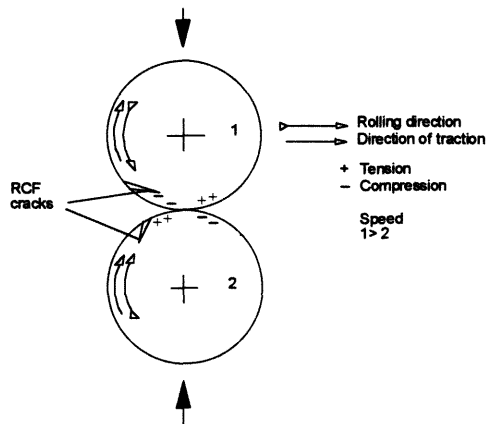


FIGURE (7.12): SCHEMATIC REPRESENTATION OF RCF CRACK DIRECTION OF PROPAGATION IN A ROLLING-SLIDING SYSTEM

Chapter 8

DETERIORATION OF ROLLING CONTACT FATIGUE LIFE OF PEARLITIC RAIL STEEL DUE TO DRY-WET ROLLING -SLIDING CONTACT

I. INTRODUCTION

In the previous four chapters wear and rolling contact fatigue of pearlitic rail steels have been independently investigated. Rail wear has been studied in chapters 4 and 5 under dry conditions, whereas, since the presence of liquid lubricant is essential for RCF cracks to propagate⁽¹⁻³⁾, this phenomenon has been studied in chapters 6 and 7, using water as a lubricant. The actual contact condition of the wheel/rail system is neither continuously dry nor permanently wet. The same piece of rail may see the two conditions many times a day, where some loading cycles caused by certain trains, or even wheels, are dry while the rest may be wet, then dry again and so on. Under such contact conditions, where the dominant deterioration during the dry stage is wear and during the wet phase is RCF, there may exist an interaction between the two forms of deterioration. This can lead to a very complicated deformed state. Since wet running induces lower surface traction, different stress levels are imposed at different locations, at or below the contact surface, under non-proportional and complicated cycling regimes. Conducting laboratory contact tests with such a range of variables can lead nowhere, since it becomes very difficult to isolate the effect of any particular parameter. The problem may be better approached by separating those variables and investigating the effect of either a single parameter or a properly selected combination of more than one.

Since the mechanical properties of the rail surface layer change continuously in wheel/rail contact, mainly due to strain hardening, a combination of dry-wet conditions may give different results if applied at different stages of the life span of the rail.

The effect of application of a liquid lubricant may have two effects: first, it reduces the coefficient of friction, and as a result shifts the maximum orthogonal shear stress $\tau_{zx(max)}$ to below the contact surface. The value of τ_{zx} at the surface is a function of the coefficient of friction μ . Second, the presence of the liquid lubricant in the contact area plays an important role in crack propagation.

It has been shown in chapters 4 and 5 that during dry rolling-sliding, ratchetting, which is sometimes referred to as incremental collapse, takes place at the contact surface if:

- a. the coefficient of traction is above 0.25, and
- b. the load exceeds the ratchetting threshold.

During the dry phase of a dry-wet rolling-sliding process ratchetting causes continuous removal of the surface layer. The effect of this damage and associated phenomena, such as strain hardening and accumulation of plastic strain, on RCF life of the driven (rail) disc will be investigated in this chapter. The study has been restricted to a simple combination of dry-wet rolling-sliding, where tests were run for a certain number of dry cycles, then continued under wet (water lubricated) conditions to failure by RCF.

The results may not be applicable to other dry-wet combinations or regimes, for example, conditions of wet-dry instead of dry-wet, or in the case of splitting the number of dry cycles among the wet phase. However, these results may represent a starting point for the investigation of more complicated dry-wet combinations.

The general test procedures were those described in chapter 3. Tests were run dry for different number of dry rolling-sliding cycles before they were continued wet (water lubricated) until RCF failure. BS11 rail steel have been tested against W8A wheel steel. Test conditions, as well as the orientation of the rail discs in relation to the rail section are shown in tables (8.1) for $p_0=1500$ MPa and (8.2) under $p_0=1200$ Mpa.

The work presented in this chapter has been a subject of a paper submitted for publication in *Wear*.

8.2. RESULTS

Test results under the two maximum contact pressures of 1500 and 1200 MPa are summarised in tables (8.1) and (8.2), respectively. RCF life is defined as the number of rail disc rolling-sliding cycles required to initiate a fatigue crack and propagate it to a certain depth below the contact surface, as detected in situ by the eddy current system.

The relationship between the number of initial dry cycles and RCF life for the two contact pressures used is shown in figure (8.1). This relationship is characterised by a significant and sudden drop in RCF life after a certain number of dry rolling-sliding cycles.

Under $p_o=1500$ MPa, the initial 100 dry cycles, test number 141, have resulted in an increase in RCF life, whereas a sharp and sudden drop in fatigue life, from 32382 to 15017 cycles, is observed when the initial dry phase was 500 cycles. Similarly, under $p_o=1200$ MPa the initial 100 dry cycles, test 148, have also resulted in an increase in the fatigue life. In contrast, the initial 200 dry cycles of test number 147 have led to a sudden drop in the fatigue life, from 119947 to 45837 cycles. Additional dry cycles caused additional deterioration in RCF life, as seen in figure (8.1).

It can be noticed that the initial dry cycling effect on the subsequent RCF life is characterised by three stages:

a: No deterioration (ignoring the increase in RCF life mentioned earlier): if the number of dry cycles is below a critical level.

b: A transition stage: which is characterised by a sharp and sudden drop in RCF life if the critical level of dry cycles is exceeded.

c: A severe effect stage: if the critical level of dry cycles is significantly exceeded.

8.2.1. Coefficient of friction

The Coulombic friction coefficient μ , which was calculated from the traction coefficient monitored during each test, was found to rise at the start of the dry phase to around 0.12, where it stabilised for a short period before it started to rise again. It reached a maximum value of around 0.48 after a certain number of dry cycles. This number varies from one test to another. After reaching its maximum, it gradually dropped again. The rate of drop falls with number of cycles. Similar behaviour has been observed by others^(4,5). Figure (8.2) shows a typical pattern for μ as a function of number of dry rolling-sliding cycles. During the initial wet cycles, the behaviour resembled that during the initial dry cycles of the test. However, the maximum coefficient of friction during the wet phase was much lower. The numbers of cycles where μ exceeded 0.25, invariably in the dry phase, was also recorded, since it is this value above which the maximum orthogonal shear stress $\tau_{zx(\max)}$ occurs at the surface⁽⁶⁾. This number of cycles was also found to be different for different tests because of the varying time taken to reach the high friction level at the start of the test, and not just because of the diverse total number of cycles.

Three values of the coefficient of friction μ are reported in tables (8.1) and (8.2). First, μ_{\max} which represents the maximum value during the dry phase of the test. Second,

the effective coefficient of friction μ_{eff} , defined as the average during N_{eff} , where N_{eff} is the number of dry cycles when μ is greater than 0.25. For example, if the total number of initial dry cycles is 500 and μ is less than 0.25 during the first 200 cycles, then N_{eff} is 300 cycles. Finally, the coefficient of friction at the end of the wet phase, and thus at the end of the test, μ_{fin} , is also reported.

8.2.2. Hardness below the contact surface

Figure (8.3) shows the strain hardening behaviour below the contact surface of the rail disc under different dry-wet cycling regimes with $p_0=1500$ MPa. It can be seen that the maximum hardening (as a percentage of the undeformed, bulk hardness) is below the surface for all tests where the initial dry cycles are fewer than 500 cycles. For a higher initial number of dry cycles there is a maximum at the surface. Only under conditions of 500 initial dry cycles are there two maxima, surface and subsurface. Similar hardening behaviour was observed under $p_0=1200$ MPa. In both cases the maximum surface hardness appears to be a function of number of dry cycles where μ_{eff} is greater than 0.25. This implies that during the earliest dry cycles, where μ is less than 0.25, strain hardening will not peak at the surface.

8.3. DISCUSSION

8.3.1. A physical model

At the start of the test (dry) the friction coefficient is low, figure (8.2), and the maximum of the orthogonal shear stress $\tau_{zx(\text{max})}$ occurs below the surface. The shakedown limit (p_0/k) for a coefficient of friction of 0.1 is greater than 3. The operating maximum pressures of 1500 and 1200 MPa are above this shakedown limit and lead to plastic flow and accumulation of strain in the direction of the friction force. As a result the material work hardens, figure (8.3). Further dry cycling causes the friction coefficient to increase and when it exceeds 0.25 the maximum orthogonal shear stress occurs at the surface. A thin surface layer accumulates plastic strain and hardens up. The change in friction coefficient and the resulting moving up to the surface of $\tau_{zx(\text{max})}$ causes hardening at the surface as well as below it, figure (8.3) (500 dry cycles). It must be stressed, though, that these hardness profiles are after the subsequent wet cycles. The wet phase produces the bulk of the subsurface hardening since the number of cycles is much greater than the few early dry cycles at a friction coefficient below 0.25. Continuing to run dry at $\mu > 0.25$

produces a dominant surface hardening curve with its maximum at the surface (2000 dry cycles, figure (8.3)). The subsurface hardness for the test with 2000 dry cycles is lower than the other hardness curves since it has had far fewer subsequent wet cycles (a mere 564 cycles, table (8.1)); it is the wet phase - at low friction - which produces the bulk of the subsurface hardening.

The effect of accumulation of plastic strain can now be considered. Naturally the material cannot keep accumulating strain indefinitely^(7,8). Kapoor⁽⁹⁾ has shown that the material will fail after accumulating a critical plastic strain, a failure termed ratchetting failure. This failure manifests itself in the form of small surface cracks⁽⁹⁾. Further dry cycling results in propagation of these cracks.

When wet rolling is then started the fluid pressure mechanism of crack propagation, as suggested Way⁽¹⁾ and analysed by Bower⁽¹⁰⁾, will come into play.

A physical model to describe the effect of dry cycling on the subsequent RCF life is schematically illustrated in figure (8.4). Dry cycling under a coefficient of friction higher than 0.25 will cause ratchetting of the surface layer, provided the ratchetting threshold load is exceeded, figure (8.4a). When the accumulated plastic strain reaches a critical value, in relation to the size of the contact patch, surface cracks will initiate, figure (8.4b). Further cycling will propagate these cracks to a critical length, figure (8.4c). The nature of these critical values will be discussed later.

Upon application of the fluid lubricant, at the start of the wet phase, liquid enters the crack cavity, figure (8.4d). The approaching loaded contact closes the crack mouth, raising the pressure of trapped fluid and causing mode I crack propagation⁽¹⁰⁾, figure (8.4e). When the maximum load passes the crack mouth the pressurised fluid escapes from the crack cavity to lubricate the crack faces, causing mode II crack propagation, figure (8.4f). Since the two discs in a rolling-sliding test experience different permutations of the rolling and sliding directions, it is in the driven (rail) disc that cracks are formed in a direction which allows the fluid pressurisation effect to occur. The driving (wheel) disc has cracks (if at all - the stress state is not conducive to crack formation) oriented in the other direction such that the approaching loaded contact squeezes the root of the crack before the mouth. Bower's proposed mechanism for fluid pressurisation and crack face friction⁽¹⁰⁾ has been extended by Tyfour and Beynon by introducing the variable crack face friction mechanism⁽¹¹⁾. An attempt will now be made to quantify this physical model, in particular

the pivotal role of ratchetting.

8.3.2. The role of ratchetting

In rolling-sliding contacts, the amount of ratchetting is a function of the coefficient of friction μ^* , the maximum contact pressure p_o , number of cycles, and the shear yield strength of the material k . In the present work p_o is treated as constant^{**}. However, μ changes with number of cycles as described earlier and illustrated in figure (8.2). The shear yield strength of the surface layer also changes according to the strain hardening behaviour of the material.

To assess the degree of surface layer ratchetting due to a certain number of dry cycles, it is necessary to know the number of effective cycles N_{eff} and μ_{eff} , as defined earlier, and then to find k_{eff} which is the average value of k during the effective cycles. The next step is to find the shakedown limit, and then to calculate the effective ratchetting load, as shown later.

In a previous study⁽⁷⁾, also in chapter 4, the strain hardening behaviour of the pearlitic rail steel used in this work has been studied under dry rolling-sliding conditions identical to those shown in table (8.2). A set of hardening curves showing the relationship between hardness, depth below the contact surface and number of dry cycles has been produced, see figure (4.6) in chapter 4. From those curves a relationship between "surface" hardness, measured at 0.05 mm below the surface, and number of cycles could be obtained for $p_o=1500$ MPa. This relationship is shown in figure (8.5). (The depth 0.05 mm has been chosen since trying to measure hardness nearer to the surface, where metal can break away during indentation testing, is prone to error⁽⁸⁾.)

Knowing that k_{eff} is a linear function of hardness⁽¹²⁾, it becomes possible to find k_{eff} during any number of cycles by:

$$k_{\text{eff}} = k_o (H_{\text{eff}}/H_o) \quad (8.1)$$

* If μ is greater than 0.25 ratchetting starts after elastic behaviour without a plastic shakedown stage.

** If the elastic shakedown limit is exceeded the material deforms plastically and the actual contact area and, as a result, the maximum contact pressure would be different from those calculated using the Hertzian elastic analysis. However, allowing for this is beyond the scope of this work.

where k_0 is the shear yield strength of the unstrained material, H_{eff} is the average hardness during the effective dry cycles N_{eff} , and H_0 is bulk hardness of the undeformed material. For $p_0=1200$ MPa, it is assumed that hardening is directly proportional to the contact pressure, so that k_{eff} for $p_0=1200$ MPa is equal to k_{eff} for $p_0=1500$ MPa multiplied by the factor 1200/1500. This assumption is reasonable if the difference between the two contact pressures is small and the number of cycles involved is also relatively small.

It is now possible to calculate p_0/k_{eff} , which is here called the effective ratchetting load P_{eff} , a normalised quantity. In this case p_0 is the maximum contact pressure and k_{eff} is the effective shear yield strength, found from equation (8.1) by substituting for H_{eff} the value of the hardness corresponding to the number of effective dry cycles N_{eff} . Using the shakedown map of two elastically similar cylinders rolling with partial slip, suggested in Hills et al⁽¹³⁾, the plastic shakedown limit, P_s , corresponding to μ_{eff} can also be found.

By subtracting the shakedown limit P_s from the effective ratchetting load P_{eff} , it becomes possible to estimate the severity of loading above the plastic shakedown limit at the contact surface, named here P_r ;

$$P_r = P_{\text{eff}} - P_s \quad (8.2)$$

It is this measure of the severity of loading above the ratchetting threshold which will dictate the rate of plastic deformation by ratchetting: the higher is P_r , the greater is the plastic deformation per cycle.

Since the strain hardening is accounted for in calculating the effective ratchetting loads P_{eff} , ratchetting as accumulated unidirectional plastic strain, referred to here as Rd , becomes a linear function of the net ratchetting load P_r and the number of cycles at that load N_{eff} :

$$Rd = c (P_r) N_{\text{eff}} = c (P_{\text{eff}} - P_s) N_{\text{eff}} \quad (8.3)$$

The constant c in equation (8.3) is independent of stress. It represents the conversion factor of net ratchetting load, taking into consideration the number of cycles run at that load, to ratchetting strain. The total shear strain (ratchetting) is measured as $\tan \gamma$. In this case γ is the angle of the deformed structure measured at 0.05 mm below the contact surface, see figure (8.6) for illustration. The constant c can be evaluated empirically by plotting the relationship between the net ratchetting load P_r multiplied by the number of cycles at that load N_{eff} and the total ratchetting shear strain, as shown in figure (8.7). A

linear relationship has been assumed, not unreasonably. From the plot of figure (8.7), the value of c is 0.00237. Substituting in equation (8.3), we obtain:

$$Rd = 0.00237 (P_v) N_{\text{eff}} \quad (8.4)$$

Figure (8.8) is a schematic representation of the definition of k_{eff} , μ_{eff} and N_{eff} and the method of finding P_s , P_{eff} and P_r , described above.

Figure (8.9) shows the relationship between the total accumulated strain Rd and RCF life. This relationship shows an interesting transition (sudden drop) in the fatigue life if this ratchetting strain rises above zero. However, it is expected that this transition takes place after a certain amount of ratchetting, which is enough to initiate a surface crack and propagate it to a certain length. The exact number of dry cycles to cause this amount of ratchetting lies between 100 and 200 cycles for $p_o=1200$ MPa and between 200 and 500 cycles for $p_o=1500$ MPa, as seen in figure (8.1). To locate the transition cycles more precisely, more experiments under initial dry cycles between 100 and 500 cycles would be needed.

It can be noticed that the first two points of both the plots in figure (8.9) lie on the y axis. This indicates that for those points Rd is zero since μ never rose above 0.25.

The role of ratchetting in the wear mechanism and the initiation of surface cracks in pearlitic rail steel have been discussed earlier in chapters 4 and 5, where it has been shown that surface failure takes place if the surface layer accumulates unidirectional plastic strain higher than the critical strain to failure^(7,8). If, after those cracks initiate and propagate to a certain length, a fluid lubricant is applied to the contact area, the coefficient of friction will drop to less than 0.2, resulting in a shift in the maximum shear stress $\tau_{zx(\text{max})}$ to below the contact surface. Meanwhile, the trapped fluid mechanism of crack propagation⁽¹⁰⁾ will be triggered and RCF failure will take place after a certain number of wet rolling-sliding cycles. This number of cycles to failure depends on the size of the crack prior to the application of the liquid lubricant. Since most of the fatigue life is consumed in initiating the crack, rather than propagating it, the effect of the ratchetting stages in initiating the crack is expected to cause a significant drop in RCF life. This is better revealed in figure (8.10), where ratchetting due to the two contact pressures used is plotted against the drop in RCF life. It is interesting to note that the same degree of ratchetting caused by different combinations of contact stresses, degrees of hardening and coefficients of friction, caused the same percentage reduction in RCF life. Regression analysis of the data shows that it fits

an equation of the form:

$$\% \text{ drop in RCF life} = 53(Rd)^{0.49} \quad 0 < Rd < 3 \quad (8.5)$$

which can be simplified to:

$$\% \text{ drop in RCF life} = 53(Rd)^{0.5} \quad 0 < Rd < 3 \quad (8.6)$$

This equation enables prediction of the deterioration of RCF due to any degree of ratchetting strain caused by any initial dry cycling regime up to a value of about 3, beyond which the drop in RCF life asymptotes near to 100% reduction compared with no dry cycles.

The same equation can be written in terms of P_r and N_{eff} using equation (8.4), to give:

$$\% \text{ drop in RCF life} = 2.74 \{(P_r/N_{eff})\}^{0.5} \quad (8.7)$$

Equations (8.6) and (8.7) represent two routes to calculate the percentage drop in RCF life due to initial dry cycling. Equation (8.6) represents the percentage deterioration in RCF fatigue in terms of accumulated unidirectional plastic strain (ratchetting), whereas equation (8.7) gives this deterioration in terms of net ratchetting load and number of cycles run at that load. Equation (8.7) is more convenient to use since it does not require the estimation of the accumulated plastic strain, rather it uses operating conditions.

8.3.3. The effect of dry-wet cycling

The difference between dry and wet rolling-sliding can be discussed from two main viewpoints:

a. The different coefficient of friction between the two cases and its subsequent effect on the location and the value of $\tau_{zx(max)}$ and, as a result, the effect on the plastic shakedown limit and the net ratchetting load discussed earlier.

b. The presence of the liquid lubricant in the contact area during wet rolling-sliding, which is essential for crack propagation.

The difficulty in studying the ratchetting behaviour under rolling-sliding conditions arises from the continuous change in the shear yield strength of the material, mainly due to strain hardening. This difficulty has lead researchers to tackle the problem by introducing assumptions and simplifications. Bower et al⁽¹⁴⁾ assumed elastic, perfectly plastic behaviour. Ham et al⁽¹⁵⁾ have idealised the problem by assuming a bilinear stress strain

hysteresis loop referred to as elastic-linear-kinematic-hardening-plastic (ELKP) behaviour. The method described here uses the actual hardening behaviour of the material.

The effect of plastic deformation on the subsequent RCF life has been observed by many researchers. These observations can be summarised by the following:

1. Higher rates of RCF failure are noticed on the gauge corner of curved tracks where plastic deformation, due to the wheel flange forces, is higher⁽¹⁶⁾. Equation (8.7) accords with this type of behaviour, since P_{eff} , and subsequently P_r , is higher in case of higher flange forces.

2. The roundness profiles of the discs recorded after failing by RCF show greater plastic deformation in the cracked area, see figure (8.11). This is evidence that even for the same disc, areas of higher ratchetting strain fail first. This can also be predicted. Substituting a higher value for Rd in equation (8.6) results in a larger drop in RCF life. The reasons for different ratchetting levels at different locations on the disc surface could be related to localised material or microstructural defects, such as inclusions or variation of interlamellar pearlitic spacing.

3. The RCF life of the driving (wheel) disc is higher than that of the driven (rail) disc⁽¹⁷⁾. Ratchetting initiated surface cracks on the driving disc cannot propagate by the trapped fluid mechanism since the crack root in this case enters the contact area before the mouth. This prevents the fluid from entering the crack cavity.

4. Head-hardened rails, which have higher shear yield strength k_o , resist crack initiation⁽¹⁸⁾. Higher k_o means lower P_r in equation (8.7). Confirmation that higher k_o is of beneficial effect on RCF life under dry-wet rolling sliding contact can be achieved by testing a rail disc where hardness changes across the disc circumference. Since hardness, and as a result k_o , changes with depth below the MHT rail surface, as shown in figure (3.8) of chapter 3, a disc machined from such rail with its axis parallel to the rail long axis, as seen in table (8.2) can serve the purpose. As expected, test number 153, which has been run dry for 750 cycles, failed by RCF from the location of minimum hardness corresponding to the part of the disc which is nearer to the rail web.

5. Earlier crack initiation has been observed under conditions of higher contact stresses⁽¹⁹⁾. The effect of P_o on the value of P_r in equation (8.7) is obvious.

6. In pure rolling contacts, where μ_{eff} is low, RCF life is exceedingly high⁽²⁰⁾. Lower

μ_{eff} means higher Ps in equation (8.7) and consequently higher RCF life.

7. Grinding the contact surface to remove the plastically deformed layer and the possible surface initiated cracks has proved to be an effective measure in reducing the rate of occurrence of RCF failures. Preventive rail grinding is a well established maintenance technique⁽²¹⁾. Zaretsky⁽²²⁾ reported extended life of rolling elements of bearings due to grinding away a thin surface layer. Clearly, removal of material which has accumulated plastic strain by ratchetting restores the surface to its original state. However, it should be stressed here that surface removal by grinding differs from surface removal by wear. Grinding removes partially or completely the layer which has accumulated ratchetting strain, whereas removal of the surface layer by wear maintains maximum ratchetting strain at the surface. This argument is schematically illustrated in figure (8.12) which shows the effect of removal of the same thickness of material from the contact surface by grinding, figure (8.12a), and by wear, figure (8.12b).

9. The morphology of the dry-wet RCF crack mouth, which represents the initiation stage, is similar to that of the flake root observed under dry rolling conditions, see figure (8.13). This may indicate that the two cracks are initiated by the same ratchetting mechanism.

The increase in RCF life due to a low number of dry cycles, noticed in figure (8.1), is difficult to explain. It could be due to the compact oxide layer formed at the surface prior to application of the water lubricant and the reduction in surface roughness associated with the appearance of this layer.

To summarise, the mechanism by which initial dry cycling causes deterioration in RCF resistance appears to be ratchetting damage to the surface layer. If this ratchetting exceeds a certain level, it initiates surface cracks which, during the wet phase, propagate to cause RCF failure. The degree of ratchetting is governed by the maximum contact pressure, the hardening properties of the material, the effective coefficient of friction and the effective number of dry cycles. A certain degree of ratchetting above the threshold level, caused by any combination of these factors, results in the same percentage reduction in RCF life.

8.4. CONCLUSIONS

1. In pearlitic rail steel initial dry cycling above a certain number has a negative effect on the subsequent RCF life of the driven body in a rolling-sliding contact system. This

effect is a function of the degree of ratchetting above a critical level.

2. The earliest dry cycles, where μ is less than 0.25, do not cause deterioration in RCF life.

3. The coefficient of friction during the earliest dry cycles of a dry-wet cycling regime has a significant effect on the subsequent RCF life.

4. The role of initial dry cycling in RCF life deterioration can be explained using the ratchetting argument (exhaustion of ductility) and the subsequent formation of surface cracks, which can propagate during the wet stage according to the trapped fluid mechanism.

5. Using the hardening behaviour of the material enables accurate assessment of the effective shear yield strength during any number of rolling-sliding cycles.

6. It is possible to estimate the deterioration in RCF life due to any regime of initial dry cycling using equation (8.6) or (8.7).

REFERENCES

1. S. Way, Pitting due to rolling contact, *Trans. ASME, Journal of Applied Mechanics*, Vol. 2, (1935), pp A49-A58.
2. Keer L M and Bryant M D. A Pitting Model for Rolling Contact Fatigue. *Transactions of ASME, Journal of Lubrication Technology*, 105, (1983), 198-205.
3. M. Kaneta, Y. Murakami and H. Yatsuzuka, Propagation of surface cracks in rolling line contact, *Proceedings of the JSLE International Tribology Conference*, Tokyo, Japan, (1985), 911-916.
4. H. Krause and H. Demirci, Factors Influencing the Real Trend of the Coefficient of Friction of Two Elastic Bodies Rolling Over Each Other in Presence of Dry Friction, *The Mechanics of Contact Between Deformable Bodies* (1975), Delft University Press, Eds. A. D. Pater and J. J. Kalker.
5. A. F. Bower and K. L. Johnson, The Influence of Strain Hardening on Cumulative Plastic Deformation in Rolling and Sliding Line Contact, *J. Mech. Phys. Solids*, 37, 4 (1989) 471-493.
6. K. Zum Gahr, *Microstructure and Wear of Materials*, Tribology Series, 10, Elsevier, (1987).
7. W. R. Tyfour, J. H. Beynon and A Kapoor, The Steady State Wear Behaviour of Pearlitic Rail Steel Under Dry Rolling-Sliding Contact Conditions, *Wear*, 180, (1995), 79-89.
8. W. R. Tyfour and J. H. Beynon, The Effect of Rolling Direction Reversal on the Wear Mechanism of Pearlitic Rail Steel, *Tribology International*, 27, 6, (1994), 401-412.
9. A. Kapoor, A Re-evaluation of the Life to Rupture of Ductile Metals by Cyclic plastic Strain, *Fatigue Fract. Engng. Mater. Struct.*, 17, 2 (1994) 201-219.
10. A. F. Bower, The Influence of Crack Face Friction and Trapped Fluid on Surface Initiated Rolling Contact Fatigue Cracks, *Trans. ASME, J. of Tribology*, 110 (1988) 704-711.
11. W. R. Tyfour and J. H. Beynon, The Effect of Rolling Direction Reversal on Fatigue Crack Morphology and Propagation. *Tribology International*, 27, 4, (1994), 273-

282.

12. J. F. Archard, Wear Theory and Mechanisms, in Wear Control Handbook, ASME, (1980), Eds. M. B. Peterson and W. O. Winer, 35-80.

13. D. A. Hills, D. Nowell and A. Sackfield, *Mechanics of Elastic Contacts*, Butterworth Heinemann, 1993.

14. A. F. Bower, K. L. Johnson and J. Kalousek, A Ratchetting limit for plastic Deformation of a Quarter-Space Under Rolling Contact Loads, *Proc. of the Second Intl. Symp. on Contact Mechanics and Wear of Rail/Wheel Systems*, University of Waterloo Press, (1987) 117-131.

15. G. L. Ham, G. T. Hahn, C. A. Rubin and V. Bhargava, Finite Element Analysis of the Influence of Kinematic Hardening in Two-Dimensional Repeated Rolling-Sliding Contact, *STLE Tribology Transactions*, 32, 3 (1989) 311-316.

16. R. Steele, The Effect of Metal Removal, Steel Cleanliness and Wheel Load on the Fatigue Life of rail, *Wear*, 144 (1991) 71-87.

17. J. H. Beynon, J. E. Garnham and K. Sawley, Rolling Contact Fatigue of Four Pearlitic Rail Steels, I: Early Crack Formation, To appear.

18. V. Dikshit, P. Clayton and D. Christensen, Investigation of Rolling Contact Fatigue in Head Hardened Rail, *Wear*, 144 (1991) 89-102.

19. P. Clayton and D. Hill, Rolling Contact Fatigue of a Rail Steel, *Wear*, 117 (1987) 319-334.

20. K. Hirakawa, K. Toyama and M. Yamamoto, Fundamental Study of Shelling in Railway Wheel Materials, *Proc. of the 8th Intl. Wheelset Congress, Madrid, Spain* (1985) 4/1-4/14.

21. J. Kalousek and J. Ignemezie, Shell-Like Defects and Microgeometry of Grinding, *Proc. of The Intl. Conf. on Rail Steel-Development, Manufacture and Performance*, Pub. G. Kuhn (1992) 139-145.

22. E. V. Zaretsky, Effect of Surface Removal on Rolling Element Fatigue, *Proc. of the Intl. Conf. on Tribology-Friction, Lubrication and Wear, Fifty Years on*, Proc. of I Mech E, C147/87 (1987) 829-838.

Test conditions and results	Test Number				
	114	141	143	140	142
Disc material : Rail/ Wheel	BS11/W8A				
Orientation of rail disc specimen in relation to rail section					
Initial surface roughness (Ra) : Rail/Wheel	0.38/0.39	0.36/0.40	0.27/0.41	0.36/0.49	0.30/0.52
Max. Contact pressure (MPa)	1500				
Percentage creepage : Rail disk (%)	-1				
Test speed (RPM)	402/406				
Contact area (mm ²)	11.35				
No. of initial dry cycles (Rail revs)	0	100	200	500	2000
Lubrication during the wet phase	water				
RCF life ⁽¹⁾	37422	45088	32382	15017	2564 ⁽²⁾
Coefficient of traction : Max. during dry phase μ_{max}	-----	0.175	0.256	0.387	0.450
	-----	-----	-----	0.35	0.42
	-----	0.137	0.105	0.137	0.17
At the end of the test μ_{en}	0.125				

⁽¹⁾: Including the initial dry cycles.
⁽²⁾: Eddy current signal was beyond the failure level just after the dry phase. However test continued for another 564 cycles to ensure a sustainable signal.

TABLE (8.1): TEST CONDITIONS AND RESULTS FOR $p_c = 1500$ MPa

Test conditions and results		Test Number						
Disc material : Rail/Wheel	144	148	147	146	145	153		
Orientation of rail disc specimen in relation to rail section								
Initial surface roughness (Ra): Rail/Wheel	0.44/0.47	0.24/0.28	0.23/0.31	0.27/0.24	0.37/0.36	0.19/0.45		
Max. Contact pressure (MPa)	1200							
Percentage creepage : Rail disk (%)	-1							
Test speed (RPM)	402/406							
No. of initial dry cycles (Rail revs)	0	100	200	500	1000	750		
Lubrication during the wet phase	water							
RCF life ⁽¹⁾	96897	119947	45837	27119	8787	40706		
Coefficient of traction : Max. during dry phase μ_{max}	-----	0.247	0.447	0.497	0.483	0.441		
: Effective μ_{eff}	-----	-----	0.38	0.45	0.44	0.37		
: At the end of the test μ_{fin}	0.115	0.115	0.125	0.125	0.140	0.140		

⁽¹⁾: Including the initial dry cycles.

TABLE (8.2): TEST CONDITIONS AND RESULTS FOR $p_o = 1200$ MPa

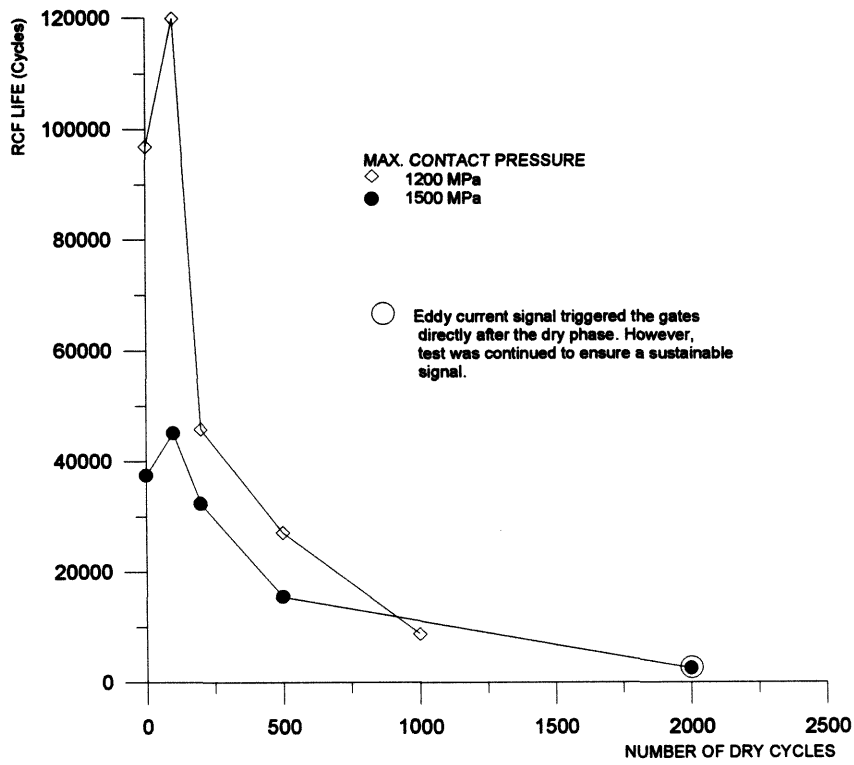


FIGURE (8.1): EFFECT OF INITIAL DRY CYCLING ON THE SUBSEQUENT RCF LIFE

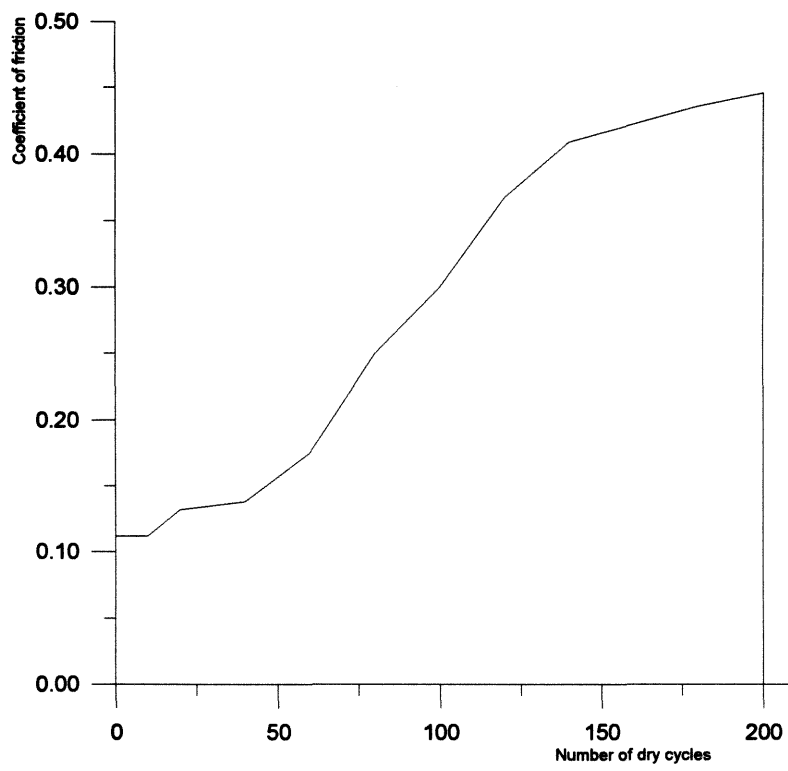


FIGURE (8.2): COEFFICIENT OF FRICTION EVOLUTION WITH NUMBER OF DRY CYCLES (TEST NUMBER 147)

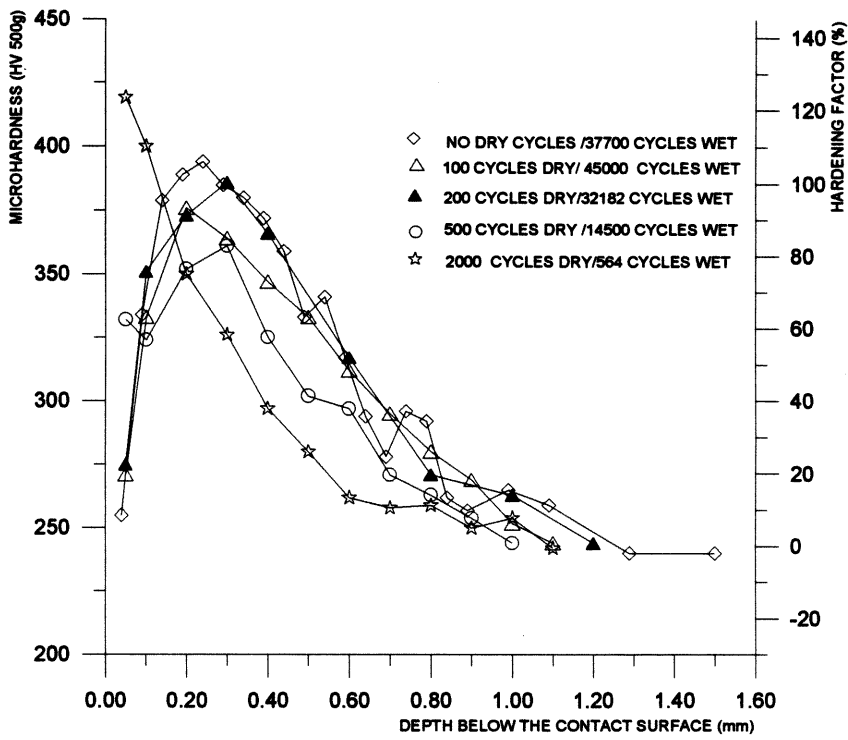


FIGURE (8.3): STRAIN HARDENING DUE TO DIFFERENT DRY-WET ROLLING-SLIDING REGIMES AT $P_0 = 1500$ MPa

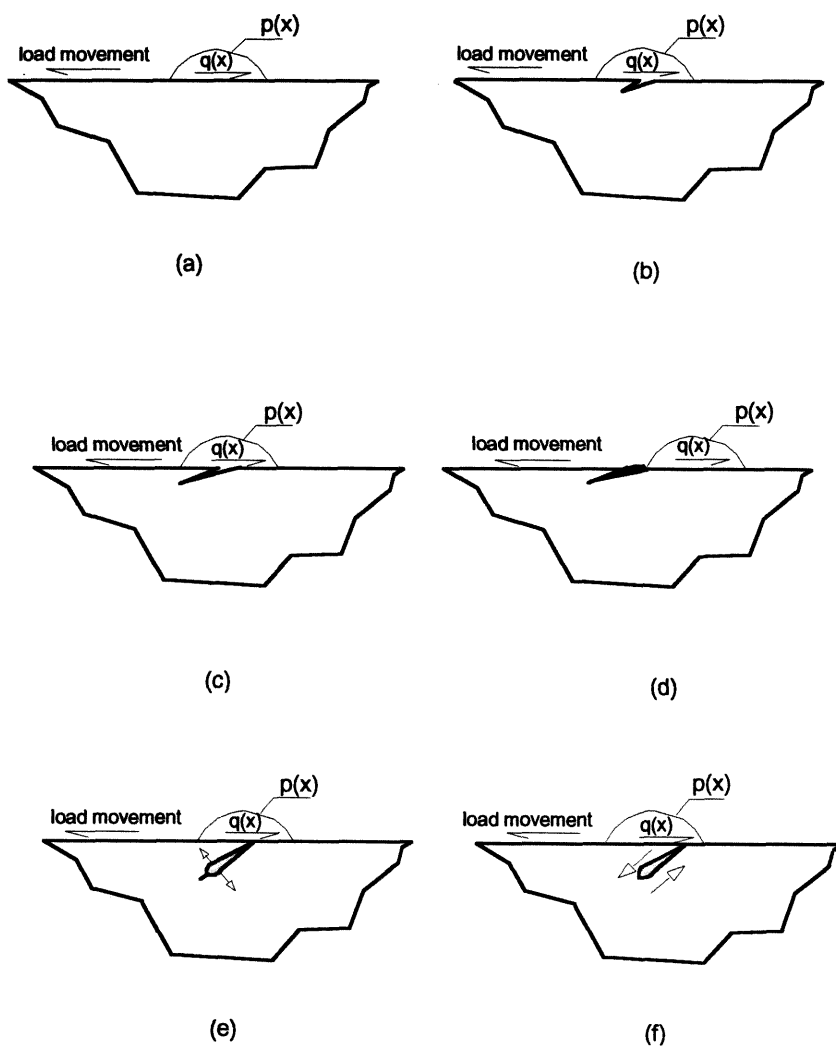


FIGURE (8.4): THE PHYSICAL MODEL OF THE EFFECT OF RATCHETTING ON RCF LIFE. (d), (e) AND (f) AFTER BOWER⁽¹¹⁾ ($p(x)$ IS THE SPATIAL DISTRIBUTION OF THE CONTACT PRESSURE AND $q(x)$ THE CONSEQUENT TRACTION DISTRIBUTION)

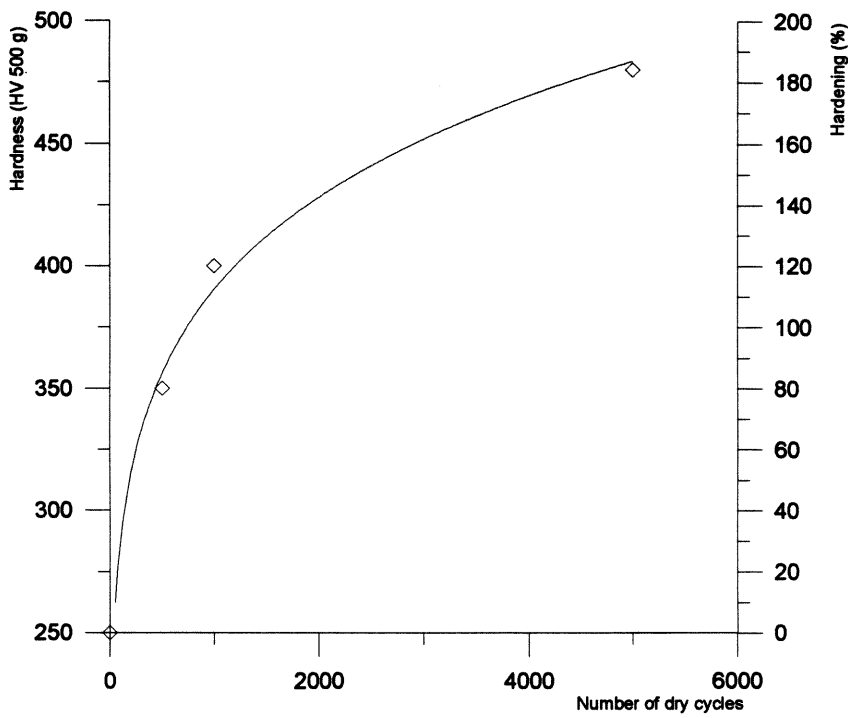


FIGURE (8.5): STRAIN HARDENING OF THE SURFACE LAYER (0.05 mm BELOW THE CONTACT SURFACE) OF THE RAIL DISC FOR $p_0 = 1500$ Mpa

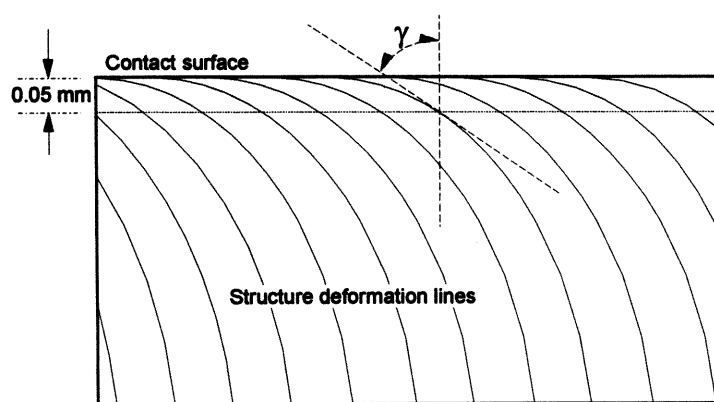


FIGURE (8.6): SCHEMATIC REPRESENTATION OF THE METHOD USED TO MEASURE THE ACCUMULATED PLASTIC SHEAR STRAIN

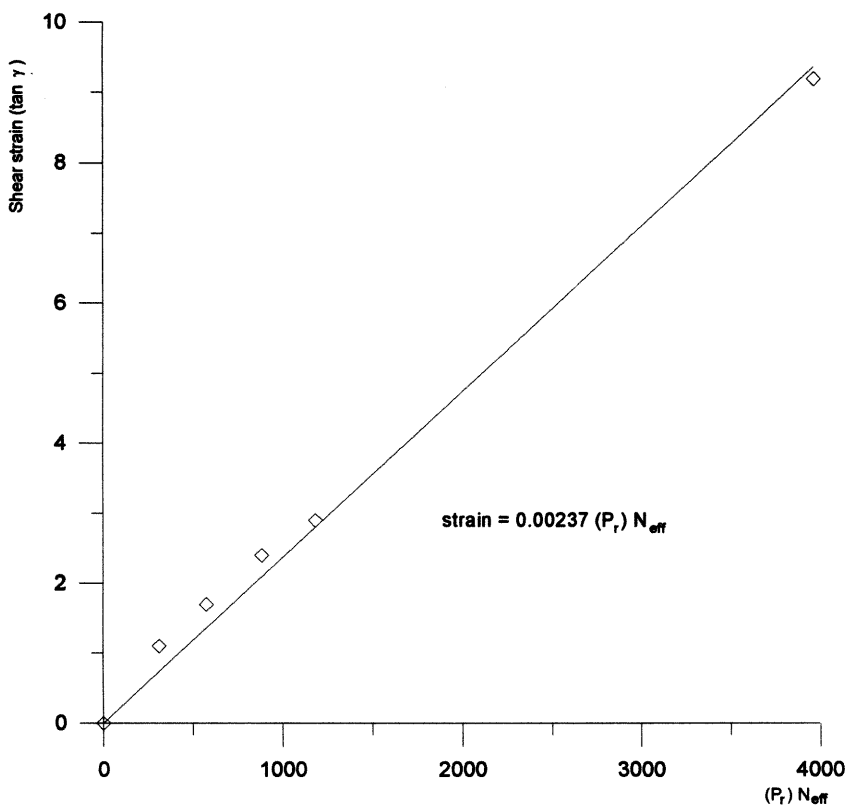


FIGURE (8.7): SHEAR STRAIN AS A FUNCTION OF NET RATCHETTING LOAD AND NUMBER OF EFFECTIVE CYCLES

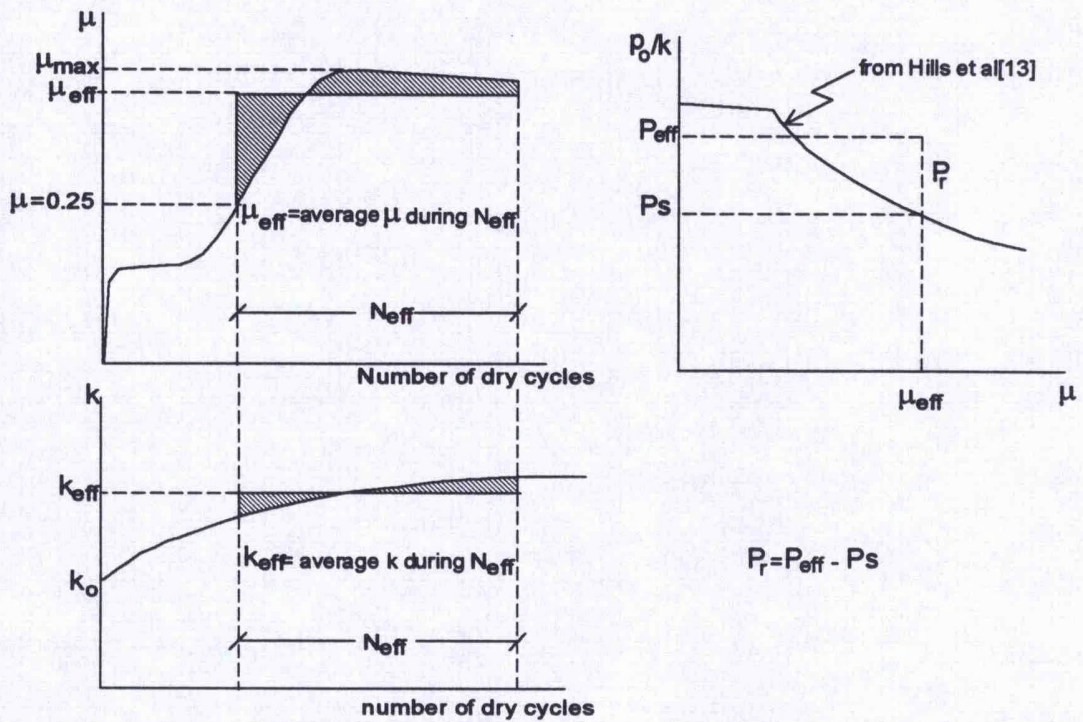


FIGURE (8.8): SCHEMATIC REPRESENTATION OF THE METHOD OF FINDING μ_{eff} , N_{eff} , AND P_r

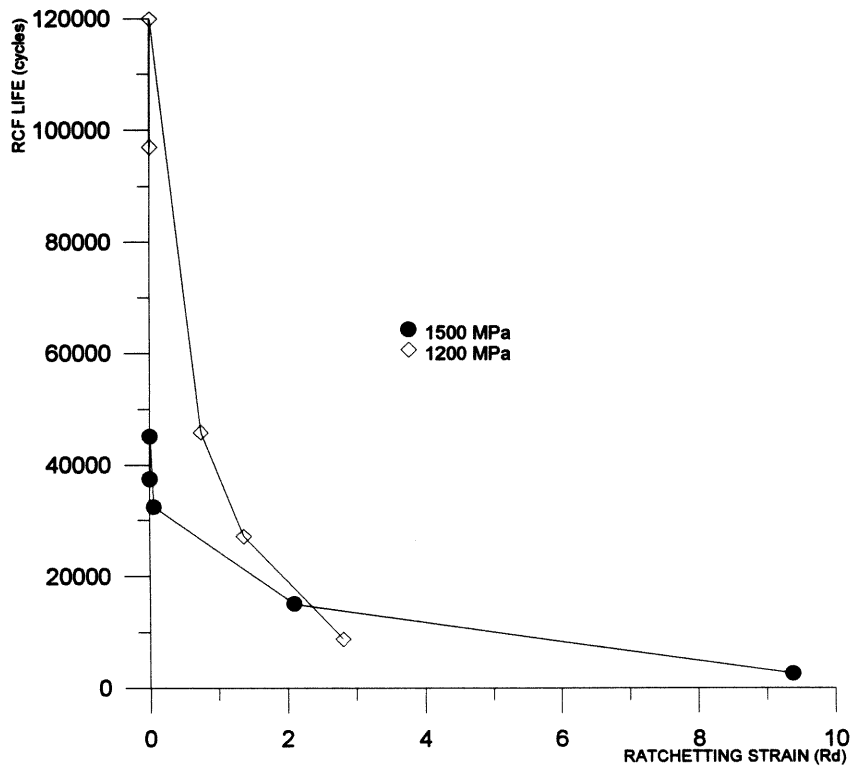


FIGURE (8.9): RCF LIFE AS A FUNCTION OF TOTAL RATCHETTING STRAIN (R_d IN EQUATION (7))

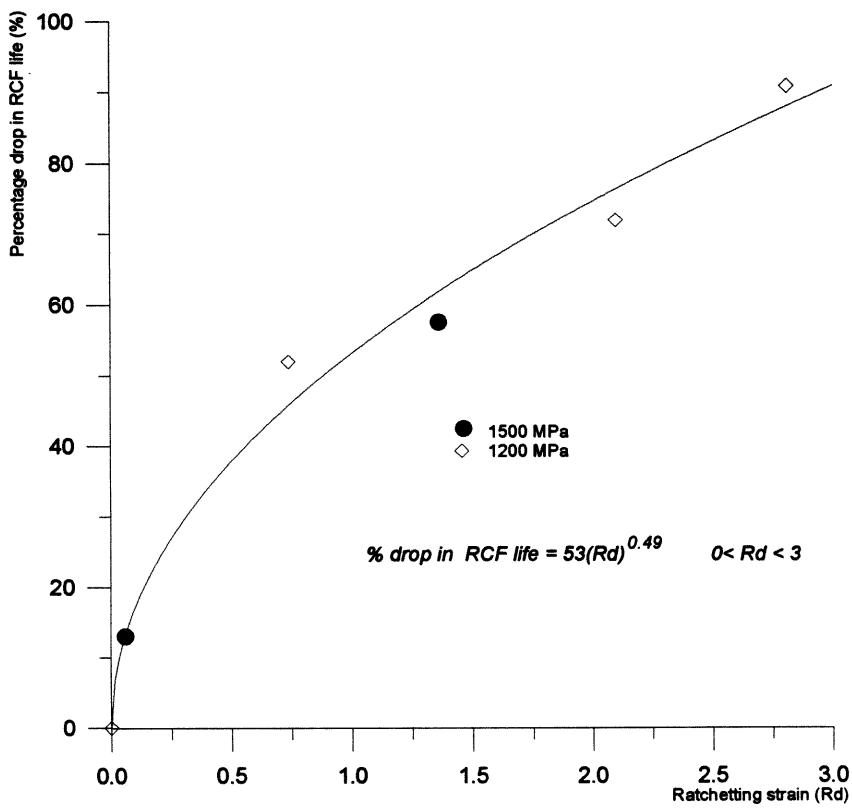


FIGURE (8.10): DETERIORATION IN RCF LIFE AS A FUNCTION OF RATCHETTING STRAIN (Rd IN EQUATION (8.4))

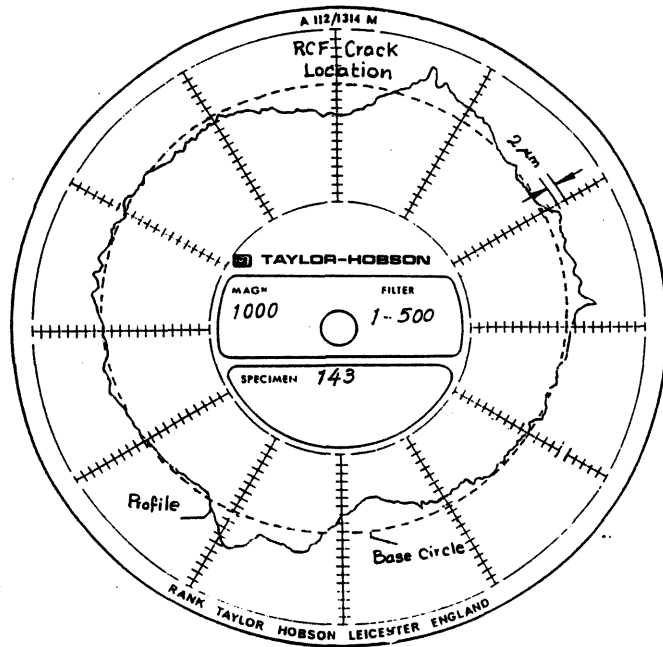


FIGURE (8.11): ROUNDNESS PROFILE SHOWING THE PLASTIC DEFORMATION IN THE LOCATION OF RCF FAILURE

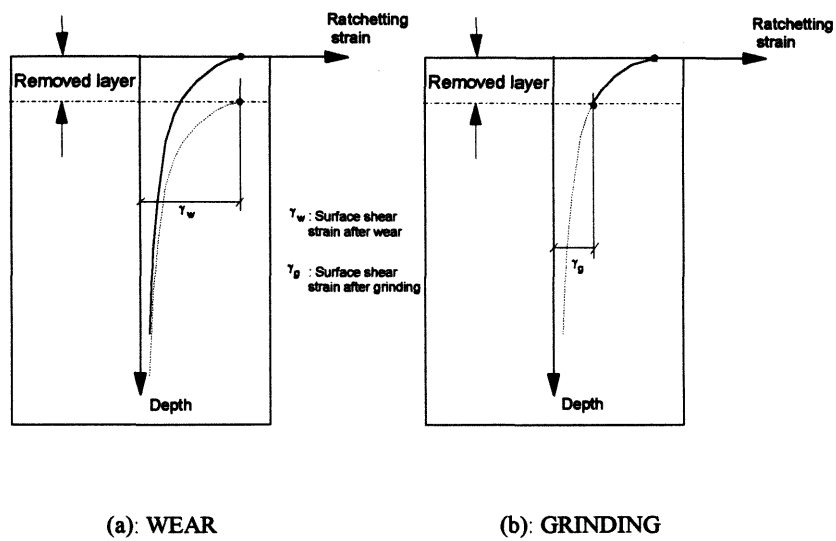
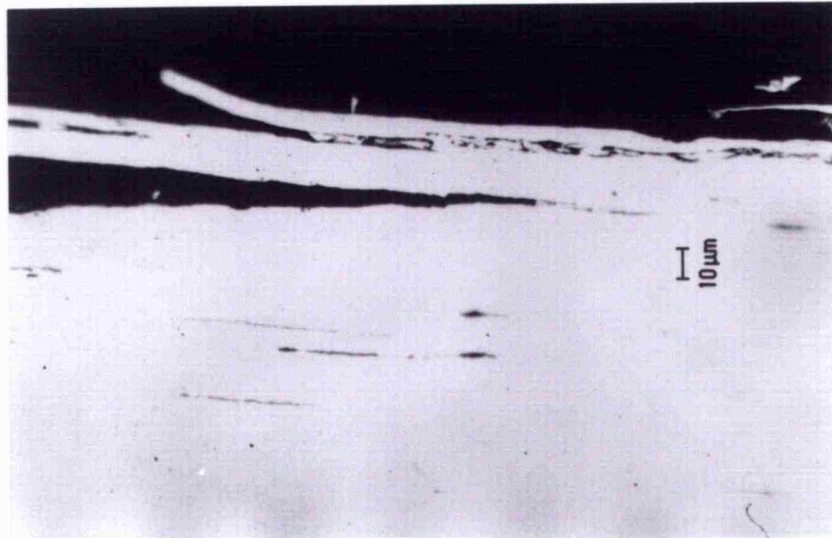


FIGURE (8.12): SCHEMATIC REPRESENTATION OF THE EFFECT OF SURFACE REMOVAL BY WEAR AND GRINDING ON THE RATCHETTING STRAIN AT THE SURFACE



(a): FLAKE MOUTH AFTER 40000 DRY ROLLING-SLIDING CYCLES (TEST CONDITIONS ARE IDENTICAL TO THOSE IN TABLE (2))



(b): RCF CRACK MOUTH CAUSED BY A DRY-WET CYCLING REGIME OF 500 DRY FOLLOWED BY 26119 WET ROLLING-SLIDING CYCLES (TEST 146 OF TABLE (8.2))

FIGURE (8.13): THE SIMILARITY IN MOUTH MORPHOLOGY OF A FLAKE AND A RCF CRACK

Chapter 9

GENERAL DISCUSSION AND CONCLUSIONS

9.1. INTRODUCTION

The results of the experimental programme presented in chapters four to eight have been discussed in each chapter. Conclusions drawn from those results have also been listed at the end of each chapter. To eliminate duplication, this chapter will be restricted to discuss:

- a) Interaction between wear and RCF
- b) general conclusions.

9.1.1. Interaction between wear and RCF

It has been shown in chapters four to eight that both wear and RCF failures in pearlitic rail steel are due to cracking originating in the surface layer of the rail material. However, wear cracks (described in chapters four and five as delamination cracking) appear to be driven by the accumulation of unidirectional plastic strain (ratchetting). It has also been shown that detachment of wear particles from the contact surface, in the form of flakes, occurs when the accumulated strain in the surface layer reaches the critical strain to failure of the material. One important characteristic of wear cracks is that their propagation is confined within the plastically deformed layer, whereas RCF cracks propagate beyond this layer. This indicates that propagation of RCF cracks beyond the plastically deformed layer does not require loading above the shakedown limit of the material. However, many researchers have indicated that the initiation of RCF cracks is also driven by the accumulation of plastic strain. Kalousek⁽¹⁾ found that the initiation of cracks is accelerated under dry rolling condition, where the shakedown limit is low due to the high traction and friction coefficients. He concluded that the effect of lubrication on crack initiation is opposite to its effect on crack propagation. Clayton et al⁽²⁾ have reported similar observations and have shown that all RCF cracks in rails are associated with plastic flow and that crack initiation results from the accumulation of plastic strain. Chiou and Hwang⁽³⁾, Ghonem and Kalousek⁽⁴⁾, Gray et al⁽⁵⁾ and Zhou et al⁽⁶⁾ have shown a strong correlation between plastic flow and RCF crack initiation. These observations, along with the fact that the early stages of crack propagation occurs under a hydrostatic stress state, where ductility is improved and stress intensities cannot operate, represent sufficient

evidence that RCF crack initiation is driven by the accumulation of unidirectional shear strain (ratchetting). This argument is supported by the dominant direction of RCF crack propagation under unidirectional rolling-sliding; *i.e.* parallel to the direction of maximum shear but opposite to the direction of traction, as shown in figures (6.1) and (6.9).

As has been shown in chapters 4 and 5^(7,8), and supported by Johnson⁽⁹⁾, delamination cracks are also shear cracks of a ductile nature, driven by plastic strain rather than elastic stress intensity. This shows that the same mechanism is responsible for initiation of both wear and RCF cracks in rail steels. However, RCF crack propagation beyond the plastically deformed layer appears to be driven by stress intensity as suggested by Way⁽¹⁰⁾ and analysed by Bower⁽¹¹⁾ and others^(12,13).

The question remains as to how to explain the initiation of RCF cracks under loads less than those of shakedown limit. Kapoor and Johnson⁽¹⁴⁾ have shown that even when the apparent contact load is below the shakedown limit, repeated localised asperity-asperity (pummelling) contact can result in loading above this limit. Ratchetting in this case can take place even under modest loads. However, no attempt has been made during this project to investigate wear and RCF under such loading conditions.

Kalousek⁽¹⁾ has explained the absence of RCF failure during dry wear by arguing that the rate of surface removal during dry rolling-sliding is higher than the rate of RCF crack propagation and hence the nascent RCF cracks are removed by wear. This may not be the case, since it has been shown in tables (8.1) and (8.2) that the number of initial dry rolling-sliding cycles required to cause a significant reduction in RCF life did not result in any significant surface removal. This is supported by the work of Sato et al⁽¹⁵⁾, who showed that deformation during the dry stage prepares the material for extensive cracking during the lubricated stage.

9.2. GENERAL CONCLUSIONS

9.2.1. The results presented in chapter 4 showed that under the wheel-rail contact conditions simulated on LEROS, a steady state wear behaviour, characterised by a constant wear rate, is established after a certain number of passes of the load. This steady state coincides with the cessation of strain hardening and the accumulation of unidirectional plastic strain.

9.2.2. Under the test conditions used, the mechanism by which rail loses material during the steady state is accumulation of unidirectional plastic strain beyond the critical strain to failure (ratchetting). The failure stage is characterised by the detachment of wear particles in the form of flakes preceded by delamination ductile cracks propagating parallel to the plane of maximum shear stress.

9.2.3. Ratchetting, as a wear mechanism, can explain the beneficial effect of rolling direction reversal on the wear rate of pearlitic rail steel. In this case, the accumulation of plastic strain changes direction upon reversal, resulting in less strain accumulation in a particular direction.

9.2.4. The performance of the High Strength (Mill Heat Treated) pearlitic rail steel under in RCF conditions is superior to that of the BS11 rail steel.

9.2.5. Rolling direction reversal has a beneficial effect on the fatigue life of BS11 rail steel. This effect is a function of the reversal regime. Multiple reversal of short intervals results in the highest RCF life. The effect of rolling direction reversal on rolling contact fatigue crack and cracking morphology can be explained by the variable crack face friction mechanism, which assumes an increasing friction coefficient with the crack depth.

9.2.6. Initiation of both wear and rolling contact fatigue cracks is due to the same mechanism. In both the cases the early stages of cracking (within the plastically deformed layer) is of a ductile nature, driven by the accumulation of unidirectional plastic strain (ratchetting).

9.2.7. Propagation of rolling fatigue cracks beyond the plastically deformed layer is driven by stress intensity. Mode I stress intensity is caused by the fluid pressure in the crack cavity, while the lubrication effect of the fluid on the crack faces causes mode II stress intensity.

9.2.8. Since ratchetting is a function of traction coefficient, which is higher during dry rolling-sliding, crack initiation and propagation within the plastically deformed layer during dry cycling occurs earlier than during lubricated rolling-sliding. In this case the initial dry rolling-sliding causes deterioration in rolling contact fatigue life. This deterioration can be predicted using the operating conditions, as described in chapter 8.

REFERENCES

1. J. Kalousek, Wear and Rolling Contact Fatigue Model for Railway Rail, Technical Report No. TR-WE-50, *Canadian National Research Council*, (1986).
2. P. Clayton, R. Devanathan, V. Dikshit, D. E. Christensen, D. Danks and R. Steele, Recent Research on Wear, Deformation and Fatigue of Steels in Rolling Contact, *Proc. International Symp. on: Rail steels-Development, Manufacture and performance*, Montreal, Canada, Published by Lawrence G. Kuhn, (1992), 161-174.
3. Y. C. Chiou and J. R. Hwang, Relationship Between the Propagation of Fatigue Cracks and the Behaviour of Plastic Flow Under Rolling/Sliding Contact - Effect of Slip Ratio, *Tribology International*, 24, 2, (1991), 101-107.
4. H. Ghonem and J. Kalousek, study of Surface Crack Initiation Due to Biaxial Compression/Shear Loading, *Engineering Fracture Mechanics*, 30, 5, (1988), 667-683.
5. G. T. Gray, A. W. Thompson and J. C. Williams, Influence of Microstructure on Fatigue Crack Initiation in Fully Pearlitic Steels, *Metallurgical Transactions*, 16A, (1985), 753-760.
6. R. S. Zhou, H. S. Cheng and T. Mura, Micropitting in Rolling and Sliding Contact Under Mixed Lubrication, *Transaction of ASME, J. of Tribology*, 111, (1989), 605-613.
7. W. R. Tyfour, J. H. Beynon and A Kapoor, The Steady State Wear Behaviour of Pearlitic Rail Steel Under Dry Rolling-Sliding Contact Conditions, *Wear*, 180, (1995), 79-89.
8. W. R. Tyfour and J. H. Beynon, The Effect of Rolling Direction Reversal on the Wear Mechanism of Pearlitic Rail Steel, *Tribology International*, 27, 6, (1994), 401-412.
9. K. L. Johnson, Contact Mechanics and Wear of Metals, *Mechanical Colloquium, Cambridge University*, Jan., (1995). Also to appear in *Wear*.
10. S. Way, Pitting due to rolling contact, *Trans. ASME, Journal of Applied Mechanics*, Vol. 2, (1935), A49-A58.
11. A. F. Bower, The Influence of Crack Face Friction and Trapped Fluid on Surface Initiated Rolling Contact Fatigue Cracks. *Transactions of ASME, Journal of Tribology*, (1988), 110. 704-711.
12. Keer L M and Bryant M D. A Pitting Model for Rolling Contact Fatigue. *Transactions of ASME, Journal of Lubrication Technology*, 105, (1983), 198-205.

13. M. Kaneta, Y. Murakami and H. Yatsuzuka, Propagation of surface cracks in rolling line contact, *Proceedings of the JSLE International Tribology Conference*, Tokyo, Japan, (1985), 911-916.
14. A. Kapoor and K. L. Johnson. Plastic Ratchetting as a Possible Wear Mechanism, *Proc. R. Soc. Lond. A*, 445, (1994), 367-381.
15. M. Sato, P. M. Anderson and D. A. Rigney, Rolling-Sliding Behaviour of Rail Steels, *Wear*, 162-164, (1991), 159-172.

Chapter 10

SUGGESTIONS FOR FURTHER RESEARCH

10.1. Most of the work presented in this thesis has been conducted under a maximum contact pressure of 1500 MPa. Understanding the effect of other loading conditions on some of the phenomena contributing to the wear behaviour of pearlitic rail steel, such as the accumulation of plastic strain and strain hardening, is essential before generalised conclusions can be made.

10.2. The steady state wear behaviour and the effect of rolling direction reversal on the wear rate and wear mechanism of pearlitic rail steel, presented in chapters 4 and 5, have been explained using the ratchetting argument. Further theoretical analysis using the shakedown theory may be beneficial in arriving at models to predict wear rates using operating conditions and material parameters. The suggestion in 10.1 will help in testing such modelling work.

10.3. The traction coefficient during rolling sliding contact plays an important role in dictating the shakedown limits of the material. The behaviour of this coefficient during rolling-sliding contact, mainly during the initial stage but also its down drift during long tests, could not be explained. It is suggested that this behaviour be investigated under different contact conditions.

10.4. It has been concluded in chapter 9 that RCF crack initiation is caused by ratchetting of the contact surface layer. This can be confirmed by conducting rolling sliding contact experiments where the surface layer is ratcheted by dry rolling-sliding before reversing the rolling direction and continue the test under lubricated contact conditions. Crack initiation in this case should be delayed, since a number of cycles will be needed to reverse the direction of strain before the test surface can accumulate plastic strain in the other direction. If ratchetting during the dry phase is sufficient to initiate surface cracks, upon reversal these cracks will not be in the preferential direction of the fluid entrapment crack propagation mechanism.

10.5. To isolate the effect of strain hardening, the experiments suggested in 10.4 above may be repeated using materials which do not strain harden.

10.6. The difference between the effect of surface removal by wear and by grinding on RCF performance of rail steels can be investigated by conducting two sets of

experiments:

i. Starting rolling-sliding experiments where tests are run until RCF cracks develop (to a certain depth), say after N number of cycles. Tests then can be continued under dry conditions until a certain thickness of the surface layer, say (T), is removed by wear before continuing the test until RCF failure. In this case the effect of surface removal by wear can be monitored.

ii. in another set of experiments, tests may be run again for N number of cycles mentioned in (i) above before a surface layer equal to that lost by dry wear, N in (i) above, is removed by grinding. The effect of removing the same thickness of the surface layer, in the first case by wear and the second by grinding can then be assessed. The difference in residual strains in the two cases can then be investigated. The same work can be extended to cover the optimisation of rail grinding strategies.

APPENDIX 1



The steady state wear behaviour of pearlitic rail steel under dry rolling–sliding contact conditions

W.R. Tyfour, J.H. Beynon, A. Kapoor

Department of Engineering, University of Leicester, Leicester LE1 7RH, UK

Received 11 July 1994; accepted 25 August 1994

Abstract

The present study is aimed at studying the onset of steady state wear behaviour of pearlitic rail steel. Wheel–rail contact is simulated by a rolling–sliding line contact. The results show that steady state wear rate prevails after a certain number of rolling–sliding cycles. The effect of strain hardening and uni-directional plastic strain accumulation on the wear behaviour has also been studied. It has been shown that the start of the steady state wear rate coincides with the cessation of plastic strain accumulation and additional strain hardening. The ratchetting failure mechanism has been employed to explain this coincidence.

Keywords: Rail steel; Rolling–sliding contact; Strain hardening; Accumulated plastic strain; Ratchetting; Coefficient of traction

1. Introduction

The cost of the attention paid to the different forms of rail deterioration caused by wheel–rail contact forms a substantial proportion of the overall cost of track maintenance. Wear is the main criterion for rail replacement. It was estimated that the North American Railroads was spending \$600 million annually for the replacement of deteriorated rails in the early 1980s [1]. This figure does not include the cost of direct labour, maintenance equipment or loss of revenue as a result of line closure for rail replacement. This explains why wear resistance is the main criterion for the selection of rail material.

Pearlitic steel is still the most widely used material for rails. Research has been, and still is, focused on the reasons behind the superiority of pearlitic rails, compared with other steels, in resisting wear.

A previous study by Tyfour and Beynon [2] has shown that the accumulation of uni-directional plastic strain, along with the modification of microstructure, can explain the wear behaviour of pearlitic rail steel. However, no attempt was made during that study to investigate the strain accumulation or work hardening behaviour with number of rolling–sliding cycles.

In this work, experiments have been conducted to study the role of those parameters in the wear behaviour of pearlitic rail steel under rolling–sliding dry

contact conditions identical to those of the previous study.

The results show a strong correlation between the number of rolling–sliding cycles required to establish steady state wear behaviour and those needed to cause cessation of hardening and plastic strain accumulation. Ratchetting, as a failure mechanism, is used to explain this correlation.

The importance of quantifying the number of cycles to establish steady state wear behaviour and the mechanism by which it is achieved may lead to a reasonable estimation of the wear rate of rails under certain operating conditions.

2. Procedure

Wheel and rail test discs were cut from wheel rims and rail sections, kindly supplied by ABB British Wheelset Ltd. and the British Railways Board, respectively. The orientation of the discs in relation to the wheel and rail is shown in Fig. 1. Discs were machined to the dimensions shown in Fig. 2. The diameter of the discs is limited by the dimensions of the rail head. The 47 mm disc diameter is the maximum obtainable from the rails supplied.

The chemical composition and mechanical properties of the disc materials are given in Table 1. To ensure uniformity of properties rail discs were cut with their

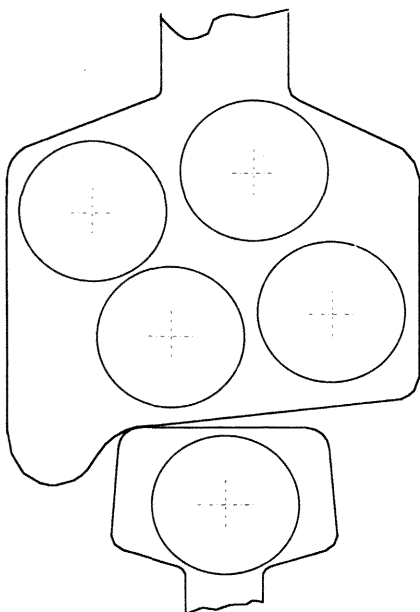


Fig. 1. The orientation of disc specimens relative to rail section and wheel rim.

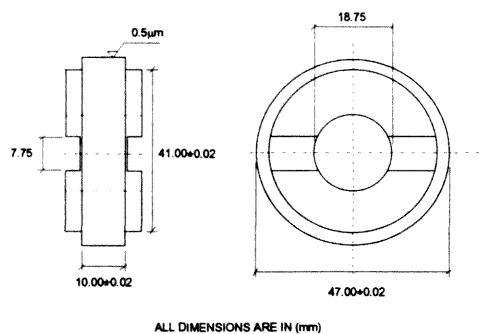


Fig. 2. Dimensions of disc specimens.

axis parallel to the rail long axis, whereas wheel discs were cut with their axis parallel to the wheel tread tangent. All cutting and machining operations were conducted to maintain the original microstructure and properties.

The dimensional tolerances of the discs were measured for roundness and possible eccentricity between the track surface and the bore using a Talyrond 200 profilometer (Rank Taylor Hobson Ltd.).

Table 1
Chemical composition and mechanical properties of the test material

Material	Rail	Wheel
Specification	BS11	W8A
Chemical composition (wt.%)		
C	0.52	0.64
Si	0.2	0.23
Mn	1.07	0.71
Ni	0.03	0.17
Cr	<0.01	0.18
Mo	<0.01	0.03
S	0.018	0.041
P	0.013	0.023
Mechanical properties		
Average hardness (HV 500 g)	240	275
Ultimate tensile strength (MPa)	781	857
Yield strength (MPa)	406	325
Total plastic elongation (%)	21.9	20.3
Young's modulus (GPa)	209	199

Since the type of wheel–rail motion is known to be that of combined rolling and sliding, it was decided to use the LEROS (LEicester ROLLing Sliding wear machine), which is described in detail elsewhere [3]. The machine is basically a Colchester Mascott 1600 lathe modified to suit the purpose. A 4 kW DC motor is mounted on the tail stock end of the machine bed. A drive shaft consisting of universal joints and splines is powered by the DC motor through an interchangeable gear box of 5:1 gear ratio. The other end of the drive shaft is fitted with a machine tool arbor, supported through a pivoted bearing assembly. The wheel disc specimen (driving disc) is bolted to the end of the arbor. This assembly can swing by the action of a hydraulic jack powered by an electric motor driven hydraulic pump to facilitate the loading mechanism. The rail material disc (braking disc) is secured to an arbor at the end of another drive shaft supported between a bearing housing and the lathe chuck. The mid-section of this drive shaft is a torque transducer, which enables measurement of the tractional torque between the two discs. The centre lines of the two drive shafts are parallel when the discs are loaded. The required slip ratio (creepage) is achieved by adjusting the rotational speeds of the two drive shafts.

The machine is equipped with manual as well as computer creepage control through a number of shaft encoders, transducers and a computer interface. Contact load is easily applied and controlled by electronically adjusting the opening of the hydraulic control valve that passes the oil to the jack, which in turn raises the bottom (wheel disc) shaft bearing assembly.

The hydraulic system enables loads up to 29 kN to be applied. Assuming, for the sake of illustration, a Hertzian elastic contact, for the dimensions of disc

specimens used in the present work this represents a maximum contact pressure of 3000 MPa. Such a large capacity means that wide track discs can be accommodated while maintaining realistic contact pressure. Wider tracks are less affected by stress drop off at the edges.

The formula used to calculate the maximum contact pressure p_0 (MPa) is that suggested by Timoshenko and Goodier [4]:

$$p_0 = 0.418 \left(\frac{WE}{TR} \right)^{1/2} \quad (1)$$

where W is the contact load (N), T is the line contact length (mm), E is the modulus of elasticity of steel (MPa) and R is given by

$$\frac{1}{R} = \frac{1}{R_R} + \frac{1}{R_W} \quad (2)$$

where R_R and R_W (mm) are the radii of the rail (top) and wheel (bottom) disc, respectively.

The creepage or slip ratio is calculated using the formula

$$g(\%) = \frac{200(R_R N_R - R_W N_W)}{R_R N_R + R_W N_W} \quad (3)$$

where R_R and R_W are as defined in Eq. (2), and N_R and N_W are the revolution counts of the top and bottom discs, respectively.

All tests were conducted under a maximum contact pressure of 1500 ± 5 MPa and a creepage of $-1 \pm 0.01\%$. The contact area was air cooled using a dry pressurised air supply. Test conditions are shown in Table 2.

All tests but one were non-stop tests. Only test number 130 was stopped every 2500 cycles to monitor the wear rate.

At the end of each test, discs were sectioned and prepared for metallographic observation and microhardness measurements using established techniques.

3. Results

Test results are summarised in Table 3. Hardening is calculated as the percentage ratio between the hardened material and that of the bulk. Wear rates are presented as total weight loss of the test disc. Disc track width gain due to the lateral plastic flow at the free sides, as well as loss in disc diameter, are also reported.

The strains are estimated by measuring the shear angle (γ) between the tangent to the deformed grain boundaries or lamellar pearlite and the normal to the contact surface, and are calculated by:

$$\epsilon = \tan \gamma \quad (4)$$

The coefficient of traction is calculated and presented as maximum as well as end-of-test values. It is derived from the chart record by which the torque transmitted between the two test discs is monitored.

3.1. Number of rolling-sliding cycles to establish steady state wear rate

Measuring the weight loss of the discs of test number 130 at regular intervals of 2500 cycles enabled the wear behaviour to be monitored as the rolling-sliding proceeds. Weight loss per cycle of the rail disc is plotted in Fig. 3 against number of rolling cycles. It can be seen that the wear rate is almost negligible during the

Table 2
Test conditions

Test conditions	Test number						
	134	136	137	136	138	130	139
Disc material	BS11						
Top (rail)	WBA						
Bottom (wheel)							
Initial surface roughness R_a (μm)							
Rail	0.10	0.12	0.34	0.12	0.49	0.16	0.20
Wheel	0.44	0.12	0.14	0.12	0.55	0.16	0.40
Maximum contact pressure (Eq. (1)) (MPa)	1500						
Percentage creepage (Eq. (3)) (%)	-1						
Test speed (rail-wheel) (rev min^{-1})	406-410						
Total number of cycles (rail)	500	1000	5000	10 000	17 500	40 000 *	40 000
Test environment	Dry, air cooled						

* Test stopped every 2500 cycles for weight loss measurements.

Table 3
Test results

Results	Test number						
	134	136	137	135	138	130	139
Total number of cycles	500	1000	5000	10 000	17 500	40 000	40 000
Coefficient of traction							
Maximum	0.405	0.432	0.441	0.441	0.441	0.441	0.441
End of test	0.405	0.432	0.386	0.322	0.300	0.340	0.268
Contact area (mm ²)	6.11						
Total disc weight loss (g)							
Rail	0.0005	0.0029	0.0348	0.1341	0.2490	0.6520	0.6198
Wheel	0.0005	0.0001	0.0382	0.1694	0.6320	1.3650	1.6732
Total disc diameter loss (mm)							
Rail	NM	0.005	0.005	0.045	0.085	0.200	0.200
Wheel	NM	0.005	0.005	0.030	0.162	0.330	0.400
Total disc track width gain (mm)							
Rail	NM	0.130	0.220	0.385	0.720	1.060	1.145
Wheel	NM	0.080	0.170	0.215	0.485	0.960	0.675
Accumulated shear strain 0.2 mm below the contact surface of rail disc	2.0	2.4	4.3	5.7	11.4	11.4	NM
Total strain hardening 0.2 mm below the contact surface of rail disc (%)	29.2	37.9	69.6	80.8	88.8	88.8	NM
End-of-test surface roughness (rail) R_a (μm)	0.26	0.26	7.3	8.11	NM	NM	NM

NM: value not measured due to the limitation of the measuring equipment.

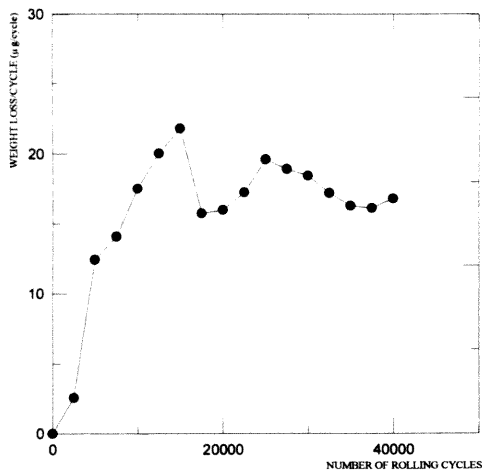


Fig. 3. Relationship between the wear rate of the rail disc, expressed as weight loss per rolling cycle, and number of rolling cycles.

first 2500 cycles, thereafter increasing with number of rolling cycles until around 15 000–17 500 cycles, where it stabilises at around 18 μg per cycle for the remainder of the test.

The running track appearance indicates that the mechanism by which the rail disc loses material prior to the steady state stage is oxidative wear, where the disc track was observed to be covered by a thin, grey

oxide layer. However, during steady state the track appearance is characterised by a shiny flaked surface. The transition to steady state is characterised by the gradual loss of the oxide layer and the exposure of the disc material to the surface. At the same time, fine surface cracks start to appear at the running track. These cracks are thought to be the origins of the flakes noticed during the steady state stage. These surface features are shown in Fig. 4, which is a low magnification photograph of the rail disc running track after different numbers of rolling cycles. The similar oxidised surface features after 500 and 1000 cycles may indicate a similarity in the wear mechanism. Likewise, it is difficult to differentiate between the tracks of the discs tested for 17 500 and 40 000 cycles. Both are characterised by a shiny flaked surface of the similar scale. In this case the wear rates are also at the same level. Moreover, regardless of the initial surface roughness of the disc pairing, measurement of the after-test track surface roughness revealed identical values after 500 and 1000 cycles. In both the cases this roughness was $R_a = 0.26 \mu\text{m}$, whereas it is around $R_a = 8 \mu\text{m}$ after 5000 cycles, see Table 3. Surface roughness after 17 500 and 40 000 cycles appears to be higher than that after 5000 cycles. However numerical values could not be obtained since the size of the flakes is too large compared with the sampling range of the measuring equipment.

In all but one case the driving wheel disc wear rate was higher than that of the driven rail disc. A comparison between the wear rates of the two discs from test 130 is shown in Fig. 5. No attempt has been made to study

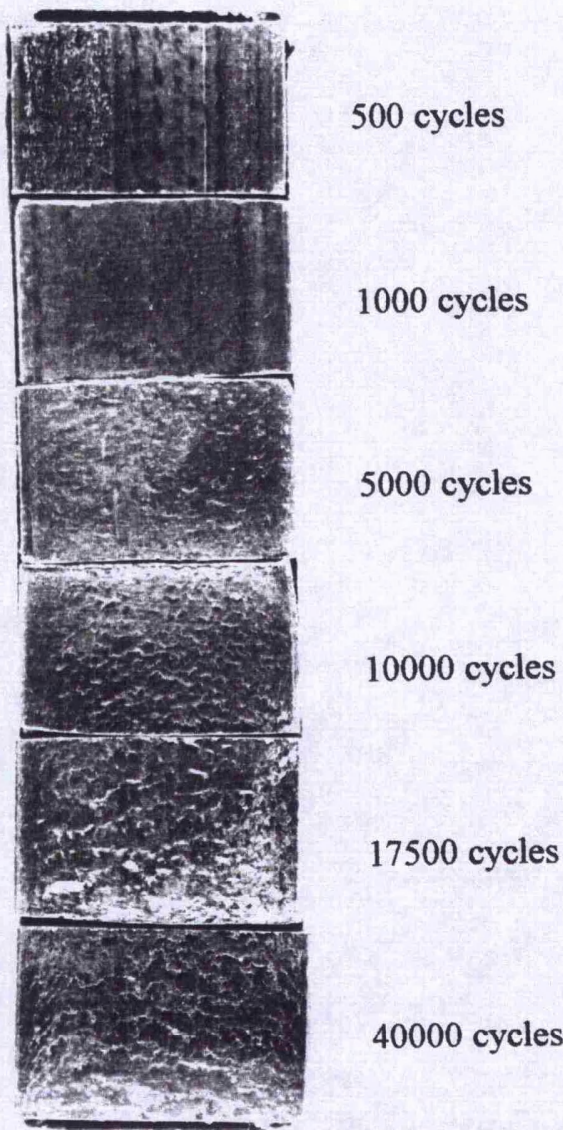


Fig. 4. Rail disc running track appearance after different rolling distances.

the strains and the strain hardening behaviour of the wheel disc material, attention being focused on the rail disc.

3.2. Strain hardening behaviour

Measurement of the hardness at and very near to the worn contact surface does not give accurate results. At a shallow depth below the contact surface hardness values are affected by the existence of flake roots, subsurface cracks and by the directionality in the properties of the heavily deformed layer where, due to the shear stress, a lamellar structure is dominant [2]. To reduce the influence of these factors, hardness at depths less than 0.2 mm below the contact surface was measured with the indenter perpendicular to the disc axis. Pro-

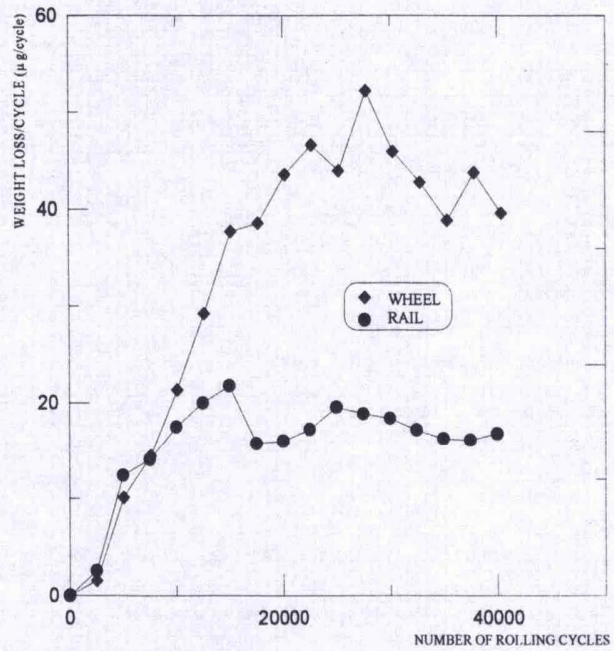


Fig. 5. A comparison between the wear rates of the rail and wheel test discs for test 130.

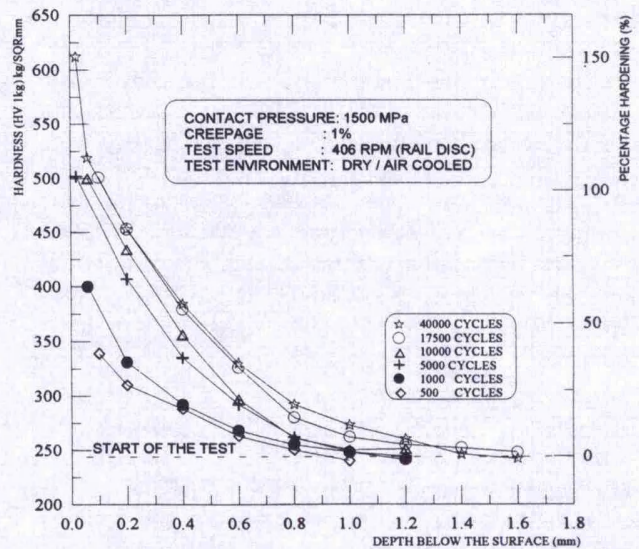


Fig. 6. Hardness profile below the contact surface of the rail disc after different rolling distances.

gressive grinding and polishing of the disc wear track enabled this kind of measurement to be carried out. Hardness profiles below the contact surface are shown in Fig. 6 for different test cycles. These profiles indicate that the material is hardening in a non-linear manner, where hardening rate is highest during the initial stages

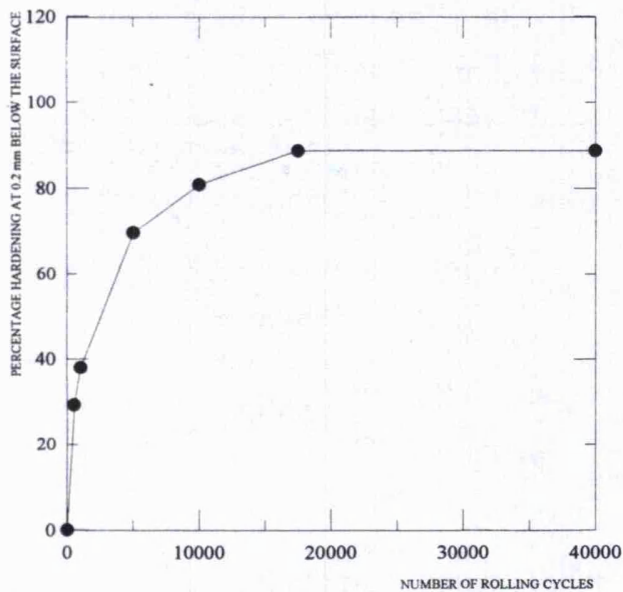


Fig. 7. Percentage hardening of the rail disc material at 0.2 mm below the surface as a function of test duration.

of the test. No further hardening is noticed beyond 17 500 cycles. This is better revealed in Fig. 7, where the percentage hardening at 0.2 mm below the contact surface is plotted against number of rolling cycles. The depth 0.2 mm was chosen for the reasons mentioned at the beginning of Section 3.2. The maximum percentage hardening, 86% above the bulk material hardness, is established after 17 500 cycles. However, almost 30% hardening is achieved during the first 500 cycles. The hardening rate decelerates with number of rolling cycles until it becomes zero beyond 17 500 cycles (no measurements were taken between 10 000 and 17 500 cycles). The degree of strain hardening is maximum at the contact surface. At steady state, the rail disc surface hardness reaches a value 2.5 times that of the bulk material.

3.3. Accumulated plastic strain

It was shown in Section 3.2 that most of the hardening is established during the initial stages of the rolling process. The deformed structure due to the different cycling distances indicates that most of the shear strain is also accumulated during the early rolling cycles. To quantify this accumulation, shear strains after the different number of rolling cycles used during the course of the present work were measured using the method described at the beginning of Section 3. Fig. 8 shows the shear strains, measured at 0.2 mm below the contact surface, plotted as a function of number of rolling cycles. The plot reveals a high strain accumulation rate during the initial stages. This rate decelerates with number of rolling cycles until it is zero after 17 500

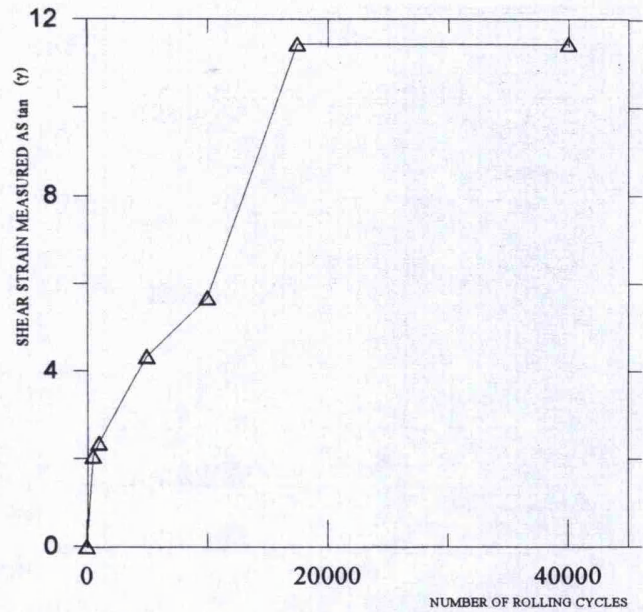


Fig. 8. Accumulated shear strain at 0.2 mm below the contact surface of the rail disc as a function of rolling distance.

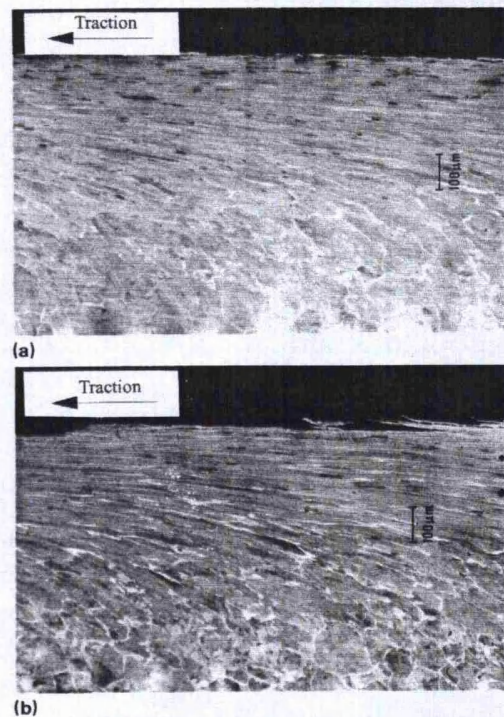


Fig. 9. Deformed structure below the contact surface of the pearlitic rail steel disc after 17 500 and 40 000 cycles (tests 138 and 139, respectively).

cycles, where the accumulated strain achieves its maximum value. No further strains were observed beyond these cycles. This is illustrated in Fig. 9 which shows the deformation of the pearlitic structure after different numbers of rolling cycles. The similarity of the deformation after 17 500 and 40 000 cycles is very close.

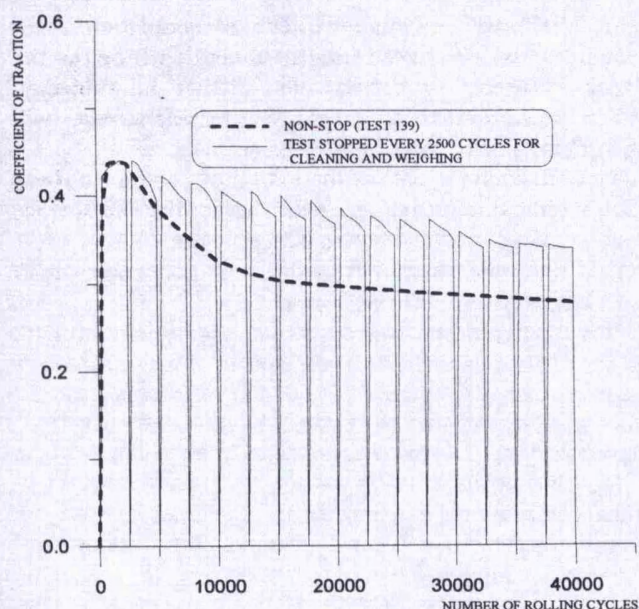


Fig. 10. Effect of rolling distance and disc cleaning on the traction coefficient.

3.4. Coefficient of traction

Recording the torque transmitted between the two test discs during a non-stop test of 4 000 cycles enabled the behaviour of traction coefficient to be monitored as the rolling process proceeded. This coefficient is plotted in Fig. 10 as a function of number of rolling cycles. The plot reveals that the coefficient of traction starts to increase with number of cycles and reaches its maximum, 0.441, after around 2000 cycles before it starts to fall again. The rate of fall decelerates slowly until it sustains a constant fall rate after around 15 000 cycles. After 4 0000 cycles, the traction coefficient drops to 0.268. No attempt has been made to investigate the traction coefficient behaviour beyond 4 0000 cycles. The same behaviour was noticed during all other non-stop tests.

Cleaning the test discs prior to weighing, as in test number 130 where the test was being stopped every 2500 cycles, seems to affect the traction coefficient. After each cleaning, nearly 500 cycles are required to raise the traction to its pre-cleaning level before it exceeds that level and then drifts downward again, see Fig. 10.

4. Discussion

4.1. Weight loss and side plastic flow

During rolling-sliding testing, material is lost from the contact surface by detachment of wear flakes as well as by plastic flow into lips to the sides of the test

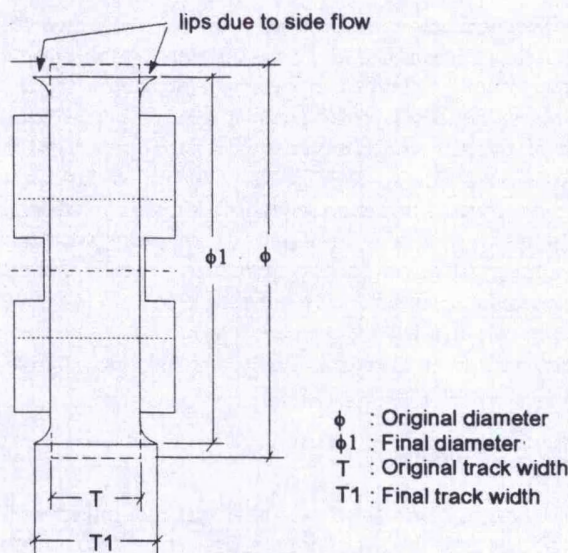


Fig. 11. Plastic flow at the edges of the contact area of the test disc.

disc track. Table 3 shows that the diameter loss of the disc specimens is more than what could be contributed by the weight loss. It also shows the track widening in the form of lips at the sides of the track, schematically exaggerated in Fig. 11. Although track widening increases the apparent contact area, it may not affect the contact stresses since the extra area is in the form of lips which may not support load. That is why this type of flow can be considered as wear. The same type of flow is also noticed on the gauge face of curved rails [5]. However, the term 'wear' will be used here to describe the weight loss only. No attempt will be made to discuss the effect of plastic side flow.

The steady state wear rate of $18 \mu\text{g cycle}^{-1}$, mentioned in Section 3.1. corresponds to 1.54 nm per cycle depth loss, assuming all the metal is lost and no plastic lip is formed. Since such a lip does form, the diameter loss will actually be larger. From our measurements of diameter change, the depth loss is about 80% more than that calculated from the weight loss alone. Thus just under 3 nm per cycle is lost from the surface. Such small amounts are not found in the debris, where flakes of the order of 3–10 μm thick are observed. Thus the process of metal loss by flaking must be a discrete event occurring periodically rather than a continuous process. However, this discrete event gives a fairly uniform weight loss curve, rather than a discrete stair shaped curve, since it happens at different places of the running track surface of the disc.

4.2. Measurement of the accumulated plastic strain

The method used to measure the accumulated uni-directional plastic strains reported in Section 3 may

not be very accurate at or very near to the contact surface, where a small change in the shear angle corresponds to a significant increase in the shear strain. However, at depths of 0.2 mm and deeper below the contact surface the method gives a reasonably accurate measure of the strain. The method is similar to that used by Bower and Johnson [6] who used spark eroded slots filled with dental amalgam to measure surface displacement during sliding wear tests. A similar technique has also been used by Bhargava et al. [7]. Zhang and Alpas [8] used a marker platelet inserted in the test piece surface to visualise and measure displacement during sliding contact testing.

4.3. Ratchetting failure

The contact pressure ($p_0 = 1500$ MPa) and the coefficient of traction ($\mu > 0.3$) in the case of the present work are known to cause a shear stress (τ_{xz}) higher than the shear yield strength of the material (k). In this case two failure mechanisms may be considered. If the cyclic straining of the material does not result in accumulation of plastic strain, the surface layer fails by low cycle fatigue [9,10]. Alternatively, if the surface layer accumulates unidirectional plastic strain with number of cycles, the material fails due to an alternative failure mechanism, 'ratchetting failure', in which failure takes place when the material accumulates uni-directional plastic strain equal to its critical strain to failure [11]. Kapoor [12] showed that the two mechanisms are independent and competitive and that the material fails by whichever is satisfied in the shorter number of cycles.

It has been shown in Fig. 8 that the test conditions of the present work have resulted in strain accumulation with number of rolling cycles. Accordingly, the failure mechanism is expected to be that of ratchetting. As a wear mechanism, ratchetting implies that material should start to detach from the surface (fail) after accumulating plastic strain equal to its critical strain to failure. Consequently, the material has to be subjected to a certain number of rolling-sliding cycles before the first weight loss can be observed. In these experiments, wear rate increases gradually before the steady state is observed, see Fig. 3. This behaviour can be explained by the following arguments.

- Ratchetting is not the only wear mechanism operating during rolling-sliding contact. Oxidative wear is dominant during the initial stages. Under the test conditions of this work oxidative wear was observed to prevail during the first 5000 cycles
- Every time material is removed from the surface, a new layer of a different accumulated strain history is exposed to contact surface.

The argument in (b) may be better understood if we consider three material elements at different depths below the contact surface, with the first element at the

surface. The three elements will be subjected to different shear stress levels according to their depth below the surface, where the surface element will be subjected to the maximum shear stress. These shear stresses will have two main effects, as follows.

- With each passage of the load they produce a shear strain which decreases with the depth. The surface element will see the maximum strain.
- This leads to strain hardening, the maximum of which is also at the surface.

At the beginning of the test, the shear yield strength k of the material is constant across the depth below the surface, Figs. 6 and 12(a). The distribution of the shear stress (τ_{xz}) divides the material below the surface into two regions. Down to a certain depth, point S on Fig. 12, the shear stress is higher than k . Since the surface element has not strain hardened and is still relatively soft, its strain rate will be higher. This explains the high hardening and straining rates during the initial stages of the test, see Figs. 7 and 8, respectively. As the rolling continues, this element strain hardens, Fig. 12(b) and, as a result, the strain accumulated per cycle decreases. As deformation proceeds, the surface element reaches a stage where further strain is not possible due to the exhaustion of ductility, Figs. 8 and 12(c). The material of the element would be expected to fail when it accumulates plastic strain equal to its critical strain to failure. This failure is the detachment of metal from the surface as a flake.

Once the surface element detaches from the surface, the second element will be exposed to the contact. However, the difference between the two is that the second element will reach the surface partially damaged (partially strained since part of its ductility has already been exhausted while it was still below the surface).

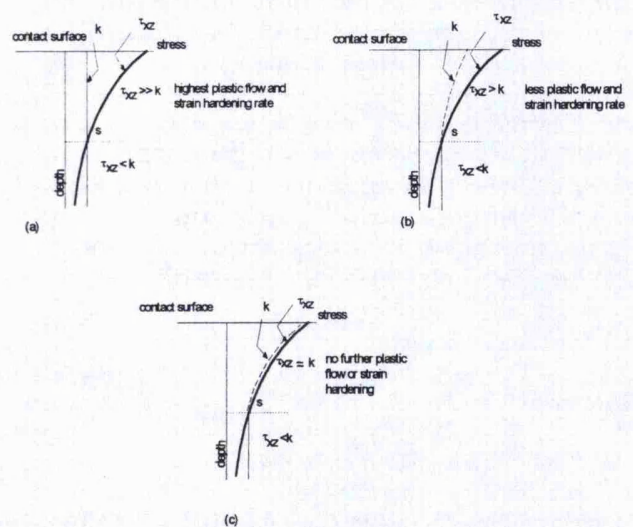


Fig. 12. Schematic illustration of the strain hardening and damage accumulation during the different stages of the rolling sliding process.

This implies that it requires fewer cycles to fail by ratchetting. This may explain the increase in wear with number of rolling cycles before the steady state.

As far as the third, deepest, element is concerned, it is expected to reach the surface with a previous damage higher than that of the second element and it should fail even earlier leading to a higher wear rate.

If the same argument is applied to more elements, a stage will be reached where all the material reaching the surface will have the same prior history of accumulated strain and loss of ductility. The steady state wear rate is expected when the first of the layers of such material reaches the surface. In the case of the present work this stage starts after about 17 500 cycles.

The diameter loss corresponding to a test of 17 500 cycles' duration, number 138 in Table 3, is 85 μm , or just over 40 μm loss in radius. It is interesting to observe in Fig. 6 that this is very close to the surface compared with the depth of penetration of the plastic deformation. Thus steady state conditions do not require the feeding through of the subsurface material from below the work hardened layer.

The above argument is supported by the measurements of the accumulated plastic strain plotted in Fig. 8 as a function of number of rolling cycles. It shows that after a certain rolling distance, in this case about 17 500 cycles, further strain accumulation ceases and no further strain accumulation is observed up to the end of the test, (4 0000 cycles). Similar behaviour of rail steel can be seen in Fig. 12(b) of Bower and Johnson [6] under conditions of dry sliding contact. Likewise, between 17 500 and 4 0000 cycles no additional hardening could be observed, see Fig. 7. Similar results have been obtained by Zhang and Alpas [8], who reported a work hardening rate close to zero near the surface of Al–7%Si alloy tested under sliding conditions.

It can be concluded that steady state wear behaviour is established when material elements of the same strain hardening and accumulated plastic strain history start to reach the surface. This is evident in Fig. 13 where the percentage strain hardening, the accumulated uni-directional plastic strain and the wear rate are plotted against number of rolling cycles. Further evidence is the similarity of the deformed structure and the test disc running track appearance after 17 500 and 4 0000 cycles, Figs. 9(a) and 9(b), respectively.

The complexity of the stress state and the hardening behaviour during rolling–sliding contact conditions has led some researchers to simplify these conditions. Controlled cycling tests under conditions of tension–compression, tension–torsion and compression–torsion [6,13,14], at different mean stress levels and cycling regimes have been aimed at quantifying the hardening and ratchetting behaviour under rolling–sliding conditions.

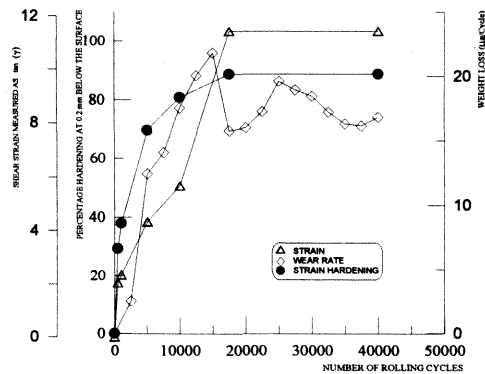


Fig. 13. Effect of rolling distance on the accumulated shear strain, percentage hardening and wear rate of rail steel.

The hardening behaviour observed in this work could not be correlated with the results of those studies. This could be due to the following factors.

- As it approaches the contact surface, deformed pearlitic steel exhibits directionality in its mechanical properties [2,15]. As a result, the assumption of isotropic material properties in studying the near-surface stress state is not appropriate.
- The simulations used to represent the rolling–sliding stress state mentioned above do not include the element of wear and the consequent continuous changes of the stress state of the near-surface layer as this layer approaches the contact surface.
- Studying the coefficient of traction recorded under the test conditions adds further complications to the surface layer stress state. The plastic strains are governed by the difference between the operating contact pressure and the shakedown limit of the material [6]. Since the plastic shakedown limit of the material is a function of the coefficient of traction, any change in this coefficient results in a new strain cycle. In studying the hardening behaviour under rolling–sliding conditions, researchers usually assume a constant traction coefficient with each cycle. However, Fig. 10 shows a significant difference between the maximum and the end-of-test traction coefficients, 0.441 and 0.268, respectively. This difference cannot be ignored.
- The high hydrostatic pressure, caused by the contact load, enhances the ductility of the material. This is evident in Fig. 9 where severe deformation of the surface layer can be observed.

To summarise, it has been shown that, if pearlitic rail steel is subjected to the rolling–sliding conditions used during this work, steady state wear is established when material layers of the same previous history of strain hardening and uni-directional plastic strain are

exposed to the contact surface. There, material reaches its critical strain to failure and fails by detaching from the surface. This allows the next layer to be exposed to the contact surface to face the same end result. Reversing the direction of the strain is known to delay the steady state wear behaviour and to reduce the wear rate. Using the test conditions of the present work, Tyfour and Beynon [2] have studied different rolling direction reversal regimes and have shown that the steady state wear behaviour is also a function of strain direction reversal. This represents further evidence that the accumulation of the uni-directional strain is an important factor in establishing the steady state wear behaviour.

4.4. Traction coefficient

It is preferable to refer to the ratio between the traction and normal force between the two discs as the 'coefficient of traction' rather than the coefficient of friction. According to Amonton's laws of friction the coefficient of friction is a constant and is determined only by the material pairing. This implies that friction is not a function of rolling distance. The plot in Fig. 10 shows that the traction coefficient does change with number of rolling cycles. Similar behaviour has also been reported by others [16]. No attempt has been made to study the effect of surface layer deformation on the traction transmitted between the two discs. However, there is evidence that the mechanical and chemical properties of the surface layer of the disc change with number of rolling cycles [17,18]. A study of the relationship between the coefficient of traction and the changes to the surface layer was conducted by Krause and Demerci [17] who showed that the behaviour of the traction coefficient under dry rolling-sliding conditions is affected by the structural changes to the deformed surface layer, such as the changes to the crystal orientation and subgrain size.

The effect of cleaning the test discs on the traction behaviour could be explained by arguing that cleaning involves the removal of the oxide layer, mainly off the wheel disc where it is more prevalent. This oxide is known to act as a lubricant between the two discs. The sharp peaks observed after every cleaning, Fig. 10, supports this argument. The traction coefficient drop after the initial peak coincides with the formation of a new oxide layer.

5. Conclusions

5.1. If pearlitic rail steel is subjected to rolling-sliding loads above its ratchetting threshold it exhibits a steady state wear rate, characterised by a constant weight loss per rolling cycle, after a certain number

of rolling cycles. Under the conditions used in this work, this number is around 17 500 cycles.

- 5.2. The steady state wear rate is established when material of the same history of strain hardening and accumulated uni-directional plastic strain reaches the surface and the uni-directional plastic strain limit to failure is reached.
- 5.3. Strain accumulation and strain hardening rates are maxima at the beginning of the rolling-sliding process and decrease in a non-linear fashion to cease after a certain number of cycles.
- 5.4. During the initial stages of the rolling-sliding process, oxidative wear is the main mechanism by which material is lost from the surface of the pearlitic rail steel.
- 5.5. The coefficient of traction is a function of rolling distance and cannot be assumed to be constant since it changes significantly with number of rolling cycles. Interrupting the test to clean the test discs affects the coefficient of traction by increasing it momentarily. This increase is due to the removal of the oxide layer, mainly off the wheel disc, which acts as a lubricant between the two discs.

Acknowledgements

The authors would like to thank the British Railways Board and ABB British Wheelset Ltd. who supplied the rail and wheel materials used during this work. The financial support of Mu'tah University of Jordan and The British Council is also appreciated.

References

- [1] W. Jamison, Wear of steel in combined rolling and sliding, *ASLE Trans.*, 25 (1) (1980) 71–78.
- [2] W.R. Tyfour and J.H. Beynon, The effect of rolling direction reversal on the wear rate and wear mechanism of pearlitic rail steel, *Tribol. Int.*, in press.
- [3] J.E. Garnham and J.H. Beynon, The early detection of rolling-sliding contact fatigue cracks, *Wear*, 144 (1991) 103–116.
- [4] S.P. Timoshenko and D.N. Goodier, *Theory of Elasticity*, McGraw-Hill, 1970.
- [5] P. Clayton, B.P. Allery and P.J. Bolton, Surface damage phenomena in rails, *Proc. Int. Symp. on Contact Mechanics and Wear of Wheel/Rail Systems*, 1983, pp. 419–441.
- [6] A.F. Bower and K.L. Johnson, The influence of strain hardening on cumulative plastic deformation in rolling and sliding line contact, *J. Mech. Phys. Solids*, 37 (4) (1989) 471–493.
- [7] V. Bhargava, G.T. Hahn and C.A. Rubin, Analysis of rolling contact with kinematic hardening for rail steel properties, *Wear*, 122 (1988) 267–283.
- [8] J. Zhang and A.T. Alpas, Delamination wear in ductile materials containing second phase particles, *Mater. Sci. Eng.*, A160 (1993) 25–35.
- [9] B.S. Hockenhull, E.M. Kopalinsky and P.L.B. Oxley, An investigation of the role of low cycle fatigue in producing surface damage in sliding metallic friction, *Wear*, 148 (1991) 135–146.

- [10] L.F. Coffin and J.R. Schenectady, A study of the effect of cyclic thermal stresses on a ductile metal, *Trans. ASME*, (August 1954) 931–950.
- [11] P.F. Benham and H. Ford, Low endurance of a mild steel and an aluminium alloy, *J. Mech. Eng. Sci.*, 3 (2) (1961) 119–132
- [12] A. Kapoor, A re-evaluation of the life to rupture of ductile metals by cyclic plastic strain, *Fatigue Fract. Eng. Mater. Struct.*, 17 (2) (1994) 201–219.
- [13] A.F. Bower, Cyclic hardening properties of hard-drawn copper and rail steel, *J. Mech. Phys. Solids*, 37 (4) (1989) 455–470.
- [14] H. Sehitoglu and R.Y. Jiang, Cyclic ratchetting behaviour of 1070 steel and experimental simulation of rolling contact, *American Association of Railroads Progress Rep. 5*, University of Illinois, 1992.
- [15] G. Langford, Deformation of pearlite, *Metall. Trans.*, 8A (1977) 861–875.
- [16] H. Krause and H. Lehna, Investigation of the tribological characteristics of rolling-sliding friction systems by means of systematic wear experiments under well-defined conditions, *Wear*, 119 (1987) 153–174.
- [17] H. Krause and H. Demirci, Factors influencing the real trend of the coefficient of friction of two elastic bodies rolling over each other in presence of dry friction, in A.D Pater and J.J. Kalker (eds.), *The Mechanics of Contact Between Deformable Bodies*, Delft University Press, Delft, 1975.
- [18] B.I. Kostosky, The structural-energetic concept in the theory of friction and wear (synergism and self-organisation), *Wear*, 159 (1990) 1–15.

APPENDIX 2

The effect of rolling direction reversal on the wear rate and wear mechanism of pearlitic rail steel

W. R. Tyfour and J. H. Beynon

The effect of different single and multiple rolling direction reversal (RDR) regimes on wear rate and mechanism is studied in this paper. Changes in structure deformation morphology and accumulated plastic strain are also analysed. Evidence that unidirectional rolling sliding contact can result in directional mechanical properties of the deformed layer is given. Results obtained under the test conditions used show that RDR has a beneficial effect on the wear rate of pearlitic rail steel. Multiple short RDR resulted in the lowest wear rate, less than half the unidirectional value.

Keywords: *rolling/sliding contact, rolling direction, reversal, wear rate, wear mechanism, plastic strain, free path in ferrite*

Introduction

In addition to the problems of rolling contact fatigue and rail corrugations, rail wear is still one of the costliest engineering problems in almost any railway system. Efforts to minimize wear rates through wheel and rail profile design, selection of material and improving the operating conditions never stop. Although a great deal has been achieved, there remains much to be done, mainly in the area of the mechanisms by which the rail loses material.

The interesting results of a previous study¹ of the effect of rolling direction reversal (RDR) on rolling contact fatigue and crack morphology encouraged the authors to extend their research to cover the effect of this reversal on other types of rail deterioration caused by rolling contact. It was thought at that stage that although the RDR may improve rolling contact fatigue life, it may adversely affect wear rate. That is why the test conditions used during the course of the present work were chosen to be identical to those of the previous research, except that the present work involves no lubrication.

The results obtained may not be of direct applicable advantage to railway systems where double-line traffic is dominant, so it should not be understood that the authors are suggesting traffic-direction reversals.

However, these results may lead to a better understanding of the wear mechanism of pearlitic rail steels.

Procedure

Wheel and rail test disks were cut from wheel rims and rail sections, kindly supplied by ABB British Wheelset Ltd and the British Railways Board, respectively. The orientation of the disks in relation to the wheel and rail is shown in Fig 1. Disks were machined to the dimensions shown in Fig 2. The diameter of the disks is limited by the dimensions of the rail head. The 47 mm disk diameter is the maximum obtainable from the rails supplied.

The chemical composition and mechanical properties of the disk materials are given in Table 1. To ensure homogeneous properties rail disks were cut with their axis parallel to the rail long axis, whereas wheel disks were cut with their axis parallel to the wheel tread tangent. All cutting and machining operations were conducted to maintain the original microstructure and properties.

The dimensional tolerances of the disks were measured for roundness and possible eccentricity between the track surface and the bore using a Talyrond 200 profilometer (Rank Taylor Hobson Ltd).

Since the type of wheel/rail motion is known to be that of combined rolling and sliding, it was decided to use the LEROS (Leicester Rolling Sliding wear machine), which is described in detail elsewhere². The machine is basically a Colchester Mascott 1600 lathe modified to suit the purpose. A 4 kW d.c. motor is

Department of Engineering, University of Leicester, Leicester, LE1 7RH, UK
Received 20 February 1994; revised 13 June 1994; accepted 21 June 1994

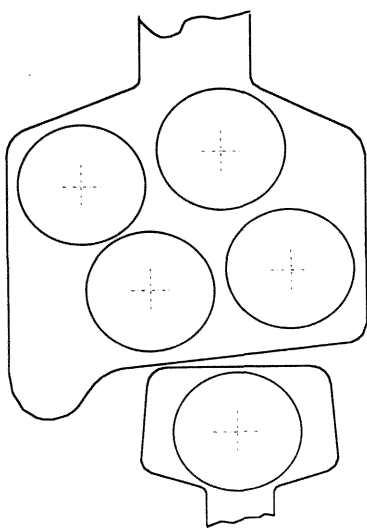


Fig 1 Orientation of disk specimens relative to rail section and wheel rim

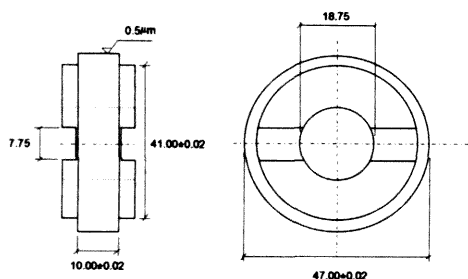


Fig 2 Dimensions (mm) of disk specimens

mounted on the tail stock end of the machine bed. A drive shaft consisting of universal joints and splines is powered by the d.c. motor through an interchangeable gearbox of a 5:1 gear ratio. The other end of the drive shaft is fitted with a machine tool arbor, supported through a pivoted bearing assembly. The wheel disk specimen (driving disk) is bolted to the end of the arbor. This assembly can swing by the action of a hydraulic jack powered by an electric motor-driven hydraulic pump to facilitate the loading mechanism. The rail material disk (braking disk) is secured to an arbor at the end of another drive shaft supported between a bearing housing and the lathe chuck. The mid-section of this drive shaft is a torque transducer, which enables measurement of the tractional torque between the two disks. The centrelines of the two drive shafts are parallel when the disks are loaded. The required slip ratio (creepage) is achieved

Table 1 Chemical composition and mechanical properties of the test materials

Material Specification	Rail BS 11	Wheel W8A
Chemical composition (wt%)		
C	0.52	0.64
Si	0.2	0.23
Mn	1.07	0.71
Ni	0.03	0.17
Cr	<0.01	0.18
Mo	<0.01	0.03
S	0.018	0.041
P	0.013	0.023
Mechanical properties		
Average hardness (HV 500 g)	240	275
Ultimate tensile strength (MPa)	781	857
Yield strength (MPa)	406	325
Total plastic elongation (%)	21.9	20.3
Young's modulus (GPa)	209	199

by adjusting the rotational speeds of the two drive shafts.

The machine is equipped with manual as well as computer creepage control through a number of shaft encoders, transducers and a computer interface. Contact load is easily applied and controlled by electronically adjusting the opening of the hydraulic control valve that passes the oil to the jack, which in turn raises the bottom (wheel disk) shaft-bearing assembly.

The hydraulic system enables loads up to 29 kN to be applied. Assuming, for the sake of illustration, a Hertzian elastic contact, for the dimensions of disk specimens used in the present work this represents a maximum contact pressure of 3000 MPa. Such a large capacity means that wider track disks can be accommodated while maintaining realistic contact pressure. Wider tracks are less affected by stress drop-off at the edges.

The formula used to calculate the maximum contact pressure p_0 (MPa) is that suggested by Timoshenko and Goodier³:

$$p_0 = 0.418 \left(\frac{WE}{TR} \right)^{1/3} \quad (1)$$

where W is the contact load (N), T is the line contact length (mm), E is the modulus of elasticity of steel (MPa) and R is given by:

$$\frac{1}{R} = \frac{1}{R_R} + \frac{1}{R_W} \quad (2)$$

where R_R and R_W (mm) are the radii of the rail (top) and wheel (bottom) disks, respectively.

The creepage or slip ratio is calculated using the formula:

$$g(\%) = \frac{200(R_R N_R - R_W N_W)}{R_R N_R + R_W N_W} \quad (3)$$

where R_R and R_W are defined in equation (2) and N_R and N_W are the revolution counts of the rail and wheel disks, respectively.

All tests were conducted under a maximum contact pressure of 1500 ± 5 MPa and a creepage of $-1 \pm 0.01\%$. The contact area was air cooled using a dry pressurized air supply. Test conditions are shown in Table 2. Rail disks were reversed every predetermined number of rolling cycles. Rail disk rotational speed was 406 revolutions per minute.

To ensure similar test conditions, all test disks were dismantled, cleaned in an ultrasonic bath of isopropanol and weighed every 2500 cycles. This number represents the minimum number of cycles per reversal used during the course of the present work. At the end of each test, disks were sectioned and prepared for metallographic observation and microhardness measurements using established techniques.

Results

A summary of test results is shown in Table 3. Wear rates are presented as total weight loss and diameter loss of the rail disk. Although the wear rates were different under different rolling direction reversal regimes, there are some features which were found to be common for all the tests. These will now be described.

Common features

Coefficient of friction

Rolling direction reversal appears to have no effect on the coefficient of friction between the two disks. It can be seen from Table 3 that this coefficient, which is calculated as a time average value, remained in the range of 0.370–0.374 for the whole series of tests. The

initial surface roughness of the disk pairs did not affect this value, even at the very early stages of the rolling-sliding contact.

Hardness below the contact surface

Measurements of the hardness below the contact surface of the rail disk revealed maximum hardening at the contact surface. The bulk hardness is reached at about 1.3 mm below the worn surface.

Measurement of the hardness very near to the contact surface with the indenter parallel to the disk axis proved to be difficult since the indenter can cause interlaminar cracking parallel to the contact surface, resulting in an indentation larger than that representing the actual hardness (Fig 3(a)). Figure 3(b) shows a satisfactory indentation. To avoid such a condition, hardness was also measured with the indenter perpendicular to the disk axis. Progressive grinding of the disk track surface enabled hardness measurements at progressive depths. Figure 4 shows the hardness profile below the contact surface of the rail disk of test 130 measured in both the directions mentioned above. The profile in both directions is almost identical except very near the surface, where the hardness value measured perpendicular to the disk axis shows a value lower than that measured parallel to the disk axis at the same depth. This behaviour is due to the delamination cracking mentioned earlier. Even at deeper indentation locations short cracks were noted near the indentation corners in the direction of structure deformation (Fig 5). This behaviour will be discussed in more detail below.

Wear mechanism

The mechanism by which the rail disk loses material appears to be that of delamination*. Surface, as well as subsurface, cracks were noticed at and below the

Table 2 Test conditions

Test number	124	125	126A	127A	128	129	130
Disk material: Top (rail)				BS 11			
Bottom (wheel)				W8A			
Initial surface roughness ($R_a, \mu\text{m}$)							
Rail	0.37	0.46	0.46	0.51	0.44	0.39	0.16
Wheel	0.31	0.4	0.44	0.53	0.41	0.39	0.16
Maximum contact pressure (eq. 1)(MPa)				1500			
Percentage creepage (eq. 3) (%)				-1			
Test speed: (rail-wheel) (RPM)				406-410			
Wear measurement intervals				Every 2500 cycles			
Total number of cycles	40 000	40 000	45 000	40 000	60 000	40 000	40 000
Reversal regime	Single	Multiple	Multiple	Multiple	Single	Single	None
Number of cycles/reversal	20 000	10 000	15 000	2500	10 000	2500	40 000
Test environment				Dry, air cooled			

Table 3 Test results

Test number	124	125	126A	127A	128	129	130
Total number of cycles	40 000	40 000	45 000	40 000	60 000	40 000	40 000
Coefficient of friction	0.370	0.370	0.371	0.371	0.370	0.374	0.373
Contact area (mm ²)			6.11				
Total rail disk weight loss (g):							
Rail	0.422	0.287	0.472	0.270	0.559	0.660	0.652
Wheel	1.285	1.022	1.451	1.249	1.562	1.294	1.366
Total rail disk diameter loss (mm):							
Rail	0.150	0.125	0.180	0.160	0.150	0.150	0.200
Wheel	0.300	0.200	0.310	0.230	0.280	0.350	0.330
Total rail disk track width gain (mm):							
Rail	0.990	0.860	1.100	1.020	0.990	1.050	1.060
Wheel	0.610	0.670	0.345	0.700	0.760	0.810	0.900

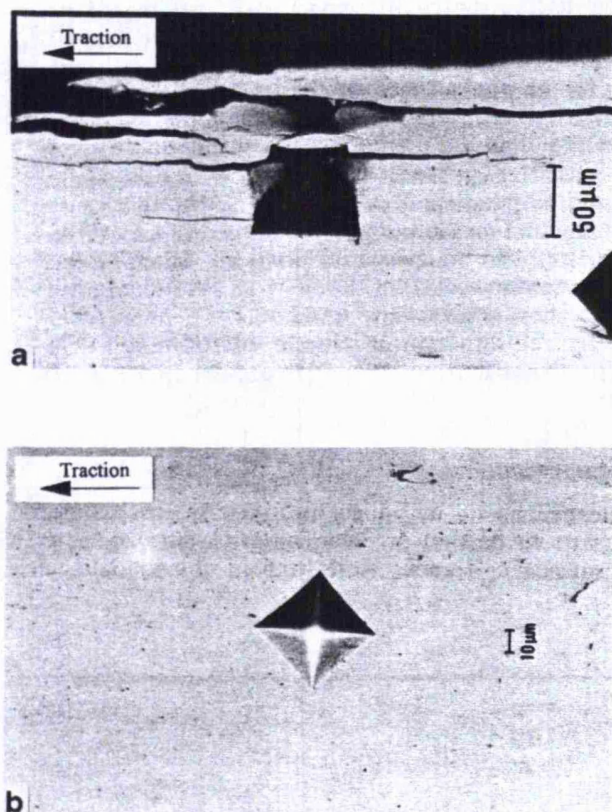


Fig 3 (a) Interlamellar cracking caused by indentation very near the contact surface. (b) Indentation mark away from the deformed structure

contact surface, in the direction of traction parallel to the deformed structure, as shown in Figs 6(a) and 6(b). The cracks appear to propagate between the laminates parallel to the contact surface. Cracks propagating at different levels of the laminar structure can join only if they can break through the laminates perpendicular to the direction of deformation, as shown in Fig 7. Figure 8 illustrates a number of such cracks propagating at different levels of the stacked structure without joining, even though they are only a few microns apart. Flakes are formed when a

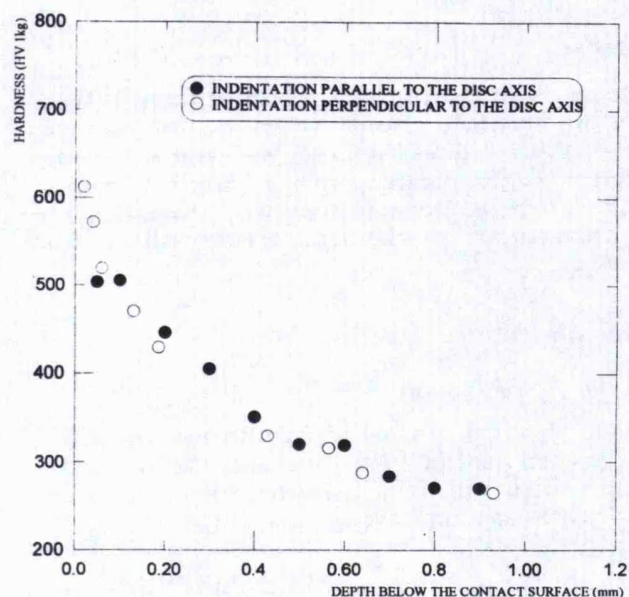


Fig 4 The hardness profile below the surface of the rail disk of test 130

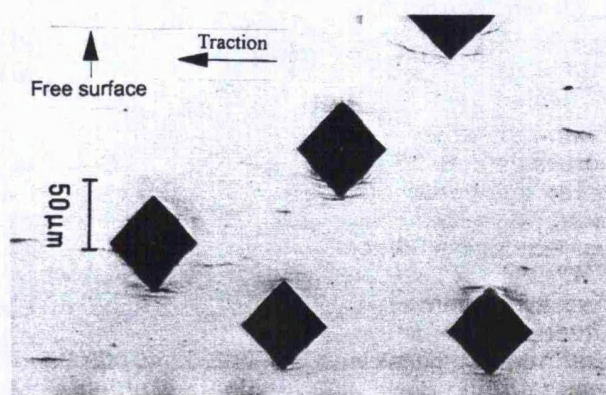


Fig 5 Cracking caused by indentation at different depths below the contact surface of the rail disk (the worn surface is above the top of the micrograph)

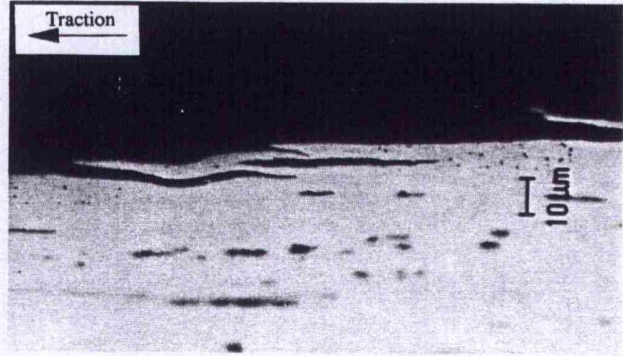
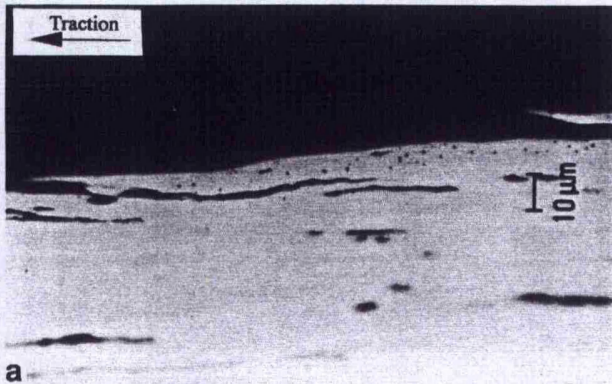


Fig 8 Cracks propagating at different levels of the stacked structure without joining

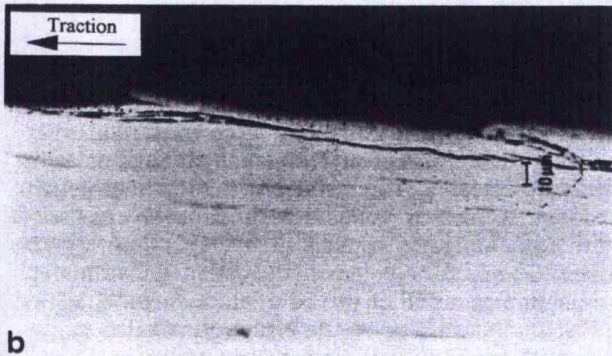


Fig 6 Delamination cracks caused by the loaded contact of the rail disk. (a) Surface cracks; (b) subsurface cracks

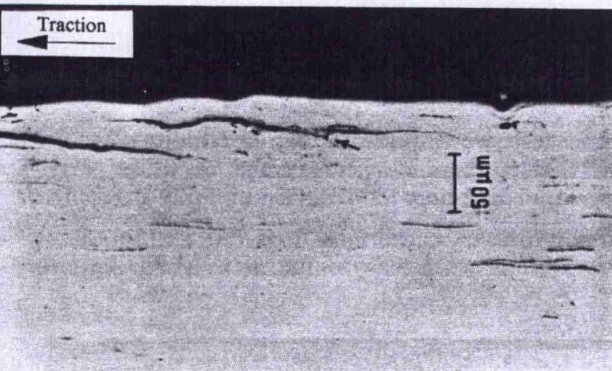


Fig 7 Crack propagation across the laminates

laminate breaks to the contact surface. Debris are formed by these flakes detaching from the disk surface.

Metallographic sections cut at a tangent to the worn surface show that the cracks propagate along the laminate borders even when those are corrugated. This is shown in Fig 9, which is a micrograph of the deformed structure of the rail disk of test 130, sectioned parallel to the disk axis, looking down on the wear track but on a section cut at a tangent to it.



Fig 9 Deformed microstructure of the rail disk sectioned parallel to the disk axis of the rail disk of test 130 (cracking in the ferrite phase)

Wheel disk wear rate

Reversal of the rail disk rolling direction appears to have no significant effect on the wear rate of the wheel disk regardless of the reversal regime. The wear rate of the wheel disk was noted to be always higher than that of the rail. The wear mechanism in this case is that of the oxidative type. Prior to cleaning, a grey oxide layer, which is easy to remove, was found to cover the running track of the rail disk. The number of cycles required to establish a steady state is around 17500, which is identical to that of the rail disk. However, neither the steady-state behaviour nor the wear mechanism appears to be affected by the rail disk rolling direction reversal.

Uni-directional rolling

Test 130 was run under conditions of unidirectional rolling in order to establish a reference for comparison with the remainder of the tests. The wear rate due to unidirectional rolling is characterized by a relatively low rate during the first few thousand cycles before it starts to increase rapidly to reach a constant steady-

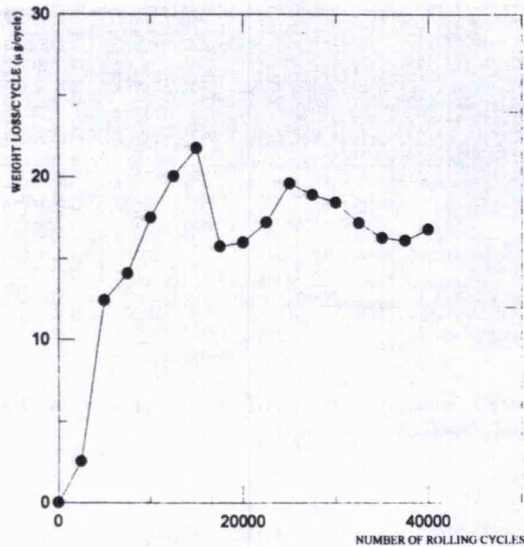


Fig 10 Relationship between weight loss per cycle and number of rolling cycles of the rail disk of test 130

state rate which prevails to the end of the test, arbitrarily chosen to be 40 000 revolutions of the rail disk. This behaviour is illustrated in Fig 10, where the weight loss per rolling cycle is plotted against the accumulated number of rolling cycles. Under the unidirectional rolling-sliding conditions used during the course of this work the number of cycles to establish a steady state extends to almost 15 000. The nature of this period leading up to steady-state conditions will be described in a future paper.

Although the wear data are scattered in the latter period of the test (Fig 10), they still show a tendency to be steady. This scatter could be related to the cleaning before each weighing, as will be discussed later.

Since the test was conducted under dry conditions, the maximum plastic shear stress and, as a result, the maximum deformation are expected at the contact surface, as seen in Fig 11. The structure very near the surface is deformed parallel to the rolling direction. Scanning electron microscopy (SEM) spot analysis on

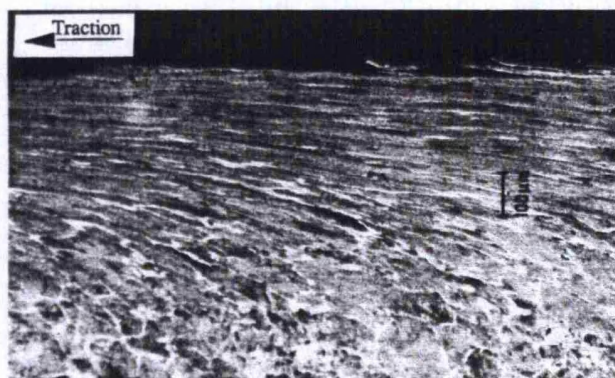


Fig 11 Deformed structure below the contact surface of the rail disk of test 130

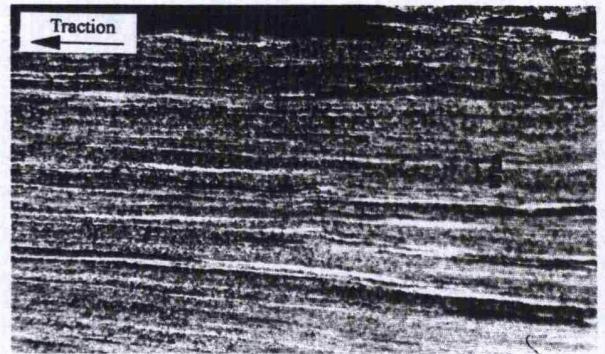


Fig 12 The straight and parallel borders between the laminates of the deformed structure near the rail disk surface of test 130

the dark parallel lines seen below the surface showed that they are stringered manganese sulphide inclusions. Those flattened inclusions may have an important role in structure deformation and crack initiation, as will be discussed later. The deformed structure just below the contact surface appears as a multi-layer stack of cementite laminates separated by layers of flattened ferrite. The border between the adjacent laminates is a straight line parallel to the contact surface, as seen in Fig 12. Indentation in the direction parallel to those laminates showed that they can separate easily (see Fig 4).

Sections parallel to the disk axis, such as that of Fig 9, show another view of the deformed structure. It can be seen that the flake root cracks follow the deformation lines of the structure. Multi-layered delamination flakes were noted at the contact surface (Fig 13).

Tests under conditions of single rolling direction reversal (SRDR)

Three tests were conducted under conditions of different SRDR regimes. The results of those tests are shown under numbers 124, 128 and 129 in Table 3.

Under the test conditions used during the course of the present work it was found that RDRs have a

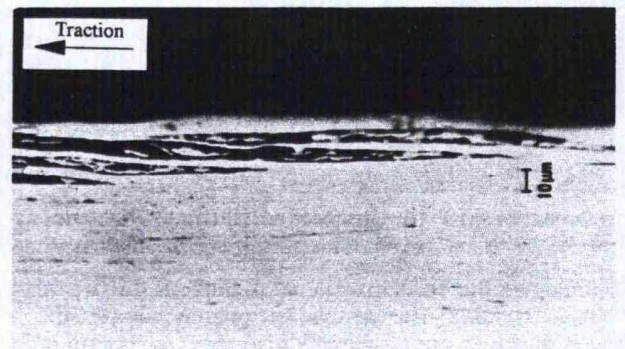


Fig 13 Multi-layered delamination flakes of the rail disk of test 130

significant effect on the wear rate of the pearlitic rail steel disks. Figure 14 shows a comparison between the different wear rates obtained under the three different SRDR regimes and those under unidirectional rolling conditions, plotted as accumulated rail disk weight loss per cycle against number of cycles rolled. It can be seen that the wear rates were almost equal before the RDR. Upon reversal, those rates suddenly drop to a significantly lower level.

The behaviour after the RDR depends on whether the reversal is carried out during or after the period required to establish a steady state under unidirectional conditions. If reversal is carried out during this period, as in test 129 where the rolling direction was reversed after the first 2500 cycles, the effect of reversal is to lower the wear rate temporarily, leading to an extension of the period required to establish a steady-state wear rate from around 15 000 cycles during the unidirectional rolling (test 130) to around 22 500 cycles during test 129, as shown in Fig 14. On the other hand, if RDR is carried out once steady-state wear has been established, the wear rate drops suddenly from the unidirectional steady-state wear level, which is in the range of 15–17.5 $\mu\text{g}/\text{cycle}$, to a significantly lower level of around 7 $\mu\text{g}/\text{cycle}$ as in tests 124 and 128, where reversal was carried out after 20 000 and 10 000 cycles, respectively.

It appears from Fig 14 that the wear rate well after reversal depends mainly on the number of cycles rolled in the first direction. In test 128, RDR was carried out after the first 10 000 cycles before continuing the test for another 50 000 cycles in the opposite direction to examine whether the wear rate recovered its pre-reversal level. It was found that the minimum weight loss/cycle is achieved directly after the reversal. This wear rate then starts to increase slowly. However, even after 50 000 cycles in the reverse direction, the wear rate is barely half-way to its pre-reversal level. On the other hand, when the rolling direction was reversed after only 2500 cycles before continuing for

another 37 500 cycles in the reverse direction, as in test 129, the wear rate was lower than that of the unidirectional rolling up to 22 500 cycles. After this the wear rate was at a steady-state level, slightly higher than that for the unidirectional condition.

The micrographs of the deformed structures of tests 124, 128 and 129, which were run under conditions of single RDR after 20 000, 10 000 and 2500 cycles, respectively, are shown in Figs 15(a)–15(c). When the initial phase was 20 000 cycles and equal to the reversal period, as in Fig 15(a), the deformation shows some recovery to an undeformed arrangement. This recovery is incomplete in spite of the equal number of cycles in each direction. Strain hardening is thought to hinder full undoing of the deformation by reversal. Similarly, when 10 000 cycles is followed by 30 000 cycles in the reverse direction, as in Fig 15(b), the deformation is confined to a shallow depth below the contact surface. This is further evidence that an accumulated deformation caused by a certain number of rolling cycles needs a higher number of cycles in the other direction to realign it. A reversal regime of

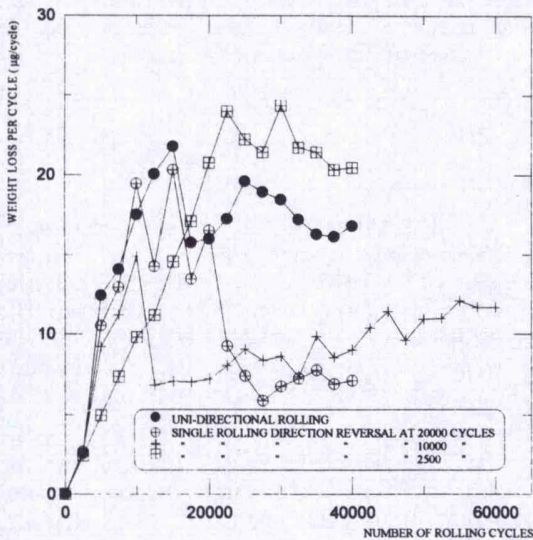


Fig 14 Effect of single reversal on the weight loss per cycle of the rail disk

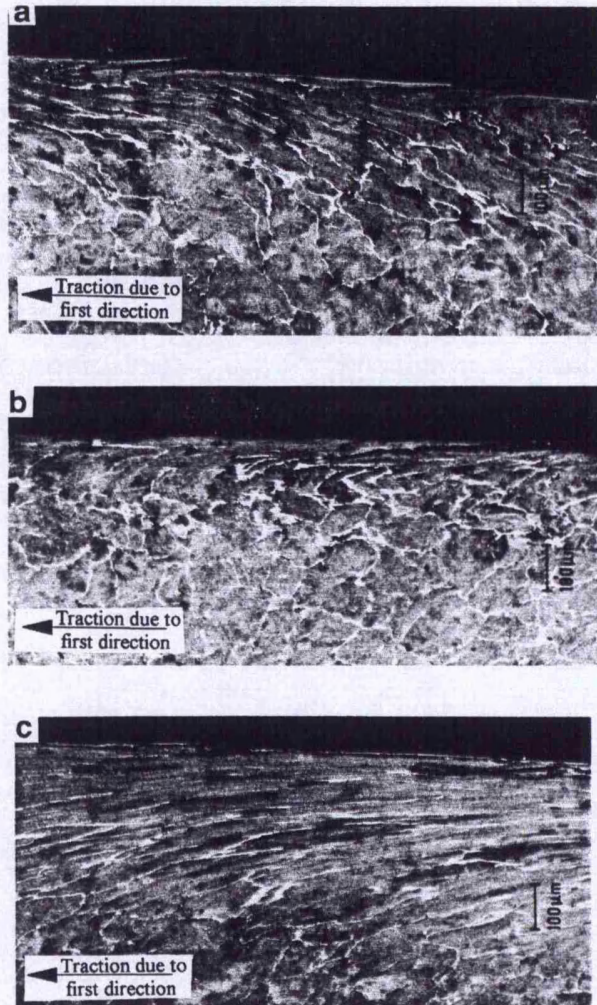


Fig 15 Deformed structure of the rail disk under different single reversal regimes, (a) after the first 20 000 cycles, (b) after the first 10 000 cycles and (c) after the first 2500 cycles

2500 cycles followed by 37500 cycles in the reverse direction (Fig 15(c)) shows no trace of deformation due to the first 2500 cycles.

Tests under conditions of multiple RDR

Three tests were conducted under conditions of multiple reversals using three different reversal regimes. Tests 125, 126A and 127A were reversed every 15 000, 10 000 and 2500 cycles, respectively. Figure 16 shows that upon the first reversal the wear behaviour is identical to that obtained under single RDR of the same cycle interval. The effect of further reversals depends on the cycle interval. The first reversal in the multiple reversal regime of 15 000 cycles per reversal shows a significant effect on the weight loss per rolling cycle. However, the effect of the second reversal, after 30 000 cycles, is barely distinguishable. The second reversal during test 125, in which the rolling direction was reversed every 10 000 cycles, produced a slight reduction in wear rate followed by a small increase, whereas the third reversal, at 30 000 cycles, indicated a higher reduction which was more sustained (Fig 16).

The average wear rates after the first RDR are almost equal under the three multiple reversal regimes (Fig 16). All the three multiple reversal regimes used cause a significant reduction in the wear rate.

The effect of multiple RDR on the deformation of the microstructure below the contact surface is shown in Figs 17(a)–17(c). (Contrast differences are due to different amounts of etching during metallographic preparation.) Test 127A, in which the reversal interval was only 2500 cycles, resulted in a complicated wavy structure nearer to the worn surface (Fig 17(c)). In contrast, the longer cycle interval of test 126A produced a deformation pattern similar to that of unidirectional rolling (Fig 17(a)). It is worth noting that such different deformation patterns have similar wear rates.

Comparison between the effect of single and multiple reversal on the wear rate under the 10 000- and 2500-

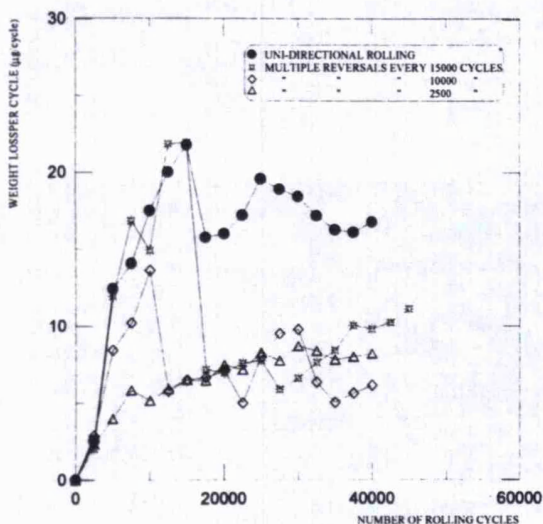


Fig 16 Effect of multiple rolling direction reversal on the weight loss per rolling cycle of the rail disk

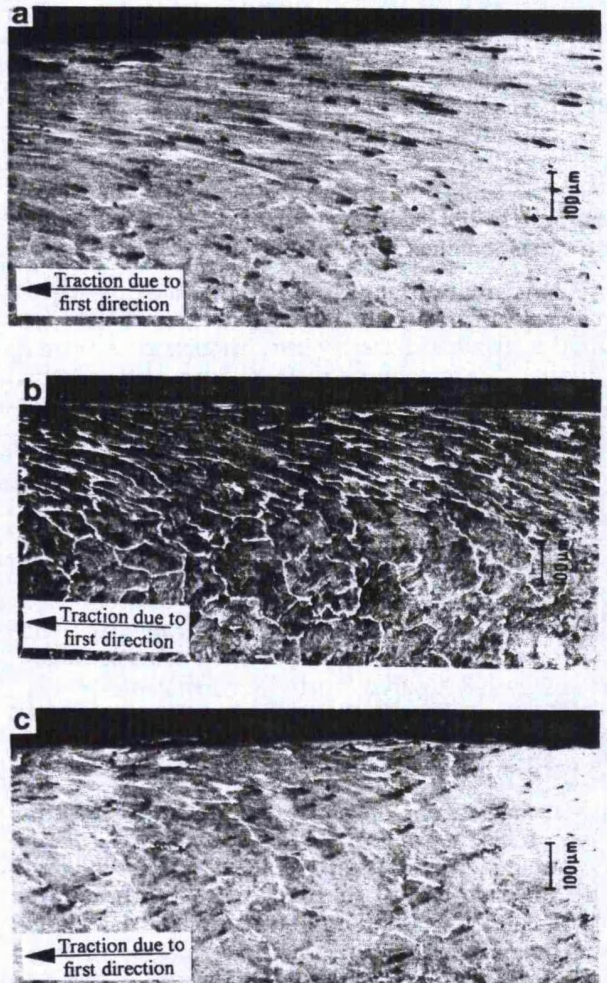


Fig 17 Structure deformation due to multiple rolling direction reversals (a) every 15 000 cycles (test 126A), (b) every 10 000 cycles (test 125) and (c) every 2500 cycles (test 127A)

cycle interval regimes is shown in Figs 18 and 19, respectively. It can be seen that the difference between single and multiple reversal rates increases as the number of cycles per reversal is reduced.

Discussion

Reliability of results

The design features of the LEROS machine, mentioned above, enable accurate control of the test conditions. The ability to control the contact pressure (equation (1)) and the creepage (equation (4)) to within 0.01% made reproducibility of the test results easily achieved. Identical wear rates under similar test conditions is evident. See, for example, the wear rates before RDR in Fig 18.

In spite of the extreme care taken during disk cleaning and weighing, the wear rate data expressed as disk weight loss per rolling cycle against number of rolling cycles in Figs 10 and 16 show slightly scattered patterns. This scatter is greater during the unidirectional test and tests of a high number of cycles in a certain

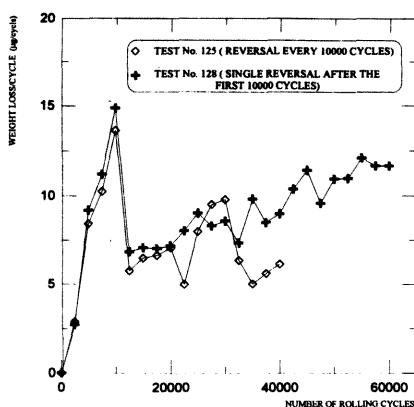


Fig 18 Comparison between the effect of single and multiple rolling direction reversal over an interval of 10,000 cycles

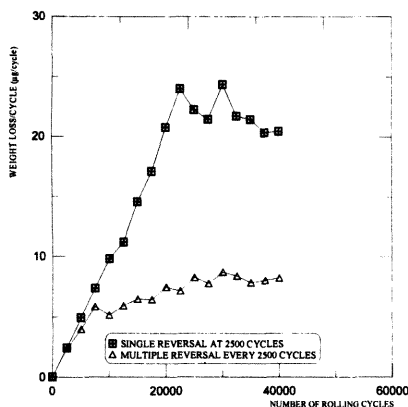


Fig 19 Comparison between the effect of single and multiple rolling direction reversal over an interval of 2,500 cycles

direction. This behaviour could be related to the larger flake size and longer pitch between the flakes, where during cleaning the effect of an extra flake detaching from the surface will be significant in weight loss measurement.

The unidirectional rolling-sliding wear

The present work shows that RDR under the test conditions used has a beneficial effect on the wear rate of pearlitic rail steel. The strength of this effect is a function of the reversal regime, including whether this regime consists of single or multiple reversals. Among the different wear rates obtained under the different reversal regimes the lowest wear rate was

recorded under a multiple reversal regime of 2500 cycles per reversal, the smallest value attempted. The mechanism by which RDR affects the wear rate of the pearlitic rail steel may be better studied if the unidirectional rolling-sliding wear mechanism of pearlitic steel is first understood.

The widely accepted theories of wear use the concept of surface fatigue and fracture mechanics to explain wear mechanisms⁴. However, many researchers⁵⁻⁷ have shown that the strength parameters are not the only factors affecting wear rates. Grozier and Bucher⁵ showed that although there is a good correlation between the wear behaviour and the strength of the material, very little correlation exists between wear rate and work hardening or wear rate and uni-axial fracture properties. Clayton⁶ demonstrated a good inverse relationship between wear rate and total plastic strain obtained in a tensile test. These findings may indicate that the wear rate is a function of many factors, including material composition and microstructure.

During a study of the deformation of pearlitic steels Langford⁷ described this deformation as an interlamellar slip, the analogy being a deck of cards, which takes place when a highly stressed slip system in the ferrite is almost parallel to the plane of cementite lamellae. Figure 11 shows the deformed structure of the pearlitic rail steel disk near to the surface layer caused by the unidirectional rolling-sliding motion, and reveals that the type of deformation prevailing under such conditions is like a deck of cards: one where the deformed structure is parallel to the direction of maximum shear stress. Under such loading conditions it is expected that the surface layer will suffer maximum strain. This strain falls gradually with the depth below the contact surface. Although the stress level caused by a certain rolling-sliding loaded contact at any particular circumferential location in the rail disk is assumed to be constant, it is still possible to increase the total plastic strain by cyclic increments^{6,8}. After a certain number of unidirectional rolling-sliding cycles the accumulated plastic strain could exceed the critical unidirectional plastic strain and cause fracture, which is expected to be within the surface layer of the disk. However, material deficiencies, such as dislocations and inclusions, may encourage subsurface cracking similar to those shown in Fig 6(b). Such cracks were also reported by Jahanmir *et al.*¹⁰.

The deformed structure caused by unidirectional rolling and shown in Fig 11 appears to exhibit directional properties near the contact surface. Crack propagation in a direction perpendicular to the structure laminates proved to be difficult. Indentation parallel to the laminates, at a depth of less than 50 μm below the contact surface, caused laminar separation type of cracks (Fig 3(a)). Even when the indenter corner was very near the free surface, no cracking towards the surface was noted. The indentation mark shown in Fig 3(a) revealed that the indenter caused a separation of a significant width without the separated layer breaking through to the surface. This can be seen from the indentation mark borderline nearer the surface, which indicates that the separation crack has closed back, but not completely, after releasing the

indenter. This directionality in mechanical properties was also reported by Bucher¹¹ during a study of the effect of inclusions on the brittle fracture of hot-rolled steel. Indentation in the bulk material, away from the deformed structure, showed no evidence of directional properties, as revealed from the indentation borders and corners shown in Fig 3(b).

Perez-Unzueta and Beynon¹² showed that the wear rate of pearlitic rail steel decreases with shorter cementite interlamellar spacing. Clayton⁶ demonstrated a strong correlation between wear rate of pearlitic steel and the mean-free path in ferrite. This path is defined as the average distance a dislocation can travel in any direction before encountering an obstacle, whether a carbide plate or a grain boundary. Shorter interlamellar spacing leads to a shorter free path in ferrite. During unidirectional rolling-sliding contact the pearlitic microstructure nearer the surface is deformed in such a way that both the carbide lamellae and the grain boundaries are aligned parallel to the contact surface, as shown in Fig 11. In this case the unit length in the direction parallel to the surface contains the minimum number of obstacles facing the dislocation propagation. On the other hand, perpendicular to the contact surface the obstacle density is at a maximum and increases with shorter interlamellar spacing, as shown schematically in Fig 20. This argument may partially explain the cracking parallel to the contact surface shown in Fig 8, where subsurface cracks are propagating at different levels of the laminar structure without joining, despite the very short distance separating them.

The wear behaviour and the relationship between rail disk weight loss per cycle and the accumulated number of unidirectional rolling cycles shown in Fig 10 can be explained by using the arguments of the critical accumulated plastic strain and the free path in ferrite. The relatively low wear rate during the early cycles could be related to the following:

- (1) The accumulated plastic strain is still below the critical level for fracture.
- (2) The deformed structure is not yet fully aligned and, as a result, the effect of a longer free path

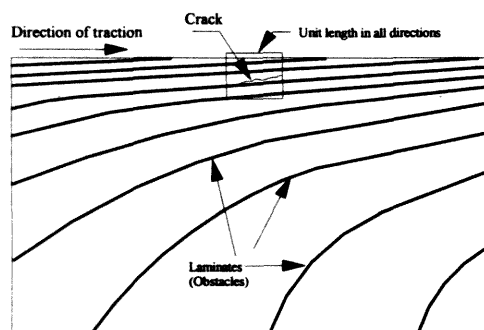


Fig 20 Schematic representation of the lamellar obstacles facing the dislocation movement in a pearlitic deformed structure

in ferrite parallel to the lamellae is still not significant.

The later steady-state wear rate behaviour, which is dominated by delamination and flaking, could be explained using the same arguments of the free path in ferrite and the accumulated critical plastic strain since the effect of both is a function of the number of rolling cycles. Since the maximum shear stress during dry rolling-sliding is known to be at the contact surface, the surface layer will reach the critical plastic strain level before the rest of the material. At the same time, the structure at the surface will be forced to align parallel to the surface. The effect of both actions will result in delaminations and subsequent flaking of the surface layer. Once the first layer has worn off, another layer, partially deformed and strained, is exposed to the surface to face the same result. However, the exact location of cracking could be affected by localized material deficiencies such as inclusions.

Effect of manganese sulphide inclusions

Manganese sulphide inclusions are thought to be suitable sites for crack initiation and propagation and, as a result, they could increase the wear rate^{13,14}. The role of these inclusions in assisting fracture could be explained by arguing that, since they are known to be soft inclusions, their strength is less than that of the bulk material. This can result in a higher localized plastic strain in and around the inclusions. This argument is supported by the work of Krause and Schroelkamp¹⁴, who detected such inclusions within a crack. Bucher¹¹ also reported flat voids around the stringered manganese sulphide inclusions in hot rolled steel sections. Crack initiation at local deformation bands ahead of an inclusion and due to decohesion of the material-matrix interface have recently been reported for four-point bending fatigue of rail steels¹⁵. It should be noted, however, that the MnS inclusion content of the steels used in this work is too low for the wear to be dominated by such a mechanism.

Effect of strain hardening and deformation morphology on wear

Deforming strain-hardened materials is easier before they establish their full hardening. Krause and Schroelkamp¹⁴ showed that most of the strain hardening due to rolling contact takes place during the initial stages of the rolling process. Although no attempt has been made to determine the number of rolling cycles needed to establish the full strain hardening under the test conditions used during the course of this work, it is expected that most of this hardening takes place during the early period when the wear rate is below its steady-state value. This hardening could be the reason for the wavy structure caused by a single RDR at half the total number of rolling-sliding cycles and shown in Fig 15(a). This is a micrograph of the deformed structure of test 124 which was run 20000 cycles in each direction. It can be seen that while the first cycle interval caused the structure to deform parallel to the rolling direction, the length of the reversed cycle

interval was not sufficient to reverse completely the structure deformation to the other direction. Only the part of the structure nearest the surface, where the shear stress is at a maximum, is reversed, causing the wavy structure shown. The single reversal appears to have two effects on the structure's morphology. First, the transition region between the two directions of the deformation moves down below the contact surface as the ratio between the number of cycles in the first direction and that of the second increases. Second, recovery of the deformation caused by the first rolling interval is also noted. Figure 15 shows the structural changes below the rail disk surface caused by the three different single reversal regimes of tests 124, 128 and 129. A complete reversal of the direction of deformation is noted in test 129 where, compared with the other two tests, the ratio of the first to the second cycle interval is very low. In this case the deformed structure is very similar to that of unidirectional rolling shown in Fig 11. This similarity in the deformed structure is associated with an almost similar wear rate nearer the end of the two tests (See Fig 14).

Effect of the RDR regime

Single reversal

Among the three single RDR regimes, that of test 124, in which reversal was carried out after 20000 cycles, resulted in a minimum wear rate after 40000 cycles. According to the criteria of maximum unidirectional plastic strain and the free path in ferrite such behaviour is expected since reversal appeared to have delayed the critical plastic strain limit in addition to its effect on reducing the free path in ferrite. On the other hand, the maximum wear rate is that of test 129, where the rolling direction was reversed after the first 2500 cycles. This behaviour was also expected since the number of rolling cycles after reversal was enough to recover fully the deformation caused by the first cycle interval and to accumulate plastic strain in the opposite direction.

Multiple reversals

The above arguments can be used to explain the wear behaviour under multiple RDR. The approximately equal steady-state wear rates noted during such conditions and shown in Fig 16 could be related to two factors:

- (1) Multiple RDR can result in reducing the plastic strain accumulated in one particular rolling direction.
- (2) It can also produce a structure-deformation morphology which is more complicated than that of single RDR, resulting in additional obstacles to dislocation movement and leading to a smaller flake size.

Both arguments are supported by Fig 21, which shows low-magnification scanning electron micrographs of the running track of the three rail disks tested under different multiple reversal regimes. It can be seen that the minimum flake size (Fig 21(c)) corresponds to the multiple RDR regime of the minimum number of cycles per reversal (in this case, 2500).

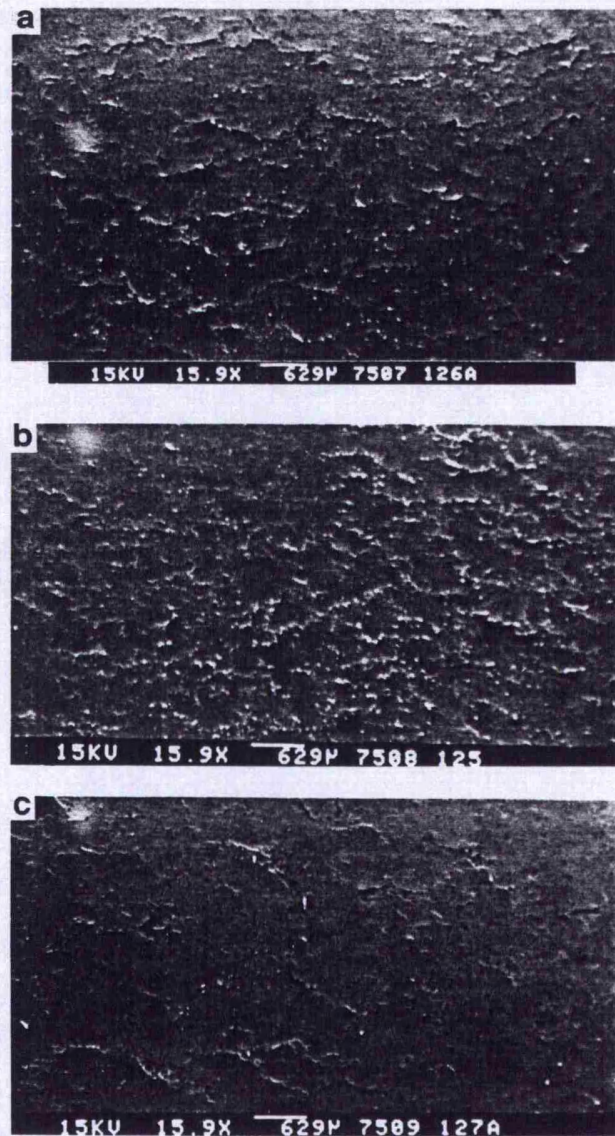


Fig 21 Scanning electron micrographs of the running track of the three rail disks tested under different multiple reversal regimes. (a) 15 000 cycles per reversal, (b) 10 000 cycles per reversal, (c) 2000 cycles per reversal

Summary

To summarize, under the test conditions used during the course of this work, the mechanism by which rolling direction reversal reduces the wear rate of pearlitic rail steel is believed to operate as follows:

- (1) In unidirectional rolling the direction of both the accumulated plastic strain and the pearlitic structure deformation are the same. This can result in:
 - (a) The accumulation of unidirectional plastic strain at and below the contact surface, which is thought to be the reason for surface and subsurface cracking when the unidirectional plastic strain exceeds the critical strain (ductility).

- (b) The deformation of the microstructure leads to the alignment of the carbide lamellae, as well as the grain boundaries, in a straight laminar pattern parallel to the wear surface, resulting in easier interlamellar slip.
- (2) RDR has the following two results acting in contrast to those in (a) and (b) above:
- (a) It reduces the amount of unidirectional plastic strain since a large proportion of the reversed cycles is consumed in turning back the shear deformation accumulated during the previous rolling direction, resulting in a delay for the critical unidirectional strain limit for fracture.
 - (b) It produces a complicated wavy structure hindering dislocation movement and interlamellar slip. The effect of both actions (a) and (b) is to decrease the wear rate.
- (3) Soft manganese sulphide inclusions are believed to have an adverse effect on increasing the wear rate of pearlitic rail steel by causing localized concentration of plastic strain.

Conclusions

- (1) Under the test conditions used during the course of the present work RDR proved to have a beneficial effect on the wear rate of pearlitic rail steel.
- (2) The morphology of the pearlitic deformed structure plays an important role in the wear mechanism and rate.
- (3) Multiple reversals at short cycle intervals gave the minimum wear rate.
- (4) Soft manganese sulphide inclusion increases the wear rate of pearlitic rail steel.
- (5) The mechanism by which the pearlitic rail steel disk loses material appears to be that of delamination caused by accumulated unidirectional plastic strain.
- (6) RDR of the rail disk has no effect on the wear behaviour of the wheel disk.

Acknowledgements

The authors would like to thank the British Railways Board and ABB British Wheelset Ltd who supplied the rail and wheel materials used during this work. The financial support of Mu'tah University of Jordan and the British Council is also appreciated. Dr A. Kapoor is thanked for his helpful comments.

References

1. Tyfour W.R. and Beynon J.H. The effect of rolling direction reversal on fatigue crack morphology and propagation. *Tribology International* 1994, 27, 4, 273–282
2. Garnham J.E. and Beynon J.H. The early detection of rolling-sliding contact fatigue cracks. *Wear* 1991, 144, 103–116
3. Timoshenko S.P. and Goodier D.N. *Theory of Elasticity*, McGraw-Hill, New York, 1970
4. Suh N.P. An overview of the delamination theory of wear. *Wear* 1977, 44, 1–6
5. Grozier J.D. and Bucher J.H. Correlation of fatigue limit with microstructure and composition of ferrite-pearlite steels. *Journal of Materials* 1967, 2, No. 2, 393–407
6. Clayton P. The relations between wear behaviour and basic material properties for pearlitic steels. *Wear* 1980, 60, 75–93
7. Langford G. Deformation of pearlite. *Metallurgical Transactions* 1977, 8A, 861–875
8. Garnham J.E. and Beynon J.H. Dry rolling-sliding wear of bainitic and pearlitic steels. *Wear* 1992, 157, 81–109
9. Kapoor A. A re-evaluation of the life to rupture of ductile metals by cyclic plastic strain. *Int. J. of Fatigue and Fracture of Engineering Materials and Structures* 1994
10. Jahanmir S.J., Suh N.P. and Abrahamson E.P. Microscopic observations of the wear sheet formation by delamination. *Wear* 1974, 28, 235–249
11. Bucher J.H. The effect of inclusions on the brittle fracture of hot rolled steel. *Journal of Materials* 1967, 2, No. 2, 432–445
12. Perez-Unzueta A. and Beynon J.H. Microstructure and wear resistance of pearlitic rail steels. *Wear* 1993, 162–164, 173–182
13. Steel R.K. and Stone D.H. Developments in railroad rails. *Proc. of The American Railway Engg. Assoc.* 1986, 87, 311–358
14. Krause H. and Schroelkamp C. Influence of non-metallic inclusions on the wear behaviour of ferrous metals in nominally dry friction systems. *Wear* 1987, 120, 353–367
15. Lui C.D., Bassim M.N. and Lawrence S.St. Evaluation of fatigue crack initiation at inclusions in fully pearlitic steels. *Materials Science and Engineering* 1993, A167, 107–113
16. Krause H. and Demirci H. Factors influencing the real trend of the coefficient of friction of two elastic bodies rolling over each other in presence of dry friction. In: *The Mechanics of Contact Between Deformable Bodies*, Pater A.D. and Kalker J.J. (Eds), Delft University Press, 1975

APPENDIX 3

Journal Offprint Paper

BUTTERWORTH
HEINEMANN

 A member of the Reed Elsevier group

Linacre House, Jordan Hill, Oxford OX2 8DP, UK

OFFPRINT PAPERS

Butterworth-Heinemann are leading international publishers of a range of highly respected academic journals in Applied Science, Information Technology, Engineering, Materials Science, Policy Studies, Social Sciences, Biomedical Sciences and Medicine. Our journals are renowned for their high quality of both content and presentation. Papers are peer-reviewed and all our journals have distinguished editorial boards.

If you would like to receive subscription details, a sample copy or other information about the journal in which this offprint appeared, please complete and return the form provided below. Information about our other titles is available from our price list or catalogue (see form below).

Notes for Authors

To obtain details on how to submit papers to one of our journals, please contact:
The Group Editor at the Oxford address below (please state the appropriate journal title).

Reprints

We can reprint any article appearing in our journals and tailor it to your needs with an advert or logo. For a quotation on your reprint requirements, please contact:
The Reprints Department at the Oxford address below.

For further information about any other aspect of our journals, please contact us at:
Butterworth-Heinemann Ltd., Linacre House, Jordan Hill, Oxford, OX2 8DP, UK
Tel: +44 (0) 865 310366 Fax: +44 (0) 865 310898

✂ Please cut here

Return Form

Area(s) of Interest:

Journal Title(s)

Subscription Details Request

Please send me full subscription details and information about the above journal title(s)

Sample Copy Request Form

Please send me a free sample copy of the above journal title(s)

Journals Price List

Please send me a full price list for all your journals

Catalogue

Please send me a catalogue of your journals

Name

Organisation

Address

Postcode / Zipcode Country

Telephone E-mail

Fax Signature Date

Please return this form to:

Butterworth-Heinemann Ltd.
Turpin Distribution Services Ltd.
Blackhorse Road
Letchworth
Herts, SG6 1HN, UK
Tel: +44 (0) 462 672555
Fax: +44 (0) 462 480947

OR

Journal Fulfilment Department
Butterworth-Heinemann US
80 Montvale Avenue
Stonham
MA 02180, USA
Tel: +1 617 438 8464
Fax: +1 617 438 1479

The effect of rolling direction reversal on fatigue crack morphology and propagation

W. R. Tyfour and J. H. Beynon

The effect of repeated rolling direction reversal on crack morphology, propagation and RCF life of rail steel is investigated in this paper. It has been established that reversal is of beneficial effect on RCF life. This effect is a function of the reversal regime. An optimum reversal is achieved when the number of rolling cycles per reversal is between 25% and 37% of the uni-directional RCF life cycles of the material. Under such a reversal regime, the RCF life is almost doubled. Rolling direction reversal appears to affect RCF cracking propagation as well as morphology. A new mechanism, the 'variable crack face friction mechanism', is proposed to explain this effect.

Keywords: rolling contact fatigue (RCF), rolling direction, reversal, crack morphology, crack propagation

Introduction

Among the different forms of rail damage caused by the counter form contact between railway wheel and rail, rolling contact fatigue (RCF) failure in particular is given considerable attention since its potential to develop transverse rail fracture and cause derailments remains a real threat. Research had been focused on improving the RCF life of rail by proper selection of rail steel, reducing its inclusion content, and trying to understand the effect of the different conditions under which RCF develops.

The present work is aimed at studying one of the service conditions prevailing in some railway systems, where a single line is used for two-directional traffic. The condition is simulated in the laboratory by using a rolling contact disk machine, where two cylindrical disks machined from rail and wheel are loaded and rolled. The rolling direction reversal is achieved by inverting the rail specimen at every certain number of rolling cycles.

The study may not be of direct applicable advantage to double line railway systems, where rolling is unidirectional. However, it may help in a better understanding of some of the phenomena associated with RCF in general, such as the role of lubricant and RCF cracking morphology.

Procedure

Wheel and rail test disks are cut from wheel rims and rail sections, kindly supplied by ABB British Wheelset Ltd and the British Railways Board, respectively. The orientation of the disks in relation to the wheel and rail are shown in Fig 1. Disks were machined to the dimensions shown in Fig 2. The diameter of the disks is limited by the dimensions of the rail head. The 47 mm disk diameter is the maximum obtainable from the rails supplied.

The chemical composition and mechanical properties of the disk materials are given in Table 1. To ensure homogeneous properties, rail disks were cut with their axis parallel to the rail long axis, whereas wheel disks were cut with their axis parallel to the wheel tread tangent. All cutting and machining operations were conducted to maintain the original microstructure and properties. The dimensional tolerances of the disks were measured for roundness and possible eccentricity between the track surface and the bore using a Talyrond 200 profilometer (Rank Taylor Hobson Ltd). Prior to test start, disks were scanned for surface defects using an Elotest B1 eddy current flow detector (Rohmann UK Ltd), then cleaned in an ultrasonic bath of isopropanol.

Since the type of wheel/rail motion is known to be that of combined rolling and sliding, it was decided to use the LEROS (Leicester Rolling Sliding wear machine), which is described in detail elsewhere¹. The machine is basically a Colchester Mascott 1600 lathe modified to suit the purpose. A 4 kW d.c. motor is mounted on the tail stock end of the machine bed. A drive shaft consisting of universal joints and splines is

Department of Engineering, University of Leicester, University Road, Leicester LE1 7RH, UK.
Received 29 November 1993; revised 21 February 1994

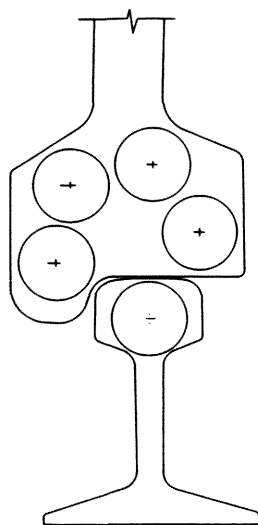


Fig 1 The orientation of the disk specimens relative to the rail head and wheel rim

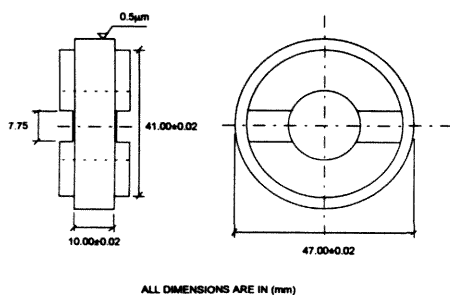


Fig 2 Dimensions of the test disks

powered by the d.c. motor through an interchangeable gearbox of 5:1 gear ratio. The other end of the drive shaft is fitted with a machine tool arbor, supported through a pivoted bearing assembly. The wheel disk specimen (driving disk) is bolted to the end of the arbor. This assembly can swing by the action of a hydraulic jack powered by an electric motor-driven hydraulic pump to facilitate the loading mechanism. The rail material disk (braking disk) is secured to an arbor at the end of another drive shaft supported between a bearing housing and the lathe chuck. The mid-section of this drive shaft is a torque transducer, which enables measurement of the tractional torque between the two disks. The centre lines of the two drive shafts are parallel when disks are loaded. The required slip ratio (creepage) is achieved by adjusting the rotational speeds of the two drive shafts.

Table 1 Chemical composition and mechanical properties of the test materials

Material	Rail	Wheel
Specification	BS 11	W8A
Chemical composition (wt%)		
C	0.52	0.64
Si	0.2	0.23
Mn	1.07	0.71
Ni	0.03	0.17
Cr	<0.01	0.18
Mo	<0.01	0.03
S	0.018	0.041
P	0.013	0.023
Mechanical properties		
Average hardness (HV 500g)	240	270
Ultimate tensile strength (MPa)	781	857
Yield strength (MPa)	406	325
Total plastic elongation (%)	21.9	20.3
Young's modulus (GPa)	209	199

The machine is equipped with manual as well as computer creepage control through a number of shaft encoders, transducers and a computer interface. Contact load is easily applied and controlled by electronically adjusting the opening of the hydraulic control valve that passes the oil to the jack, which in turn raises the bottom shaft bearing assembly.

The hydraulic loading system enables loads up to 29 kN to be applied. Assuming, for the sake of illustration, a Hertzian elastic contact, for the dimensions of disk specimens used in the present work this represents a maximum contact pressure of 3000 MPa. This feature of the machine results in minimizing the disk track edge effect since wider track disks can be accommodated.

To detect RCF cracks, a computer-controlled non-contact eddy current crack scanning system is used. This scanning system represents a reliable method in which an alarm level can be adjusted to activate a signal when RCF cracking reaches a certain stage. It also enables the defect area to be located with sufficient accuracy.

The formula used to calculate the maximum contact pressure p_0 (MPa) is that suggested by Timoshenko and Goodier²:

$$p_0 = 0.418 \left(\frac{WE}{TR} \right)^{1/3} \quad (1)$$

where W is the contact load (N), T is the line contact length (mm), E is the modulus of elasticity of steel (MPa) and R is given by:

$$\frac{1}{R} = \frac{1}{R_T} + \frac{1}{R_B} \quad (2)$$

where R_T and R_B (mm) are the radii of the top and bottom disks, respectively.

The creepage or slip ratio is calculated by

$$g(\%) = \frac{200(R_T N_T - R_B N_B)}{R_T N_T + R_B N_B} \quad (3)$$

where R_T and R_B are as defined in equation (2), and N_T and N_B are the revolution counts of the top and bottom disks, respectively.

All tests of the present work were conducted under a maximum contact pressure of 1500 ± 5 MPa and a creepage of $1 \pm 0.01\%$. The contact area was water lubricated using a gravity drip system supplying approximately 1 drip per second. Test conditions are shown in Table 2. Rail disks were reversed every predetermined number of rolling cycles. The non-dimensional term 'reversal factor' is used during this work to define the regime of rolling direction reversal for the rail disk and is defined by:

$$RF = \frac{C_r}{L_u} \quad (4)$$

where C_r is the number of rolling cycles per reversal and L_u is the number of rolling cycles to cause RCF failure in a uni-directional rolling test under the same conditions of load and creepage.

For the purpose of the present work, the RCF life is defined as the number of rolling cycles required to

initiate and propagate a RCF crack deep enough to trigger a pre-set alarm level on the eddy current flow detection unit. This alarm level was set by using a calibration disk, machined from the same rail material, in which an artificial crack has been spark eroded to a certain depth below the track surface.

Upon failure, defects were located and marked, disks were removed, cleaned, and final dimensions, roundness and surface roughness profiles were recorded. All disks were sectioned and optical metallography of crack morphology and microstructural changes were studied and photographed. The microhardness across the depth below the contact surface was also measured.

Results

A summary of the test results is shown in Table 3. The non-dimensional term 'life factor' is introduced to evaluate the change in RCF life under conditions of different reversal factors. Life factors of more than unity mean an increase in the RCF life over that obtained in the uni-directional test and vice versa.

Crack location is the distance of the maximum signal from the track edge nearest to its drive shaft. Crack dimensions are reported for all cracks over $180 \mu\text{m}$ deep and are presented as average values, except for the crack depth, where the maximum depth is also presented. The term 'crack direction competition factor' (CDC factor) is introduced to evaluate the direction for the crack propagation and is defined as

Table 2 Summary of test conditions

Test conditions	Test number						
	113	114	115	116	119	120	121
Disk material							
Top (rail)				BS 11			
Bottom (wheel)				W8A			
Maximum contact pressure (MPa)				1500			
Percentage creepage (%)				1			
Test speed (RPM)							
Rail/wheel				402/406			
Initial surface roughness (R_a)							
Rail/wheel	0.38/ 0.47	0.38/ 0.39	0.28/ 0.37	0.32/ 0.33	0.20/ 0.21	0.20/ 0.19	0.21/ 0.32
Number of cycles per reversal (rail)	5000	37422	10000	18711	28066	14033	2000
Reversal factor ^a (rail)	0.133	1 ^b	0.267	0.5	0.75	0.375	0.0534
Lubrication	Water (one drip per second)						

^aReversal factor is the ratio between the number of rolling cycles per reversal and the number of cycles to RCF failure in unidirectional rolling
^bUnidirectional test

Table 3 Summary of test results

Test results	Test number						
	113	114	115	116	119	120	121
Number of rolling cycles to failure (rail disk revolutions)	55000	37422	70000	52119	41365	69123	50980
Number of reversals to failure	11	*	7	2.87	1.47	4.92	25.49
Life factor ^b	1.469	1	1.870	1.392	1.015	1.847	1.362
Contact area (mm ²)				6.11			
Crack location ^c (mm from the reference track edge)	3.7	4.5	4	5.2	5.7	4	5
Maximum crack length (μm)	586	1226	276	920	Not measured	920	908
Average crack length (μm)	536.9	881	276	759	Not measured	893	908
Average crack depth (μm)	296	410	180	445	Not measured	585	403
Crack direction competition factor ^d	0.65	0.57	0.85	0.71	Not measured	0.85	0.53
Steady state coefficient of friction	0.1320	0.1248	0.123	0.1250	0.1255	0.1320	0.1487
Average coefficient of friction	0.128	0.104	0.117	0.119	0.125	0.128	0.144
Weight loss (μg/cycle)	0.821	1.460	0.932	1.030	0.964	1.328	1.570
Diameter loss (nm/cycle)	0.909	0.668	0.857	0.767	0.725	0.578	1.210
Track width gain (nm/cycle)	4.380	4.810	4.710	6.040	6.040	3.970	8.730

^aUnidirectional test

^bLife factor is the ratio of the life cycles of rail disks tested under reversal conditions and those obtained under unidirectional conditions

^cAs defined in the text

^dCrack direction competition (CDC) factor is the ratio of crack propagation length in the radial direction and that in the circumferential direction

the ratio between crack depth, measured radially from the track surface, and the crack circumferential length measured parallel to the surface between the mouth and the tip of the crack (Fig 3). This method of reporting the crack morphology was preferred since it takes into consideration the crack branching and changing direction.

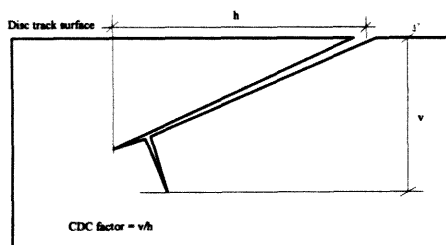


Fig 3 Schematic representation of the definition of the CDC factor (section cut normal to the rotation axis of the disk)

The coefficient of friction is calculated from the torque-time chart recorded during each test. It is reported as steady state as well as average values. The steady-state coefficient of friction does not include the effect of the running-in period, which in this case is characterized by a low coefficient of friction for the first few thousand cycles, which is thought to be caused by the formation of an oxide layer on the surface of the rail disk track. The coefficient of friction starts to rise as the oxide layer gradually disappears, starting from the track edge where a shiny fresh metal band begins to grow across the track. The coefficient of friction stabilizes as the oxide layer completely disappears. The mean value of friction coefficient is obtained as a time average value.

The effect of rolling direction reversal on the RCF life of pearlitic rail steel is shown in Fig 4, in which the reversal regime is represented by the reversal factor and the change in RCF life by the life factor. It can be seen from the plot that any reversal regime has a beneficial effect on the RCF life of pearlitic rail steel. This effect ranges from +10.5% for a reversal factor of 0.75 to +87.4% for 0.267. The maximum

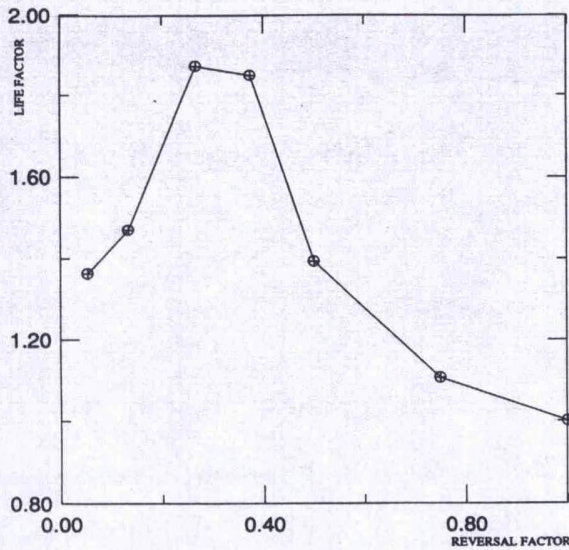


Fig 4 Effect of rolling direction reversal on RCF life

RCF life improvement appears to be achieved between reversal factors of 0.267 and 0.375.

The relationship between the life factor and the crack direction competition (CDC) factor is shown in Fig 5. Although the data are scattered, they still show a trend of higher life factor with higher CDC factor.

Figure 6 shows the relationship between the reversal factor and the CDC factor, where it can be seen that the CDC factor is at its maximum value when the reversal factor is between 0.267 and 0.375. Superimposing this relationship on that between reversal factor and life factor shows that the optimum life factor and the maximum CDC factor are coincident and obtained under the same reversal factor.

Optical microscopy of sections perpendicular to the rotation axis of the disk through the crack face reveals different crack morphologies under different reversal regimes. RCF cracks in the rail specimen run unidirectionally in test number 114 are characterized by a

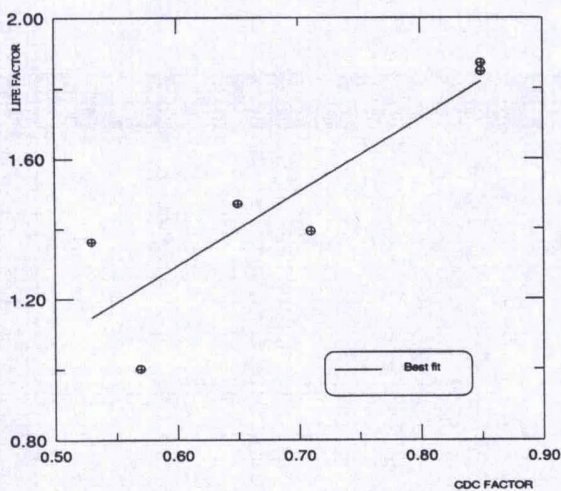


Fig 5 Relationship between life factor and CDC factor

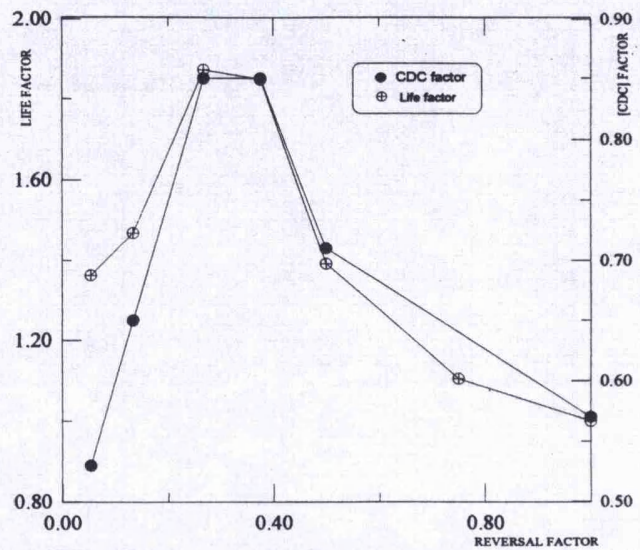


Fig 6 Effect of reversal factor on life factor and CDC factor

main straight crack, propagating at an angle of approximately 30° to the surface in the direction of load movement, as shown in Fig 7. In this case crack branching is mostly perpendicular to the main crack towards the contact surface. A crack network is formed by these branches joining parallel main cracks.

The cracks in the specimen run under a reversal factor of 0.267 (10 000 cycles/reversal), which gave the maximum life factor during test number 115, are of a quite different morphology. They can be classified into two types: first, the 'branched' type, which is characterized by a primary crack propagating to a shallow depth below the contact surface before it diverts its direction to the opposite sense. It then branches parallel to the initial direction to produce a two-branch crack as shown in Fig 8. The second type is the 'double' cracking type, which is characterized by two cracks of different initiation points but of opposite senses of direction, as shown in Fig 9. The

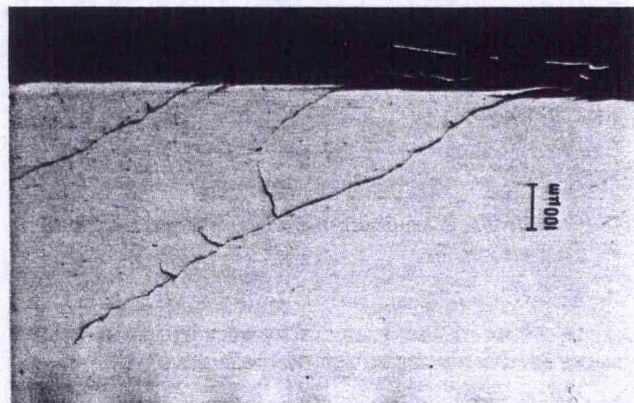


Fig 7 RCF cracking under unidirectional rolling conditions (test no. 114)

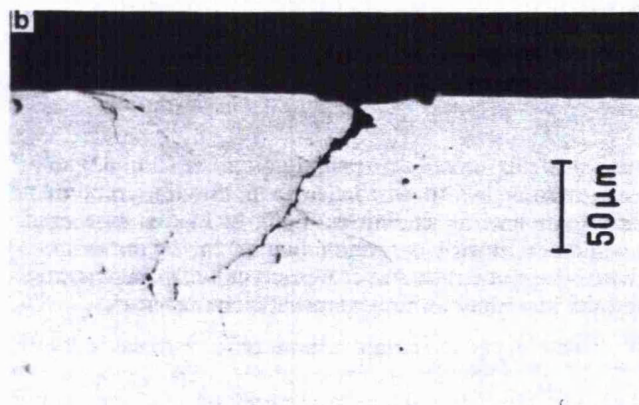
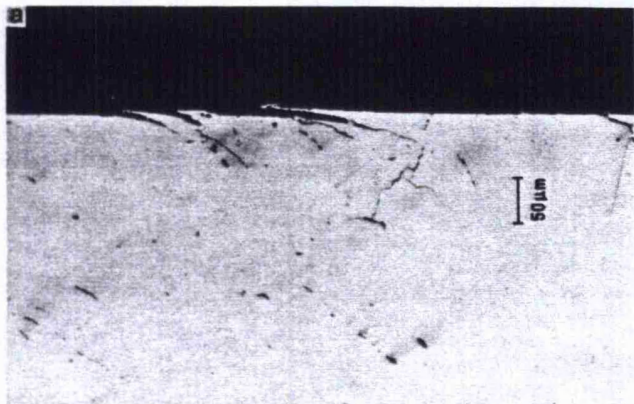


Fig 8 Branched type RCF crack under a reversal factor of 0.267 (test no. 115)

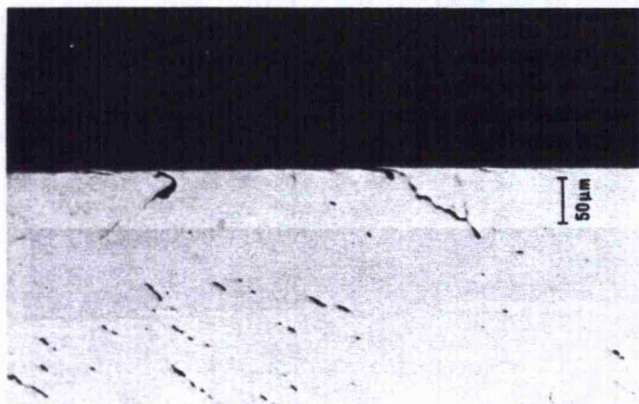


Fig 9 Double RCF cracking under a reversal factor of 0.267 (test no. 115)

angle between the two cracks is very close to that between the two branches of the branched type.

Figure 10 shows a crack of the branched type, with a longer primary crack, found in the rail test disk of test number 116 which was conducted under a reversal factor of 0.5 (18711 cycles/reversal). Cracks in test

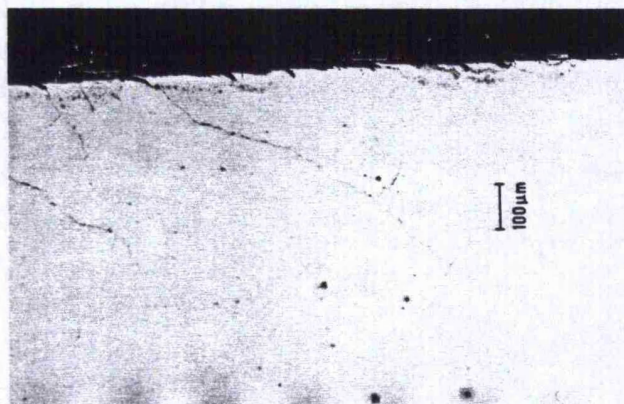


Fig 10 RCF cracking under 0.5 reversal factor (test no. 116)

disks run under a reversal factor of 0.053, which represents the lowest reversal factor used and corresponds to 2000 cycles/reversal, were similar to those of the unidirectional test number 114, except that the crack line is slightly wavy, as shown in Fig 11. All cracks studied during the present work were observed to originate from either a pit or a flake root. A summary of the different crack morphologies under conditions of different reversal factors is represented schematically in Fig 12, which shows a braking elastic half-space subjected to a driving load travelling in the x y plane in the direction of the box arrows. $p(x)$ and $q(x)$ are the pressure and traction distributions, respectively, at a distance x from the centre of the contact. The arrows within the half-space represent the direction of load movement under which the marked portion of the crack has propagated.

The relationship between the microhardness and the depth below the contact surface for the rail disks is shown in Fig 13. It appears that the reversal factor has no effect on the depth of maximum hardening. Best-fit analysis shows that the data fit a fourth-degree polynomial relationship with a peak hardness value at 0.25 mm below the contact surface. This figure is very



Fig 11 The wavy shape RCF cracking under a reversal factor of 0.053 (test no. 121)

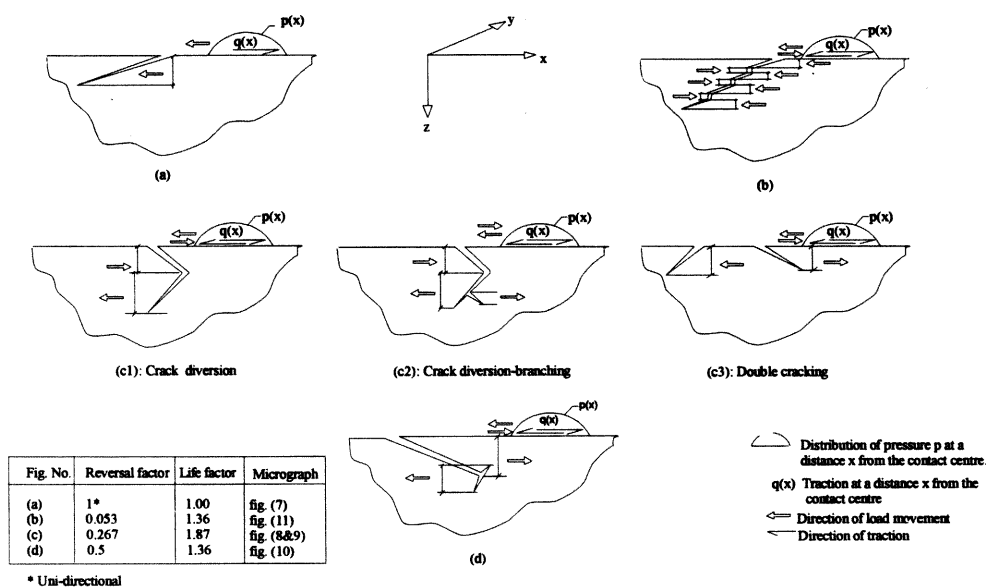


Fig 12 Schematic representation of cracking morphology under different reversal factors

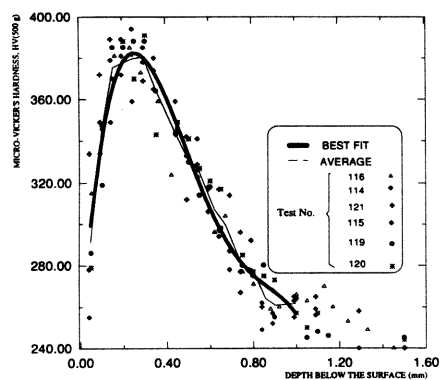


Fig 13 Effect of rolling direction reversal on hardness profile

near to 0.238 mm, which is the theoretical location of the maximum shear stress obtained by applying the Hertzian analysis and calculated by²

$$Z_m = 0.78a \quad (5)$$

where Z_m is the depth of maximum shear stress and a is the semi-contact width of two elastic cylinders calculated from:

$$a = 1.52 \left(\frac{WR}{TE} \right)^{1/3} \quad (6)$$

where W , R , T and E are as defined in equation (1).

The number of rolling cycles seems to affect neither the value nor the location of maximum hardening. This supports the suggestion that strain hardening takes place during the initial stages of the loaded rolling contact process³.

Wear rates were measured at the end of each test and reported as weight loss/cycle. Similarly, diameter loss and track width gain are also presented. No significant trend was found between reversal factor and these values.

Discussion

The results presented in the previous section suggest that rolling direction reversal is of beneficial effect on RCF life of pearlitic rail steel. They also indicate that reversal affects the morphology of RCF cracking.

Several researchers have indicated similar effects³⁻⁵. Fujita *et al.*³ carried out oil-lubricated rolling direction reversal experiments on carbon steel under a reversal regime of just one reversal after varying number of cycles and reported significant improvement in RCF life. Ichinose *et al.*⁴ also indicated an extended fatigue life and suggested that if the rolling direction is reversed the cracks formed in the primary direction cease to propagate.

The mechanism by which the rolling direction reversal improves the RCF life may be better understood if it is possible to understand the effect of reversal on crack propagation. Crack propagation in unidirectional rolling has been the subject of considerable attention by researchers using the theory of fracture mechanics

to study the stress field around the tip of a propagating RCF crack⁶⁻⁹. Since the presence of a fluid lubricant is known to be essential for RCF cracking, most of the theories by which this cracking is explained are focused on the role of the fluid lubricant in the crack-propagation process. This role seems to remain an area of debate. Some suggest that the fluid enters the crack and acts as a lubricant, resulting in a reduction of the coefficient of friction between the two faces of the crack to allow them to slide relative to each other, so that the crack can propagate in mode II¹⁰. Others^{5,8} supported and developed the pressurizing mechanism of Way¹¹. Bower⁸ introduced further improvements to the pressurizing mechanism and called it the trapped fluid mechanism. According to this mechanism, the crack is filled with the fluid just before its mouth reaches the contact area. Afterwards, the mouth is sealed under the contact area. As a result, the crack cavity is pressurized and the fluid is forced towards the crack tip to generate mode I stress intensities. Under pressure, the fluid escapes from the crack cavity and keeps part of the crack open to allow relative motion between the two faces of the crack and generate mode II stress intensities.

If the rolling direction is reversed, the crack tip enters the contact pressure zone between the two disks before the mouth. In this case no fluid is expected to be trapped since the crack cavity is gradually closed starting from the crack tip, while the crack mouth is still open. As a result, the RCF crack formed in the preceding rolling direction is not expected to propagate in mode I when the rolling direction is reversed. Similarly, in the absence of the lubricant, the compressive load will increase the frictional force between the two faces of the crack and will reduce the mode II propagation.

The implication of Bower's model⁸ was that the primary RCF crack would not divert or branch upon reversal of the rolling direction, nor would it grow significantly during the reversal period. In the present work, cracks have clearly demonstrated that they branch and continue to grow in a direction different from the primary crack during the reversal.

RCF cracks propagate in the braking part of the rolling/sliding system in a 'preferential direction' which is the direction of the driving load movement as shown in Fig 14. Upon reversal, many parameters in the stress cycle are affected.

The following descriptive mechanism is proposed to explain crack propagation under rolling direction reversal conditions and will be referred to as the 'variable crack face friction mechanism'. No attempt will be made to explain the initiation or early propagation of the primary crack.

First, it is assumed that the primary crack propagates in the direction of load movement to a certain length during a certain cycle interval. Upon reversing the rolling direction, the crack tip will start to enter the Hertzian pressure-dominated area before the mouth, leading to the gradual closure of the crack starting from the tip. The coefficient of the friction between the crack faces is expected to be at its maximum value

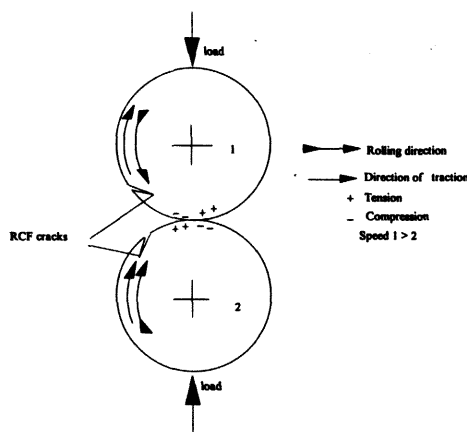


Fig 14 A schematic representation of the rolling/sliding system showing the direction of crack propagation

nearest to the crack tip and to decrease gradually towards the crack mouth. Lower crack face friction nearer to the crack mouth can be explained by one or more of the following arguments:

1. The lubrication effect of the residual fluid which is assumed to have entered the crack during the preceding rolling direction cycles.
2. Reduction of crack face surface roughness due to the plastic deformation of the crack faces caused by the rubbing action. Such a rubbing action was reported by Ichinose *et al.*⁴
3. The chemical changes of the crack surfaces caused by exposure to the environment, notably oxidation. The role of oxidation in reducing the coefficient of friction, and subsequently the torque between the two disks during the running-in period, had been mentioned earlier. A similar effect of oxidation between the two faces of the crack has been reported by Kalousek¹⁵.

It is expected that the maximum effect of these actions will be in that part of the crack which is nearest to the mouth, since it is this part of the crack which has been subjected to a higher number of rolling cycles, is nearer to the surrounding environment and has a wider opening. This leads to the conclusion that freedom of the crack faces to slide relative to each other decreases with distance from the crack mouth. As a result, at a certain distance from the crack mouth the crack is expected to lock up, and mode II propagation can no longer operate at the crack tip. The point of the crack corresponding to this lock-up will be subjected to tensile stresses in a plane perpendicular to the direction of the relative motion between the two surfaces. This type of loading causes the crack to branch from that point and to start propagation by mode I. This argument is supported by the work of Smith¹⁴, who tried to propagate mode II cracks while they were under compressive loading

and found that under such conditions the crack branches to propagate in mode I.

In modelling the mechanism by which RCF cracks propagate, most workers assume a constant coefficient of friction over the whole crack length⁶⁻⁹. They also show that mode II crack propagation is very sensitive to crack face friction. Smith¹⁴ suggested that crack face friction is the main reason for mode II crack branching and that friction can lock up the crack tip and reduce the difference in mode II stress intensity factor (ΔK_{II}) to zero. Under such conditions, mode II crack growth will be arrested. If a mode II crack is arrested by friction, it would start to grow again only if a much higher load is applied after it had branched to mode I¹³. This may partially explain the improvement in life factor if the rolling direction is reversed.

The question remains as to how a particular reversal regime results in maximum RCF life. The effect of rolling direction reversal on crack initiation is beyond the scope of the present work and no attempt will be made to discuss this effect. Instead, discussion will be focused on the effect of three reversal regimes on the RCF life according to the variable crack face friction mechanism. Tests with reversal factor of 0.053 and 0.5 represent two regimes below and above the optimum reversal factor of 0.267.

Reversal under a reversal factor of 0.053 (test number 121)

The crack morphology in this case is shown in Fig 11 and schematically represented in Fig 12(b). Comparing this morphology with that of the unidirectional rolling crack of Fig 7 reveals that the crack of the 0.053 reversal factor is not as straight as that of unidirectional rolling. It is suggested that the wavy shape of the crack in this case is due to the rolling direction reversal. According to the proposed crack propagation mechanism, the short reversal intervals were not sufficient to cause complete crack direction inversion or branching. Instead, it seems that the cycle reversal was being carried out just after the beginning of the crack direction diversion. These small diversions, which are schematically shown in Fig 12(b), should slightly increase the angle of the crack to the free surface. However, the angle in this case is found to be slightly less than that of the unidirectional case shown in Fig 12(a). This behaviour can be explained by arguing that RCF cracks observed under unidirectional rolling conditions do not keep an exact prevailing propagation angle. This angle can vary slightly for tests conducted under the same conditions due to material structural heterogeneities.

The improvement in life factor in this case could be related to the arrest of mode II propagation by crack face friction during the cycle interval when the direction of the crack is opposite to that of the load movement. This action is supported by work of Smith¹⁴, which has been mentioned earlier. The evidence clarifying crack propagation under a regime of reversals becomes clearer at larger reversal factors, as will now be discussed.

Reversal under a reversal factor of 0.267 (test number 115)

Figures 8 and 12(c) show the crack of the maximum life factor, caused by a reversal factor of 0.267, which corresponds to 10000 cycles/reversal. It can be seen that the cracks in both the micrographs of Fig 8 are of nearly an identical geometry. Each has diverted its direction by nearly 90° in relation to the primary crack and then branched later in a direction parallel to the primary crack. This diversion and branching is thought to be caused by crack face friction variations as described earlier. The angle between the secondary branches and the free surface is larger than that of the unidirectional crack shown in Fig 7. The improvement in life factor in this case is greater than with a reversal factor of 0.053. In addition to the arrest of mode II propagation mentioned above, the large angle between the crack and the free surface also reduces both mode I and II stress intensities⁶⁻⁹. It seems that the cycle interval in this case was sufficiently long to divert the crack in the first reversal after the crack initiation and branch it during the next reversal from a point nearer to the surface than the tip of the original crack. This branching point corresponds to the onset of the crack lock-up where tensile stresses encourage branching under mode I. The new branch will consume a proportion of the cycle interval to merely reach the depth of the main crack (Fig 12(c)).

The argument that RCF cracks such as those shown in Fig 8 are hard to propagate and that rolling direction reversal arrests the cracks formed during a previous opposite rolling direction is supported by the cracking morphology shown in Fig 9, which illustrates two cracks of almost the same angle to the surface but of opposite direction. This morphology suggests that only one crack – which is in the direction of load movement – is propagating during each cycle interval. If this were the only mechanism, such a cracking morphology should result in a life factor of 2. Figure 4 shows that at the optimum reversal factor between 0.267 and 0.375 this factor of 2 is almost reached, indicating that there is little propagation of cracks which are not favourably oriented to the prevailing loading direction. This must apply whether the cracks are branching, as in Fig 12 (c1 and c2), or growing separately, as in Fig 12 (c3).

Reversal under a reversal factor of 0.5 (test number 116)

Figure 10 is a micrograph and Fig 12(d) a schematic representation of the cracking of a rail specimen tested under a reversal factor of 0.5, which corresponds to a change in rolling direction every 18711 cycles. It is noted that the primary crack has propagated to a relatively deeper distance as a unidirectional RCF crack before it starts to branch from the tip. The large branch seen above the tip is not expected to be due to reversal. It may have taken place in a similar mechanism to that of the unidirectional crack branching shown in Fig 7, since in both cases the branching is upwards. In addition, such a branch may cause a pit rather than a transverse defect. The branch at the tip

is expected to be caused by the reversal. However, it seems that the cycle interval in this case was sufficiently long to propagate the crack almost to failure. The failure appears to have been delayed by the reversal which, according to the proposed mechanism, arrested mode II propagation by the high friction at the crack tip before leading to mode I propagation. This may explain why the improvement in life factor in this case is not as large as for the optimum reversal strategy.

To summarize, the different mechanisms by which RCF crack propagation is explained⁶⁻⁹ were found to be unable to predict the type of crack morphology and propagation prevailing under conditions of repeated rolling direction reversal.

The proposed variable crack face friction mechanism, discussed above, predicts crack branching or direction inversion at the lock-up point of the crack. In the reversed cycle interval, where the crack tip reaches the pressure zone before the mouth, the lock-up point is expected to lie in the part of the crack which is nearest to the crack tip. Crack face friction rises from a minimum at the crack mouth to a maximum nearest to the tip, leading to each long crack having a slip and a stick crack face region. A crack locks up at the transition point between the two regions, giving rise to tensile stresses and encouraging mode I propagation in a direction perpendicular to the crack faces. The assumption that the crack face friction increases away from the mouth, rather than remaining constant as suggested by others⁶⁻⁹, has a sound foundation which has been discussed earlier.

Finally, it is expected that the variable crack face friction mechanism proposed in this work to explain the effect of rolling direction reversal may be extended to explain the branching of unidirectional RCF cracks. However, this is beyond the scope of this work.

CONCLUSIONS

1. Rolling direction reversal has a beneficial effect on the RCF life of pearlitic rail steel. The life factor is almost doubled when the reversal is repeated in cycle intervals of 25–37% of the unidirectional RCF life.
2. Cracking morphology is affected by the rolling direction reversal. The degree of this effect depends on the reversal factor.
3. The variable crack face friction mechanism can explain the improvement in rolling contact fatigue life under rolling direction reversal conditions.
4. Rolling direction reversal has no effect on the magnitude or the location of maximum strain hardening. After a certain number of cycles, hardening reaches its peak and further cycling has no effect.

5. It is expected that reversing the rolling direction has the same effect on other materials and components loaded under conditions akin to those of the wheel and rail, such as gears, rolling bearings and belts.

Acknowledgements

The authors would like to thank the British Railways Board and ABB British Wheelset Ltd who supplied the rail and wheel materials used during this work.

References

1. Garnham J.E. and Beynon J.H. The early detection of rolling-sliding contact fatigue cracks. *Wear* 1991, **144**, 103–116
2. Timoshenko S.P. and Goodier D.N. *Theory of Elasticity*, McGraw-Hill, New York, 1970
3. Fujita K. and Yoshida Y. The effect of changing rolling direction on the rolling contact fatigue life of annealed and head hardened steel rollers. *Wear* 1977, **43**, 315–327
4. Ichinose H., Takehara J., Iwasaki N. and Ueda M. An investigation on contact fatigue and wear resistance behaviour in rail steels. *Heavy Haul Railway Conference, Perth, Australia, September 1987*
5. Kaneta M. and Murakami Y. Effect of oil hydraulic pressure on surface crack growth in rolling/sliding contact. *Tribology International* 1987, **20**, 210–217
6. Keer L.M. and Bryant M.D. A pitting model for rolling contact fatigue. *Transactions of ASME, Journal of Lubrication Technology* 1983, **105**, 198–205
7. Hills D.A., Sackfield A. and Uzel A.R. Stress concentration in tractive rolling. *Proceedings of the 12th Leeds-Lyon Symposium on Tribology, Lyon, France, 1985*, pp. 171–177
8. Bower A.F. The influence of crack face friction and trapped fluid on surface initiated rolling contact fatigue cracks. *Transactions of ASME, Journal of Tribology* 1988, **10**, 704–711
9. Kaneta M., Murakami Y. and Yatsuzuka H. Propagation of surface cracks in rolling line contact. *Proceedings of the JSLE International Tribology Conference, Tokyo, Japan 1985*, pp. 911–916
10. Rosenfield A.R. A fracture mechanics approach to wear. *Wear* 1980, **61**, 125–132
11. Way S. Pitting due to rolling contact. *ASME Journal of Applied Mechanics* 1935, **2**, A47–A58
12. Kaneta M., Yatsuzuka H. and Murakami Y. Mechanics of crack growth in lubricated rolling/sliding contact. *ASLE Transactions* 1985, **28**, 407–414
13. Bold P.E., Brown M.W. and Allen R.J. A review of fatigue crack growth in steels under mode I and mode II loading. *Fatigue Fracture of Engg Materials and Structures* 1992, **15**, 965–977
14. Smith E.W. and Pascoe K.J. The behaviour of fatigue cracks subjected to biaxial stress: a review of the experimental evidence. *Fatigue Fracture of Engg Materials and Structures* 1983, **6**, 201–224
15. Kalousek J. General discussion. Third International Conference on Contact Mechanics and Wear of Rail/Wheel Systems, Cambridge, July, 1990. *Wear* 1991, **144**, 385–393

APPENDIX 4

The paper entitled "**Deterioration of rolling contact fatigue of pearlitic rail steel due to dry-wet rolling-sliding line contact**" was submitted to *WEAR* on 1.9.1994.

Referees' comments were received on 20.1.1995.

A reply to those comments was sent to the journal on 15.2.1995.